CARBON NITRIDE DEPOSITION BY MAGNETRON SPUTTERING: STRUCTURAL, MECHANICAL, ELECTRICAL AND OPTICAL PROPERTIES

Presented by

MIGUEL ALBERTO MONCLUS PALAZON

as the fulfilment of the requirement for the degree of

DOCTOR OF PHILOSOPHY

at

DUBLIN CITY UNIVERSITY
SCHOOL OF ELECTRONIC ENGINEERING

Research supervisor
Dr. David Cameron

February 2000

Caminante no hay camino,
se hace camino al andar.

Antonio Machado

DECLARATION

I declare that all the unreferred work described in this thesis is entirely my own, and no portion of the work contained in this thesis has been taken from the work of others save and to the extent that such work has been cited and acknowledged within the text of my work.

SIGNED: Miguel Morales **Date** 22-2-00

I.D. Number 95970614

ACKNOWLEDGEMENTS

Firstly, I'd like to thank my supervisor Dr. David Cameron. I am extremely grateful for all the advice and suggestions given towards the problems solved. His guidance, especially during the hard times I went through kept me going until the end.

To Shaestagir Chowdhury, with whom I worked most of the time, and as a result our team work produced very valuable results. Also thanks to Dr. Robert Barkley and Michael Collins from Trinity College for their help with some measurements.

To the technicians in the electronic engineering department: Conor Maguire, Liam Meany, Robert Clare, Stephen Neville and Paul Wogan for providing me with the required supplies and for their kindness. My sincere thanks are expressed to the technicians in the mechanical engineering department and the mechanical workshop. I'm particularly grateful to Liam Domican for his technical support.

I'd also like to thank Dr. Pat McNally, for his continuous advice and support. Thanks to old and present fellow research students in D.C.U.- Michael Murphy, Emmet Caulfield, John Curley, Colm O'Leary, Ivonne Kavanagh, Jahangir Alam, David Neary, Donnacha Lowney, Jarujit Kanatharana and countless others; I appreciate their help and support. A Suzanne Carey, por sus animos de guays. Also to Denis Dowling and Kevin Donelly in Enterprise Ireland, for their valuable advice and for trusting me in the use of the Nanoindenter.

Finally, my most sincere gratitude is extended to my parents, who have given me their utmost support to all that I have tried to do. I can't ever repay them enough. Mama y papa: muchisimas gracias por todo. Also to my brother and sisters, for always supporting me along the way.

Thank you.

Miguel A. Monclus Palazon, February 2000.

CARBON NITRIDE DEPOSITION BY MAGNETRON SPUTTERING: STRUCTURAL, MECHANICAL, ELECTRICAL AND OPTICAL PROPERTIES.

ABSTRACT

Carbon nitride films were deposited using a magnetron sputtering technique based on the Penning type geometry. For deposition, graphite targets were used in a nitrogen/argon gas mixture. The technique employed consists of two opposing cathodes, with two very strong magnets placed behind them. The magnetic field created with this configuration, in conjunction with the electric field, provides a high ion flux at the substrate, which results in high deposition rates (up to 3μm/h) and increased nitrogen incorporation in the films (up to 45 at.% N). The effect of deposition parameters, such as nitrogen partial pressure (Npp), substrate bias, and deposition temperature on the film properties has been investigated.

The effect of nitrogen addition on the structural properties of carbon nitride films has been characterised in terms of its composition, infrared and Raman spectra and X-ray photoelectron spectroscopy (XPS). Nitrogen content in the films was measured by Rutherford Backscattering (RBS) and film thickness by a surface profilometer. Infrared spectra revealed that the films have an amorphous structure, in which nitrogen is mainly incorporated in C=N sp^2-type bonding configurations, with some proportion of C≡N sp-type bonding, which increases with nitrogen incorporation. Above 20 at.% N, a structural rearrangement occurs in which N preferentially bonds to itself. Core level XPS peaks due to carbon and nitrogen 1s electrons were assigned to different types of bonds in accordance with Raman and IR spectra and by comparison with other assignments found in literature.

A Nanoindenter instrument was employed to investigate the mechanical properties of the films. Nanoindentation load-displacement curves provide a 'mechanical fingerprint' of the material's response to contact deformation. Hardness and elastic modulus values obtained for carbon nitride films using the Oliver and Pharr technique ranged from 8-12 GPa and 90-120 GPa respectively. Hardness was shown to decrease with Npp but was not dependent on total nitrogen content. Hardness was better correlated to the C≡N bond concentration; the increased amount of C≡N bonds causes a weakened structure as they serve as network terminators in the carbon backbone structure. The hardness of the films correlates with the presence of a graphite-like structure dominated by sp^2 bonding structure. The effect of substrate bias, annealing and deposition

temperature on the film's hardness and structure is also described. Higher coefficients of friction were found for harder films deposited at different substrate bias. The stress is shown to be concentrated at the film-substrate interface whereas the bulk of the film is stress-free and increases at higher substrate bias as ion bombardment increases.

The XPS and ultraviolet photoelectron spectroscopy (UPS) valence band (VB) spectra have been reported. The evolution of bands corresponding to π and σ bonding with Npp reveals that there is a greater degree of sp^2 bonding as the nitrogen partial pressure (Npp) is initially increased compared to the pure carbon samples. However, with further increase in Npp (reaching 100%), the bonding becomes more sp^3-like. The films' electronic states were further investigated as a function of Npp using techniques such as electron energy loss spectroscopy (EELS) and electron spin resonance spectroscopy (ESR). The observations reported point to the reasons why crystalline β-C_3N_4 material has been found only with high Npp despite the fact that nitrogen content is not significantly enhanced in this situation.

Various electrical analysis techniques were employed to study the electrical properties of carbon nitride films. The four-point probe and van der Pauw methods were used for resistivity measurements. From these analyses, the resistivity was found to increase with Npp, and to be controlled by the amount of C≡N bonding, which causes a decrease in the number density of electrons available for conduction. N is incorporated in the films in a non-doping configuration. From temperature-dependent resistivity measurements, it was proposed a transition from metallic to semiconducting behaviour as nitrogen is incorporated in the films. A conduction mechanism typical of low mobility amorphous semiconductors was suggested. An increase in both negative substrate bias and deposition temperatue produce films with lower resistivity. The optical gap was estimated from absorption coefficient measurements in the ultraviolet-visible region. Refractive index and extinction coefficient measurements are also reported. An electron emission configuration revealed that it is possible to obtain moderate emission current from a number of carbon nitride films.

Despite the fact that the analysis techniques considered here give results consistent with an amorphous carbon nitride solid, there is some evidence of crystalline β-C_3N_4 areas co-existing with the mainly amorphous structure for films deposited at 100% Npp. There is room for further optimisation of the quality of carbon nitride films deposited by reactive Penning-type magnetron sputtering with respect to composition, structure and application-relevant properties.

CONTENTS

CHAPTER 1

INTRODUCTION

1.1 General overview

The search for interesting properties of carbon nitride thin films deposited using a recently designed and constructed deposition source led to the commencement of this project. Carbon nitride materials represent an exciting challenge to both fundamental and applied research. There has been in the last few years a significant experimental and theoretical interest in the synthesis and properties of these materials. All this research work is mainly due to the early theoretical predictions by Liu and Cohen,[1,2] suggesting that a hypothetical material, β-C_3N_4, with a structure analogous to β-Si_3N_4, would have hardness comparable to that of diamond. According to this theory, carbon nitride may surpass other high-performance engineering materials like diamond, diamond-like carbon (DLC), cubic-BN, amorphous hydrogenated carbon and Si_3N_4.

Some of the material's remarkable features would include its chemical inertness, large bandgap (~6 eV), large thermal conductivity, transparency to visible light and tuneable optical constants.[3] Regarding mechanical properties, its ultra-high hardness and extremely low wear resistance give this material great potential for industrial applications such as cutting tool, high density storage on hard disks and magnetic recording, and as wear reduction coatings on mechanical components. Carbon nitride materials can also be very useful as protective coating, for heat regulation in microelectronics, or in all kind of optical devices.

In view of all these extraordinary possibilities, it is not surprising all the effort expended on the synthesis of the carbon nitride compound. Many techniques have been used for this purpose, with a wide range of compositions and properties reported so far. Of course, the hot item in all these experimental work is the deposition of

crystalline carbon nitride. All this continuous research also enriches the theoretical background to develop new materials. Only a few of these techniques succeeded in getting polycrystalline material; most of them resulted in amorphous carbon nitride (a-C:N), in which the local carbon bonding is predominantly sp^2, which is typical of low density, graphitic structure, instead of the required uniform tetrahedral sp^3 carbon bonding expected for pure β-C_3N_4 or other high density phases.[1,2] However, carbon nitride films with an amorphous structure are also considered as promising engineering new materials, since they already possess some very interesting properties, so that they may be a very interesting research subject as well. Properties such as high hardness, low friction coefficient, chemical inertness, and variable optical gap give this material extraordinary possibilities for wear-resistant hard coating, protective optical coating, protective coating on magnetic disk drives,[4] and also as a novel semiconducting material.[5] Amorphous CN films are already being applied industrially.[6]

Initially, the project was started by undertaking a literature review of thin film deposition techniques and especially magnetron sputtering processes, in order to gain an understanding of all the factors involved in the deposition of thin films, and especially carbon nitride films. The deposition experiments were carried out in the high vacuum system existent in DCU. This system was originally designed to host a conventional planar magnetron sputtering source; with this technique, amorphous carbon nitride films have been deposited previously, with a maximum nitrogen content of 18 at.%, and results have been published.[7,8] This source was replaced by a new approach, based on the Penning type magnetron sputtering source,[9] capable of producing higher levels of ionisation at the substrate.[10] Time was spent learning the operation of the different parts of the high vacuum system, and the characteristics of this new magnetron source. The factors to bear in mind to perform thin film depositions were deeply investigated in order to get a better understanding of the correlation between deposition parameters and quality of the films to be deposited.

The first carbon nitride films deposited with this new approach were encouraging, since nitrogen incorporation of up to 39 at.% was obtained, which is close to that of

stoichiometric C_3N_4 (57 at.%). At this point, it was decided to explore further the possibilities that this new approach could offer in the deposition of novel carbon nitride thin films. The main objectives of this work, done within the Plasma Coating Group of DCU, is the deposition of novel carbon nitride films using a new magnetron sputtering technique and the characterisation of the films in terms of their structural, electrical, optical and tribological properties. In order to understand all these film properties, several characterisation techniques were used to investigate the films morphology, chemical state and electronic structure.

There are only a few complete studies on the electrical properties of carbon nitride films. These properties are closely related to the structure, which strongly depends on the film preparation method used. Different techniques for electrical measurements were investigated and applied to carbon nitride films in order to characterise the carbon nitride coating in greater detail that have been found in literature. Electrical properties such as resistivity, activation energy, band gap and density of defect states were then correlated with the internal structure of the films by investigating, for example, the chemical state of the top layers with X-ray photoelectron spectroscopy. Optical properties of the layers were also examined, such as refractive index and optical absorption in the violet/visible energy region.

There has been much interest in the mechanical properties of thin films during the past decade, due to its extensive use in microelectronic devices and as protection against wear and corrosion. The predicted high hardness and low friction of carbon nitride films might allow them to compete with DLC coatings in magnetic media protection.[11,12]

The use of nanoindentation techniques for determination of mechanical properties of thin films has gained a widespread use in recent years, and the literature contains numerous descriptions of micro and nanoindentation equipment.[13,14,15,16] In this work, a nanoindentation instrument (Nanotest 500, Micromaterials) was used for mechanical testing of carbon nitride films, with a focus on deformation behaviour and hardness measurements. In order to achieve this goal, the instrument performance was fully

investigated, along with all the factors affecting measurements of small volumes and the correct interpretation of the data obtained with this technique.

Subject of the thesis

The main subject of this thesis is the deposition of carbon nitride thin films using a magnetron sputtering technique and the characterisation of the films in terms of their electrical, mechanical and structural properties. The control of the experimental parameters such as growth temperature, sputtering gases concentration and working pressures is also a major concern of this thesis.

The remainder of this chapter is concerned with a brief discussion of possible structural modifications of carbon nitride compounds. This will be followed by a general review of carbon nitride deposition processes as well as some of the general properties of carbon nitride films. The possible doping of amorphous carbon by nitrogen is also pointed out. Finally, the organisation of this thesis will be presented.

1.2 Carbon nitride compounds – possible structures and properties

Back in 1984, C.M. Sung[17] predicted that a hypothetical material C_3N_4 may be harder than diamond. His theory suggests that C_3N_4 may exist with two phases (α and β), with the same structure as the corresponding phases of Si_3N_4. The β phase is the high temperature phase. In the structure of this material, each carbon atom has four nearest-neighbour nitrogen atoms forming an almost regular tetrahedron while each nitrogen atom has three nearest-neighbour carbon atoms forming 120° bond angles in a planar configuration. This atomic configuration produces an infinite three-dimensional covalent network with strong bonding in all directions. *Figure 1.1* shows the β-C_3N_4 structure in the a-b plane.

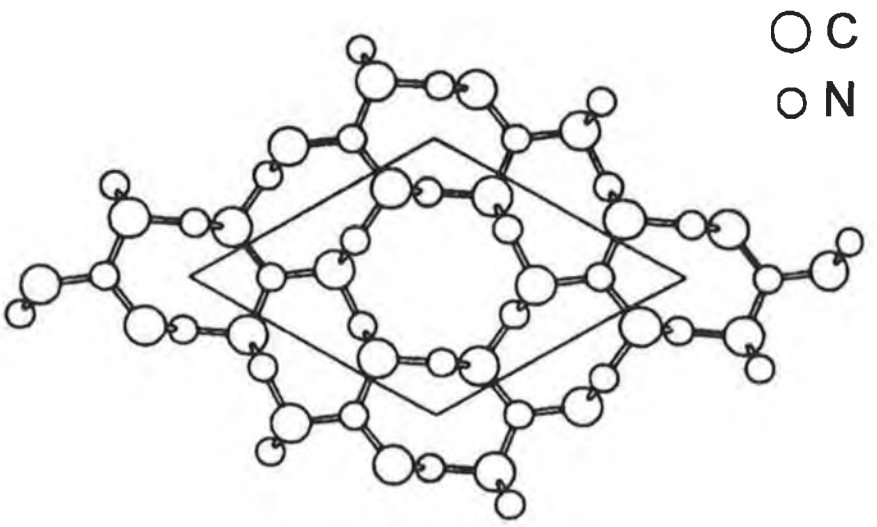

Figure 1.1: Structure of β-C_3N_4.

In the figure, the parallelogram shows the unit cell and contains two formula units (14 atoms). The structure can be seen as a complex network of CN_4 tetrahedra linked at the corners. The α-C_3N_4 structure can be described as an ABAB... stacking sequence of layers of β-C_3N_4 and its mirror image, and the unit cell contains 28 atoms. The very short interatomic distances for C_3N_4 is one of the main reasons for its expected extreme hardness.[14] Cohen calculations[1] of the bulk modulus were based on a β-Si_3N_4 type structure, where carbon atoms were substituted for the silicon atoms and predicted that β-C_3N_4 bulk modulus is about 4.83 Mb, higher to that found for diamond (4.35 Mb) and, furthermore, that β-C_3N_4 exhibits a cohesive energy which suggests that the structure may be metastable. The calculation of the bulk modulus is outlined below, where B, the bulk modulus (Mbar) is given as:[1]

$$B = \frac{19.71 - 2.2\lambda}{d^{3.5}}$$

where d is the bond length (Angstroms) and λ is the ionicity. *Table 1.1* gives theoretical and experimental values for the bulk modulii of some materials calculated by this method.

Material	d (Angstroms)	ionicity (λ)	B (Mbar) (Calc)	B (Mbar) (Expt)
Diamond	1.54	0	4.35	4.43
β-C_3N_4	1.47	0.5	4.83	-
c-BN	1.56	1	3.69	3.67
β-Si_3N_4	1.83	0.5	2.65	2.56

Table 1.1: Calculated and experimental bulk modulii for various materials.

Other possible crystal modifications with composition C_3N_4 have also been proposed.[18,19] In their work, various theoretical techniques were applied such as miscellaneous molecular-dynamics methods, first principles pseudopotentials and local-density approximations. Two other C_3N_4 phases were considered and described as defect zinc-blende-like cubic structure and defect layered graphitic-like structures.[18,19] The cubic structure is similar to β-C_3N_4 in that each C atom has four N neighbours and each N atom has three C neighbours. However, N atoms form sp^3 rather than sp^2 bond orbitals, with one lone pair directed at an empty C site. In the defect graphitic phase, each C atom is three-fold coordinated, as is one of the four N atoms per cell. The other three N atoms are near neighbours of a missing C atom and hence are only two-fold coordinated, as seen in *figure 1.2*. The interlayer bonding in this graphitic structure is weak.

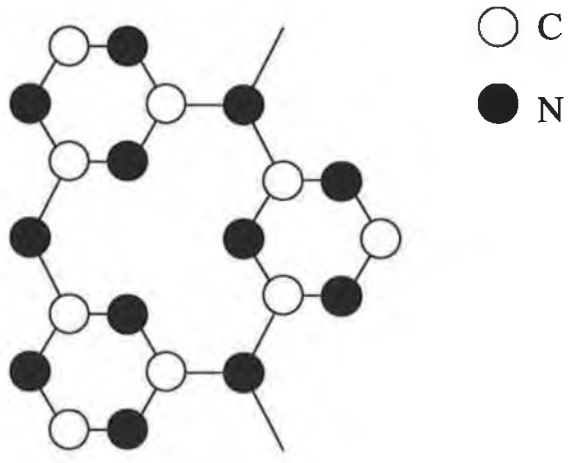

Figure 1.2: Structure of a single layer of graphitic-like C_3N_4.

It was calculated that the graphitic structure is the least dense, the most compressible and the most stable phase.[18] The cubic phase is slightly more dense than the β phase, but its C-N bonds are longer which results in a slightly smaller bulk modulus. Even though the crystalline phases of C_3N_4 may not be the lowest energy phases (the most energetically favourable structures) in the C_3N_4 system, they can still, in theory, be synthesised in the laboratory, since they are at least metastable.[19]

In addition to the structures already mentioned, other carbon nitride compounds and structures can exist since the chemistry of compounds containing the CN group is very extensive. A review of known compounds containing carbon and nitrogen along with a discussion of their chemistry can be found at Greenwood et al.[20] Nitrogen can form an amorphous compound with carbon such as in paracyanogen $(CN)_x$. Cyanogen $(CN)_2$ is a colourless poisonous gas, and a typical constituent of a comet's gas tail. When pure it possesses considerable thermal stability (800°C) but trace impurities normally facilitate polymerisation at 300-500°C to paracyanogen, which is a dark-coloured, highly inert solid of high molecular weight, which may have a condensed polycyclic structure. Such a planar six-membered ring structure is shown in *figure 1.3*. This solid paracyanogen is insoluble in water and organic solvents, and it can be completely converted into cyanogen gas by heating to about 860° C.

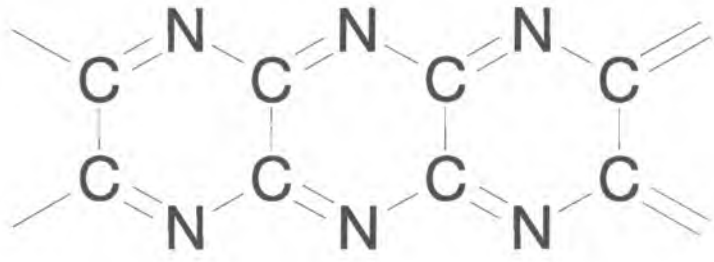

Figure 1.3: The six membered ring structure of paracyanogen.

Kaufman et al.[21] proposed a model for the nitrogen-doped carbon solid where nitrogen atoms replace one of the carbon atoms in the carbon-carbon homocyclic ring structure. This is how the carbon nitride solid can have the C=N sp^2 type matrix. C=N type bonding enables carbon to form an amorphous compound with nitrogen, which is

considered to have an structure analogue to graphite.[22] Marton et al.[23] proposed models regarding the bonding nature of a CN compound and suggested that a nanocrystalline structure which is predicted as β-C_3N_4 could be formed within the sp^2 type C=N matrix. The stability of tubule forms of graphitic carbon nitride (C_3N_4 and CN atomic composition) has been investigated by Miyamoto et al.[24] and several paracyanogen-like structures in high density amorphous carbon nitride have been theoretically simulated by Weich et al.[25] Many possible structures are possible for CN compounds depending on the deposition technique used, as briefly discussed in section 1.3.

Electronic and mechanical properties of deposited carbon nitride layers are determined by bonding of carbon and nitrogen atoms. Hardness measures the material's ability to resist deformation. The upper limit of hardness is determined by the rigidity of a material's crystal structure. There are three factors that contribute to the rigidity of a crystal structure: (1) large coordination number of the atoms, (2) high covalent character of bonds, and (3) short interatomic distance of the structure, i.e., small atoms.

A high coordination number allows atoms to be surrounded by a large number of neighbours, so that more bonds support each atom. A high degree of covalence increases the strength of these bonds, so each atom is held firm in its lattice position. Small atomic size makes bonds shorter so it improves the effectiveness of the support. The combined effect of these three factors is to concentrate the bond energy in a small volume, so a large stress is required to deform the crystal lattice.

The effect of coordination number on hardness is revealed by the contrast of hardness between diamond and graphite. Although these two phases are polymorphs of carbon and their bonds are both covalent, they differ in coordination number. Carbon atoms in diamond are in four-fold (tetrahedral sp^3) coordination. These bonds are symmetrically distributed with a bond angle of 109°47'. As a result, the crystal lattice is supported in all directions. In contrast, carbon atoms in graphite are in three-fold (ternary or sp^2) coordination. These atoms do not have enough bonds to form a three-dimensional

network, so they form two-dimensional basal planes. These planes are held together by weak van der Waals bonds. Therefore, graphite becomes one of the softest materials known. Four bonds are the least needed to support an atom in three dimensions. This is because four bonds can define a tetrahedron, the simplest polyhedron. For example Silicon atoms in Si_3N_4 are diamond-like with tetrahedral coordination. However, nitrogen atoms posses only three bonds, so they have planar coordination. Despite of this, Si_3N_4 is a well established hard ceramic material. It has two modifications, α and β phases. In both structures silicon atoms are in tetrahedral coordination, i.e. sp^3, and nitrogen atoms in ternary coordination, i.e. sp^2. The hypothetical compound C_3N_4, due to its short interatomic distances, is suspected to be very hard. The interatomic distance of C_3N_4 is more than 5% shorter than diamond.[17]

The most recent values of the bulk moduli for the cubic, α and β phases are 496, 425 and 437 GPa.[18] These values are similar to that of diamond at 433 GPa. Similarly, the velocity of sound in β-C_3N_4 has been estimated to be high ($\sim 10^6$ cms^{-1}), meaning that the material should have a high thermal conductivity. The bandgaps of all three phases have been predicted to be high (in the range 3-4 eV), with atomic densities approaching that of diamond.[18]

The film properties of the hypothetical β-C_3N_4 have been theoretically predicted.[26] β-C_3N_4 was found to be a semiconductor with a large band gap. Using β-Si_3N_4 as a prototype, Liu et al.[2] calculated the lattice constant, bulk modulus and band structure of β-C_3N_4. The calculations for β-Si_3N_4 are in good agreement with experiment, which leads to support their calculations. The charge distribution in this structure is in the bonding region stabilising the compound. Since the band gap calculated is 1eV higher than in diamond, it may find many uses as a hard transparent solid. The optical properties of β-C_3N_4 were also studied by Yao et al.[27] and their results agreed with Cohen's, indicating a very hard optical material, with a dielectric constant of 3.2.

1.3 General review of carbon nitride deposition processes

This section begins with an introduction to the main techniques used for thin film deposition, which is followed by a review about some of the techniques that have been used for the deposition of carbon nitride thin films. The particular advantages and results obtained with each technique are briefly discussed. Experimental studies have proven the difficulty to grow a true C_3N_4 film. The small carbon atoms may be responsible for the unstable structure, since Si_3N_4 is a stable structure at atmospheric pressure, and the only difference in both structures is the larger size of the Si atoms. The best hope of synthesising C_3N_4 is controlling the kinetic of the process, so that the growth of C_3N_4 is faster than other competing processes, such as the precipitation of the ubiquitous CN_x. In most of the experiments, the resulting materials are amorphous with a combination of CC and CN bonds. Some issues concerning the deposition of crystalline C_3N_4 and the validity of some claims reported in literature about the successful synthesis of the crystalline C_3N_4 phase are also briefly discussed below.

1.3.1 PVD vs. CVD deposition techniques

The most common deposition techniques used for thin film deposition are vapour deposition methods, which are divided into Chemical Vapour Deposition (CVD) and Physical Vapour Deposition (PVD). CVD processes involve a chemical reaction of a volatile compound of the material to be deposited, with other gases, to produce a non-volatile solid that deposits on a suitable placed substrate. In PVD processes, on the other hand, one or more of the reaction species undergoes sublimation from the solid phase to the vapour phase, which can occur either by evaporation of the source material or by sputtering. In an evaporation process, atoms are removed from the source by thermal means, while in sputtering, atoms are displaced from a solid target (source) surface through impact of gaseous ions. The objective of these two methods is the same: to transfer atoms, in a controlled way, from a source to a substrate where film formation and growth proceed atomistically.

In CVD processes, the source of energy for activating the chemical reaction leading to film deposition can be obtained by heating the substrate or using rf or microwave plasmas. CVD processes are usually high temperature techniques, whereas PVD can be considered a low temperature technology (<500°C). Finally, CVD techniques produce materials with larger grains than with PVD techniques, in which the fined grain structure reduces the risk of cracking and leaves a smoother surface finish. This is because in CVD, little bombardment of the surface takes place, which also results in softer films compared to PVD. The main disadvantage associated with CVD is the high substrate temperature (>600°C) required for many coatings, which often results in the softening and distortion of substrates.

Among the PVD techniques, dc or rf magnetron sputtering techniques have often been used because of their advantages of coating uniformity, higher deposition rates and producing electrically insulating films at low temperatures. Magnetron sputtering techniques are described in detail in the next chapter.

1.3.2 Deposition techniques used for carbon nitride

Owing to their flexibility, vapour phase deposition methods have been used frequently in studies aimed at producing CN_x compounds in the form of thin surface layers. Many attempts have been made to synthesise carbon nitride films by PVD and CVD techniques. PVD techniques include those such as ion beam deposition (IBD),[28] ion beam assisted deposition (IBAD),[29] pulsed laser deposition (PLD) (laser ablation of graphite in a nitrogen atmosphere),[30] filtered arc deposition (FAD) and ion assisted arc deposition (IAAD),[31,32] arc ion plating,[33,34] and electron cyclotron resonance plasma (ECR) source.[35] The carbon nitride films obtained were mainly amorphous, and the nitrogen content was usually far below that of stoichiometric β-C_3N_4. Important aspects related to the use of some of the techniques used for carbon nitride growth are now briefly described:

Ion beam deposition: nitrogen bombardment of carbon has been used on a variety of carbon substrates (glassy carbon, amorphous carbon and diamond) with a wide range of nitrogen bombardment energies and substrate temperatures (-200 to 800° C). When high nitrogen bombardment energy is used (>1 keV) there are problems related to the measurement of the nitrogen content since the nitrogen is implanted only into a certain subsurface volume of the carbon, and the size of the volume considered during the measurement of the composition determines the percentage value. At the lower energies, the N/C ratio has been reported to be controlled mainly by the ion dose, rather than the ion energy.[36] There has been no evidence of the formation of either a crystalline material or a C_3N_4 compound with this technique. Alternating carbon and nitrogen beams have also been used to directly deposit CN compounds, where both the ion energies and the relative arrival rates can be controlled.[37] Chemical sputtering of carbon and CN groups by nitrogen was found to be of great importance, with the erosion rate depending on the incident ion energy and the binding energy of the carbon groups to the substrate. The structure of the CN deposit is found to be dependent on the energy of both the carbon and nitrogen ions.[36] The only crystalline phase that has been observed was graphite.

Arc deposition: deposition using a high-current electric arc has the distinction that film growth can be made, almost completely, through the interaction of low-energy ionised species. Both filtered and unfiltered cathode arcs have been used in the preparation of carbon nitride compounds. In the unfiltered version, macroparticles of the graphite target are nearly always incorporated in the deposit. The incident energy of the carbon ions is typically ~20 eV and nitrogen-ion energies ranging from 2 to 200 eV have been used, with chemical sputtering limiting nitrogen incorporation for energies in excess of 10 eV.[38] The composition of the deposited film is strongly dependent on the relative arrival rates of carbon and nitrogen ions. None of the deposits prepared using arcs have contained crystalline CN compounds, which has been related to a decrease of sp^3 bonding for nitrogen concentrations >10%.[39,40]

Laser ablation: laser ablation of graphite targets in nitrogen or ammonia atmosphere, both with and without ion bombardment of the substrate has been used.[41,42] The laser-plasma plume generates large quantities of N_2^+ but little atomic nitrogen. Molecular nitrogen ions remove nitrogen by chemical sputtering and are inefficient at helping nitrogen incorporation. The highest nitrogen concentrations have been obtained by using large quantities of atomic nitrogen, either by using a remote secondary plasma together with the laser ablation, or by tuning the laser wavelength to cause decomposition of the nitrogen-containing gas. Most deposits to date have been amorphous forms of carbon nitride.[30] There have been some reports of the formation of small crystals using laser ablation, but there is controversy with the identification of the precise structure of the crystals.[43]

The most common CVD methods used include hot-filament CVD,[44] and plasma enhanced CVD either using microwave plasmas or rf plasmas which basically involves the excitation of a gas mixture of hydrocarbons and nitrogen containing gases.[45] The hot-filament CVD technique is a modified version of that used for diamond growth, but here CH_4 is mixed with either N_2 or NH_3+H_2. The filament and substrate temperatures are normally as high as 2100 and 800-900° C respectively. It was argued that hydrogen plays a similar role in carbon nitride formation as it does in diamond growth and that plentiful amounts of both atomic hydrogen and atomic nitrogen are required to create C_3N_4.[46]

RF plasma enhanced chemical vapour deposition (PECVD) in which nitrogen gas acts as sputtering gas and reactive precursor gas simultaneously was used to produced films composed of an amorphous matrix and microcrystalline β-C_3N_4.[47] Muhl et al.[48] used PECVD with chemical transport from a hollow graphite cathode and observed deposits of crystals of ~20 μm diameter corresponding to β-C_3N_4 according to electron and X-ray diffraction studies. It has also been shown that hydrogenated amorphous carbon nitride films (a-C:N:H) deposited by RF PECVD of methane-nitrogen mixtures can be as hard as diamond like carbon films.[49] The incorporation of small amount of nitrogen causes a considerable reduction of the internal stress, with little change in the

film's hardness. This made a variety of applications possible such as anti-reflecting coatings in IR sensors, protective coatings for computer hard disc, etc.[50]

Microwave plasma-enhanced chemical vapour deposition (MW-PECVD)[51] produced crystalline carbon nitride films at temperatures >1000°C. The large crystals observed were due to the very high substrate temperatures and the incorporation of silicon into the crystals. Large crystalline grains up to ~10 μm in size have been claimed by using a plasma assisted hot filament CVD system.[52,53]

The synthesis of carbon nitride from high-pressure pyrolysis of nitrogen bearing organic materials has been described by Sekine et al.[54] Crystalline carbon nitride (grains of 0.3 μm in diameter) were prepared by Lu et al.[55] using a photo-assisted synthetic process. They proposed this material as a future novel target to increase the crystallinity in carbon nitride films.

In the search of β-C_3N_4, every technique has advantages and disadvantages, which are now briefly discussed. In order to synthesise β-C_3N_4, CVD methods would be in principle a better choice since generally the mass transport between the gas phase and the deposit is larger, and a selective deposition of a high quality crystalline phase would be easier. Usually a hydrocarbon is used as a carbon source in CVD, but in that case, it is difficult to find hydrogen free deposition conditions. The stability of C-H and N-H bonds may preclude the formation of β-C_3N_4.[56]

For a successful synthesis of stoichiometric β-C_3N_4, a series of conditions have to be met during deposition. The simultaneous formation of paracyanogen (-$(CN)_n$-) is one of the major difficulties to overcome. In order to avoid its formation, temperatures above 800°C should be used to facilitate its evaporation, and also a suitable C/N ion ratio that provides a high concentration of atomic nitrogen to avoid the formation of C-N=C, which is characteristic of paracyanogen. Veprek et al.[57] prepared films by plasma CVD in an intense nitrogen discharge, in which sufficient excess of atomic nitrogen as compared with the concentration of CN radicals were present. They used energetic ion bombardment (100-200 eV) and temperatures of >800°C. Despite of

obtaining films with an interplanar spacing of about 3.56 Å, which agrees well with the calculated distance between double layers of β-C_3N_4, they were unable to obtain crystalline films. Wu et al.[58] used electron cyclotron resonance assisted CVD, and they used a layer of diamond deposited on Si as a substrate, resulting films with a C-N single bond state, with a bonding energy comparable to that of diamond.

Atomic hydrogen can stabilise sp^3 bonds at the expense of sp^2 bonds. Without the presence of a certain amount of atomic hydrogen to catalize the formation of diamond, the growth rate would be negligible and a true diamond film cannot be formed.[59] It is possible that during the growth of C_3N_4 a large amount of atomic hydrogen must also be used to eliminate unwanted deposition of CN_x. Sung et al.[60] described a process where C_3N_4 may be grown from a high powered dc arc that generates supersonic plasma made of predominantly dissociated gases of H_2, CH_4 and NH_3. The activated species bombard the surface of the substrate made of Si_3N_4 to catalize the nucleation of C_3N_4. The C-H and N-H bonds may be broken by irradiation of intensive energy tuned to their vibrational mode.

Crystal growth is promoted with elevated temperatures to enhance mobility of surface atoms. However, atom mobility can also be enhanced in a plasma-assisted deposition system by using appropriate substrate bias and power supplied to the plasma. In addition, stabilisation of certain crystal structures can be achieved by proper choice of substrates. For example, certain orientations of silicon and zirconium are lattice matched to some of β-C_3N_4 and C and N form strong chemical bonds with both substrate materials, thereby leading to improve the adhesion of the deposited coatings. During growth of carbon nitride films, the amount of N incorporation depends upon the effective N sticking coefficient at the growth surface, the N_2 desorption rate, and the desorption rate of volatile nitrogen-containing species such as CN radicals. All these processes are dependent upon temperature as well as the impingement rate of C and N containing precursors.[61] The differences in the experimentally observed and theoretically predicted stoichiometries and incomplete diffraction data suggest that β-C_3N_4 may not be the most stable structure or stoichiometry for binary carbon-nitride phases. The data available so far suggest that it will be dificult to prepare superhard

carbon nitride materials containing large amounts of nitrogen using physical deposition methods. Studies show that the thermodynamic and kinetic preferences of sp^2 bonded structures dominate the product materials for nitrogen compositions >12 at.%.[62] The total nitrogen concentration in the film is a less meaningful parameter since amorphous films have been obtained with nitrogen incorporation as high as 80 at.% N.[63] It is necessary to stabilise intermediate structures; for example, plasma-assisted CVD has been successfully employed to stabilise intermediate structures and has produced interesting crystalline materials.[64]

X-ray diffraction is often used to characterise the crystalline nature of the deposit but, because of the low atomic mass of both carbon and nitrogen, at least 1 μm of deposit is required to produce a clear spectrum. Additionally, as pointed out by Yu et al.[65], diffraction peaks have been observed for amorphous carbon or silicon thin films on (100) silicon substrates which coincide with those expected from the (200) reflection of β-C_3N_4. They are thought to be due to the normally forbidden (200) reflection from silicon with this becoming feasible because of the substrate stress generated by the coating. Electron diffraction is also used extensively to study the crystallinity of the deposits but sample preparation by ion milling can be expected to cause chemical sputtering with all the associated problems. However, a judicious choice of lattice parameter and group of reflections can be of great assistance in providing proof of the existence of crystals of the 'good' material in any particular study.

Most of the claims of crystalline β-C_3N_4 are based on indirect evidence and no work has yet presented unambiguous evidence for the crystallization of carbon nitrides with the proposed structures. In some cases, the successful synthesis of β-C_3N_4 has been deduced from electron diffraction studies[25,66] and crystal-structure images were taken with transmission electron microscopes. In all case, the identification has been more or less ambiguous since the crystals deposited were always small in amount and, in many cases, composed of small crystallites embedded in amorphous phases. The comparison of X-ray and electron diffraction data with those simulated for C_3N_4 structures has been, in almost all cases, the evidence given for the identification of the crystalline C_3N_4 phase.[62,67] An interesting review on the validity of the formation of crystalline

C_3N_4 has been published by Matsumoto et al.[67] They arrived to the conclusion that as far as X-ray and electron diffraction are concerned, the results of some experiments suggest the probability of the formation of disordered polytypic diamond in the presence of nitrogen and that further efforts are indispensable for synthesising materials that can unambiguously be identified as crystalline C_3N_4.

There have recently been several reports of crystalline carbon nitride films: Peng et al.[68] claim the formation of cubic C_3N_4 particles of nm size prepared in an induction thermal plasma. The results of the analysis of the structure by high-resolution transmission electron microscopy seem to provide good evidence even though they found a small amount of vacancies at the N sites and a larger lattice parameter than the predicted structure. Chen et al.[69] reported carbon nitride films deposited by reactive r.f. magnetron sputtering. Thermal annealing of the films at 900°C transformed the predominantly amorphous films into crystalline phases. The size of the crystals ranged from 0.05 to 1.2 μm, which were composed of a mixture of carbon nitride nanofibres and cubic C_3N_4 crystals embedded in an amorphous matrix. Even though the observed phases were not clearly identified, it was shown that magnetron sputtering is a promising method for producing new forms of carbon nitride materials of interesting and useful electronic and structural properties. Nano-crystalline carbon nitride was also recently prepared by ion beam sputtering.[70] Transmission electron microscopy (TEM) investigations indicated that the films contained a very dense and homogeneous distribution of nano-crystalline grains and spectroscopy studies showed a structure consisting of mainly sp^3-hydridised carbon as well as sp^2-hybridised nitrogen. However, the structure of these crystals was not determined since their TEM diffraction patterns only matched partially with the calculated pattern for β-C_3N_4. The successful production of β-C_3N_4 microcrystallites was also claimed by Hsu et al.[71] For deposition, they used an inductively coupled plasma sputtering method. The size of β-C_3N_4 crystallites was optimised with substrate temperature (up to 800° C). However, these crystals are embedded in an amorphous matrix containing C=N and C≡N bonds.

Microwave plasma chemical vapour deposition was recently used by Shi et al. [72] to synthesise crystalline C_3N_4 films composed mainly of α-C_3N_4 and β-C_3N_4. In this

case, apart from X-ray diffraction data, XPS, IR and Raman spectra also support the existence of crystalline C_3N_4. They also performed hardness test on the films and measured a very high bulk modulus of 349 GPa. This work is one of the best evidence given so far of the growth of a true crystalline C_3N_4 film.

Very few experiments have resulted in obtaining a material free of C=N type bonds. Lu et al.[73] and Zhang et al.[74] found a preferential formation of C=N bonds during deposition consistent with an extended inorganic carbon nitride solid. Reactive PLD CN_x films contained graphitic rings.[75] Baker et al. [76] proposed a model in which N is being substitutionally incorporated into regions of sp^2/sp^3 a-C type structure. Above ~20 at.% N, a nitrile-like C≡N form emerges, which occurs when a C atom has many N neighbours. The formation of these nitrile-like structures and CN radicals into the CN_x film structure presents a serious problem to form the β-C_3N_4 phase by vapour deposition methods.

To be completely convincing, the existence of a crystalline structure must be demonstrated by at least two independent methods and the results should be mutually consistent. Various characterisation techniques should be employed in parallel. The existence of crystalline C_3N_4 cannot be established definitively by incomplete XRD or electron diffraction data. However, evidence from diffraction data together with consistent information from, for example, Raman analysis would constitute a solid indication of the presence of crystalline C_3N_4.

1.4. Amorphous carbon nitride semiconductors

Since the deposited CN_x films have been mainly amorphous, an amorphous-semiconductor nature is expected. In order to understand the electrical properties that one might expect for amorphous carbon nitride films, these compounds can be regarded as nitrogen doped amorphous carbon films. One of the most significant reasons for the synthesis of this amorphous material is that it has important applications as a very good electronic material whose electronic structure and band gap can be controlled by changing the doping level of nitrogen.[77]

Amorphous carbon (a-C) is a material that greatly varies in its electrical properties depending on the deposition method and precursor species. Its semiconducting properties are poor due to a high defect density of states in the mobility gap.[78] Carbon can form tetrahedral sp^3, trigonal sp^2 and linear sp^1 hybridised bonds, consequently the resistivity values may vary between those of graphite, diamond and organic polymers. Evaporation or sputtering generally produces a-C films with graphite-like properties, i.e., small optical band gap and high electrical conductivity. In sputtered a-C, the band gap is usually small due to the presence of π and π^* states from the sp^2 sites. It has been suggested that a mixture of tetrahedral sp^3 and trigonal sp^2 bonding exists in a-C,[79] and the range of properties observed probably reflects the relative fractions of carbon atoms with these two types of bonding. Typically, it is hydrogenated to reduce the density of gap states by increasing the sp^3 to sp^2 ratio.[80]

It has been found that semiconducting forms of a-C, such as tetrahedral amorphous carbon (ta-C) and hydrogenated a-C (a-C:H) can be doped electronically using nitrogen.[81,82,83] The incorporation of nitrogen into these types of carbon films is an interesting topic in the electronic industry, due to the possibility of obtaining a semiconductor with a variable band gap. Nitrogen incorporation has led to a decrease in the optical band gap[84,85] or an invariant gap,[86,87] and the resistivity has been found to reduce as nitrogen concentration increases. The electrical properties, as already mentioned, depend very much in the deposition technique and the precursors used. For example, the optical band gap increases with increasing nitrogen concentration for films deposited with magnetron sputtering, which is different for films formed by the CVD method,[88] where the band gap decreases with increasing nitrogen concentration, due to the hydrogen-free nature of the former films. The doping effect found is always weaker than in hydrogenated amorphous silicon (a-Si:H), which is a widely used amorphous semiconductor with a continuously adjustable band gap.[89]

It is still unclear whether nitrogen incorporation in hydrogenated a-C increases the conductivity by doping (raising the Fermi level towards the conduction band) or by graphitization (narrowing the band gap). This is because nitrogen can take several bonding configurations in the a-C network,[28] which dictates its electrical properties.

Nitrogen atoms can take doping or non-doping configurations depending on the deposition technique used and the precursor materials.

Tetrahedral amorphous carbon (ta-C) is a highly sp^3 bonded form of carbon and has an optical gap of 2.0-2.5 eV.[90] Undoped, is a wide band gap semiconductor, with intrinsic p-type behaviour. Stumm et al.[91] pointed out the difficulty in achieving a good doping efficiency due to the large number of highly localized band tail states, which must be filled by an equal number of doping nitrogen atoms and the fact that the material is p type. He also studied the effect of nitrogen substitution in several diamond-like networks using a structural model and identified the possible conduction mechanisms resulting from nitrogen incorporation. Nitrogen-doped tetrahedral amorphous carbon (ta-C:N) deposited by Gerstner et al.[92] showed nonvolatile memory effects. Switching between high and low resistance states was characterised by two different conduction mechanisms. These films were used to fabricate 1-bit memory cells.

Hydrogenated amorphous carbon (a-C:H) can also be doped electronically using nitrogen. Meyerson and Smith[93] have demonstrated the n and p-type doping of this material by the incorporation of phosphorous or boron. Silva et al.[77] studied the effects of nitrogen addition on the structural and electronic properties of doped a-C:H (a-C:H:N). Amorphous hydrogenated carbon nitride (a-C:H:N) has a different structure (polymer vs. tetrahedral) from that of amorphous silicon nitride (a-Si:N).[94] The former demonstrates a decrease in both its optical band gap and structural disorder due to incorporation of nitrogen. The later displays the opposite behaviour.[95] Wood et al.[96] reported the deposition of a-C:H:N. In these films, the resistivity decreased significantly with light nitrogen doping which was attributed to the hydrogen loss in the carbon matrix, which increases the size of graphitic clusters and decreases the activation energy for thermally induced charge hoping.[97] It altered the film structure and made it more graphite like in its mechanical and electrical properties. Robertson et al.[80] concluded that for low concentrations, N is incorporated substitutionally in the tetrahedral network, whereas for high concentrations, N substitutes for carbon atoms in an sp^2-bonded carbon cluster. In all cases, the doping efficiency is low, and the

effect of different bonds between C and N in controlling the valence band is still unclear.[98]

One of the main objectives of this work is the investigation of electrical properties of magnetron sputtered CN films, and the variation of these properties with nitrogen incorporation and other deposition parameters. The above discussion will help to understand the role of the nitrogen atoms in the CN_x films investigated in this work.

1.5 Organisation of the thesis

This thesis is organised into 8 chapters. A general review of carbon nitride deposition techniques and properties has been described in this introductory chapter. The rest of the chapters are organised as follows:

- Chapter 2 presents a review of sputtering of carbon nitride. A detailed review of sputtering as a technique for thin film deposition is also given.

- Chapter 3 describes in detail the Penning type magnetron sputtering source and its use for the deposition of carbon nitride films.

- Chapter 4 deals with the structural properties of the deposited carbon nitride films. The analysis techniques used are also described.

- Chapter 5 deals with the mechanical properties of the deposited carbon nitride films. The nanoindentation technique and its use for the mechanical characterization of thin films are also described.

- Chapter 6 examines the electronic states of carbon nitride films investigated by a variety of analysis techniques.

- Chapter 7 is concerned with electrical and optical properties of the films and the experimental set ups used for the film's characterization. Field emission measurements are also presented.

- Chapter 8 presents the conclusions of this research and offers suggestions for further studies.

References

1. A.Y. Liu and M.L. Cohen, Science, 245 (1989) 841.
2. A.Y. Liu and M.L. Cohen, Phys. Rev. B, 41 (1990) 10727.
3. H, Yao and W.Y. Ching, Phys. Rev. B, 50 (1994) 11231.
4. R. W-J. Chia, A. Li, S. Sugi, G.G. Li, H. Zhu, A.R. Forouhi, Iris Bloomer, Thin Solid Films 308-309 (1997) 284.
5. J.H. Kim, D.H. Ahn, Y.H. Kim, H.K. Baik, J. Appl. Phys. 82 (1997) 658.
6. V. Hajek, K. Rusnak, J. Vlcek, L. Martinu and H.M. Hawthorne, Wear 213 (1997) 80.
7. P.V. Kola, D.C. Cameron, M.S.J. Hashmi, Surface and Coatings Technology, 68-69 (1994) 188-193.
8. P.V. Kola, D.C. Cameron, B.J. Meenan, K.A. Pischow, C.A. Anderson, N.M.D. Brown, M.S.J. Hashmi, Surface and Coatings Technology, 74-75 (1995) 696.
9. P.M. Penning, Physica 3 (1936) 873.
10. M.J. Murphy, J. Monaghan, M. Tyrrell, R. Walsh, D.C. Cameron, A.K.M.S. Chowdury, M. Monclus and M.S.J. Hashmi, J. Vac. Sci. Technol. A 17 (1999) 62.
11. A. Khurshudov, K. Kato and S. Daisuke, J. Vac. Sci. Technol. A 14 (1996) 2935.
12. P. Zou, M. Scherge, D. N. Lambert, IEEE Transactions on magnetics 31, (1995) 6.
13. D. Newey, M.A. Wilkins, and H.M. Pollock, J. Phys. E, Sci. Instrum. 15 (1982) 119.
14. J. Loubet, J.M. Georges, D. Marchesini, and G. Meille, J. Tribology (Trans. ASME) 106 (1984) 43.
15. T.W.WU, C.H. Wang, J. Lo, and P. Alexopoudos, Thin Solid Films, 153 (1987) 185.
16. K. Kinosita, Thin Solid Films, 12 (1972) 17.
17. C.M. Sung and M. Sung, Mater. Chem. Phys., 43 (1996) 1.

18. D.M. Teter and R.J. Hemley, Science 271 (1996) 53.
19. A.Y. Liu, R.M. Wentzcovitch, The American Physical Society, 50 (1994) 10362.
20. N.N. Greenwood and A. Earnshaw, Chemistry of elements, Pergamon Press, NY (1984).
21. J.H. Kauffman and S. Metin, Phys. Rev. B 39 (1989) 13053.
22. P.J. Durrant, Introduction to Advance Inorganic Chemistry, Longmans, London (1962).
23. D. Marton, K.J. Boyd, A.H. Al-Bayati, S.S. Todorov and J.W. Rabalais, Phys. Rev. Lett. 73 (1994) 118.
24. Y. Miyamoto, M.L. Cohen and S. G. Louie, Solid State Comms. 102 (1997) 605.
25. F. Weich, J. Widany and T. Frauenheim, Phys. Rev. Lett. 78 (1997) 3326.
26. Jennifer L. Corkill and Marvin L.Cohen, Phys. Rev. B 48 (1993) 17622.
27. H. Yao and W. Y. Ching, Phys. Rev. B 50 (1994) 11231.
28. T. Miyazawa, S. Misawa, S. Yoshidam, S.I. Gonda, J. Appl. Phys. 55 (1984) 188.
29. M. Kohzaki, A. Matsumuro, T. Hayashi, M. Muramatsu and K. Yamaguchi, Thin Solid Films 308-809 (1997) 239.
30. M.L. De Giorgi, G. Leggeri, A. Luches, M. Martino, A. Perrone, A. Zocco, G. Barucca, G. Majni, E. Gyorgy, I.N. Mihailescu and M. Popescu, Appl. Surf. Sci. 127-129 (1998) 481.
31. J. P. Zhao, X. Wang, Z.Y. Chen, S.Q. Yang, T.S. Shi, X. H. Liu and S. C. Zhou, Nuclear Instruments and Methods in Physics Reasearch B 127/128 (1997) 817.
32. J. P. Zhao, X. Wang, Z.Y. Chen, S.Q. Yang, T.S. Shi, X. H. Liu, Mat. Letters 33 (1997) 41.
33. O. Takai, Y. Taki, T. Kitagawa, Thin Solid Films 317 (1998) 380.
34. Y. Taki, T. Kitagawa and O. Takai, thin Solid Films 304 (1997) 183.
35. M. Diani, A. Mansour, L. Kubler, J.L. Bischoff and D. Bolmont, Diam. Relat. Mater. 3 (1994) 264.
36. N. Tsubouchi, Y. Horino, B. Enders, A. Chayaharan, A. Kinomure and K. Fujii, Appl. Phys. Lett. 72 (1998) 1412.
37. K.J. Boyd, J. Vac. Sci. Technol. A 13 (1995) 2110.
38. J. Hartman, J. Vac. Sci. Technol. A 15 (1997) 2983.

39. N. Xu, Y. Du, Z. Ying, Z. Ren, F. Li, J. Lin, Y. Ren, X. Zond, J. Phys. D: Appl. Phys. 30 (1997) 1370.
40. J.K. Walters, M. Kuhn, C. Spaeta and R.J. Newport, J. Appl. Phys. 83 (1998) 3529.
41. J. Bulir, M. Jelinek, V. Vorlicek, J. Zemekm and V. Perina, Thin Solid Films 292 (1997) 318.
42. W.-A. Zhao, C.W. Ong, Y.C. Tsang, Y.W. Wang, P.W chan and C.L. Choy, Appl. Phys. Lett. 66 (1995) 2652.
43. C. Niu, Y.Z. Lu, C.M. Lieber, Science 261 (1993) 334.
44. S. Matsumoto, K.K. Chattopadhyay, M. Mieno and T. Ando, J. Mater. Res. 13 (1997) 180.
45. H-X. Han and B. Feldman, Solid. State Comms. 65 (1988) 921.
46. P.H. Fang, Appl. Phys. Lett. 69 (1996) 136.
47. J.L. He, W.L. Chang, Thin Solid Films 312 (1998) 86.
48. S. Muhl, A. Gaona-Couto, J.M. Mendez, S. Rodil, G. Gonzalez, A. Merkulov and R. Asomoza, Thin Solid Films 308-309 (1997) 228.
49. A. Grill, V. Patel, Diamond Films Technol. 2 (1992) 25.
50. F.L. Freire Jr., Jpn. J. Appl. Phys. 36 (1997) 4886.
51. L.C. Chen, D.M. Bhusari, C.Y. Yang, K.H. Chen, T.J. Chuang, M.C. Lin, C.K. Chen and Y.F. Huang, Thin Solid Films 303 (1997) 66.
52. Y. Zhang, Z. Zhou, H. Li, Appl. Phys. Leet. 68 (1996) 634.
53. E.G. Wang, Y. Chen and L. Guo, Physica Scripta, T69 (1997) 108.
54. T. Sekine, H. Kanda, Y. Bando and M. Yokoyama, J. Mater. Sci. Lett. 9 (1990) 1376.
55. T-R. Lu, C-T. Kuo and T-M. Chen, Thin Solid Films 308-308 (1997) 126.
56. C. Niu, Y. Lu, C. M. Lieber, Science 261 (1993) 334.
57. S. Veprek, J. Weidmann, and F. Glatz, J. Vac. Sci. Technol. A 13 (1995) 2914.
58. K. Wu, E.G. Wang, J. Qing and G. Xu, J. Appl. Phys. 83 (1998) 1702.
59. H-C Tsai and D.B. Bogy, J. Vac. Sci. Technol. A 5 (1987) 3287.
60. C.M. Sung and M. Sung, Mat. Chem. and Phys. 43 (1996) 1.
61. W. Zheng and J.E. Sundgren, Chin. Phys. Lett. 15 (1998) 120.
62. J. Hu, P. Yang and C.M. Lieber, Phys. Rev. B, 57 (1998) R3185.

63. F. Fujimoto, K. Ogata, Jpn. J. Appl. Phys. Part 32, (1993) 1465.
64. Y. Chen, L. Guo and E.G. Wang, Mod. Phys. Lett. B 10 (1996) 615.
65. K.M. Yu, M.L. Cohen, E.E. Haller, W.L. Hansen, A.Y. Liu, I.C. Wu, Phys. Rev. B 49 (1994) 5034.
66. K.M. Yu, M.L. Cohen, E.E. Haller, W.L. Hansen, A.Y. Liu and I.C. Wu, Phys. Rev. B, 49 (1994) 5034.
67. S. Matsumoto, E.-Q. Xie and F. Izumi, Diam. Relat. Mater. 8 (1999) 1175.
68. Y. Peng, T. Ishigaki and S. Horiuchi, Appl. Phys. Lett. 73 (1999) 3671.
69. G.L. Chen, Y. Li, J. Lin, C.H.A. Huan and Y.P. Guo, Diam. Relat. Mater. 8 (1999) 1906.
70. T.R. Lu, C.T. Kuo, J.R. Yang, L.C. Chen, K.H. Chen and T.M. Chen, Surf. Coat. Technol. 115 (1999) 116.
71. C.Y. Hsu, F.C-N Hong, Diam. Relat. Mater. 8 (1999) 1315.
72. D.X. Shi, X.F. Zhang, L. Yuan, Y.S. Gu, Y.P. Zhang, Z.J. Duan, X.R. Chang, Z.Z. Tian and N.X. Chen, Applied Surface Science 148 (1999) 50.
73. Y.F. Lu, Z. M. Ren, W.D. Song, D.S.H. Chan and T.S. Low, J. Appl. Phys. 84 (1998) 2909.
74. Z. J. Zhang, S. Fan and C.M. Lieber, Appl. Phys. Lett. 66 (1995) 3582.
75. C.W. Ong, X.A. Zhao, Y.C. Tsang, C.L. Choy and P.W. Chang, Thin Solid Films 280 (1996) 1.
76. M.A. Baker and P. Hammer, Surface and interface analysis 25 (1997) 629.
77. S. R. P. Silva, J. Robertson, G. A. J. Amaratunga, R. Rafferty, M. L. Brown, J. Schwan, D. Franceschini and G. Mariotto. J. Appl. Phys. 81 (1997) 2626.
78. S.R.P. Silva, B. Rafferty, G.A.J. Amaratunga, J. Schwan, D.F. Franceschini, L.M. Brown, Diam. Relat. Mater. 5 (1996) 401.
79. I.J. Hauser and J.R. Patel, Solid State Comms. 18 (1976) 789.
80. J. Robertson, E.P. O'Reilly, Phys. Rev. B 35 (1987) 2946.
81. J. Robertson, C.A. Davis, Diamond Relat. Mater. 4 (1995) 441.
82. G.L. Doll, J.P. Heremans, T.A. Perry and J.V. Mantese, J. Mat. Res. Soc. 9 (1994) 85.
83. C.A. Davis, D.R. McKenzie, Y.Yin, E. Kravtchinskaia, Philos. Mag. B 69 (1994) 1133.

84. J. Schwan, W. Dworschak, K. Jung, H. Ehrbardt, Diam. Relat. Mater. 3(1994) 1034.
85. O. Amir, R. Kalish, J. Appl. Phys. 70 (1991) 5958.
86. V.S. Veerasamy, Phys. Rev. B 48 (1993) 16954.
87. S. R. P. Silva, G. A. J. Amaratunga, Thin Solid Films 270 (1995) 194.
88. K. Ogata, J.F.D. Chubaci and F. Fujimoto, J. Appl. Phys. 76 (1994) 3791.
89. J.I. Pankove, Semiconductor and Semimetals, 21 Princenton, NJ (1984).
90. A. Ilie, N.M.J. Conway, B. Kleinsorge, J. Robertson and W.I. Milne, J. Appl. Phys. 84 (1998) 5575.
91. P. Stumm, D.A. Drabold, P.A. Fedders, J. Appl. Phys. 81 (1997) 2626.
92. E.G. Gerstner and D.R. McKenzie, J. Appl. Phys. 84 (1998) 5647.
93. B. Meyerson and F.W. Smith, Solid State Comms. 34 (1980) 531.
94. H-X. Han and B. Feldman, Solid. State Comms. 65 (1988) 921.
95. T. Inuaki and K. Ono, J. Appl. Phys. 33 (1994) 2593.
96. P. Wood, T. Wydeven and O. Tsuji, Thin solid films, 258 (1995) 151.
97. O. Stenzel, M. Vogel, S. Ponitz, R. Petrich, T. Wallendorf, C.V. Borczyskowsky, F. Rozploch, Z. Krasilnik, N. Kalugin, Phys. Stat. Sol. (a) 140 (1993) 179.
98. A. Mansour and D. Ugolini, Phys. Rev. B 47 (1993) 10201.

CHAPTER 2

CARBON NITRIDE DEPOSITION: SPUTTERING TECHNIQUE

This chapter begins with a general overview of the sputtering technique, some of its applications and the different types of sputtering deposition systems existent. Magnetron sputtering systems are of particular interest since one variation of such systems was used in this research. A description is also given of how film growth occurs during sputtering and how film microstructure is affected by the deposition parameters, which will help to understand how these parameters can be controlled to achieve the desired film properties. For a comprehensive documentation of the different deposition techniques and their applications, the reader is referred to Bunshah,[1] Vossen and Kern,[2] and Scheugraf.[3] The final part of the chapter deals with a review of sputtering as a technique used for the deposition of carbon nitride thin films.

2.1 Principles of sputtering

In order to introduce the concept of sputtering as a deposition method, one has to start considering what happens when an ion collides with the surface of a solid, which is usually called the target. Depending on the type of ion (mass and charge), the nature of surface atoms involved, and most importantly, on the ion energy, one or all of the following interactions, which are depicted in *figure 2.1*, can occur:

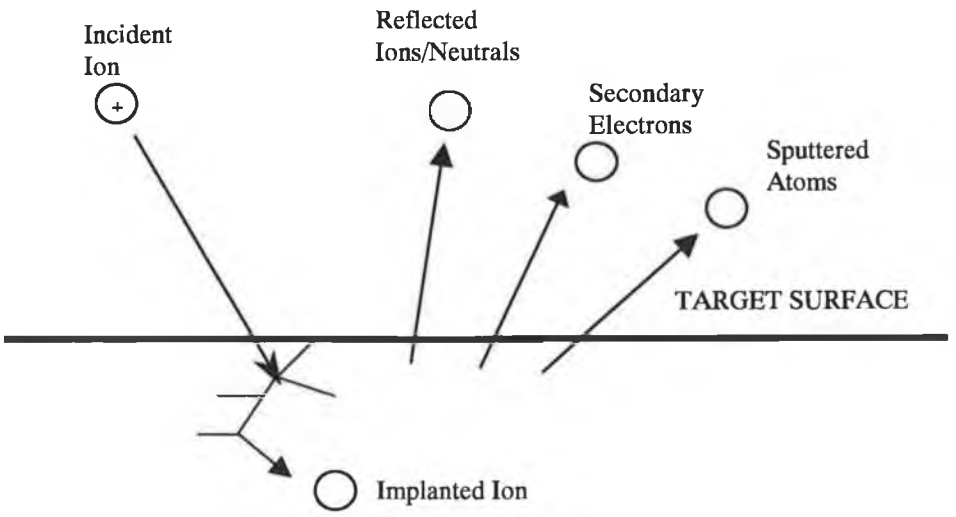

Figure 2.1: The sputtering process.

- The incident ion may be reflected and probably neutralised in the process.
- The ion impact may cause the target to eject an electron (usually called secondary electron).
- The ion may become implanted in the target.
- Structural rearrangements may also take place within the target material, which are usually referred to as radiation damage. It ranges from simple vacancies (missing atoms) and interstitials (atoms out of position) to more serious lattice defects like changes of stoichiometry in alloy compounds and changes in electrical charge levels and distribution.
- Finally, the ion impact may establish a train of collision events in the target leading to the ejection of an atom; this process is known as *sputtering*, which is used as a method of creating the flux of source material in a PVD process.

Sputtering is related to momentum transfer from energetic particles to the surface atoms of the target. This later interaction can be viewed as a series of elastic binary collisions. This is usually compared to the break in a game of atomic billiards as depicted in *figure 2.2*. The ion (cue ball) breaks up the close-packed rack of target atoms (billiard balls), scattering some backwards (toward the player) i.e. out of the target surface.

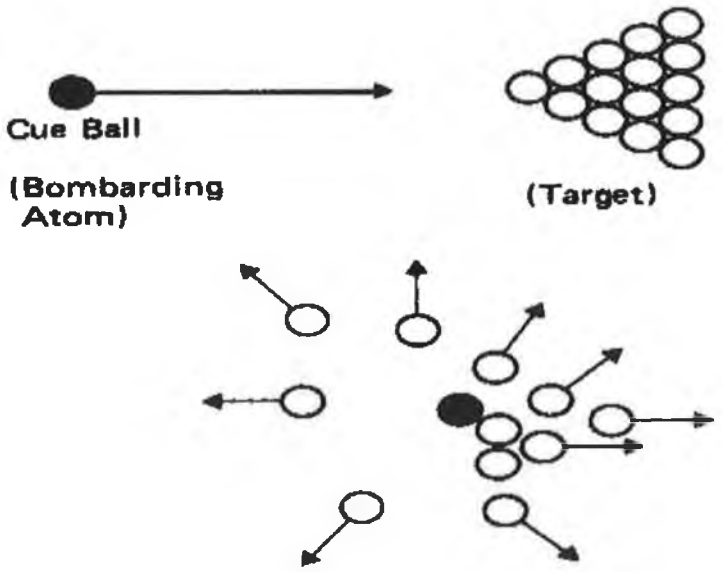

Figure 2.2: Billiard model.

This is not a realistic model, since the atoms in a solid are bound to one another by a complex interatomic potential, but nevertheless, the binary model is an useful representation of the interaction being considered under normal sputtering conditions. A binary collision is characterised by the energy transfer function (ε):

$$\varepsilon = \frac{4m_i m_t}{(m_i + m_t)^2}$$

where m_i and m_t are the masses of the colliding atoms.

One fundamental parameter for characterising sputtering is the sputtering yield S, and is defined as the number of atoms or molecules ejected from a target surface per incident ion and is a measure of the efficiency of sputtering. The following expression for the yield, assuming perpendicular ion incidence onto a target, was derived by Sigmund[4] and includes the energy transfer function ε, a term $\alpha(m_t/m_i)$ which is a linear function of (m_t/m_i), E is the kinetic energy of the incident ion, U is the heat of sublimation for the target material and K is a constant:

$$S = K\varepsilon \frac{E}{U}\alpha(m_t/m_i)$$

This expression is very useful for illustrating the dependence of important parameters and for providing good agreement with measurements for bombardment of many materials of engineering interest. According to this expression, the yield depends only on the target and bombarding species and their energy. The most common method of

providing the ion bombardment is to backfill an evacuated chamber with an inert gas (usually argon) to pressures ranging from 1 to 100 mTorr, an ignite an electric discharge so that it produces ionisation of the gas in a region adjacent to the target, which is negatively biased so that its surface is bombarded by positive ions. This process discharge is called a *glow discharge* and the ionised gas is called *plasma*. Ions used for sputtering can also be generated by an external ion beam source.

The yield is higher when the mass of the bombarding particle is of the same order of magnitude than that of the target atoms. Sputtering yields can be determined experimentally. *Figure 2.3* shows yield versus ion energy for several materials under normal ion incidence, which is generally the case for sputtering devices. The sputtering process is most efficient when the ion energies are within the linear range. In this figure, it can be noticed that the yields of most materials are within an order of magnitude of one another. This characteristic is very important, since it gives sputtering its universality. Virtually any material can be sputtered. The main applications of sputtering are discussed in the next section, along with some of its limitations.

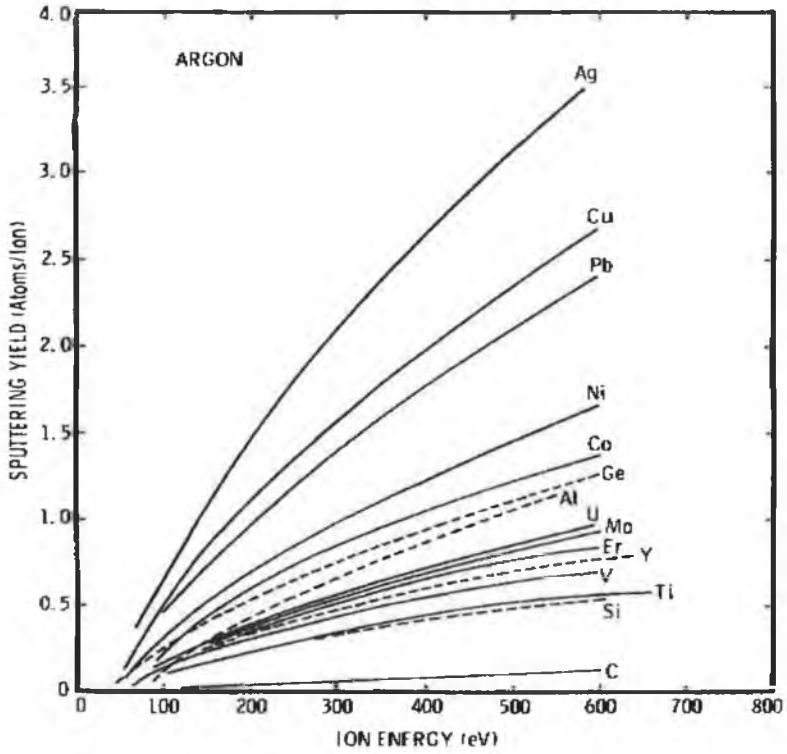

Figure 2.3: Sputtering yield.

2.2 Applications of sputtering

The range of sputtering applications is enormous; the two main applications are sputter etching and sputter deposition:

2.2.1 Sputter etching

Sputtering can be used to etch the target since it essentially involves knocking atoms out of the target surface. Applications range from sputter cleaning to selective etching to generate a topographic pattern on the surface, or simply to make the target thinner. In pattern production processes, improved etch profiles by using a suitable mask can be achieved by using sputter etching rather than wet chemicals since the anisotropy is higher. This is because ions move along electric field lines which are perpendicular to the substrate, so that the vertical etch rate is very small. *Figure 2.4* shows the different etch profiles obtained with sputter etching and wet chemicals. The problem with sputter etching is that it is non-selective, i.e. the mask is also etched since most materials etch at the same rate, which can be partially solved by using more resistant etch masks like alumina or magnesium oxide. All the different aspects of sputter etching can be reviewed in Hong et al.[5]

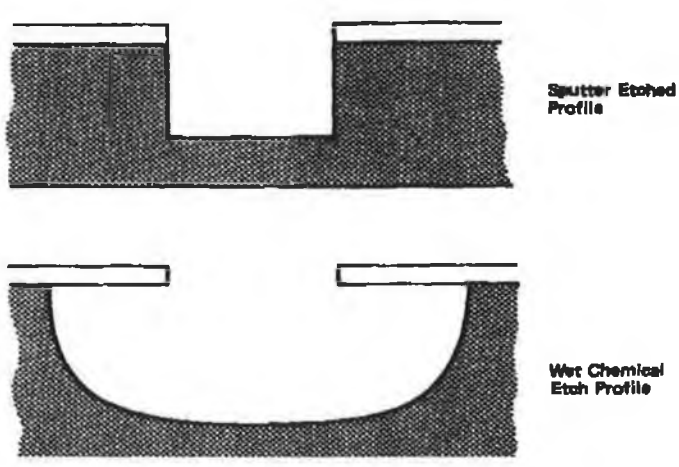

Figure 2.4: Different etch profiles.

2.2.2 Sputter deposition

The ejected atoms from the target surface can also be used. If a receiver material (known as substrate) is placed near the target, the ejected atoms can condense on its surface, forming a coating of target material on the substrate. Films containing almost every element in the periodic table have been prepared. As a result, sputtering has become a widely used thin film deposition method in the mechanical and electronic engineering industries. Typical applications are aluminium alloy and refractory metals, microcircuit metallization layers, oxide microcircuit insulation layers, transparent conducting electrodes, amorphous optical films for integrated optic devices, piezo-electric transducters, photoconductors and luminescent films for display devices, amorphous bubble memory devices, optically addressed memory devices, thin film resistors and capacitors, video-discs, solid electrolytes, thin film lasers, and microcircuit photolithographic mask blanks.

2.3 Typical deposition system

In this section, an overall picture is given about how thin films are deposited by sputtering. *Figure 2.5* shows a conventional dc sputtering system with the basic elements to turn the sputtering phenomenon discussed above into a practical deposition process. The target is a plate of the material or materials to de deposited. The target is also referred as the cathode since it is connected to the negative terminal of a dc power supply with a high negative voltage applied to it. The substrate to be coated is placed a few inches away and may be grounded, electrically floating or biased negatively. Target and substrate are placed in a chamber, which is evacuated. An inert gas (typically argon) is introduced into the chamber and serves as a medium in which a discharge is initiated and sustained.

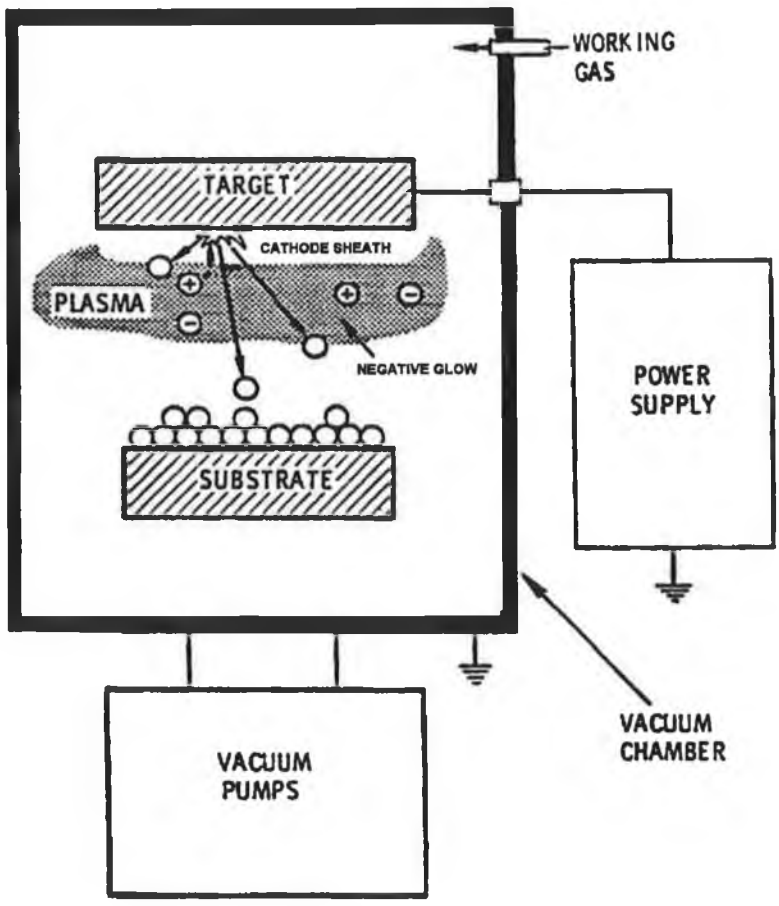

Figure 2.5: Schematic diagram for sputtering.

After the plasma (partially ionised gas) is ignited between the target material (cathode) and the substrate (anode), a phenomenon called *glow discharge* starts. Most of the applied voltage to the electrodes is dropped across a small region in front of the cathode, which is called sheath. This is explained by the relative low mobility of ions compared to the electrons. The positively charged ions from the plasma are accelerated across the cathode sheath and bombard the target surface causing ejection of atoms by momentum transfer, which travel across the electrode separation and are deposited on the substrate. As discussed in section 2.1, apart from atoms, other particles are also ejected from the target, such as reflected ions, neutrals and secondary electrons. These secondary electrons pass through the cathode sheath into the glow region of the plasma, serving the purpose of replacing electrons lost to the chamber wall. Film properties such as structure, hardness, resistivity, stress and adhesion depend on

deposition parameters such as substrate bias, pressure and target-substrate separation. Some variations of the sputtering technique are introduced next.

2.3.1 RF Sputtering

This technique is used to deposit insulating thin films. It uses an alternating voltage power supply, so that the sputtering target is alternatively bombarded by ions and then electrons so as to avoid charge build-up. The electrodes, in a typical rf sputtering configuration, reverse cathode-anode role on each half cycle. The ac discharge is operated at a frequency that is high enough so that significant ion charge accumulation does not occur during the cycle time when an electrode is serving as a cathode. Frequencies in the low MHz range are required. Most rf sputtering systems are operated at a frequency of 13.560 MHz, since it is the frequency allocated by the Federal Communications for industrial, scientific and medical purposes.

2.3.2 Reactive Sputtering

In this technique, the sputtered material from the target is combined chemically with a component from the gas phase. Its main advantages include:

1. Many complex compounds can be prepared using metallic targets, which are easily fabricated.
2. Insulating compounds can be deposited using dc power supplies.
3. Graded compositions can be formed because of the ease with which the coating composition can be varied.

Reactions can occur on the cathode surface, at the substrate, and in cases of very high working pressures, in the gas phase. At low reactive gas partial pressure and high target sputtering rate, virtually all of the compound synthesis occurs at the substrate and the stoichiometry of the film depends on the relative rates of arrival at the substrate of target material vapour and reactive gas. Examples of reactive sputtering

include Al in O_2 to form Al_2O_3, Ti in O_2 to form TiO_2, Ti in N_2 to form TiN, or Cd in H_2S to form CdS.

2.3.3 Magnetically Enhanced Sputtering

Most of the sputtering systems in the present make use of magnetic field effects. The reason is the enhancement in the sputtering rate and extendibility of operating range. Magnetron sputtering sources are devices in which magnetic fields are used in conjunction with the electric field to form electron traps near the target in order to increase the ionisation effect. Magnetron configurations can take various forms; magnetron sputtering systems will be discussed in section 2.6.

2.3.4 Bias sputtering

In bias sputtering, the flux and energy of incident charged particles are modified by changing the electric fields near the substrate. This is achieved by applying either a negative DC or RF bias to the substrate. RF bias has to be used with insulating substrates, as it was discussed for sputtering of insulating targets. The voltage distribution in a bias system is depicted in *figure 2.6*. The plasma potential V_p remains unaffected, since it 'likes' to remain positive with respect to everything in the chamber. If the applied bias is V_B volts, then a sheath of potential difference V_p-V_B will be establish in front of the substrate with polarity such as to accelerate positive ions onto the substrate. Bias voltages of -50 to -3000 V are typically used.

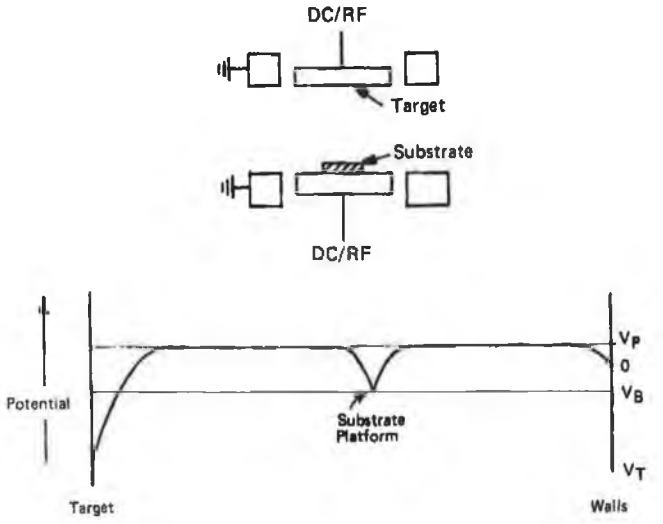

Figure 2.6: Schematic of a bias sputtering system and voltage distribution.

Biasing adds enormous flexibility to the sputter deposition technique; almost any film property can be influenced by the biasing sputtering technique, such as resistivity, hardness, residual stress, dielectric properties, etch rate, optical reflectivity, step coverage, film morphology, density and adhesion. The control of the gas content of films is also an important role of bias. There is no doubt that by changing the flux and energy of ions and electrons bombarding the substrate, many other effects on parameters affecting the nature of the films take place, such as thermal effects and influences on the nucleation and growth stages of the films.

2.4 Magnetron sputtering system

The application of magnetic fields to enhanced ionisation dates back to Penning (1936),[6] but their effective use in sputtering systems has been more recent. Magnetron sputtering is presently the most widely commercially practised sputtering method. The chief reason for its success is the high deposition rates achieved resulting from the enhancement of ionisation. In magnetron sputtering, an arrangement of magnets is placed behind the target. These magnets, in combination with the electric fields, form an electron trap in front of the target, therefore, increasing the ionisation in that area, which results in increasing bombardment of the target and hence a greater deposition rate.

The electric field (E) is perpendicular to the target surface, and the magnetic field (B) emanates from the north pole to the south pole, that is parallel to the target, as shown in the planar magnetron configuration of *figure 2.7*. Thus, the ExB electron drift current follows a closed path and consequently, the electrons are trapped near the target, which increases the ionisation probability by increasing the probability of collisions between the electrons and the atoms to create more ions. Magnetron action enables electrons to do this before being lost to the anode or chamber walls. The electron bombardment of the substrate is lowered, resulting in lower temperatures at the substrate surface. On the other hand, the intense sputtering energies generate large amounts of heat at the target, which must be dissipated by water cooling of the magnetrons.

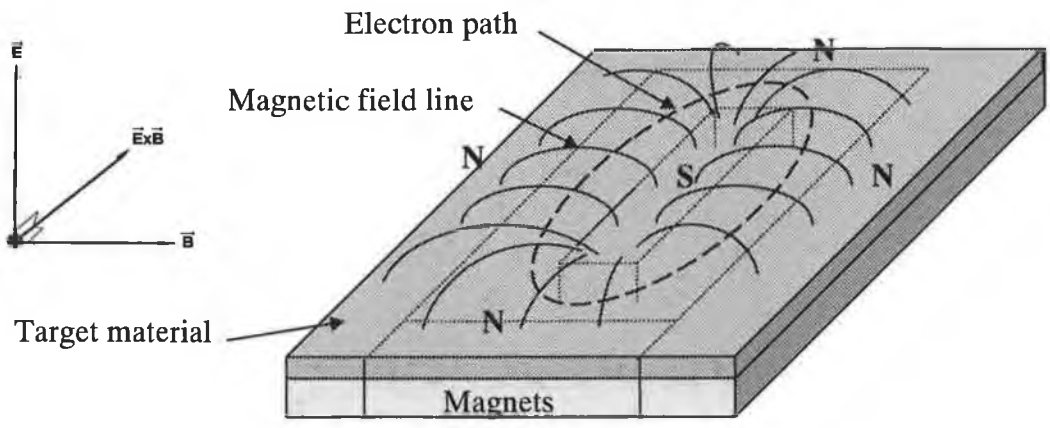

Figure 2.7: Planar magnetron sputtering configuration showing the path followed by electrons due to the action of both electric field (E) and magnetic field (B).

2.4.1 Types of magnetrons

There are several types of magnetrons for practical sputtering applications. The design of magnetrons for practical sputtering systems has been documented by Almedei.[7] A balanced magnetron is one in which the magnetic fluxes of the opposing magnetic poles are equal. This is achieved by making the surface areas of both north and south poles equal. In an unbalanced magnetron, on the other hand, the magnetic fluxes of the opposing magnetic poles are not equal, as shown in *figure 2.8*. In this configuration,

the outer ring of magnets is make stronger, so that the magnetic field lines emanating from the edges of the magnetron are directed towards the substrate. This results in an enhanced magnetic confinement between the target and the substrate. The deposition is more satisfactory and allows increased target to substrate distances to be used.

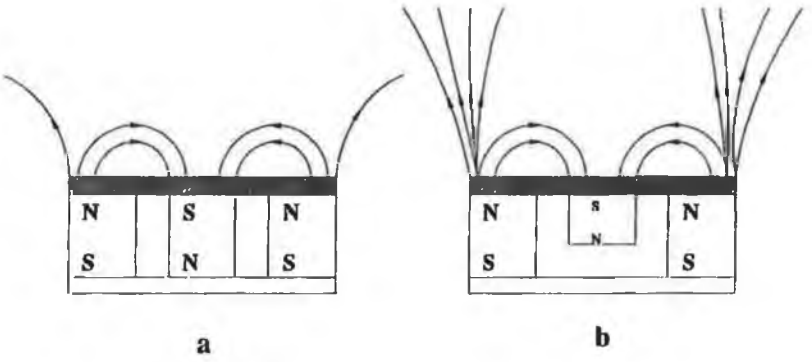

Figure 2.8: (a) Balanced magnetron, (b) Unbalanced magnetron

Figure 2.9 shows three different magnetron geometries used. The cylindrical geometry was probably the earliest (*figure 2.9a*). When the inside of the chamber becomes the target, the arrangement is known as inverted magnetron and has the capability of depositing uniform thickness films over strangely shaped substrates placed along the axis. Other possible geometry is the circular geometry (*figure 2.9b*). Here, the sputter ejected material has a pronounced forward direction perpendicular to the anode so that the substrates have to be placed on a rotating carousel to ensure good uniformity of film thickness. A third type of practical sputtering magnetron (*figure 2.9c*) is the planar magnetron; here, a 'looping' magnetic field is used, restricting the sputter erosion to a 'racetrack' area. Planar magnetrons are widely used despite the small deposition surface area because of their simplicity and the relative ease with which planar targets from a wide range of materials can be fabricated.

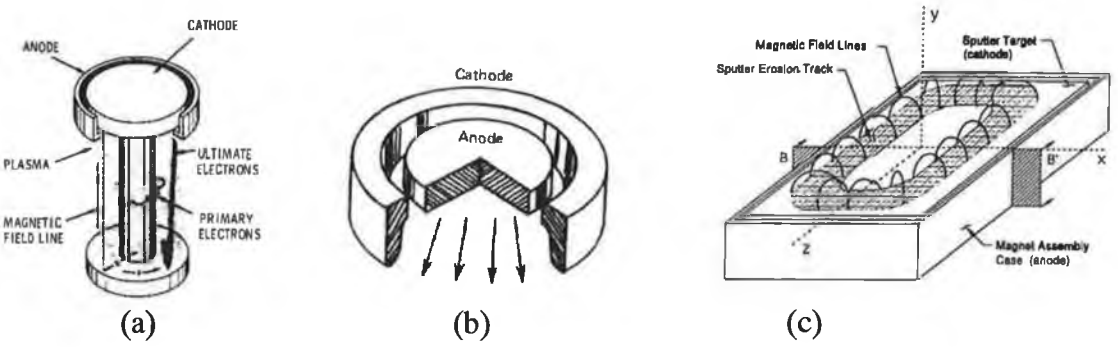

(a) (b) (c)

Figure 2.9: Magnetron configurations: (a) Cylindrical, (b) Circular, (c) Planar.

2.4.2 Summary on magnetron sputtering

Magnetrons have proved to be a very useful addition to the family of sputtering devices. Because of the efficiency of the ionisation mechanism near the target, intense plasma discharges capable of providing high sputtering rates (sometimes greater than one micron per minute) can be maintained at moderated voltages and low pressures. Furthermore, the bombardment of the substrate by fast charged particles is virtually eliminated. Magnetron sputtering sources can be used to sputter magnetic as well as nonmagnetic materials. However, when a sputtering target composed of a magnetic material is used, it must be saturated magnetically so that its magnetic behaviour is suppressed and a field of the desired shaped can be maintained over its surface. This is solved by the Penning type magnetron sputtering source, which discussed in chapter 3.

2.5 Thin film growth

In sputter deposition, material arrives to the substrate in an atomic or molecular form. The film atom condensation process can be viewed as occurring in three steps:

1. Incident atoms transfer kinetic energy to the substrate lattice and become loosely bonded "adatoms".

2. The adatoms diffuse over the surface with a motion determined by their binding energy to the substrate and is influenced by the nature as well as the temperature of the substrate. These adatoms exchange energy with the substrate and other absorbed species, until they either are desorbed, by evaporation or back-sputtering, or become trapped at low-energy sites. Islands of coating material collect at these sites during this called nucleation stage, and finally grow together to form a continuous coating.
3. The incorporated atoms readjust their positions within the lattice by bulk diffusion processes.

This thin film growth process is much more complicated than this basic picture, since the substrate and growing film are subjected to many types of bombardment. This is depicted in *figure 2.10*, which reflects the complexity of the sputtering environment and the many variables involved in the growth process. Some aspects about the different types of bombardment are pointed out next.

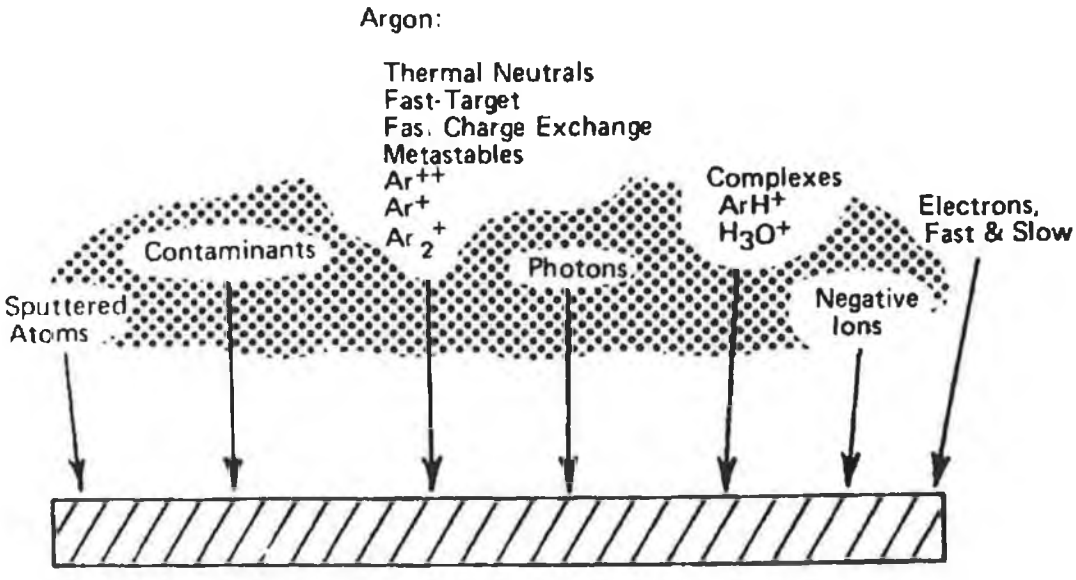

Figure 2.10: Particles bombarding the substrate in sputter deposition

Positive Ions

The plasma ions have kinetic energies of 5 to 30 eV and internal energies of about 10 eV. Ion bombardment increases the nucleation density by causing surface damage,

enhances the mobility of adatoms by transferring kinetic energy to them, and also have a large influence on the interface adhesion of coatings. The ion bombardment of the substrate when growing carbon nitride has two effects: activates the desorption of nitrogen atoms as well as water contaminants from the growing film surface and does not cause the concentration of strongly bonded nitrogen in the films to be noticeably increased. An intense ion bombardment would make more difficult the deposition of crystalline carbon nitride phases and results in a highly disordered carbon-like network matrix with nitrogen substitutions.[8]

Contaminants

Their effect will depend on their partial pressure. The contamination will be highly effective if it is chemically reactive. If the contamination results from an internal source (outgassing), its partial pressure can be minimised by maximising the pumping rate.

Sputtering gas atoms

The flux of sputtering gas (normally argon) at the substrate is extremely high compared with the fluxes of sputtered atoms and contaminants, so that is likely that some of these argon atoms get trapped in sputtered films. The argon content is a function of the substrate temperature and total argon pressure.

Electrons

The majority of them are thermal electrons from the glow, with energies of a few eV. The substrate is also subjected to bombardment by energetic (100 to 1000 eV) primary electrons from the cathode. These fast electrons can have a major influence on the structure and properties of the growing film on the substrate.

Photons

They can be produced by ion or electron bombardment on any surface. Photons can be as energetic as the ion or electron producing it, and can cause electron emission from the surface.

The film structure is very sensitive on growth conditions. The growth conditions depend on deposition parameters such as substrate bias, target power, total pressure, substrate temperature and partial pressure of the reactive gas. Next section deals with some of the effects of these parameters on the film structure.

2.6 Film microstructure

Many different parameters affect the microstructure of sputtered thin films, such as substrate material and orientation, substrate temperature, and the ion bombardment resulting from variations in deposition parameters. In a conventional magnetron sputtering system, the plasma confinement and the increased plasma ionisation results in greater ion bombardment during film growth, which largely affects the final microstructure of the films (denser coatings, increased gas incorporation...). In this section, the microstructure in sputtered films as well as the effects of deposition parameters on film microstructure are discussed.

2.6.1 Deposition Parameters affecting film microstructure

In magnetron sputtering, deposition parameters such as substrate bias, system pressure, substrate temperature and target power determine the film microstructure, which in turn determines the properties of the film. One of the most attractive features of sputtering deposition is the control of film properties that one can have by choosing the suitable deposition parameters. The next section deals with some of the effects that deposition parameters have on film microstructure.

Substrate bias

The very effective control of properties that can be achieved with substrate bias was briefly discussed before. Biasing the substrate at a small negative potential (-30 to -150 V) increases the ion bombardment on the substrate surface. This result in increased film density and increased gas incorporation in the films. In general, the deposition rate decreases as negative bias is applied to a substrate due to increased

film densification and re-sputtering of the growing film. Compressive stress also normally increases at high negative substrate bias. Films deposited at low substrate bias posses open, porous structures, while at increasing negative bias voltages, denser coating structures can be obtained.

Pressure

Operating pressure limitations are imposed by the requirements of both the glow discharge and the film deposition. The glow discharge sets a lower pressure limit. The discharge is sustained by electrons making ionising collisions with the gas and these will decrease with decreasing gas density, and hence gas pressure. On the other hand, material sputtered from the target may collide with gas atoms on its way to the substrate, at a rate that will increase with increasing pressure. The result of the collision is to deflect the sputtered atom, sometimes back towards the target, and hence decrease the deposition rate. The mean free path of the gas increases at low pressures resulting in more energetic particles due to fewer collisions. These particles impart their energy into the growing film as heat, promoting surface diffusion. At elevated inert gas pressures, adatom mobility is reduced, which promotes open boundaries. The formation of coatings with compressive stresses and entrapped working gas is a common occurrence in sputtered coatings deposited at low pressures where the reflected ions do not lose their energy in their passage to the substrate. When sputtering with a reactive-gas/argon mixture, the relationship between film properties and the reaction gas injection rate is generally very non-linear. This is because the sticking coefficient (ratio of depositing flux to re-emitted flux) of the condensing film depends in a complex way on its growth rate, composition, film structure and temperature.[9]

Target power

For each operating pressure, target material and sputtering gas, there is a specific voltage-current relationship. The energy of the bombarding particles and the flux of sputtered atoms increase at high target power which increases the impingement rate at

the substrate; this is true up to several tens of keV, where it begins to decrease. The choice of VI (target power input) is normally governed by a particular desired operating pressure. Normally, the voltage required to maintain a glow discharge having a current density of 0.1 - 2.0 mA/cm^2 is usually in the range 500 - 5000 V.

Substrate temperature

In general, films deposited at low substrate temperatures are characterised by a high density of structural defects while those deposited at elevated temperatures approach bulk physical properties. Given the fact that there is heat input to substrates from the glow discharge, control of substrate temperatures above ambient can be quite difficult to achieve. Films deposited at elevated substrate temperatures may be deficient in volatile constituents. When depositing compound semiconductors, this is particularly relevant, since one of the species is often volatile and an elevated substrate temperature is desired to promote a large grain size. The temperature range over which stoichiometric films can be grown is increased by ion bombardment. An optimum in the structure-sensitive properties (such as surface smoothness, crystallographic order and charge mobility) for many compounds of electrical interests occurs at a substrate temperature that is within a few percent of 1/3 T_b, where T_b is the boiling point of the compound.[10] High substrate temperatures affect the residual stress in the films due to re-crystallisation annealing.

2.6.2 Structure Zone Model

The first studies of how substrate temperature affects the film microstructure were made by Movchan and Demchishin.[11] They introduced a representation of thin film microstructures as a function of T/T_m (where T is the temperature of the substrate surface and T_m is the melting temperature of the material) in terms of four zones with their own characteristic structure. Thornton[12] extended this model to sputtering in the absence of ion bombardment by adding an additional axis to account for the effect of the sputtering gas. A schematic representation of this model is shown in *figure 2.11*. Zone 1 corresponds to low adatom diffusion, and it therefore forms at low

temperatures; this zone is promoted by elevated working gas pressures. It consists of tapered crystals with domed tops separated by voided boundaries. Zone T is a result of the sputtering gas and consists of poorly defined fibrous grains. Zone 1 structures can tend towards Zone T by thermal-induced adatom mobility. Zone 2 results when the growth process is dominated by adatom surface diffusion. It consists of columnar grains separated by dense crystalline boundaries. The grain sizes increase with T/T_m. Finally Zone 3 is characterised by equiaxed grains, due to recrystallization effects at such high temperatures.

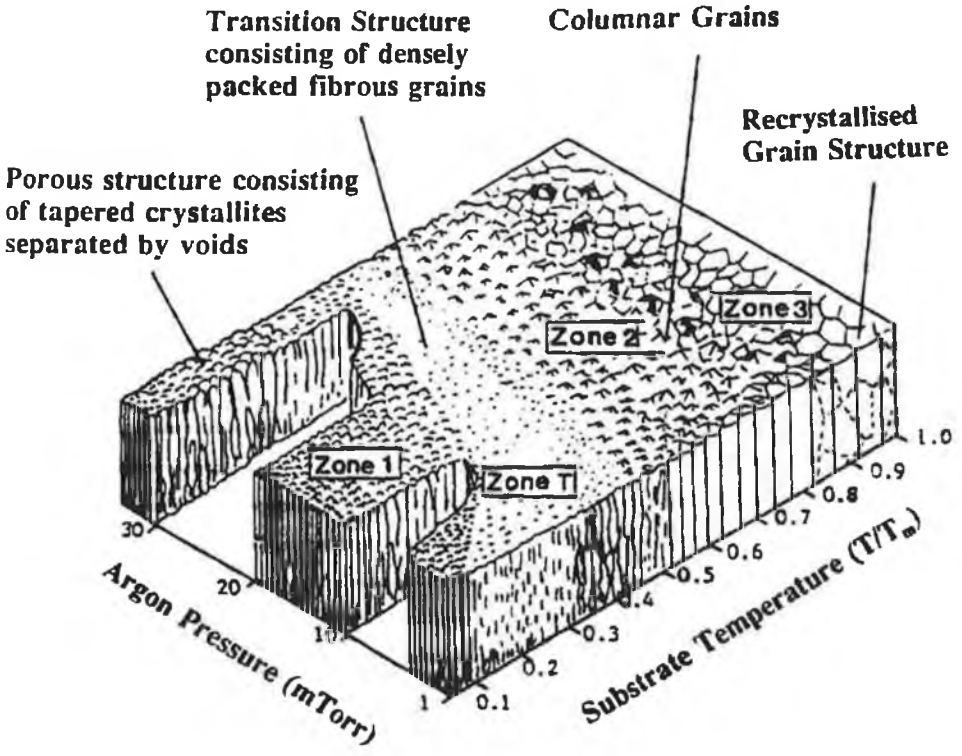

Figure 2.11: Thornton structural zone model

Various physical characteristics of the deposited films are strongly sensitive against the substrate temperature,[13] which is closely related to the energy influx to the substrate. The total energy transferred during deposition includes the contribution of different species namely sputtered target atoms, ions originating from the plasma, reflected neutrals, plasma radiation and energetic electrons. The detail of the contribution of these four species has revealed that the mechanical properties of the

deposited films are mainly governed by both flux and energy of the reflected neutrals through the inert gas entrapment phenomenon.[14] This finding explains why, for the deposition of large mass material, the choice of the sputtering gas is of primary importance for the control of the film properties at low substrate bias. A characteristic feature of thin film deposition by magnetron sputtering in comparison to thermal evaporation is the higher kinetic energy of the particles arriving at the substrate. The integral energy influx during sputtering influences the thermal conditions at the substrate surface and, hence, in addition to momentum transfer it affects the microstructure and morphology as well as adhesion and residual stress of the deposited films. The total energy influx during sputtering of thin aluminium films onto silicon wafers was investigated by Kersten et al.[15] Their results showed that the measured integral energy influx for sufficiently negative substrate potentials, as determined from the rise of the substrate temperature during the sputtering process, consists mainly of the kinetic energy of charge carriers and sputtered particles, and the released condensation heat. For the case of floating substrates the contributions of the kinetic energy of sputtered species and condensation are dominant.

2.6.3 Stress

All sputtered films are in some state of stress. The two main components of the total stress in a thin film are: 1) thermal stress due to the difference in the thermal expansion coefficients of the film and the substrate materials and 2) intrinsic stress due to the accumulation effect of atomic forces generated throughout the film volume by atoms which are out of position with respect to the minimum in the interatomic force fields. The contribution of the intrinsic stress increases with film thickness. Exceeding critical values of thickness, sometimes as low as 1000 Å may cause premature cracking at the interface.

For thin films, the intrinsic stresses are generally constant throughout the coating thickness. They are typically compressive for sputtered coatings. Stress caused by growth and thermal mismatch factors can be mitigated by using interlayers.

2.6.4 Substrate effects

Apart from the substrate temperature, other substrate factors such as condition and nature of the surface, impurity content, chemical nature and crystallographic structure determine the nature of the growing film. The crystal structure of the substrate affects the film growth through changes in the distribution, orientation and size of the crystals nucleated on the growing surface. The substrate holders should be designed so that they do not sputter excessively and introduce contamination onto the substrates, which will affect the growing film. The thermal expansivity of the substrate also influences the level of stress in the film. If α_f and α_s are the thermal expansion coefficients of the film and substrate, then a compressive stress results when $\alpha_f < \alpha_s$ and tensile stress when $\alpha_f > \alpha_s$.[16]

The position of the substrate in relation to the target is also important. Samples placed closer to the target will be bombarded with more energetic particles (which have not undergone collisional loses).

2.6.5 Adhesion

Adhesion refers to the interaction between the closely contiguous surfaces of adjacent bodies and is dependent on the interfacial region between them and the bonding across this region. A good adhesion of the film to the substrate is critical and is the first attribute a film must posses before any of its other properties are further successfully exploited. There are four main types of interfacial region:[17]

1. Abrupt interface: characterised by an abrupt change between film and substrate, with lack of interaction between them, i.e. very low interdiffusion and chemical reactions
2. Compound interface: there is chemical interaction between film and substrate.
3. Diffusion interface: there is a gradual change in composition between film and substrate. A good mutual solubility of film and substrate and enough energy to overcome the activation energy for bulk diffusion promotes this type of interface.

4. Mechanical interface: is characterised by mechanical interlocking of the depositing material with a rough substrate surface

Several combinations of these interfacial regions may occur in magnetron sputtering. By sputter etching the substrate prior to film deposition, a rough surface is formed on which mechanical interlocking of the film can occur. A diffusion interface can be promoted by elevated substrate temperatures, which enhance diffusion, but are prevented by contamination layers that act as diffusion barriers. Compound interface regions are strong, since they involve chemical bonds, but have the disadvantage of being brittle. They are also promoted by elevated substrate temperatures. Ion bombardment on the substrate has been found to have a large influence on the adhesion of coatings. It removes loose contamination and imparts energy to the growing film increasing the density nucleation sites and reducing the void formation that occurs during the initial island growth.

2.7 Conclusions on the sputtering technique

Different aspects of the sputtering process as well as how different film properties are dependent on the sputtering environment were discussed. Three main effects occur at a substrate during sputtering: (1) condensation of energetic vapour, (2) heating, and (3) bombardment by a variety of energetic species. All three must be carefully controlled since these factors critically determine film microstructure.

The main points of the sputtering technique can be summarise as follows:

- The sputtering process is a relatively high energy process compared to many coating technologies.
- The surface of the target can be cleaned of undesirable species before growing the coating by sputter etching.
- The energy imparted to the surface atoms of the film determines the adatom mobility. This energy can be increased by thermal means (increasing the substrate temperature) and by ion bombardment (applying a bias to the

substrate or increasing the system pressure). The increased energy imparted to the surface atoms aids in the "filling-in" of holes/pores on the film surface, thereby increasing the density of the film and promoting even coverage of the substrate.

- The independent control of the deposition parameters is relatively easy, which is an important consideration in a research environment.
- The essential advantage of sputtering processes is versatility both in terms of materials that can be deposited and process parameters that can be controlled to tailor the properties of thin films as desired. However, process parameters are all interdependent, and quite often make their control difficult.

2.8 The use of the sputtering technique for carbon nitride deposition

In the previous sections, the sputtering process was described in detail, as well as some different modifications of the technique, which can be successfully applied for thin film deposition. In this section, some aspects about the use of this technique for carbon nitride deposition are discussed.

Reactive DC sputtering is normally carried out using graphite targets in a pure nitrogen or nitrogen-argon mixture in the mtorr pressure range. A DC magnetron sputtering system has been used to deposit a-CN_x overcoats onto thin film recording media.[18] Higher-pressure work (~8 torr) using a nitrogen-helium mixture has also been reported,[19] where the resulted material was a mixture of amorphous carbon and paracyanogen. Independently of the gas mixture used, the nitrogen content and the deposition rate are found to be inversely proportional to the substrate temperature, with little or no deposit above 600° C. Also, the nitrogen content and the deposition rate increased with increasing nitrogen gas proportion, but does not vary greatly with the gas pressure in pure nitrogen. These observations demonstrate the importance of chemical sputtering and the relative arrival rate to the substrate of carbon and nitrogen species. A number of DC sputtering arrangements have been attempted, including single and double unbalanced magnetron, and sputtering by ion extraction from helicon sources.[20,21] With the unbalanced cathode work, the film characteristics and

their dependence on the experimental conditions were very similar to the case of conventional DC sputtering. Most of the unbalanced studies used pulsed DC biasing, which effectively promote ion bombardment of the deposit. In this work, a novel scheme of reactive DC magnetron sputtering was used for production of carbon nitride films. It uses two facing, unbalanced graphite targets with reversed magnetic field, with the substrates mounted perpendicular to the target and to one side. This scheme is described in detail in the next chapter.

RF sputtering, as DC sputtering, has normally been carried out in pure N_2 or N_2+Ar atmospheres. In terms of experimental parameters, studies have been performed by using substrate temperatures from ambient to 800° C, plasma powers from 30 to 100 W, gas pressures from 5 to 500 mtorr and with grounded, DC-biased and pulse DC-biased substrates. The great majority of the deposits have been found to be amorphous, with little or no deposit formation at substrate temperature in excess of 700° C. The nitrogen content has little dependence on the gas pressure used and the inclusion of argon in the sputtering gas normally leads to lower levels of nitrogen incorporation in the deposit, probably because of increased bombardment of the deposit by high-energy atoms that have rebounded from the target.[22] In general, the properties of carbon nitride compounds have a complicated dependence on the plasma properties; the ion and electron fluxes and energies depend on a variety of factors such as plasma power, relative size of the electrodes, the magnetic field, the system geometry, gas pressure and gas composition.

One of the earliest reports on CN_x synthesis was made by Cuomo et al.[23] This group used reactive RF sputtering in mixed Ar-N_2 discharges onto substrates held between 20 and 450°C. Above this temperature no film growth took place. The films were found to have an N/C ratio of approximately unity and a polymer-like structure resembling paracyanogen (-$(CN)_n$-). Usually this technique has produced CN_x films with an amorphous structure and maximum nitrogen content of 37-44 at.% N.[24,25,26,27] Axen et al.[28] reported magnetron sputtered amorphous films with 55-58 at.% N, which is similar to the stoichiometry required to form β-C_3N_4 (57 at.%), however all the films were amorphous. Okada et al.[29] used rf magnetron sputtering at high pressures.

They argue that higher plasma densities promote the formation of a steady C-N bond and thermal stability of CN_x. Only in a few cases, the synthesised films showed a small volume fraction of nanocrystallites.[30] Reactive magnetron sputtering results in CN_x films, which are normally structurally disordered with multiple bond types.

It takes a certain amount of ion bombardment energy for atomic displacement, which is important in defect reduction and crystalline formation. However, excess energy results in disorder. Choosing the right ion energy and flux is crucial for the formation of nitride coatings with optimum hardness. Unfortunately, although unbalance magnetron sputtering can increase ion bombardment of the substrate surface, the ionisation fraction in the plasma is only a few percent, the majority of the species being neutrals. The energetic neutrals are difficult to control and may cause disorder in the films. Using ionised magnetron sputtering, one can increase the ionization fraction. Appropriate substrate biasing can control the energy of the ionised species.

Physical and chemical sputtering are involved in the deposition process. In true chemical sputtering, the process gas reacts with the target to yield a compound that is easily volatilised from the target owing to its low boiling or melting point. In chemical enhanced sputtering the reaction yields a product which is more easily removable by physical sputtering. At low pressures, nitrogen and carbon ion bombardment energies are greater than ~15 eV and ~50 eV, respectively, causing erosion of the deposited CN. Such nitrogen-ion bombardment also selectively removes nitrogen from the deposit; at present, it is not clear if carbon causes a similar effect. At low nitrogen concentration, this removal occurs through the formation of CN or C_2N_2 groups; at higher concentrations, the formation of molecular nitrogen within the film also becomes important. The presence of hydrogen is known to increase the erosion rate strongly and probably the nitrogen extraction.[19] These two process rates of erosion and selective nitrogen removal also increase with increasing substrate temperature, as expected for a chemical process. Overall, it is apparent that chemical sputtering does not aid the preferential growth of C_3N_4 by removing weakly bonded carbon or CN groups, as is the situation for diamond and polymer-like deposition.[31]

In the methods mentioned so far, the main issues to bear in mind for a successful synthesis of high-modulus C_3N_4 materials are: (1) chemical sputtering; (2) achieving the right stoichiometry with low levels of impurities such as silicon, oxygen or hydrogen; (3) establishing the correct bonding coordination sp^3 for carbon atoms and trigonal sp^2 bonding for nitrogen atoms; and (4) the ability to produce an adequate amount of crystalline material with grains sufficiently large to allow definitive tribological testing.

In most sputtering experiments involving ion beam deposition and laser ablation, the sputtered carbon and nitrogen species are mixed together and deposited onto the substrate. The energy of the species and reaction processes varies and yields multiple bond states. From all the discussions presented so far, the following are probably recommendable factors for the synthesis of crystalline C_3N_4:

1. A substrate temperature in excess of 800° C if the process uses gaseous precursors. Such temperatures should help inhibit the formation of polymeric and inorganic CN_x compounds.
2. Atomic nitrogen and CN are probably preferable as precursors rather than molecular nitrogen and hydrocarbon ions and radicals.
3. At low pressures, ion energies below 10 eV are necessary to avoid chemical sputtering and the concurrent reduction in nitrogen content.
4. For gas-phase processes, the use of medium to high pressures helps to ensure that the kinetic energy of the incident neutrals is kept below 10 eV. Use of high to ultrahigh pre-deposition vacuums is recommendable to minimise the residual concentration of water vapour in the reaction chamber.
5. Substrate effects are complex but important; reasonable adhesion between the carbon nitride and the substrate is needed. Additionally, some substrate materials may enhance carbon nitride formation; there are indications that there are advantages in using nickel, titanium or Si_3N_4 coated substrates.

References

1. R.F. Bunshah et al, Deposition Technology for Films and Coatings, Noyes Publications, Park Ridge, NJ, (1982).
2. J.L. Vossen and W. Kern (eds.), Thin Film Processes, Academic Press, London, (1978).
3. K. Scheugraf , Handbook of Thin Film Deposition Processes & Technologies, Noyes Publications, NJ (1988).
4. P. Sigmund, J. Vac. Sci. Technol. 184 (1969) 383.
5. Hong. H.Lee, Fundamentals of Microelectronics Processing, McGraw-Hill, NY (1990).
6. F.M. Penning, Physica 3, (1936), 873.
7. J.B. Almedie, Vacuum, 39 (1989) 717.
8. R. Kaltofen, T. Sebald and G. Weise, Thin Solid Films, 308-309 (1997) 118.
9. J. Freyer, J. Electrochem. Soc. 122 (1975) 1238.
10. P.S. Vincett, W.A. Barlow and G.G. Roberts, J. Appl. Phys. 48 (1977) 3800.
11. B.A. Movchan and A.V. Demchishin, fiz. Met. Metalloved, 28 (1969) 653.
12. J.A. Thornton, Ann. Rev. Mater. Sci. 7 (1977) 239.
13. H. Steffen, H. Kersten, H. Wulff, J. Vac. Sci. Technol. A12 (1994) 2780.
14. C. Paturaud, G. Farges, M.C. Sainte Catherine and J. Machet, Surf. Coat. Technol. 98 (1998) 1257.
15. H. Kersten, G.M.W. Kroesen, R. Hippler, Thin Solid Films, 332 (1998) 282.
16. D.S. Rickerby and S.J. Bull, Surf. Coat. Technol. 39/40 (1989) 315.
17. B. Bhushan and B.K. Gupta, Handbook of Tribology, Materials, Coatings and Surface treatments, McGraw-Hill (1991).
18. B. Zhang, B. Wei, D.J.D. Sullivan and H. E. Gotts, IEEEE Trans. on Magnetics 33 (1997) 3109.
19. B.C. Holloway, Thin Solid Films, 290-291 (1996) 94.
20. N. Hellgren, M. P. Johansson, E. Broitman, L. Hultman and J-E. Sundgren, Phys. Rev. B, 59 (1999) 5162.

21. W.T. Zheng, U. Gelivs, K. Z. Xing, N. Hellgren, M. Lögdlund, A. Johansson, W. R. Salaneck and J. -E. Sundgren, J. Electron Spectrosc. Relat. Phenom. 87 (1997) 45.
22. D. Li, J. Vac. Sci. Technol. A 13 (1995) 1063.
23. J.J. Cuomo, P.A. Leary, D. Yu, W. Reuter and M. Frisch, J. Vac. Sci. Technol. 16 (1979) 299.
24. S. Kumar and T.L. Tansley, Thin Solid Films, 256 (1995) 44.
25. S. Kumar and T.L. Tansley, J. Appl. Phys. 76 (1994) 4390.
26. W. Zheng and J.E. Sundgren, Chin. Phys. Lett. 15 (1998) 120.
27. A. Czyzniewski, W. Pretch, M. Pancielejko, P. Myslinski and W. Walkowiak. Thin Solid Films, 317 (1998) 348.
28. N. Axen, G.A. Botton, H.Q. Lou, R.E. Somekh and I.M. Hutchings, Surf. Coat. Technol. 81 (1996) 262.
29. T. Okada, S. Yamada, Y. Takeuchi and T. Wada, J. Appl. Phys. 78 (1995) 7416.
30. M.Y. Cheng, D.Li, X. Lin, V.P. Dravid, Y.W. Chung, M-S. Wong and W.D. Sproul, J. Vac. Sci. Technol. A, 11 (1993) 521.
31. S.F. Durrant, Thin Solid Films, 259 (1995) 139.

CHAPTER 3

PENNING TYPE MAGNETRON SPUTTERING SOURCE AND ITS USE FOR CARBON NITRIDE DEPOSITION

3.1 Introduction

The sputtering source used for carbon nitride deposition is based on the Penning type geometry,[1] which is used in devices such as pressure gauges and ion beam sources. The Penning geometry consists of two opposing cathodes with a magnetic field perpendicular to the cathode surfaces. With this configuration, secondary electrons emitted during sputtering are constrained to reside within the volume between the cathodes for an extended period. Therefore, a very intense discharge is created which is sustainable to pressures well below those attainable with conventional magnetron sputtering.[2]

Penning discharges were first used in the early eighties by Naoe and Kadokura et al.[3,4,5] Their motivation was to prepare magnetic films at higher deposition rates than with typical magnetron sputtering discharges. By using a Penning type discharge, the problem of achieving a large magnetic field parallel to the surface of a ferromagnetic material in order to sustain the plasma discharge was avoided. Later, a Penning type device was used to produce hard coatings, such as TiN, by Window.[6] He was more interested in achieving high ion fluxes in the vicinity of the substrate, where they can be accelerated across the sheath region into the substrate surface. This ion bombardment of the growing film alters the properties of the coating and can be used to deposit films with superior mechanical properties.

Magnetron sputtering has been successfully employed in the deposition of non-stoichiometric carbon nitride films with high nitrogen incorporation. The incorporation of nitrogen in the films during reactive sputtering depends on the

competition between the trapping of nitrogen and the desorption of nitrogen containing species from the growth surface.

Thus, both thermodynamics and kinetics will limit the nitrogen content in the films. The dominant mechanism of nitrogen incorporation in the films is a result of chemisorption of atomic nitrogen and/or low energy implantation of energetic nitrogen species impinging on the growth surface with an energy high enough to become implanted and trapped. The loss of nitrogen-containing species from the growth surface will either occur through re-sputtering or through thermal desorption. The relatively low fraction of atomic nitrogen species in typical magnetron sputtering systems results in an upper limit of the maximum achievable nitrogen concentration.

The Penning type sputtering configuration was believed to represent a way forward in the search for new carbon nitride films with better properties. In 1996, a sputtering source based on the Penning geometry was designed and built by M.J. Murphy.[2] Since then, the possibilities of this sputtering source for the deposition of carbon nitride films have been thoroughly investigated by the Plasma Coating Group in Dublin City University.

This chapter describes the Penning type sputter magnetron source as well as the high vacuum station and some variations of the deposition system, such as the introduction of a substrate heater. The experimental details for the deposition of carbon nitride coatings are given in the final section.

3.2 Penning type sputtering source

The Penning type sputter apparatus was designed from calculations of the magnetic field that exists within the device. A full description of the practical design of this Penning source is given by M.J. Murphy.[2] The next sections describe the most important characteristics of this device. One of the main differences in the Penning type magnetron configuration mentioned here of other typical magnetron sputtering processes is the higher magnetically confinement of the plasma. The confined plasma

increases the electron temperature of the plasma from standard magnetron sputtering. This can be interpreted as a higher ionisation fraction of the molecular and atomic species in the plasma. The efficient dissociation of species and the higher density of ions present in the plasma are believed to be a key advantage in the deposition of carbon nitride films.

3.2.1 Physical Description

A schematic of the Penning type sputter apparatus is given in *Figure 3.1*, where the resulting plasma is also illustrated. Very strong Neodymium Iron Boron (NdFeB) magnets, which are placed in an aluminium magnetron body, are positioned behind the 12 cm diameter targets, which must be efficiently water-cooled. The targets are backed by copper plates which are in contact with copper cooling plates where an electrical cable and the water inlet and outlet are connected. The target is electrically isolated from the grounded outer body by means of a Teflon sheet and Nylon bushes. The magnetic field can be changed by either reducing the number of magnets behind each target or changing the inter-target distance by changing the height of the magnet supports. The substrate holder is placed to the side of the two Penning sources and can be electrically biased.

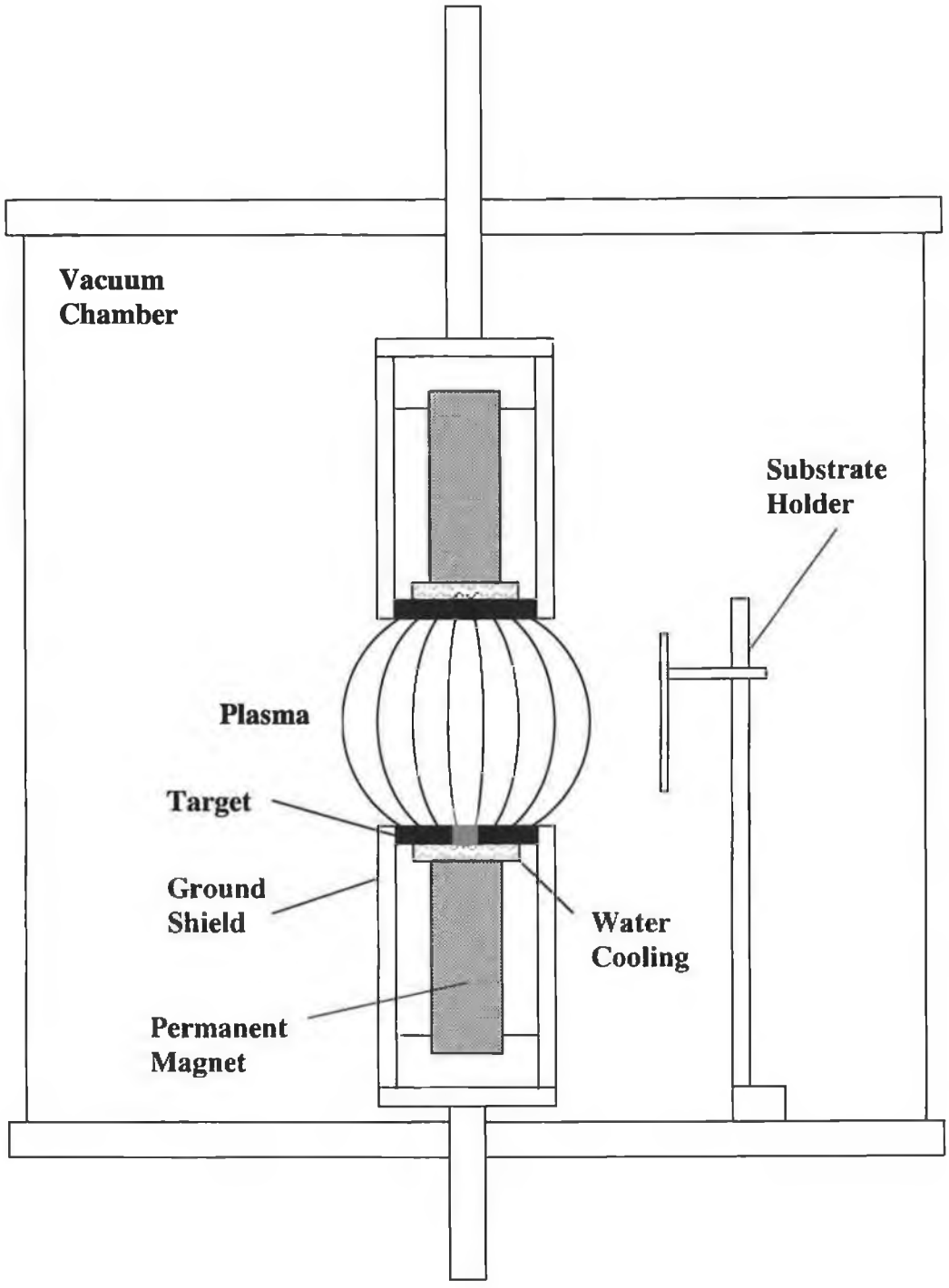

Figure 3.1: Penning type sputtering source.

3.2.2 Plasma Characteristics

The plasma shape obtained with the Penning source is photographed in *figure 3.2*. The use of the strong NdFeB magnets provides a very high flux density in the inter-target region, where the electrons are magnetically confined leading to a very intense ionisation in the plasma and a high ion flux at the substrate. Target erosion is concentrated within a circular area of roughly $20cm^2$. A full description and derivation of the equations for magnetic field calculations are given by Murphy.[2] His results describe the magnetic flux, the radial component and the axial component of the magnetic field for a single pole of a cylindrical magnet and the effective potential well for energetic electrons/ions. They show that the use of the strong NdFeB magnets ensure a very high flux density in the inter-target region and a very effective confinement of electrons by the magnetic field trap. *Figure 3.3* shows the magnetic flux lines calculated for an inter-target spacing of ~10 cm.[2]

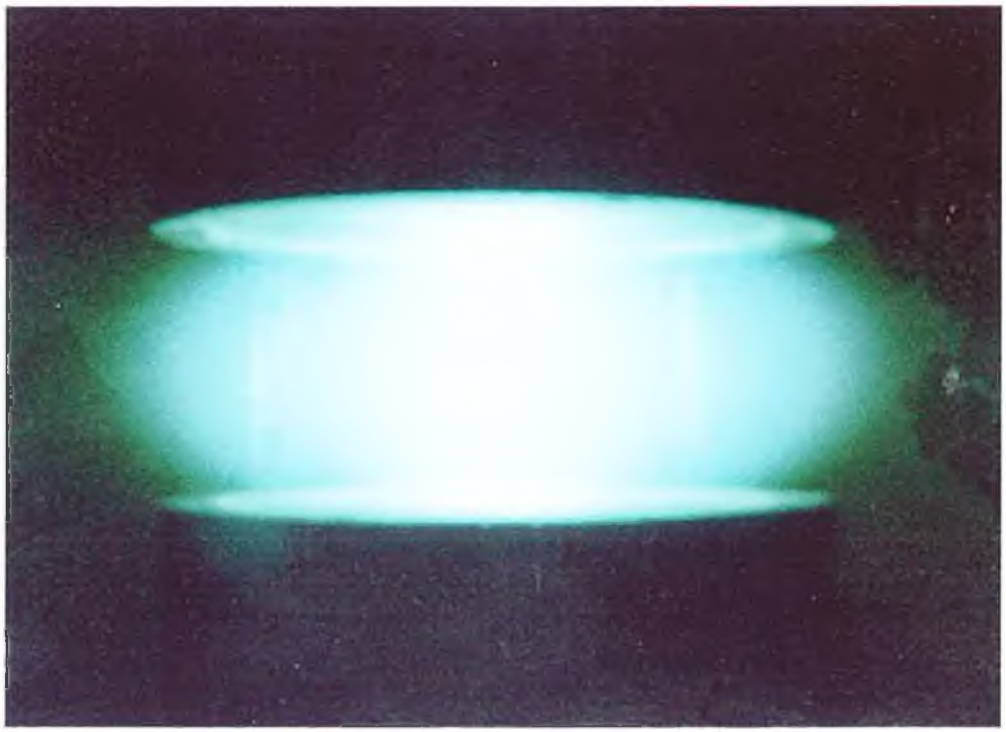

Figure 3.2: Plasma glowing between the targets.

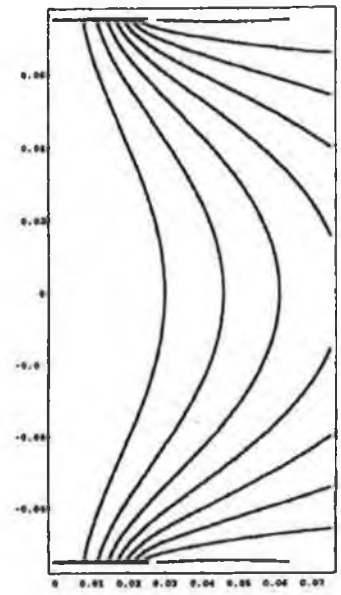

Figure 3.3: Magnetic flux distribution for an inter-magnet spacing of 15 cm (inter-target spacing ~ 10 cm).

Optical emission spectroscopy (OES)

OES measurements were performed using a Digitwin Sofie instrument. The light emitted from the plasma was transmitted to the spectrometer by means of an optical quartz fibre. The observed peak positions are compared with the reference peaks given by the instrumental data library. The magnetron current discharge was 3A and the N_2 working gas pressure was $1x10^{-3}$ mbar.

Figure 3.4 shows the optical emission from the plasma during sputtering. The emission spectra were scanned in the wavelength range of 200-900 nm. The main active species appear to be N_2^+ ions, showing a high level with respect to the neutral nitrogen molecules. Another interesting feature is the presence of CN radicals in the plasma, which arises due to nitrogen incorporation in the graphite targets. This is proved by the fact that if argon replaces nitrogen as the sputtering gas then the emission due to CN does not instantaneously stops, but slowly disappears as material is sputtered from the target surface.

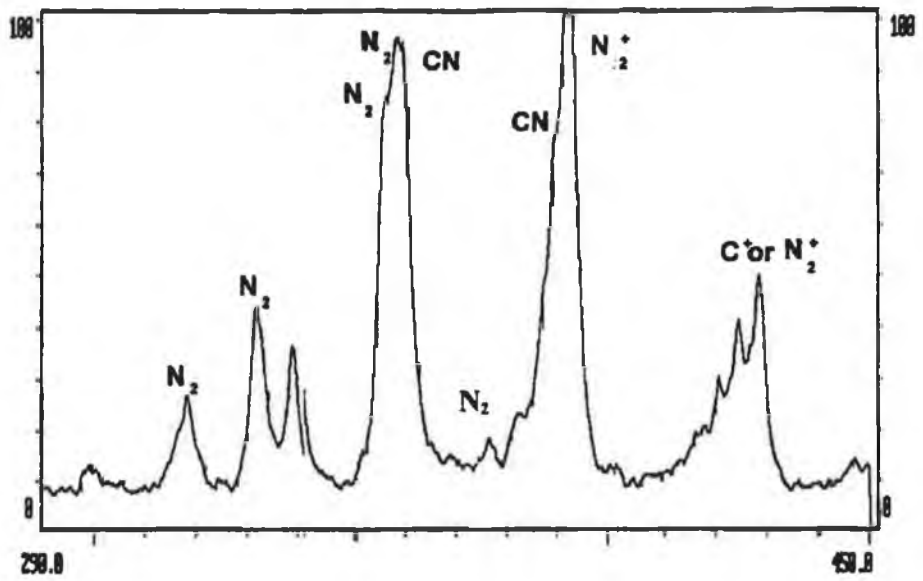

Figure 3.4: Optical emission spectra for nitrogen plasma during carbon nitride deposition.

The N_2^+ ion intensity as a function of discharge current is shown in *Figure 3.5* for two different deposition pressures. The two main conclusions to be drawn are that ionised nitrogen species increase with discharge current and the increase of nitrogen pressure does not increase significantly the number of ionised nitrogen species.

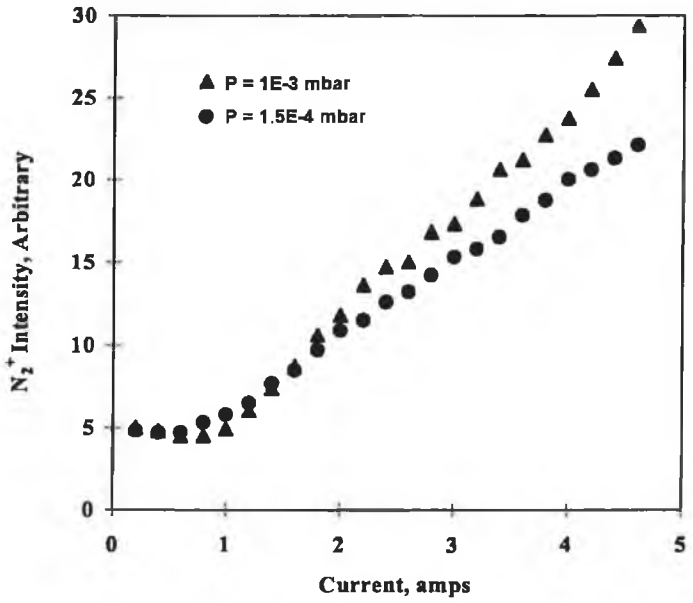

Figure 3.5: N_2^+ ion intensity as a function of discharge current.

Langmuir probe

The basic plasma characteristics, i.e., electron density, electron temperature, and plasma potential were investigated by a Langmuir probe. The maximum insertion distance of the probe corresponds to the outer edge of the cathodes. It was not possible to obtain readings of the inner cathode space since the insertion of the probe in this region caused the extinction of the plasma. A detailed description of such measurements is given by Chowdhury et al.[7] The measurements show that the Penning source gives rise to magnetic confinement of the hot electrons in the inter-target space and that an electric field exists outside the anode and cathode sheaths. Because of the electron confinement, the plasma potential remains negative for a long distance away from the cathode sheath and only becomes positive near the chamber walls. The electron density at the edge of the inter-cathode space was about 1.8×10^{11} cm^{-3} (for p= 6×10^{-4} mbar) and 8×10^{10} cm^{-3} (for p=1.5×10^{-4} mbar), and is expected to be considerably higher on the cathode axis. This corresponds to an ionisation rate of > 2%. Therefore, a very intense activation of the molecules is expected on the cathode axis. From ion flux measurements and approximate calculations based on the film composition, the ion to carbon atom rate at the substrate is estimated as ~ 50 and the ratio between ionised and neutral nitrogen molecules at the substrate as ~ 0.25. From these results, it can be concluded that the film deposition process is highly activated because of the high ion to neutral arrival at the substrate.

3.2.3 Operating Characteristics

The plasma is sustainable down to 1×10^{-4} mbar of nitrogen. The only factor preventing higher plasma intensity operation at lower pressures is the voltage limitation (~1500 V) of the available 5kW power supply. A pressure range of 1×10^{-3} mbar to 1.5×10^{-4} mbar was maintained for carbon nitride film deposition. The usual inter-target distance was 10cm.

Figure 3.6 shows a plot of the conductance of the discharge as a function of discharge current. The conductance (G) is given by $G=(\sigma A)/L$, where A is the cross section of the medium, L is the length and σ is the conductivity, which is proportional to the

number of charged particles in a conductive medium.[8] So, the conductance is proportional to the conductivity of the medium and depends on the geometrical shape of the conducting medium. The plot shows a quasi-linear relationship between conductance and current, possibly due to the shape of the plasma volume between the targets being a bulged cylinder.

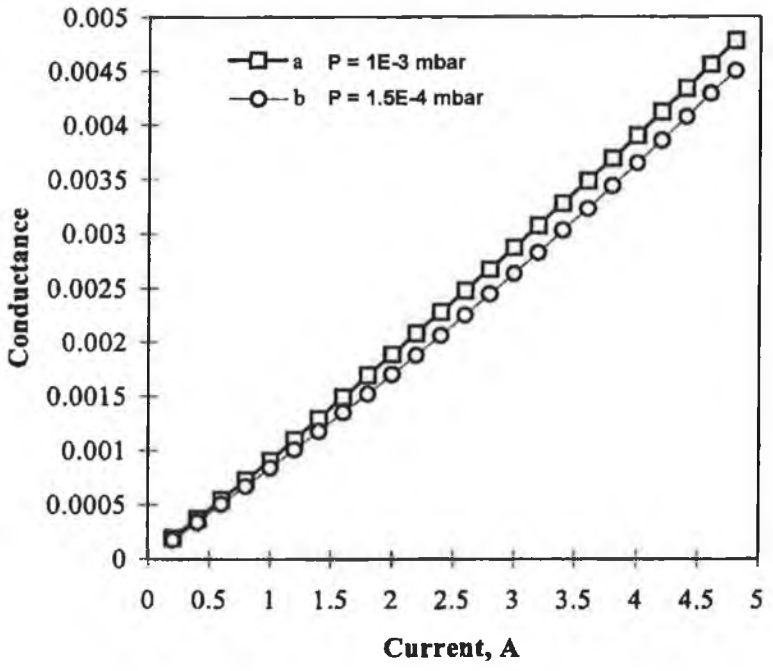

Figure 3.6: Conductance of the conducting media as a function of discharge current

3.3 High vacuum system description

A schematic diagram of the vacuum system housing the Penning source is depicted in *Figure 3.7*. It comprises a vacuum chamber and standard high vacuum equipment. The vacuum chamber is a non-magnetic AISI 304 stainless steel cylinder, with an inner diameter of 603 mm and a height of 610 mm. It includes view-ports, gas inlets and four magnetron ports that were originally design for running a conventional magnetron sputtering system. Other feedthroughs include 1 thermocouple flange (KF25), 1 high vacuum port (200 mm diameter), 1 backing line port (KF40) and 4 spectrometer ports. The chamber is opened by using a chain block attached to the top plate in order to load the substrates and for maintenance purposes. All the flanges are O-ring sealed, using

either Viton or Nitrile elastometers, and QF hardware was used to facilitate the sealing in the system joints and feedthroughs. Detailed drawings of the chamber and accessories are given by P.V. Kola.[9]

The pumping system consists of a Varian VHS-6 oil diffusion pump (2400 l/s) backed by a Varian SD-700 rotary pump (765 l/min). A Varian Block valve (roughing valve) connects the roughing pump to the chamber and a similar valve (backing valve) connects the roughing pump to the diffusion pump backing port. A VAT control gate valve connects the diffusion pump to the chamber. All the valves are pneumatically actuated and an electrical control box is used for electrical switching of the pumps and valves. A foreline trap (filled with rechargeable Zeolite molecular sieve) is used to filter the backing line connecting the rotary and the diffusion pumps. At the time being used, this pumping system was capable of pumping down the deposition chamber to $2x10^{-6}$ mbar.

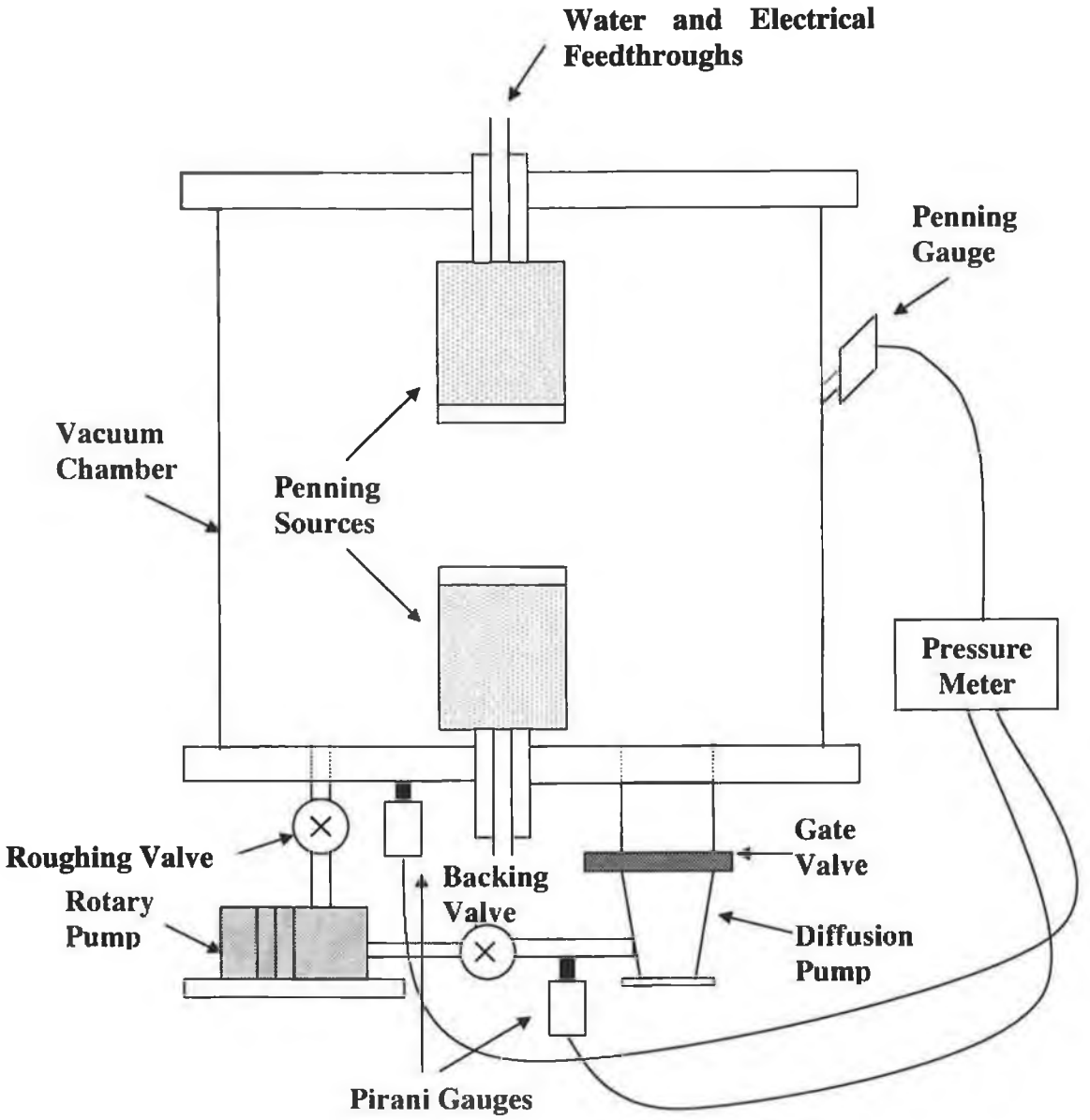

Figure 3.7: Schematic of the vacuum system housing the Penning sources.

High purity argon and nitrogen cylinders are connected to the chamber via a Tylan mass flow controller (FC280A) and a Tylan mass flow meter (FC260) respectively, with a capacity of 100 sccm. The flow rate of both working gas (argon) and reactive gas (nitrogen) were controlled and monitored by a Tylan flow control unit (RO28). The total pressure of the chamber is monitored by the use of Edwards Penning and Pirani gauges, which are controlled through an Edward Pirani/Penning controller (type 1005). A second Pirani gauge monitored the pressure on the backing line. In order to analyse the residual gases in the system and also to provide a method of leak detection (aided by a helium sniffer), a mass spectrometer was connected to the system when required.

The magnetrons were powered by Advance Energy MDX magnetron drives, with a maximum power output of 5 kW. The substrate holder was biased using an Advanced Energy RFX 1250 RF power supply with an automatic matching unit. The purpose of the matching unit is to introduce inductance and capacitance into the circuit. When the variable matching unit is tuned to resonance, the current passing from the power supply is in phase with the load (substrate holder). The "reflected power" should be minimised and is monitored by an Advance Energy ATX tuner. The RF matching network converts the complex impedance of the plasma at 13.56 MHz to 50 Ω resistive.

Figure 3.8 shows how the magnetrons are powered by the MDX drives and the grounding configuration for negative output. The cathodes, which are the live part of the Penning sources where the targets are mounted, are connected to the negative terminal of the MDX magnetron drives. A high negative voltage is applied to them, so that positive ions bombard the target material producing the phenomenon of sputtering discussed in chapter 2. The substrate holder can be electrically floating or biased negatively. *Figure 3.9* shows a picture of the high vacuum system.

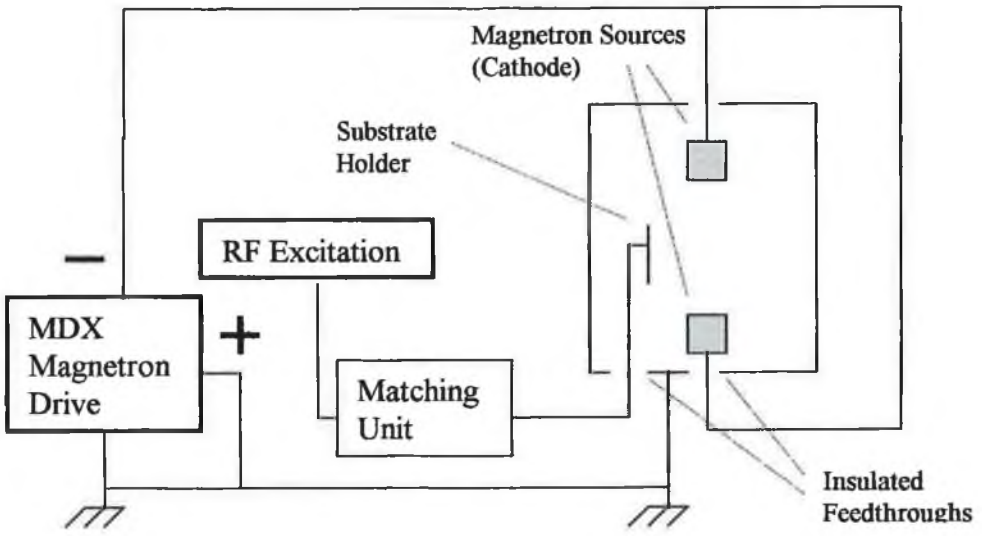

Figure 3.8: Electrical connection to magnetrons and substrate.

Figure 3.9: High vacuum system

Some system modifications had to be made to improve the quality of the carbon nitride films. For instance, Rutherford backscattering (RBS) studies showed that a small amount of iron was present in the film (3-4 at.% Fe). This iron contamination was due to the sputtering of the stainless steel screws used for mounting the backing plate and target. New graphite targets were fabricated to cover the backing plate screws. Graphite caps were also used for the screws clamping the target, which did not work well since due to the high sputtering intensity during deposition, the graphite caps tended to break. Another solution was tried using small stainless steel covers for the screws clamping the targets, which were attached to the outer magnetron grounded body surrounding the target so that the screws were protected from being sputtered. The problem faced with this approach was that, somehow, the plasma was affected and a higher voltage was required to maintain the plasma with the same conditions as before. To get around this problem, two MDX magnetron drives were connected in series; one was operated at constant current and the other drive at constant voltage, according to the specification of the MDX magnetron drives.

Sometimes oil contamination was observed inside the chamber walls. Backstreaming of diffusion pump working fluid vapour seemed the more likely explanation. This effect of backstreaming is often a serious problem and a major concern when roughing the chamber and crossing over to the diffusion pump.[10] A water-cooled baffle (trap) was installed in the system. It was fitted in between the gate valve and the diffusion pump mouth, and no more contamination was observed in following experiments.

3.4 Carbon nitride deposition

This section deals with the general experimental details in the deposition of carbon nitride films using the system described previously. In the final part, the design of a new substrate holder with the possibility of heating the substrates during deposition is discussed, as well as the temperature profiles obtained during the deposition experiments.

3.4.1 Experimental details

The deposition system described above was used to grow different series of carbon nitride films of various compositions. The substrates used included polished n-type silicon (100), borosilicate glasses, and oxidise silicon. Two graphite targets of 12 cm diameter and 99.95% purity with copper backing plates were fitted to the Penning source. The inter-target separation was 10 cm. The sputtering gas was a mixture of argon and nitrogen of variable composition. The gas purity was 99.999% in each case. The substrate holder consisted of a stainless-steel frame upon which the substrates were clamped in a vertical position. The substrates were located 6cm apart from the outer body of the magnetrons, or 13.6 cm away of the centre line between the targets. Typical deposition parameters were –50 V substrate bias, $1x10^{-3}$ mbar working pressure and a current density of ~132 A/m^2 (target power of ~13 W/cm^2).

Once the samples were loaded, the pumpdown sequence was started by roughing down the chamber from atmospheric pressure to $3x10^{-1}$ mbar using the rotary pump. Then, by using the diffusion pump, the chamber was evacuated down to a background pressure of about $2x10^{-6}$ mbar in a few hours.

3.4.1.1 Substrates types and cleaning

Depending on the analysis to be carried out on the samples (i.e. electrical, optical or structural measurements), different types of substrates needed to be used for depositing the carbon nitride films, such as:

- Polished n-type (100) silicon substrates were used for spectroscopy and mechanical (nanoindentation/friction) analysis. Two types of silicon wafers with different resistivities ($\rho \sim 5\text{-}9\ \Omega cm$ and $\rho \sim 100\ \Omega cm$) were used.
- Silicon oxide coated substrates were used for resistivity and Hall effect measurements. To obtain these substrates, the silicon wafers were oxidised at 1300°C for 4 hours in a high temperature furnace, giving an insulating oxide layer of about 0.2 μm.
- Soda lime and borosilicate glasses were also used for resistivity and optical measurements.
- Aluminium coated silicon substrates were required for specific electrical measurements. Aluminium was deposited by an evaporation process. Details of the evaporation system used are given in appendix C.

Before loading, the silicon substrates were cleaned with acetone and methanol in an ultrasonic bath for 20 minutes. Prior to deposition and in order to remove surface contamination, the substrates were sputter etched in situ at an argon pressure of approximately 1.5×10^{-4} mbar with –450 V bias during 10 minutes. For this purpose, a 13.56 MHz RF supply was used. After deposition, before opening the chamber, the films were allowed to cool down for 1 hour to minimise delamination due to thermal shock. The glass substrates were cleaned by immersing them in a solution of HCl.

3.4.1.2 Carbon nitride films series

The first carbon nitride films (PCNX series) were grown in a 100% nitrogen atmosphere, at a total working pressure of 1.5×10^{-4} mbar. The plasma was ignited at a constant magnetron current of 3 A, and the substrate bias voltage was varied from floating (-4Volts) to -75 V DC. The deposition time was 30 minutes, and the resulting thickness varied from 1 to 1.5 μm. Details of thickness measurements are given in next chapter. This gives a deposition rate of 100-500 Å/min.

The following films (series PCN1X) were grown at a total working pressure of 1×10^{-3} mbar, varying the nitrogen partial pressure in the argon/nitrogen sputtering gas

mixture from 0% to 100%. The films deposited with 0% N_2 were representative of pure carbon films. The substrate bias was -50 Volts, and the magnetron current was 3 Amps. The deposition time was 30 minutes, and the resulting thickness varied from 1 to 1.4 μm, thicker films resulting with higher nitrogen partial pressures. This might be due to higher sputtering yield from the graphite target since the mass of nitrogen is closer to that of carbon than is the case for argon. This results in more momentum transferred from nitrogen ions to carbon atoms.[11] Another series of films (PCN2X) were grown with the same deposition parameters as the last series but with a total working pressure of $1x10^{-2}$ mbar. These films showed high levels of stress, and they started breaking up from the edges a few minutes after the chamber was opened. At this high pressure, the diffusion pump does not efficiently pump down the chamber. The residual moisture inside the chamber environment takes part in the sputtering process, and acts as the only source of hydrogen contamination in the film. Holloway et al.[12] mentioned that the addition of small amounts (as little as 1.5 at.%) of molecular hydrogen in the growth chamber caused a total disruption (poisoning) of film growth.

A similar series of films to the PCN1X series (now called PCNG series) were also grown, but this time, soda lime and borosilicate glasses slides were also used as substrates. The deposition time for this series was reduced to 5-10 minutes, since the adhesion between the glass substrate and the film was very poor. The thickness varied this time from 0.2 to 0.5 μm.

Two last series of samples were grown at different bias and substrate temperatures. PCNB series was grown with 100% nitrogen atmosphere, varying the substrate bias voltage from –25 to –175 V, in steps of –25 V. For the last series, a new substrate holder plate with an arrangement of lamps was used. Details are given in next section. With this new design, it was possible to heat the substrates during deposition.

3.4.2 Substrate heater

Both resistance and radiant heating have been used in an attempt to control the substrate temperature above ambient. Substrate temperature is a difficult parameter to control because of the heat input provided to the substrates by the glow discharge. The temperature is usually measured and controlled with a thermocouple feeding a power controller. The main concern is the electrical isolation problem, since it is necessary to preserve the thermoelectric emf of the couple whilst removing both the RF and DC offset components. This might be partially solved by using a thin insulator of mica or ceramic between the couple junction and the substrate plate. An insulating transformer at the power source eliminates the need for electrical isolation (and consequent thermal isolation). It is problematic to measure the exact temperature of the substrate due to the thermal barriers present such as the electrical isolation between the substrate and the thermocouple pressed down onto it, or due to thermal isolation between a substrate and the substrate plate. The substrate surface temperature is greater than that of the bulk due to power input from the glow.

3.4.2.1 Substrate heating configuration

A new substrate plate with a radiant heater configuration was designed in order to see the effect of higher deposition temperatures on the grown carbon nitride films. The holder plate and heating set up were assembled in a stainless-steel base plate which fitted in any of the four rectangular magnetron ports in the chamber walls and it was designed so that the substrate plate was 6 cm away from the outer body of the magnetrons. A picture of the substrate holder plate is shown in *figure 3.10*.

Figure 3.10: Heating plate inside the vacuum chamber. The top magnetron is also shown.

The plate where the substrates are clamped was made of molybdenum because of its machinability, high-thermal conductivity and resistance to warping. The heat is provided by four heat lamps mounted at the back of the plate. A K type thermocouple was used to measure the growth temperature. The ends of the lamps got very hot during the first bench tests performed, so it was decided to water cool all eight ends. An schematic of the design indicating the different parts is given in appendix A. A thermocouple and liquid feedthroughs were fitted in the base plate, and the whole set up assembled together. The thermocouple was positioned in between two glass slides pressed onto the substrate plate surface. This was done to isolate the thermocouple from the plasma and plate. The substrate plate is electrically isolated from the heating assembly by the use of glass ceramic spacers, and it can be electrically biased. If RF

excitation is used to bias the substrate plate, a decoupling network must be employed to prevent RF interference with the thermocouple controls and heat-input circuits.

3.4.2.2 Substrate temperature

The next step was to test the maximum growth temperature that could be achieved by the introduction of this heat method. The temperature was recorded by PicoLog software, which is a real-time data acquisition tool, that could sample the temperature every second and the resulting profile monitored in the computer screen. The temperature measurements were done for 30 minutes deposition times, with no bias (since the RF excitation affected the measurements), 100% nitrogen atmosphere, and a pressure of $1x10^{-3}$ mbar. The lamps were powered by means of a variac Regavolt transformer controlling the percentage of input volts applied to the lamps. It was observed that above 45% input volts, a power cut out occurred. The temperature profiles obtained for 0 (no additional heat), 30, 40 and 45% input volts are plotted in *figure 3.12*. The profiles were taken with no pre-cleaning treatment.

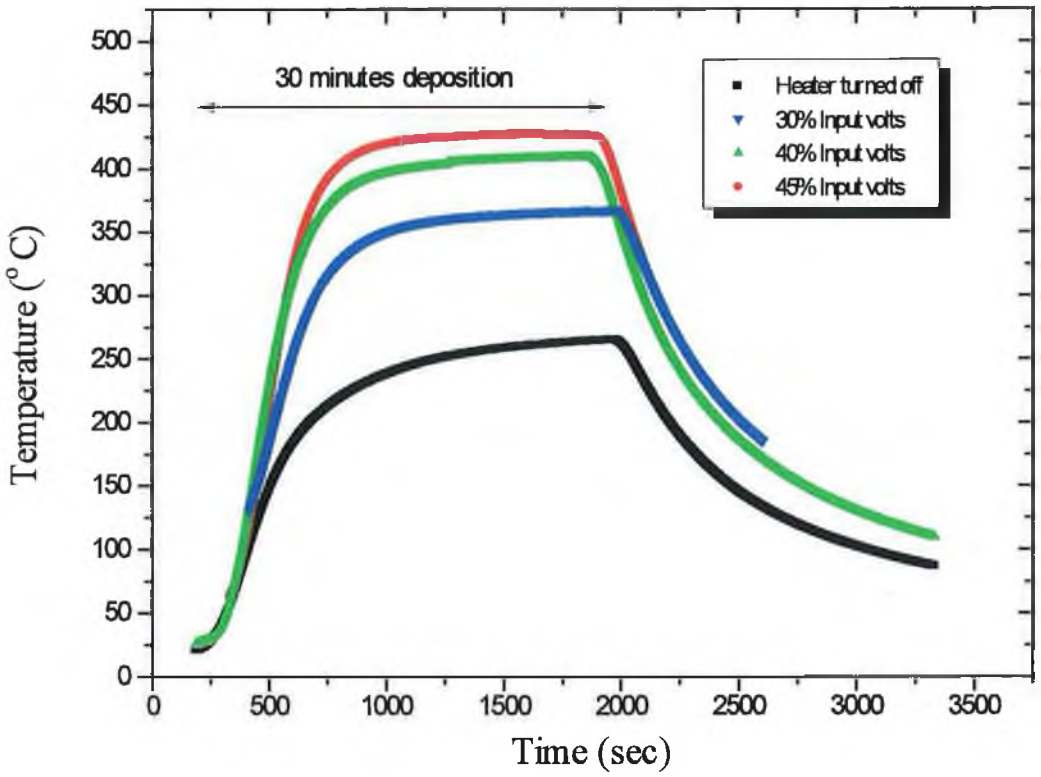

Figure 3.12: Temperature profile recorded for 30 minutes deposition for different heat applied to the substrate plate.

After sputter cleaning, the temperature recorded was 120°C. When samples were grown for settings 0, 30 and 45% input volts, the temperature after deposition reached 285, 360 and 420°C, respectively. The –50 V substrate bias has a small effect in the growth temperatue.

3.5 Summary

One of the main differences in the Penning type magnetron configuration described here with respect to other typical magnetron sputtering processes is the higher magnetically confinement of the plasma. The confined plasma increases the electron temperature of the plasma from standard magnetron sputtering. This means higher ionisation fraction of the molecular and atomic species in the plasma. The efficient

dissociation of species and the higher density of ions present in the plasma are believed to be a key advantage for the deposition of superior carbon nitride thin films compared to the conventional methods. In the next four chapters, structural, physical, electrical and optical properties of carbon nitride films deposited with this technique are explored.

References

1. F.M. Penning, Physica 3, 873 (1936).
2. M.J. Murphy, Ph.D. Thesis, Dublin City University, Ireland, (1996).
3. M. Naoe, S. Yamanaka and Y. Hoshi, IEEE Trans. Magn., 16, 5 (1980) 646.
4. S. Kadokura, T. Tomie and M. Naoe, IEEE Trans. Magn., 17, 6 (1981) 3175.
5. S. Kadokura, M. Naoe, IEEE Trans. Magn., 18, 6 (1982) 1113.
6. B. Window, F. Sharples and N. Savvides, J. Vac. Sci. Technol., A 3, 6 (1985) 2368.
7. A.K.M.S. Chowdhury, D.C. Cameron, M.B. Hopkins, C.O.'Morain and M.S.J. Hashmi, "Plasma characterisation of a Penning-type sputtering source during CNx thin film deposition", presented at Final Workshop, COST 515 programme, Nancy, France, 11-12th Sept 1997.
8. A.M. Ferendeci, Physical Foundations of Solid State and Electron Devices, McGraw-Hill, NY (1991).
9. P.V. Kola, Ph.D. Thesis, Dublin City University, Ireland (1995).
10. J. F. O'Hanlon, A user's guide to vacuum technology, 2nd ed. Wiley (1989) 356.
11. M.Y. Chen, X. Lin, V.P. Dravid, Y.W. Chung, M.S. Wang and W.D. Sproul, Surf. Coat. Technol., 360 (1992) 54.
12. B.C. Holloway, D.K. Shuh, M.A. Kelly, W. Tong, J.A. Carlisle, I. Jimenez, D.G.J. Sutherland, L.J. Terminello, P. Pianetta, S. Hanstrong, Thin Solid Films, 290 (1996) 94.

CHAPTER 4

STRUCTURAL PROPERTIES OF CARBON NITRIDE

This chapter deals with the main aspects of the bonding structure of carbon nitride films, in order to understand the nature of the film's microstructure, and how it relates with the mechanical and electrical properties of the films. The chapter starts with a brief introduction of the spectroscopy techniques and how they can be used to get information of the structure of matter. The analysis techniques considered here are infrared spectroscopy, Raman spectroscopy and x-ray photoelectron spectroscopy. In the following sections, the composition and bonding structure of deposited carbon nitride films and how nitrogen incorporation affects the microstructure of the films are investigated. The amount of nitrogen was controlled by changing the nitrogen partial pressure in the Ar/N_2 gas mixture used for deposition. The variation of film structure with deposition parameters such as substrate bias and deposition temperature is also discussed. The first section describes in simple terms the principle of spectroscopy techniques that were employed for the characterization of the films in terms of their structural properties. Film thickness measurements and nitrogen incorporation in the films as measured by RBS are also described throughout this chapter. In the last section, a discussion about the bonding structure data gathered with the different techniques applied for the film's characterization is given.

4.1 Spectroscopy techniques

Spectroscopy normally defines an analytic technique concerned with the measurement of the interaction (usually the absorption or emission) of radiant energy with matter, with the instruments necessary to make such measurements, and with the interpretation of the interaction both at the fundamental level and for practical analysis. A display of such data is called spectrum, that is, a plot of the intensity of emitted or transmitted radiant energy (or some function of the intensity) versus the energy of that light. Interpretation of spectra provides fundamental information on atomic and molecular energy levels, the distribution of species within those levels, chemical bonding, etc. The change in energy of an ion, atom or molecule associated with absorption and emission of radiant energy may be measured by the frequency of the radiant energy according to Max Planck as $E = h\nu$ where E is energy, ν is frequency and h is the Plank constant.

The frequency (ν) is related to the wavelength (λ) by the relation $\nu\lambda = c/n$, where c is the velocity of radiant energy in vacuum, and n is the refractive index of the medium through which it passes. Units most commonly employed to describe these characteristics of light are:

* Wavelength: 1μm (10^{-6} m) / 1nm (10^{-9} m)
* Frequency: 1 Hertz (Hz) = $1s^{-1}$

For convenience, the wavenumber, the reciprocal of the wavelength, may be used; for this, the common units are cm^{-1}. This number equals the number of oscillations per cm.

The energy of the photon (quantum of radiant energy) emitted or absorbed by the material under investigation corresponds to the difference between two permitted values of the energy of the species, or energy levels. This is the origin of the spectra. The absorption of radiant energy is accompanied by the promotion of the species from a lower to a higher energy level. The emission of radiant energy is accompanied by falling from a higher to a lower state. The next table shows the principal regions of the

spectra of light, along with the transitions in the material that can be studied within each region.

Spectra regions	Wavelength	Energy transitions studied
GAMMA	1-100 pm	Nuclear transitions and disintegrations
X-RAYS	6-100 nm	Ionisation by inner electron removal
VACUUM ULTRAVIOLET	10-200 nm	Ionisation by outer electron removal
ULTRAVIOLET	200-400 nm	Excitation of valence electrons
VISIBLE	400-800 nm	Excitation of valence electrons
NEAR-INFRARED	0.8-2.5 μm	Excitation of valence electrons Molecular vibrational overtones
INFRARED	2.5-50 μm	Molecular vibrations: stretching, bending
FAR-INFRARED	50-500 μm	Molecular rotations
MICROWAVE	0.1-300 cm	Molecular rotations; electron spin resonance
RADIO-FREQUENCY	10^{-1}-10^{3} m	Molecular rotations Nuclear magnetic resonance

Transitions between energy levels associated with electrons range from the near infrared, the visible, and ultraviolet for outermost, or highest-energy electrons, that is, those which can be involved in bonding, to the X-ray region for the electrons nearest the nucleus. At low pressures, such transitions in gaseous atoms produce sharply defined lines because the energy levels are sharply defined. Transitions between energy levels of the nucleus are observed in the gamma-ray region.

Electronic transitions in molecules are also observed. Transitions can occur between levels associated with the vibrations and rotations of molecules. Spacing between electronic levels are greater than vibrational levels, and those between vibrational levels are greater than between rotational levels; each vibrational level has a set of rotational levels associated with it, and each electronic level a set of vibrational levels. This is depicted in *figure 4.1*. Transition between vibrational levels of the same electronic level correspond to photons in the infrared region; transitions between rotational levels, to photons in the far-infrared and microwave region.

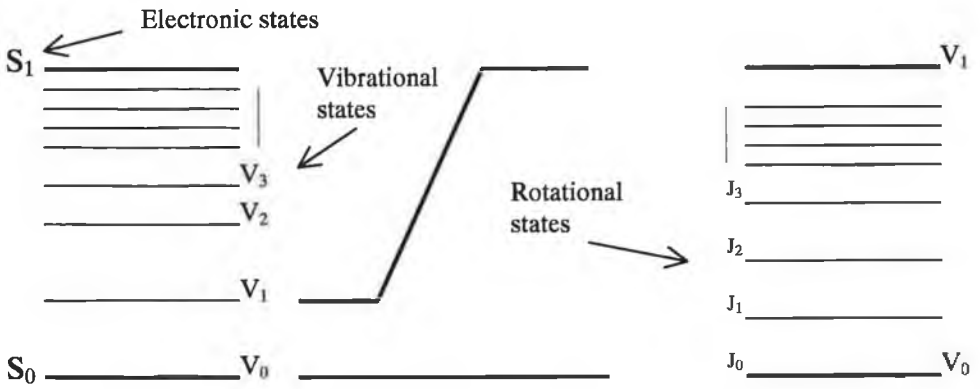

Figure 4.1: Energy levels associated with specimens

Instrumentation

Spectrometers require a source of radiation, a dispersion device, and a detector. For emission spectra, the source may be taken as the sample to be measured itself, although another source of radiation may be needed to excite the sample to an excited state. Absorption spectra require a source to generate appropriate radiation across the range of energies needed for the experiment. These radiant sources produce spectra (continuous) and can be distinguished from those which produce discontinuous spectra. Except for the eye and photographic methods used sometimes in the regions for gamma-ray to visible, a detector is used to convert the signal into an electrical response which is amplified before transmittal to a recording device.

4.1.1 Infrared spectroscopy

The interaction with matter of electromagnetic radiation of wavelength between 1 and 300 μm induces either rotational or vibrational energy level transitions, or both, within the molecules involved. The frequencies of infrared radiation absorbed by a molecule are determined by its rotational energy levels and by the force constants of the bonds in the molecule. Since these energy levels and force constants are usually unique for each molecule, so also the infrared spectrum is usually unique.

For radiation sources, infrared instruments usually use a hot filament called a Nernst glower, or a hot carborundum rod called a Globar. The infrared region is used primarily for analysis of organic compounds because they have unique and complex spectra. In Infrared spectroscopy, the film is irradiated with light with frequencies in the Infrared region. The molecules in the film will only absorb the radiation energy at specific frequencies, which match the natural vibrational frequencies of the molecule, which occur, as mentioned before, in the infrared region of the electromagnetic spectrum.

For a vibration to be IR active, it is necessary a change in the dipole moment. The dipole moment is defined as the magnitude of either charge in a dipole multiplied by the charge spacing. If an atom has the same number of protons and electrons, it is electrically neutral and does not contribute to the dipole moment. The chemical forces that exist in the molecule tend to redistribute the electrons so that a given atom may have a defect or an excess of electrons, being considered as a particle with a small positive or negative charge. When applying IR excitation, this charge may change due to molecular vibration. If the negatively charged atom vibrates in one direction, and the positively charged one in the opposite direction, the vibration is IR active. However, if the molecule retains the centre of symmetry so that the dipole moment remains unchanged, the vibration is IR inactive. The degree of absorption depends on the concentration of IR active bonding within the sample, the molecular absorption coefficient and the thickness of the sample according to the equation

$$I = I_0 e^{-\alpha c t}$$

where I_0 is the light intensity without absorption, I is the intensity of light which has passed through the sample, t is the sample thickness, α is the molecular absorption coefficient and c is the concentration of material under test.

4.1.2 Raman spectroscopy

When a beam of light, of a wavelength not corresponding to an absorption in the sample, passes through it, a small fraction of the light is scattered by the molecules,

and so, exits the sample at a different angle. This is called Rayleigh scattering if the wavelength of the scattered light is the same as the original wavelength; but, if the wavelength is different, it is called Raman scattering. Differences in wavelengths correspond to the wavelength of certain vibrational and rotational processes. The information obtained is of use in structural chemistry, because the rules allowing and forbidding transitions are different from those in absorption spectroscopy.

In Raman spectroscopy, the sample is irradiated with an intense source of monochromatic radiation, whose frequency is generally much higher than the vibrational frequencies, so that radiation scattering occurs. The Raman effect is the inelastic collision between incident photons and the molecules where, as a result of the collision, the vibrational or rotational energy of the molecule is changed by an amount ΔE_m. The energy of the scattered photon $h\nu_S$ must be different from the energy of the incident photon $h\nu_i$ by an amount equal to ΔEm. In Raman scattering, the frequency of the incident photon is usually much greater than the molecular frequency ν_m. If a molecule gains energy, then ΔEm is positive and $\nu_S < \nu_i$ which results in Stokes lines in the Raman spectrum. If a molecule loses energy, ΔEm is negative and $\nu_S > \nu_i$ which results is anti-Stokes lines in the Raman spectrum. In order for a molecular vibration to be Raman active, the vibration must be accompanied by a change in the polarizability of the molecule.

4.1.3 X-ray spectroscopy

The excitation of inner electrons is manifested as X-ray absorption. Emission of a photon as an electron falls from a higher level into the vacancy thus created is X-ray fluorescence. This technique is used for chemical analysis. Extended X-ray absorption fine structure, obtained under the conditions of high resolution, shows change in the energy of inner electrons due to the presence of neighbouring atoms, and can be used in structural chemistry for the determination of the nature and location of neighbour atoms nearest to that being studied. When high energy photons in the X-ray energy range are used, and electrons are emitted, the technique is called X-ray photoelectron

spectroscopy (XPS), which is used to define the electronic structure of solid surfaces as well as to chemically identify surface components.

The bombardment of material by X-rays result in the ejection of electrons from the material. When mono-energetic X-rays are used, the kinetic energy of the ejected electrons E_k is determined by the difference between the binding energy of the electron E_b and the energy of the X-ray incident photon hν. If the kinetic energy of the ejected electron is determined, the binding energy of the electron can be evaluated from

$$E_b = h\nu - E_k$$

The radiation is obtained from X-ray tubes with Al or Mg anodes which give lines at 1487 eV and 1254 eV respectively. This technique can be used to identify atoms at film surfaces by comparing the lines either observed with calculated core level binding energies or experimentally derived from standards. The exact binding energy of core level electrons depend on the chemical environment of the atom, therefore, information about bonding structure can be extracted from the XPS spectra.

4.2 Film thickness

A Tencor Instruments surface profilometer was used to evaluate film thickness by measuring the step increase between the uncoated substrate and the coated substrate. The instrument amplifies and records in a scaled paper the vertical motion of a stylus while moving at a constant velocity relative to the specimen surface. The minimum detectable step is 0.02 μm. After manually levelling the sample, the stylus is positioned over the uncoated portion of the sample, and then allowed to transverse along a path such that it crossed the uncoated/coated boundary onto the coated sample side; this gives a measure of the coating thickness, like shown in *figure 4.2a* and *b*. The two measurements correspond to two different scan speeds. The higher the scan speed selected, the lower the horizontal magnification, but the resulting step is better defined. The vertical magnification in this case is $2x10^4$ and can be adjusted in the control unit of the instrument.

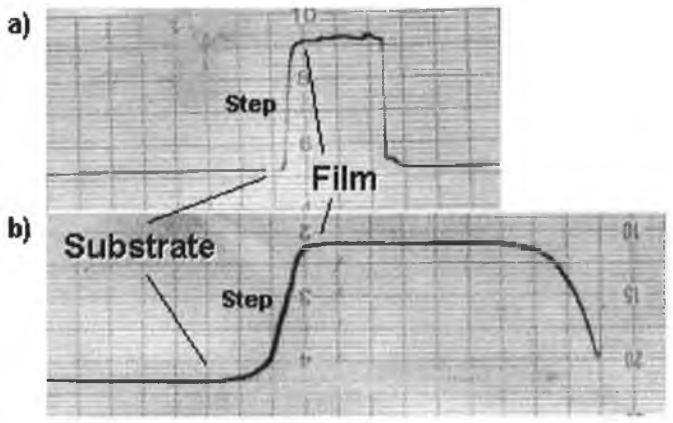

Figure 4.2: Thickness measurement at two different recording speeds: a) 1 mm/sec, b) 0.25 mm/sec.

The deposition rate of carbon nitride films as a function of nitrogen fraction in the Ar/N_2 gas mixture used for deposition, at total pressures of $1x10^{-3}$ and $1x10^{-2}$ mbar is shown in *figure 4.3*. It can be seen that the total pressure in the deposition chamber has a strong influence in the deposition rate. An increase in pressure from $1x10^{-3}$ to $1x10^{-2}$ mbar for a nitrogen partial pressure (Npp) greater than 50% increased the deposition rate almost twice from 2.2 μm/h to 3.9 μm/h. At lower pressures, an increased substrate bombardment is expected due to longer mean free path, and sputtering of the growing film is expected. At higher pressures, the motion of both the ions and sputtered species is impeded by numerous collisions in the gas phase. Consequently, fewer ions collide with the target and more of the sputtered species loose their energy before reaching the substrate. For both pressures, the deposition rate also increases with nitrogen concentration in the working gas. All films were grown using –50 V substrate bias voltage. The substrate position in the chamber was kept as close as possible to the centre of the opposing cathodes. Thinner films resulted if the substrates were placed above or below the centre of the cathodes (targets).

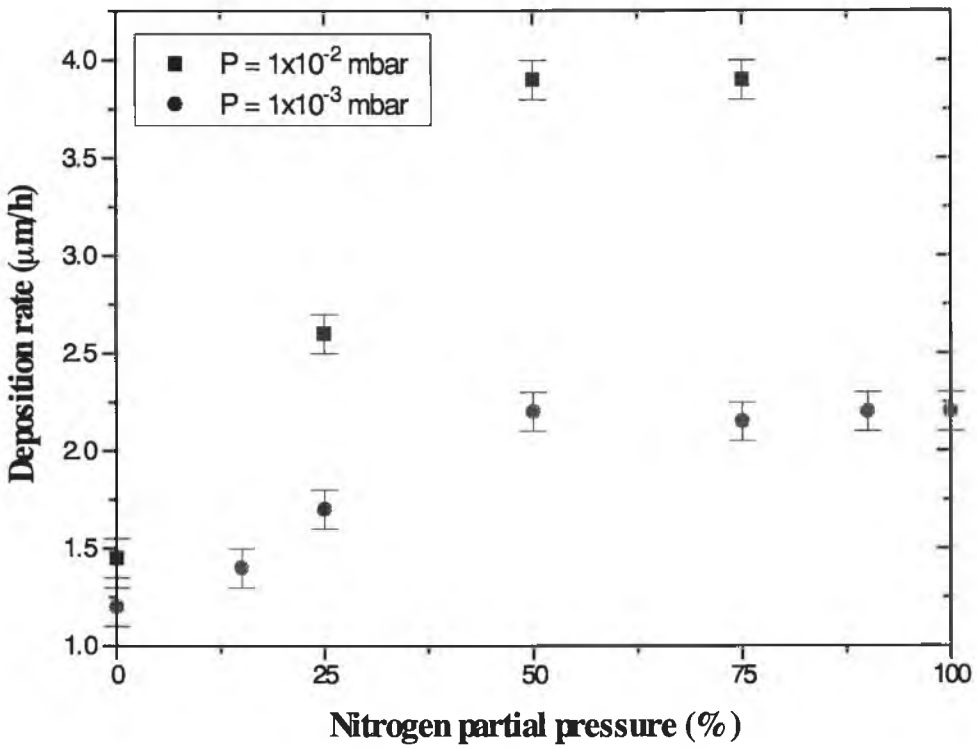

Figure 4.3: Deposition rates of carbon nitride films as a function of nitrogen partial pressure (Npp) for films grown at different pressures.

A likely explanation is that the atomic mass of nitrogen atoms is closer to that of carbon than argon. This fact results in better momentum transfer during sputtering, and hence higher sputter deposition rates. In chapter 2 it was seen that the sputtering yield S, defined as the number of atoms ejected from the target surface per incident ion is higher when the mass of the bombarding particle is of the same order of magnitude than that of the target atoms. Films deposited at $1x10^{-2}$ mbar became detached from the surface shortly after deposition probably due to the high stresses in the films. From this point onwards, the investigation was mainly focused on carbon nitride films deposited at $1x10^{-3}$ mbar. As seen in *figure 4.3*, the deposition rates for these films increases from 1.2 μm/h at 0% Npp to 2.2 μm/h at 100% Npp. These values are among the highest reported for sputtered carbon nitride films.[1,2]

4.3 Film composition

The film composition was measured by RBS (Rutherford backscattering) using a 1.5 MeV beam of He^+ particles. RBS is based on collisions between atomic nuclei. The sample under investigation is targeted by a beam of energetic (MeV) ions. The incident beam particles interact with the nuclei of the target material, scattered backwards and then detected. The processes involved are of classical nature and easily quantifiable.[3] In a head on collision of an incident particle of mass M_1 with a target atom of mass M_2, the ion energy E is reduced to

$$\left\{\frac{M_2 - M_1}{M_2 + M_1}\right\}^2 E$$

after scattering. Thus from the energy of the back-scattered particles, the target atoms can be identified. The yield from a target is given by the differential cross-section, which is proportional to

$$\left(\frac{Z_1 Z_2}{E}\right) Co\sec^4(\theta/2)$$

where Z_1 and Z_2 are the atomic numbers of the incident and target atoms, E is the beam energy and θ is the scattering angle. Thus target stoichiometry may be determined.

The scattering angle was 160° in the IBM geometry, i.e. with the detector located in a horizontal plane with the beam. Different angles of incidence were used to separate the carbon and nitrogen signals from the signal due to the silicon substrate, which differed from sample to sample due to the different thickness of the films. The atomic percentage ratios were determined with an error of between 5 and 10%. This was possible to achieve because of the absence of background due to heavy elements.

It was found that the nitrogen content and the deposition rate of the films increased as the percentage of nitrogen in the nitrogen/argon sputtering gas was increased, as shown in *figure 4.4*. The elemental analysis of these films, corresponding to the M

series is given in *table 4.1*. The films were grown with ground shield covers on the top of the screws to minimise iron contamination, caused by sputtering of steel components used for mounting the graphite targets in the magnetron assembly. The increase in nitrogen incorporation does not relate well with nitrogen gas percentage during deposition. As Npp was increased up to ~50% Npp, the nitrogen content in the films increased markedly. From 50 to 100% Npp, the nitrogen incorporation seems to reach a saturation value in the range 33-37 at.% N.

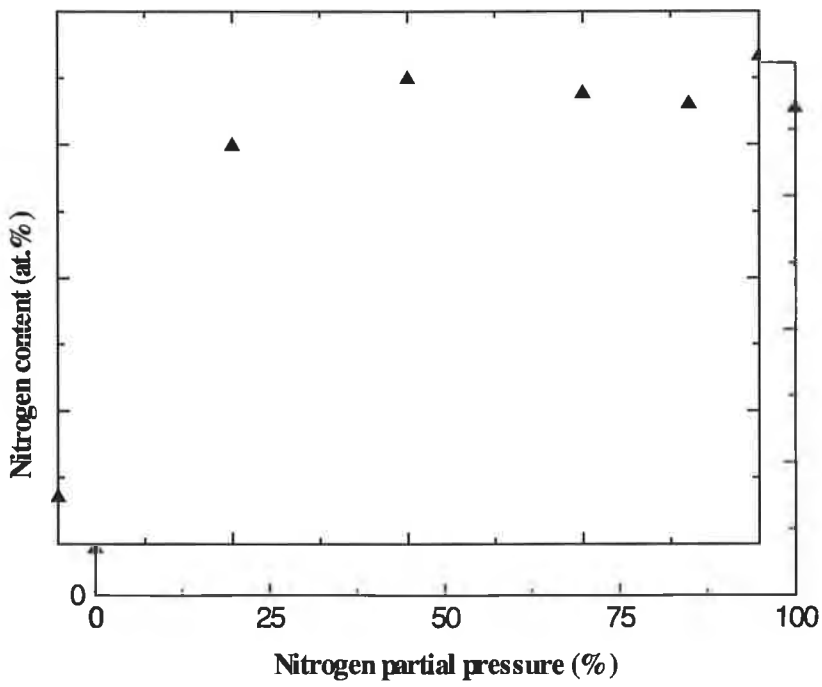

Figure 4.4: Nitrogen content in the films as determined by RBS, as a function of nitrogen content in the sputtering gas.

Zheng et al.[4] found that for increasing nitrogen partial pressure, nitrogen incorporation remained fairly constant at ~30 at.%, while the deposition rate increased by more than 50%. The explanation given was reduced film density and increased impingement rate of both N and C-containing precursors at the growth surface. The use of Ar/N_2 mixture complicates the growth kinetics. The incorporation of nitrogen in the films during reactive sputtering depends on the competition between the trapping of N atoms on the growth surface and desorption of N-containing species from the growth surface. Thus, both thermodynamics and kinetics will limit the N content of the films. The dominant mechanism of N incorporation in the films is a result of chemisorption of atomic N

and/or low energy implantation of energetic species (especially N^+ and N_2^+ ions) impinging on the growth surface with an energy high enough to become implanted and trapped. The loss of N-containing species from the growth surface will occur either through re-sputtering or through thermal desorption, i.e. volatile C-N products can be expected to be a large source of N loss at elevated temperatures.[5] The deposition temperature here was ~280°C. The samples indicated in *table 4.1* were not the only ones in which the nitrogen incorporation was measured. Carbon nitride films of up to 44 at.% N were obtained.

Sample	% N_2 gas	C	N	O	Ar	Fe
M1	100	63.1	36.6	-	0.24	0.1
M2	90	66.3	33	-	0.6	0.07
M3	75	64.6	33.8	1.4	-	0.23
M4	50	63.1	34.9	2	-	-
M5	25	67.3	29.9	1.7	0.83	0.26
M6	0	91.9	3.5	1.7	2.6	-

Table 4.1: Elemental composition of carbon nitride films by RBS.

It can be seen that the amount of iron increases slightly with decreasing Npp (increasing argon concentration in the sputtering gas) due to the high sputtering yield of argon for iron.[6] Sample M6 exhibits the higher percentage of Ar gas (~2.6%) entrapped in the bulk, due to the use of 100% Ar as sputtering gas. Most films, independent of nitrogen content, were found to contain about 1.5–2 at.% of oxygen at the surface, probably originated from atmospheric contamination after deposition. Films with the minimum oxygen contamination were chosen for structural characterization. The film density of films containing > 30 at.% N is about 2.2 g/cm^3.

4.4 Infrared spectroscopy

The IR absorption was measured using a Perkin-Elmer FTIR 2000 system. The scanning resolution was 1 cm^{-1}. A deuterated tri-glycine sulphate (DTGS) detector was used for the reflected beam. All the scans were performed at room temperature and normal atmospheric conditions. The specific absorbance of the various peaks was found from the peak heights taking into account the background absorption and multiple internal reflections in the films. Strictly, the peak area should be used; however, the peak height gives an adequate demonstration of the trends.

Figure 4.5 shows the IR absorbance spectra for sample (a) containing 32.5 at.% N and deposited at P=1x10^{-3} mbar, and for sample (b) containing 40.8 at.% N and deposited at P=1x10^{-2} mbar. Both samples were grown in a pure N_2 atmosphere. In general, the IR spectra of carbon nitride materials exhibit a broad band between 1100 and 1800 cm^{-1}, which correspond to C=N, C=C and C-N stretching modes,[7] and may exhibit a band at ~ 2200 cm^{-1} corresponding to the C≡N stretching mode.[8] In the spectra of the low-pressure film (a) the two main features appeared as a broad band centred at ~1550 cm^{-1}, which main contribution comes from C=N bonds, and a very distinguishable peak centred at ~ 2200 cm^{-1}, which was assigned to C≡N bonds. The vibrational frequencies in region 2100-2250 cm^{-1} can be associated with several structures containing both nitrile (-C≡N) and isonitrile (-N≡C) groups.[9] However, in the absence of hydrogen, the most likely candidates are nitrile groups bonded to aromatic rings, for which the predicted frequency is ~ 2210-2240 cm^{-1}, and possibly isonitrile groups at frequencies ~2100-2190 cm^{-1}.

In the case of the high-pressure film (b), new bands appear at ~2900 and ~3300 cm^{-1}, which correspond to C-H and N-H bonds respectively.[9,10] The hydrogen originates from residual moisture in the deposition chamber; water vapour had been absorbed or had reacted with the films after exposure to air. The peak at 2200 cm^{-1} in the IR spectrum of the high-pressure film is much smaller than for the low-pressure film. This may be attributed to a lower collision probability of nitrogen molecules in the gas atmosphere with decreasing pressure, so that more nitrogen reaches the sample surface

as N_2 molecules and is incorporated in the film as C≡N because of the higher local concentration of nitrogen in the impact region.

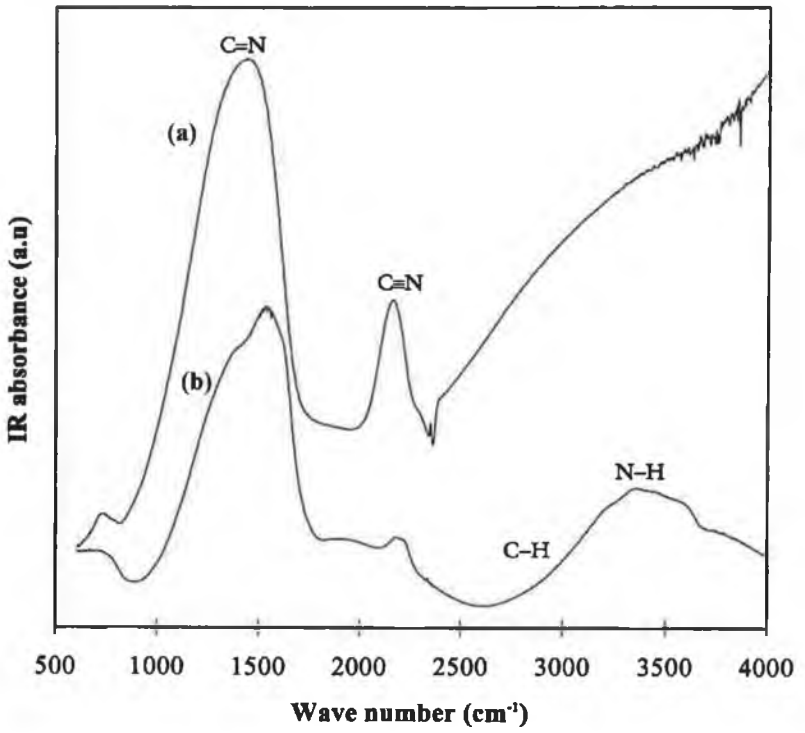

Figure 4.5: IR spectra of carbon nitride films deposited at different total pressures: (a) P=1x10^{-3} mbar, (b) P=1x10^{-2} mbar.

The IR spectra suggest clearly that nitrogen atoms are incorporated in the bonding network of amorphous carbon. If carbon is sp^3 bonded to nitrogen as in crystalline β-C_3N_4, an absorption peak should appear around 1250 cm^{-1},[11] however, because of the overlap with the strong sp^2 carbon absorption, detection of such a band is very difficult, therefore no evidence of its existence can be extracted form the IR spectra.

Figure 4.6 shows the corresponding IR absorbance spectra of samples with different nitrogen content. The C≡N stretching band at ~2200 cm^{-1} becomes more intense as the nitrogen incorporation in the film increases. The IR spectrum of the film containing ~0 at.% N shows no IR-active features. However, a weak absorption appears in the 1200-1600 cm^{-1} region, despite of the pure argon atmosphere used for deposition. This implies the presence of traces of nitrogen or oxygen in the film. The absorption at

around 700 cm^{-1} can be assigned to the out-of-plane bending mode for the graphitelike regions (sp^2 carbon), which becomes IR active due to nitrogen incorporation into the bonding network.[12] Since N has one more electron than the C atom, the substitution of N in the C lattice causes a buckled or bent C plane structure.

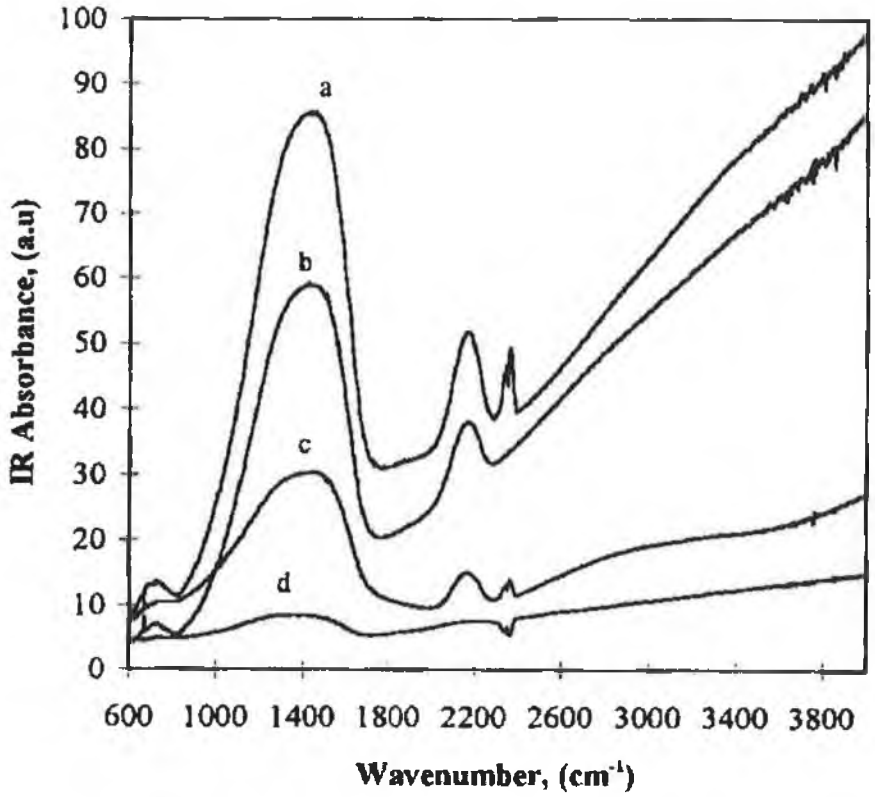

Figure 4.6: IR spectra as a function of nitrogen content: (a) ~44 at.% N, (b) ~37 at.% N, (c) ~25 at.% N, (d) ~0 at.% N.

Initially, for low concentrations of nitrogen in the N_2/Ar sputtering gas, the absorption peaks due to the C≡N bond (2200 cm^{-1}) and C-N and C=N bonds (1500 cm^{-1}) increased with nitrogen content in the film as measured by RBS. However, the IR absorption due to carbon-nitrogen bonding was observed to be independent of actual nitrogen content above ~25 at.% N, which corresponds approximately to 25% nitrogen partial pressure. *Figure 4.7* shows the absorbance per meter for the two main peaks in the IR spectra (C=N and C≡N) for a series of films grown at $1x10^{-3}$ mbar and –50 V substrate bias for varying Ar/N_2 gas ratios. It can be seen that over the range 25-44 at.% N there is no systematic variation of absorption coefficient. This implies that for

>25 at.% N content, the excess N is not bonded to C otherwise it would be visible as an increase in absorbance. No other absorption peaks within the instrumental range of 4000-600 cm^{-1} develop as the N content increases. The results suggest that the excess nitrogen is present as an IR invisible bond such as a N-N non-polar bond of some type or possibly inclusions of N_2.

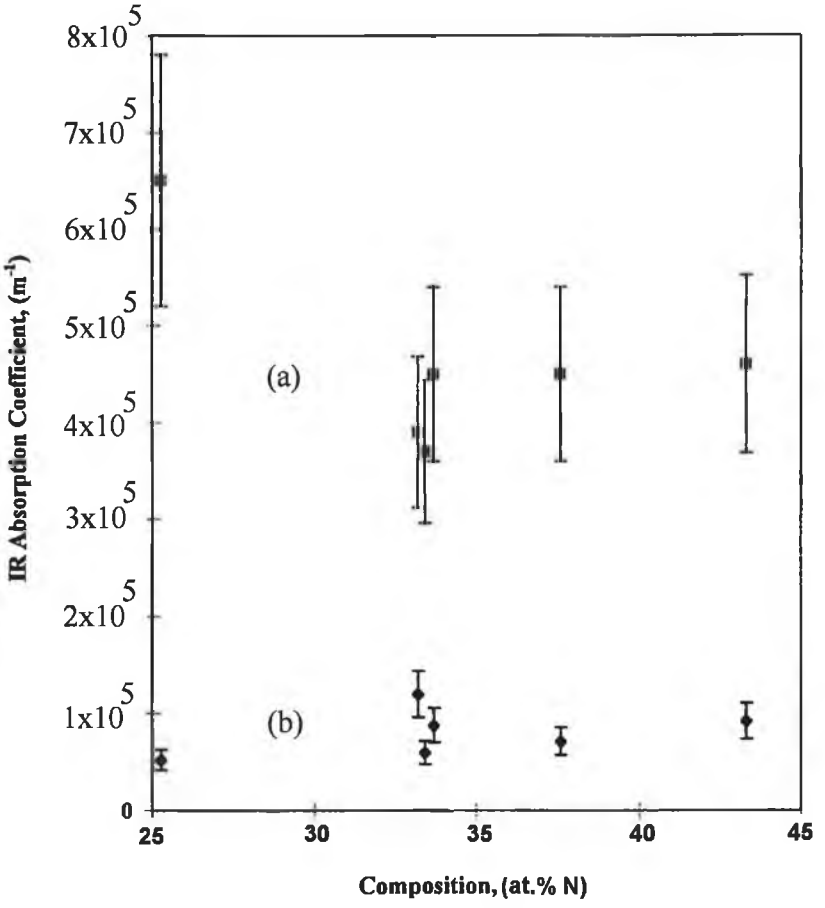

Figure 4.7: IR absorption coefficient for the two main peaks: (a) C=N peak and (b) C≡N peak as a function of at.% N.

The measurements of film composition and IR absorbance show that for films with nitrogen content <25 at.%, nitrogen is mostly bonded to carbon. With increasing nitrogen content above 25 at.%, excess nitrogen probably exists mainly as N-N bonds of some description. The broad band considered here in the region 1100-1800 cm^{-1} is too complex to be studied only by IR. Raman spectroscopy was needed to further study the bonding types in the films.

4.5 Raman spectroscopy

Raman spectra were obtained using a Kaiser system Holoprobe Raman with a He-Ne (633 nm) laser and a Peltier cooled Princeton CCD camera. The scanning resolution was 1 cm^{-1}. A Single monochromator was used, with a microscope mode with normal incidence. Rayleigh scattering was eliminated by the use of two high performance notch filters. The objective lens focal length to diameter ratio was 1.8.

Figure 4.8 shows the Raman spectra of samples with different nitrogen content. The C=N stretching band appears in the wave number range 1200-1700 cm^{-1}. Usually, two Raman active modes are observed in this region in carbon nitride films; one at approximately 1570 cm^{-1} and another at ~1360 cm^{-1}.[13] These bands are characteristic of graphitic (G) and disordered (D) sp^2-bonded carbon. The Raman active G and D bands are very prominent in these spectra. When the film contains 0 at.% nitrogen, these bands can be still resolved. The absorption at ~700 cm^{-1} attributed to an out-of-plane bending mode for graphite-like domains (a less sensitive mode than the Raman-active G band) is becoming more intense as the nitrogen incorporation in the film increases. The band at ~2200 cm^{-1} is due to the stretching vibration of C≡N bonding, as seen in the IR spectra. With increasing nitrogen, the Raman active G and D bands, and the C≡N band become stronger, indicating an increase in the sp and sp^2 hybridised carbon bonded with nitrogen. The intensity of the G and D band is sensitive to nitrogen concentration. Kaufman et al.[13] concluded that nitrogen substitution is responsible for the symmetry breaking of the sp^2 domains and the intensity of the G and D bands. At higher wave numbers (~2900 cm^{-1}) a band appears, probably due to the C-H stretching band,[14] caused by the presence of residual water vapour in the chamber during film deposition.

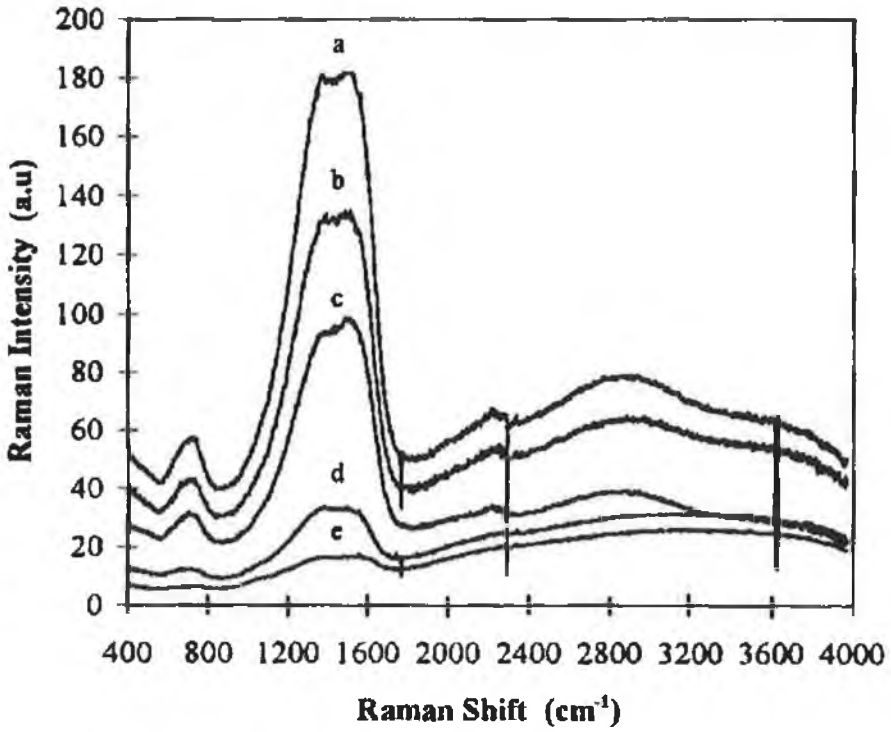

Figure 4.8: Raman spectra as a function of nitrogen content: (a) ~44 at.% N, (b) ~37 at.% N, (c) ~33 at.% N, (d) ~25 at.% N, (e) ~0 at.% N.

IR studies suggested that above 25 at.% N content in the films, N does not preferentially bond to C, since the IR absorption coefficient due to C=N and C≡N bonds did not change systematically. The excess nitrogen above 25 at.% is present in the film forming bonds other than C=N and C≡N. Weich et al.[15] derived the possibility of the formation of nitrogen-nitrogen bonding within the CN compound. They found that this bonding should increase as nitrogen incorporation increases in the film. A N=N stretching mode can be observed in vibrational Raman spectra in the region 1400-1500 cm^{-1} when nitrogen bonds with the carbon ring, especially in bonding structures such as C-N=N-C.[16] The N=N stretching vibration is forbidden in the IR spectrum as this is a symmetrical vibration in a molecule having a center of symmetry. In the Raman spectrum, the N=N stretching band overlaps with the G and D bands, so in order to investigate its evolution, it was necessary to deconvolute the Raman region 1100-1800 cm^{-1} using a Gaussian-Lorentzian fit. A linear background was assumed due to the Raman photoluminescence (PL) effect.[17]

Figure 4.9 shows the deconvoluted Raman peak in the region 1100-1800 cm^{-1} for films containing 0, 25 and 33 at.% N. For the nitrogen-free film, the region was fitted with two peaks corresponding to the G (1560 cm^{-1}) and D (1355 cm^{-1}) bands. However, for nitrogen-containing films, it was necessary to include a third intermediate peak (at ~1460 cm^{-1}) between them to match the measured spectra accurately. This peak increased with the nitrogen content of the films and was assigned to the N=N stretching band, and was called the N peak.

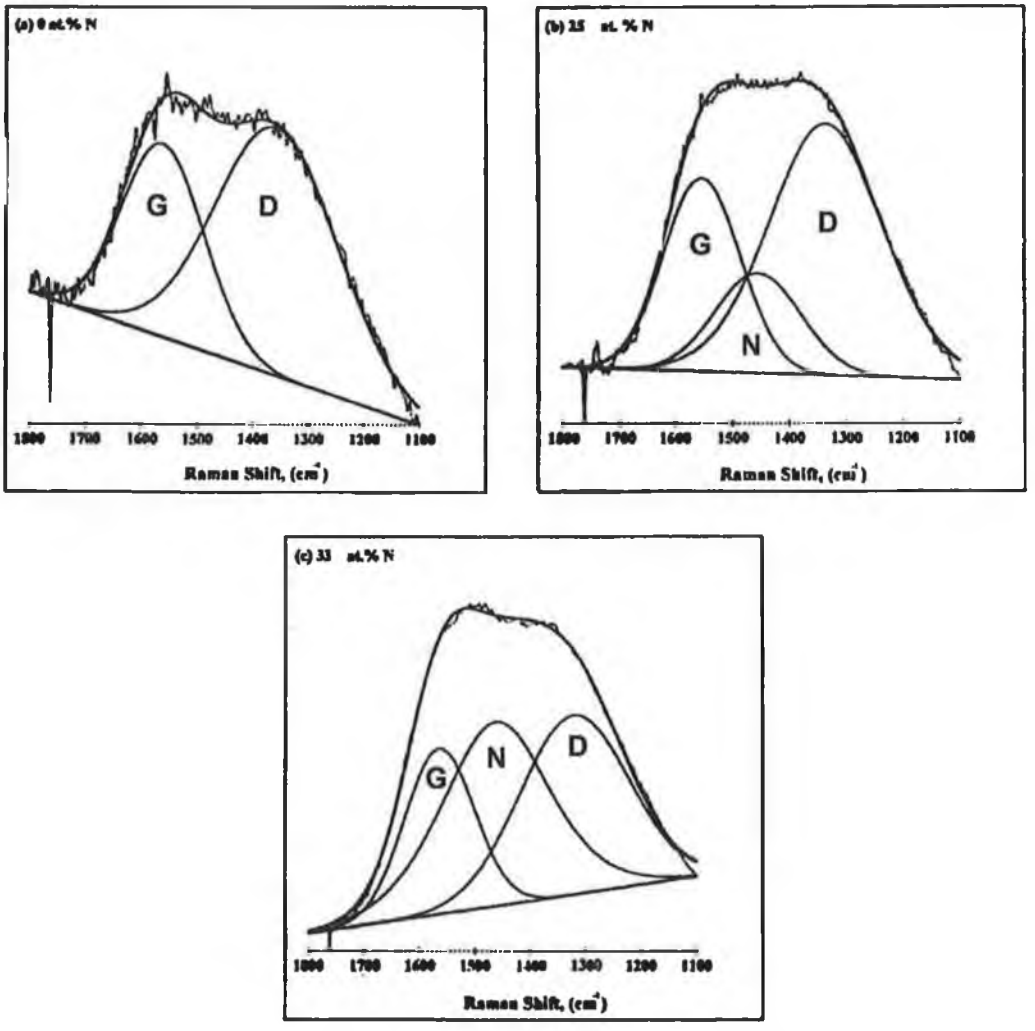

Figure 4.9: Deconvoluted region (1100-1800 cm^{-1}) of the Raman spectra of carbon nitride films: (a) ~0 at.% N, (b) ~25 at.% N, (c) ~33 at.% N.

The I_N/I_G peak ratio as a function of nitrogen concentration is shown in *figure 4.10*. It can be seen that there is a monotonic increase in the intensity of the N peak relative to the G peak, indicating that as nitrogen content in the film increases, the N=N bonding in the films also increases.

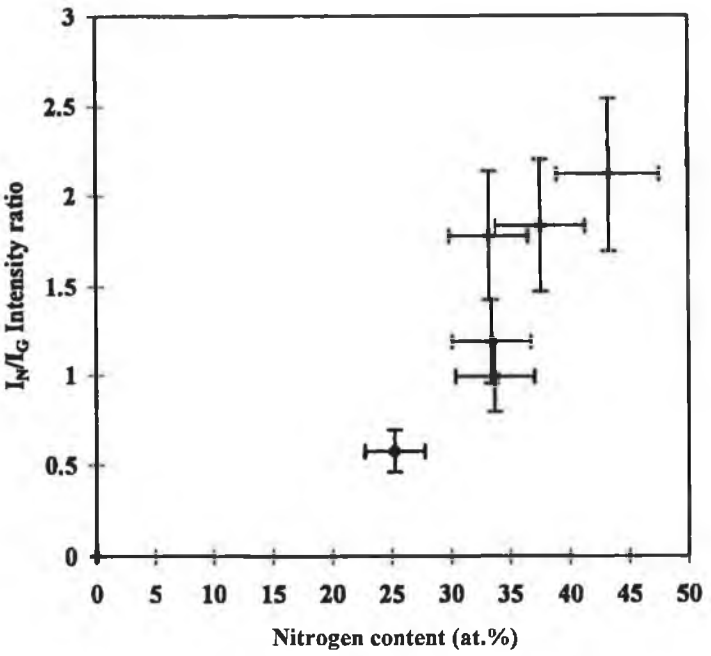

Figure 4.10: I_N/I_G peak area ratio as a function of nitrogen content.

4.6 X-ray photoemission spectroscopy

High-resolution XPS analyses were carried using a VG spectrometer with a monochromated Mg Kα (1253.6 eV) X-ray source with an energy resolution of ~0.5 eV. The binding energy values of the photoelectron peaks were measured with an accuracy of ±0.05 eV. The spectrometer was calibrated to position the $4f_{5/2,7/2}$ photoelectron lines of clean pure Au foil at binding energies of 87.74 and 84.07 eV. The films were conductive enough to ignore the charging effect.

The change in the structure of carbon nitride films should be understood from the relative variation of carbon-nitrogen bonds in the XPS spectra. *Figure 4.11* shows the N1s XPS spectra of carbon nitride films containing 33 and 43 at.% N. The C1s XPS spectra for the same films is shown in *figure 4.12*.

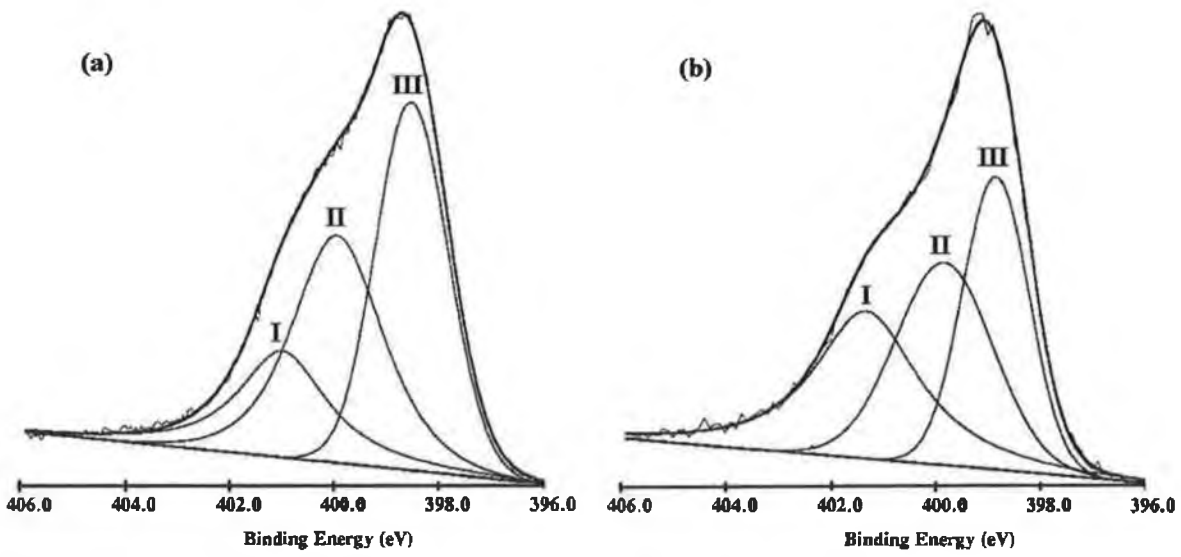

Figure 4.11: XPS spectra of N1s electrons of carbon nitride films: (a) ~33 at.% N, (b) ~43 at.% N. Peaks were assigned as: I at ~401.2 eV (due to N-N sp^2), II at ~400 eV (due to C=N sp^2) and III at ~398.8 eV (due to C≡N sp).

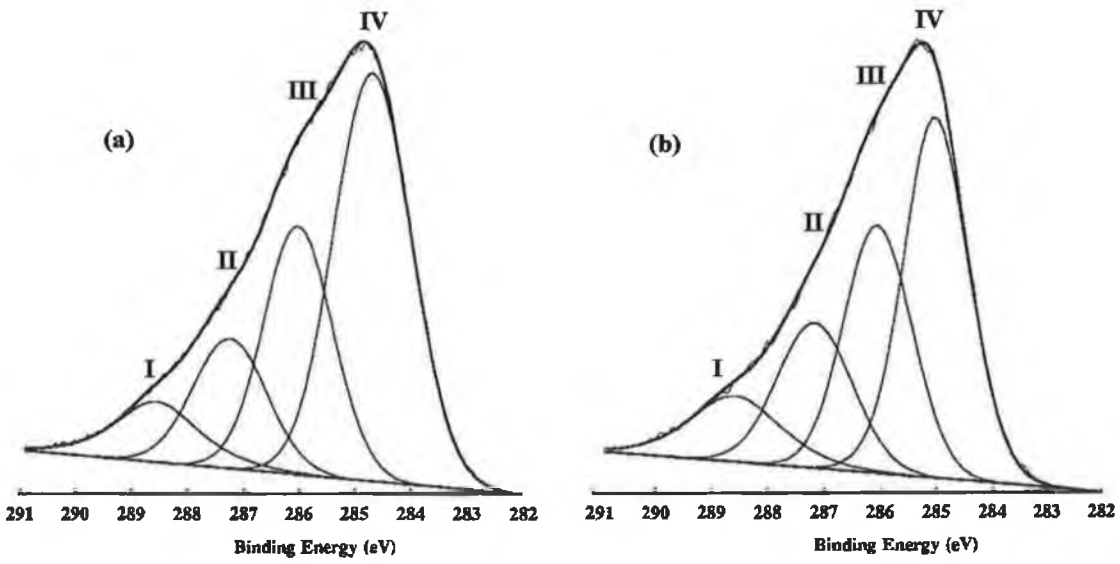

Figure 4.12: XPS spectra of C1s electrons of carbon nitride films: (a) ~33 at.% N, (b) ~43 at.% N. Peaks were assigned as: I at ~288.5 eV (due to C≡N sp), II at ~287.5 eV (due to C-C/C-N sp^3), III at ~286 eV(due to C=N sp^2) and IV at ~284.5 eV (due to adventitious carbon).

The ascription of lines to specific bonding states of carbon and nitrogen atoms found in literature is different and often contradictory. It is generally accepted that nitrogen atoms prefer to substitute carbon atoms in the graphitic carbon cluster. A common observation in nearly all past XPS studies on carbon nitride films is that two or three contributions to the N 1s peak and three or four contributions to the C 1s peak have to be assumed.[18,19,20,21] In all these studies, the peak locations for the N1s spectra are usually located around energies of 398 eV and 402 eV. Normally, the peaks are observed at ~398.3 eV (N bonded to sp^3 C) at ~400 eV (N bonded to sp^2 C) and sometimes a third peak is included at ~402 eV attributed to N-O or N-N bonding. Hammer et al[22,23] assigned the origin of this third peak to planar N-N bonding configuration and maybe to N_2 molecules trapped in the film. Gouzman et al.[24] also suggested that fragments of >N=N< and –N=N- contribute to a peak at ~401.3 eV. They also mentioned hat the C≡N bonding configuration is expected at ~398.4-399.2 eV.

The N1s spectrum shown in *figure 4.11* can be deconvoluted into three peaks. Peak I (at ~401.2 eV), typically assigned to N-N or N-O bonding, is found to increase with nitrogen incorporation. It can be seen that peak I for the film with the highest nitrogen content is relatively much higher. Since there is no observable oxygen in the films as measured by RBS, the 401.2 eV can be assigned to N-N bonds. This increase agrees with the Raman results discussed earlier, where as nitrogen incorporation in the film increases, the N peak also increases. Because there is no real evidence in the films to suggest the presence of N bonded to sp^3 C, peak III at 398.8 eV was assigned to C≡N bonds, and peak II at ~400 eV is assigned to C=N bonding, as also seen in earlier studies.[25,26,27]

Considerable variation in the C1s core-level binding energy is found in literature.[29,30,31] The C1s spectra peaked at ~284.5 eV and were found to be highly asymmetric towards higher binding energies, as shown in *figure 4.12*. Precisely, the peak centered at ~284.5 eV is due to the adventitious carbon present on the film surface due to atmospheric exposure. The binding energy value of C1s photoelectron observed for adventitious carbon on various solid surfaces is approximately 284.6

eV.[28] The C1s peak at ~286 eV is related to a polymerised chain or ring structure containing a –C=N– bonding configuration that is similar to pyridine (C_5H_5N), whose C1s energy is ~285.5-286 eV.[29,30,31] Hence, corresponding to the peak II and peak III in the N1s spectra, the C1s peak III (~ 286 eV) and peak I (288.5 eV) were assigned to C=N bonding and C≡N bonding respectively.

In most recent XPS studies on carbon nitride in which there was some evidence of N bonded to sp^3 carbon (as found in the β-C_3N_4 phase), there is an agreement on whereabouts in the XPS spectra the existence of this bond should manifest itself. In these studies, the N1s and C1s peaks are observed at ~398.8 eV and 287.7 eV,[32] 398.6 eV and 287.7 eV,[33] 399 eV and 287.4 eV,[34] and 398.46 eV and 287.32 eV,[12] respectively. In consequence, it seems that the predictions made by Marton[21] on the C1s and N1s binding energies for the bonding state of β-C_3N_4 (287.7±0.2 eV and 398.5±0.2 eV for C1s and N1s, respectively) are generally accepted.

The lack of evidence of N bonded to sp^3 carbon from the spectroscopy techniques does not necessarily mean that this bond is not present in the films. In the IR and Raman spectra a strong absorption band was observed from 1100 to 1800 cm^{-1} which covers the wavenumber where the C-N absorption in β-C_3N_4 should be (1212-1265 cm^{-1}). Therefore, the superposition of several overlapping vibration bands makes its observation very difficult. The vibration modes of crystalline C-N structures may not be significantly active for Raman scattering or IR activation at room temperature. Peak II at ~287.5 eV found on the C1s spectra in *figure 4.12* may be due to N bonded to sp^3 C, as observed by Marton, probably mixed with C-C sp^3 bonding. The corresponding N1s peak would be at ~398.8 eV, which overlaps with the contribution assigned to C≡N bonding. It is not possible either to confirm or disprove any of these identifications. As will be discussed later, areas of crystalline regions were detected in some carbon nitride films.

The XPS valence band spectra of the films, which can distinguish between graphite-like, interlinked carbon backbone and diamond-like features is considered in chapter 6.

4.7 Effects of process parameters

In this section, the effects of process parameters, namely substrate bias and substrate temperature are investigated. All the films investigated in this section were grown at 100% nitrogen atmosphere at a total pressure of $1x10^{-3}$ mbar. A clear understanding of the process parameters are required to have control on deposition of carbon nitride thin films. The annealing behaviour of carbon nitride films is also mentioned.

4.7.1 Substrate bias

Firstly, the effect of negative substrate bias on the deposition rate of the films was investigated. It can be seen in *figure 4.13* that increasing negative bias voltage on the substrate holder from 0 to –200 V markedly decreased the deposition rate by almost three times. The negative bias accelerates the positive nitrogen plasma ions towards the substrate with energy equal to the difference between the substrate and plasma potential. The nitrogen content of the films measured by Rutherford backscattering (RBS) as a function of substrate bias is shown in *figure 4.14*. Little variation in the nitrogen content in the film was found in the substrate bias voltages investigated.

Different mechanisms could contribute to the observed decline in sputtering rate with negative bias, such as: (i) preferential sputtering and a change in the film stoichiometry, (ii) a densification of the film, (iii) reduced target sputtering and (iv) chemical sputtering of the film. Since there was no observable variation in nitrogen content, the first option was ruled out. Although film density was not measured here, it is unlikely that a variation of film density (due to filling of voids/holes) could account for the observed thickness changes, since no major effect was seen on the other properties, such as the hardness, subject of chapter 5. Therefore this explanation can also be discounted. The target potential showed no significant variations with substrate bias therefore a change in sputtering rate did not occur. The most likely explanation is that the increased nitrogen ion energy at the substrate caused increased ion bombardment of the film and stimulated a desorption of carbon and nitrogen in the ratio in which they were present in the film, as suggested by Sjöström et al.[5] Higher

values of negative bias (> -300 V) are expected to cause a transition where ion etching and re-sputtering will be the dominant process, and no film growth will occur above a critical value of negative bias.

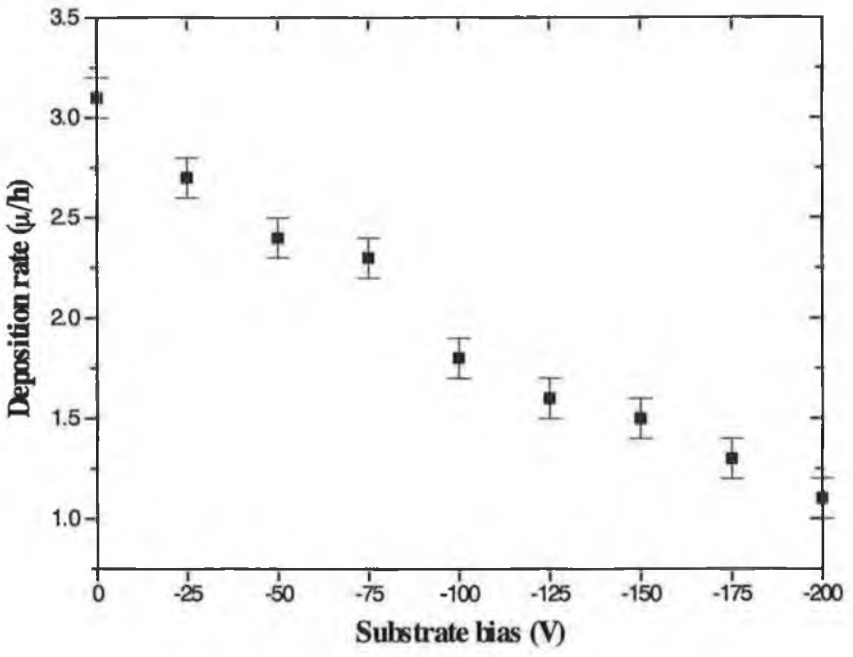

Figure 4.13: Deposition rate as a function of negative substrate bias.

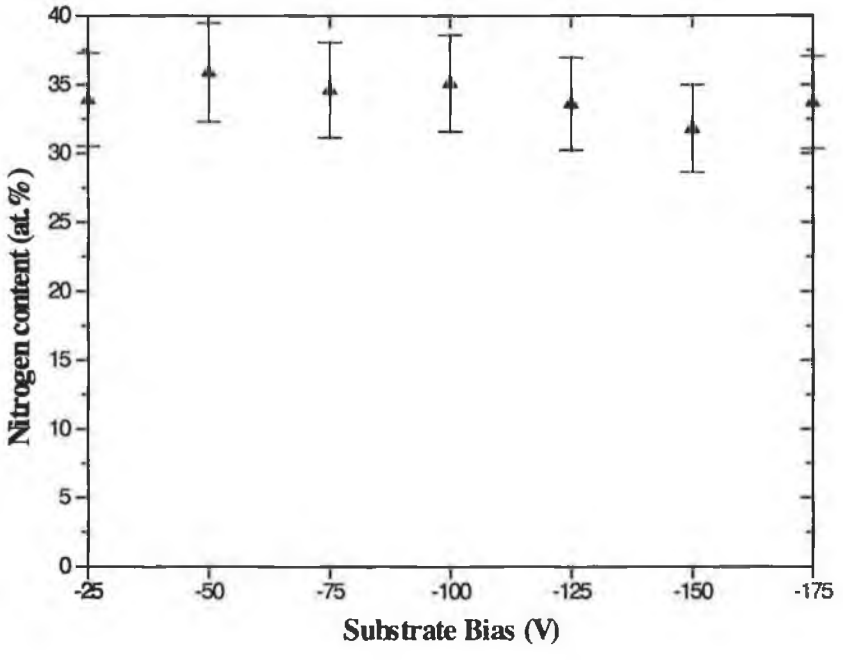

Figure 4.14: Nitrogen content as a function of negative substrate bias.

The IR spectra of films deposited at increasing negative bias is shown in *figure 4.15*. The most remarkable feature in each IR spectrum for films deposited at different bias is a strong broad absorption peak from 1100 to 1800 cm^{-1}. As discussed before, this band can be identified with the Raman active G and D bands in graphite single crystal, observed at 1550 and 1360 cm^{-1}, respectively. The symmetry breaking due to incorporation of nitrogen atoms into the carbon network turns these otherwise IR forbidden bands into IR active bands. The G band corresponds to graphite-like layers of sp^2 microdomains in the film, while the D band is attributed to the bond-angle disorder in the sp^2 graphite-like microdomains induced by the linking with sp^3 carbon atoms as well as the finite crystalline sizes of sp^2 microdomains in the film.[13]

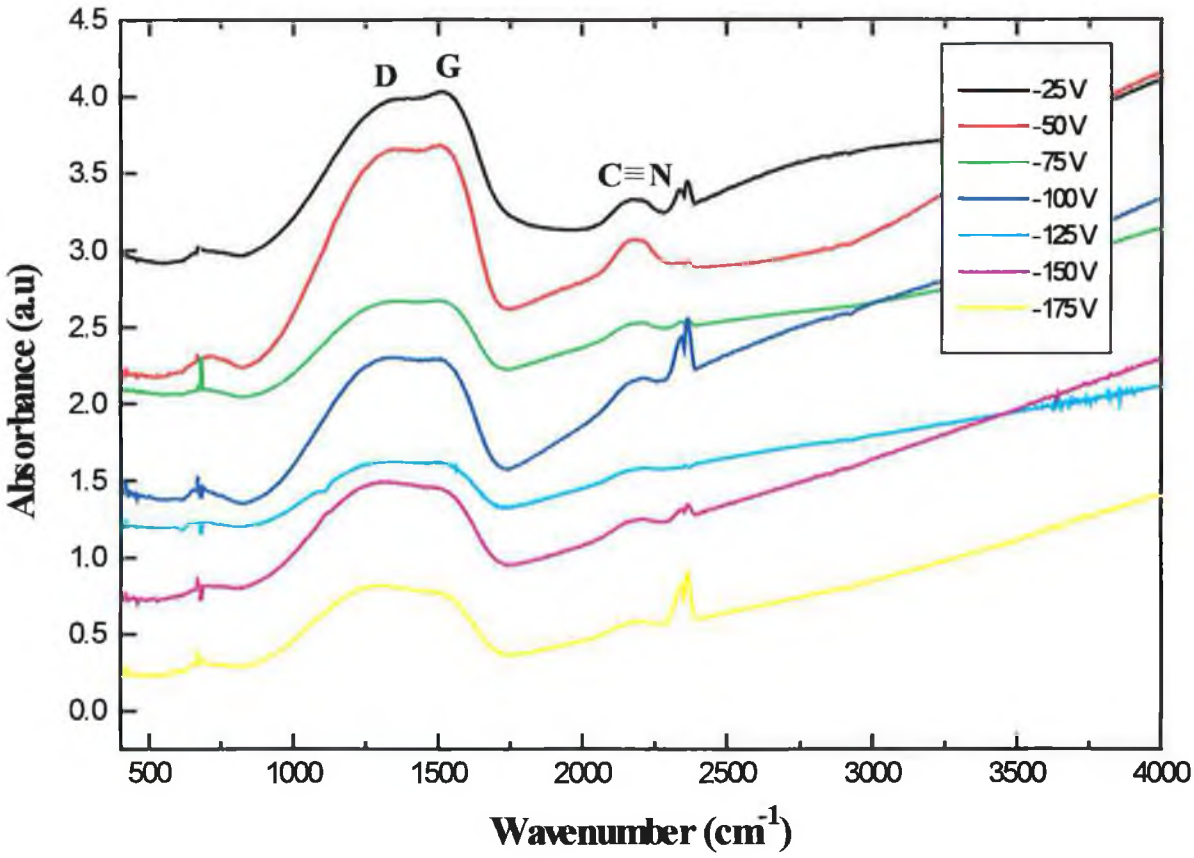

Figure 4.15: IR spectra for films deposited at different negative substrate bias.

The relative intensity of the G and D bands remained unchanged with increasing negative bias voltage. The bonding structure of the films was further probed by

measuring the Raman spectra over the range of bias and extracting the areas of the 'D', 'G', and 'N' peaks. The ratio of the 'N' to the 'G' peak did not change, neither did the ratio of the 'D' to the 'G' peak, as seen in *figure 4.16*.

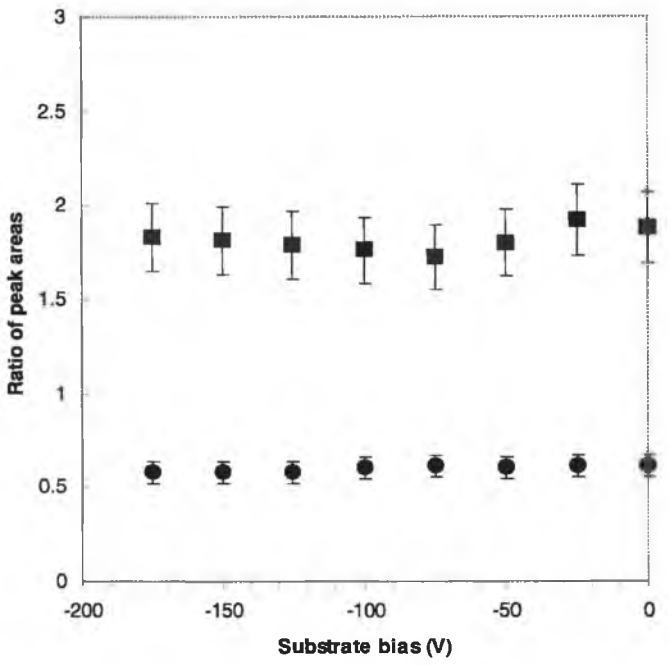

Figure 4.16: Ratio of areas of Raman peaks as a function of substrate bias: ■ - ratio of 'N' peak to 'G' peak, ● - ratio of 'G' peak to 'D' peak.

From this, it would appear that the bias has no effect. Further studies of the bonding structural changes with bias will be described in chapter 6 using valence band XPS.

The peak centered at 2200 cm^{-1} in the IR spectrum of *figure 4.15* is due to C≡N bonds, as observed earlier. The intensity of this peak in the spectra seems to decrease with negative bias. The IR absorption due to the C≡N bonds was calculated and plotted against bias voltage as in *figure 4.17*, where it can be seen that it decreases with negative bias. Taki et al.[35] found the same behaviour for their a-C:N films deposited by shielded arc ion plating. It is believed here that as substrate bias increases, due to the more energetic ions bombarding the substrate during deposition, the possibility of C≡N bonds formation decreases.

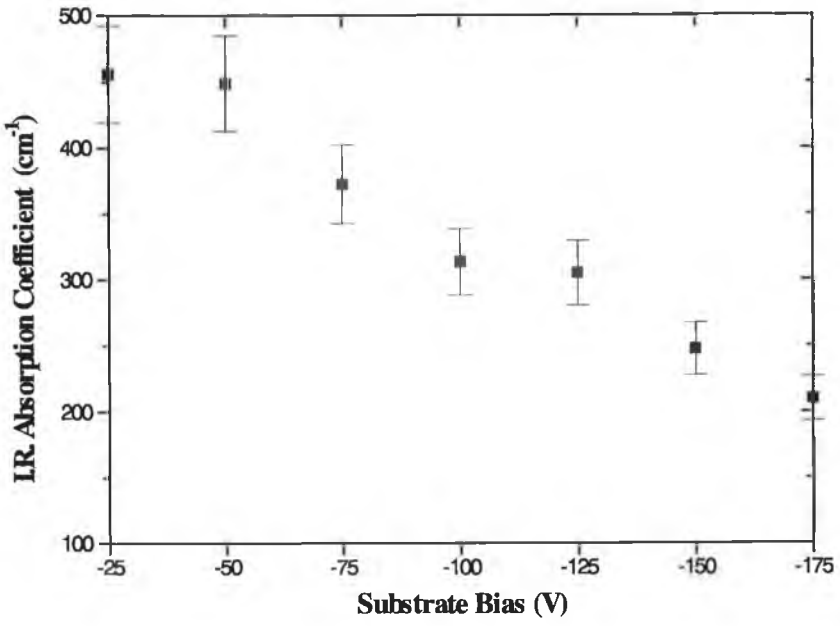

Figure 4.17: C≡N IR absorption coefficient as a function of substrate bias.

4.7.2 Deposition temperature

In order to see the effect of substrate temperature during deposition on the microstructure of carbon nitride films, two films were grown at deposition temperatures of 360°C and 420°C using the designed substrate heater. The films were compared with one grown with no additional heat during deposition, for which the substrate temperature rose to ~285°C. For higher deposition temperatures, the deposition rate decreased slightly from 2.2 to 2μm/h. The Raman spectra for the films are shown in *figure 4.18*. The D and G band become weaker as the deposition temperature increases. In addition, the intensity of the band located at 700 cm^{-1}, which becomes active with nitrogen incorporation, decreases with deposition temperature. Usually, these bands become stronger with increasing nitrogen content; this suggests that the nitrogen content in carbon nitride films decreases with deposition temperature. The decrease in the nitrogen concentration with the substrate temperature might be due to the increase desorption rate of CN species from the growth surface.[36] At high

temperatures, desorption of C≡N species from the growth surface can form volatile cyanogen molecules (C_2N_2) which results in a deficiency of nitrogen in the films.[37]

The C≡N stretching band is not well resolved in the spectra. Finally, the C-H stretching band at ~2900 cm^{-1}, due to the presence of residual water in the chamber during deposition, becomes reduced with deposition temperature. Earlier works[38,39] in the effect of substrate temperature on the Raman spectra of sputtered carbon nitride films proposed an increase in the sp^2 bonded fraction with increasing temperature, as they observed a decrease in the I_G/I_D intensity ratio and a decrease in the measured band gap. Here, no appreciable change in the I_G/I_D, or the I_N/I_G ratio was found. Increasing substrate temperature in pulsed laser deposited CN_x films caused a change in chemical structure due to a reduction in nitrogen content, with properties closer to those of graphite, such as narrowing of the band gap at high temperature.[40] The resistivity of carbon nitride films investigated here was found to decrease with substrate temperature, which supports the idea of an increased graphitization.

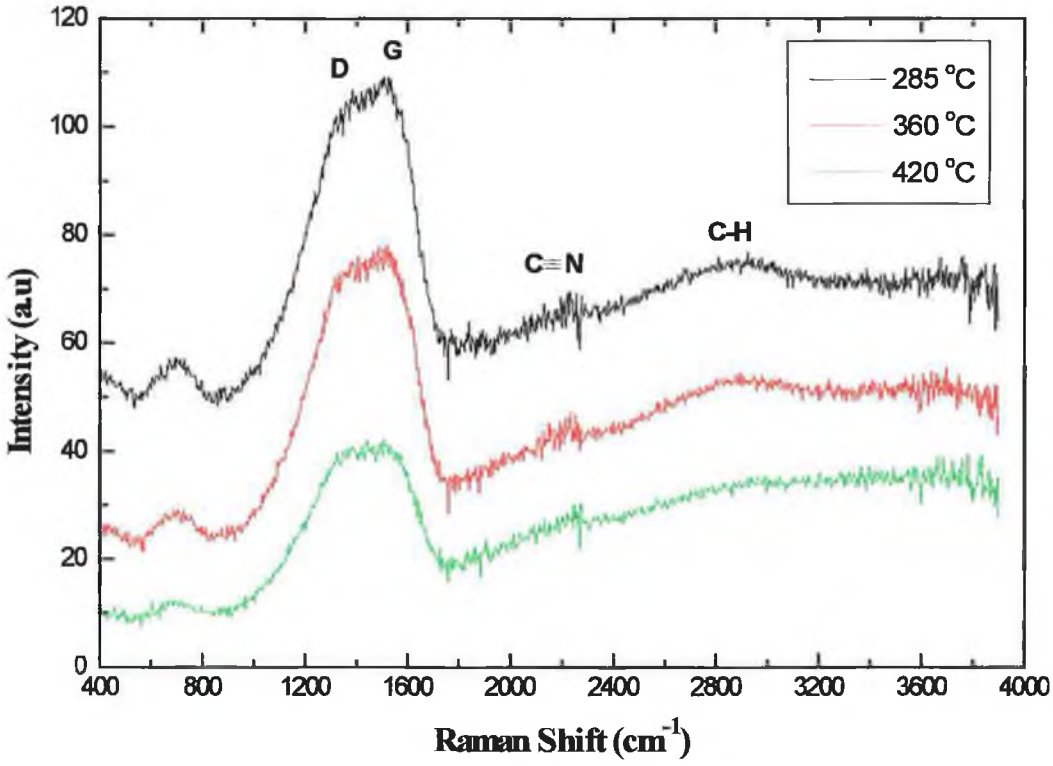

Figure 4.18: Raman spectra as a function of deposition temperature.

The annealing behaviour of the carbon nitride films was also investigated with IR, at annealing temperatures up to 600 °C (for 15 minutes). *Figure 4.19* shows the IR transmission spectra of the films after annealing. For the annealed films, the intensity of the IR peaks decrease due to loss of nitrogen. At 550°C, the C≡N peak is greatly reduced and the broad peak centered at ~1500 cm^{-1} splits in two bands corresponding to the G (at ~1560 cm^{-1}) and D (at ~1300 cm^{-1}) peaks. At 600°C, the C≡N peak disappears and the G and D peaks becomes much smaller.

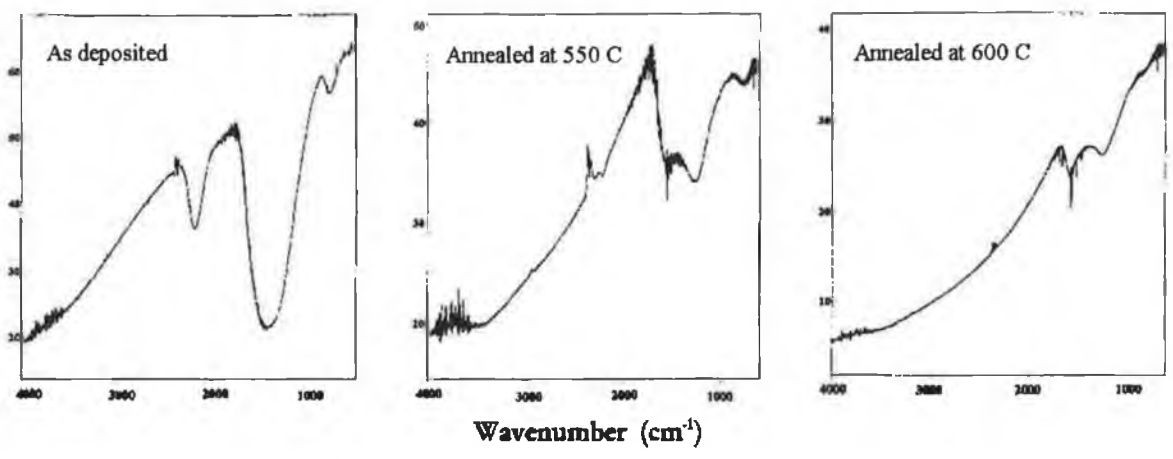

Figure 4.19: IR transmittance of as deposited carbon nitride films compared to films annealed at 550 °C and 600 °C.

4.8 Crystalline carbon nitride

All the analysis techniques considered so far gave evidence of a film structure characteristic of amorphous carbon nitride films, with a high content of sp^2 carbon. None of the spectroscopic techniques showed a real hint of the β-C_3N_4 phase. This might be caused by a resolution problem of lack of sensitivity of the spectroscopy techniques or overlapping of crystalline signals with the stronger amorphous signals.

To check for nanocrystalline areas which could exist within the mainly amorphous overall structure, films deposited in a 100% N_2 atmosphere at $1x10^{-3}$ mbar and –50 V bias voltage, containing approximately 33 at.% N as measured by RBS were investigated by plan view transmission electron microscopy (TEM). The

measurements and results are described in detail by Chowdhury.[41] Some regions exhibit electron diffraction patterns showing sharp rings associated with diffraction from a crystalline medium. A bright field image of one of these regions is shown in *figure 4.20*. Electron diffraction pattern from this area is given in *figure 4.21*. It shows only the sharp rings associated with diffraction from a crystalline medium. Moreover, calculated interplanar spacing values obtained from the nanocrystalline regions have a close correspondence with the theoretical values predicted for β-C_3N_4. *Table 4.2* shows the calculated interplanar spacings obtained from electron diffraction patterns taken from the nanocrystalline regions of the carbon nitride films. *Table 4.2* also shows the theoretical interplanar spacing values for β-C_3N_4.[42] Every observed reflection can be successfully attributed to one expected from theory, even though some reflections predicted by theory are missing, which may be attributed to a degree of preferential orientation.

The existence of impurity phases was ruled out since the crystallography data is inconsistent with other likely crystal phases. *Table 4.3* explores how the experimentally observed diffraction information compares with the diffraction expected from all the other likely phases mentioned in previous work.[42,43] As can be seen, the diamond structure gives an extremely poor fit with the observed data. Also, if the observed material were chaoite, there would be an uncomfortable number of diffraction absences in the experimental data. Lonsdaleite gives poor fit with the observed data, and for graphitic structures, there are also problems for accounting the observed reflections in the 1.2-1.4 Å range. α-C_3N_4 can account for all the observed reflections. However, the differences between observed data and that predicted from theory is greater than for β-C_3N_4, and there would be 11 reflections absent due to orientation rather than 2. This discussion therefore shows that the crystallography of the observed regions is not only consistent with β-C_3N_4 but is also inconsistent with other likely crystal phases. Over the measured sample, the relative amount of crystalline to amorphous material is estimated to be ~20%. Despite this fact, the amorphous regions of the films seem to dominate the structure of the films as well as properties such as the films' mechanical and electrical behaviour, as will be seen later.

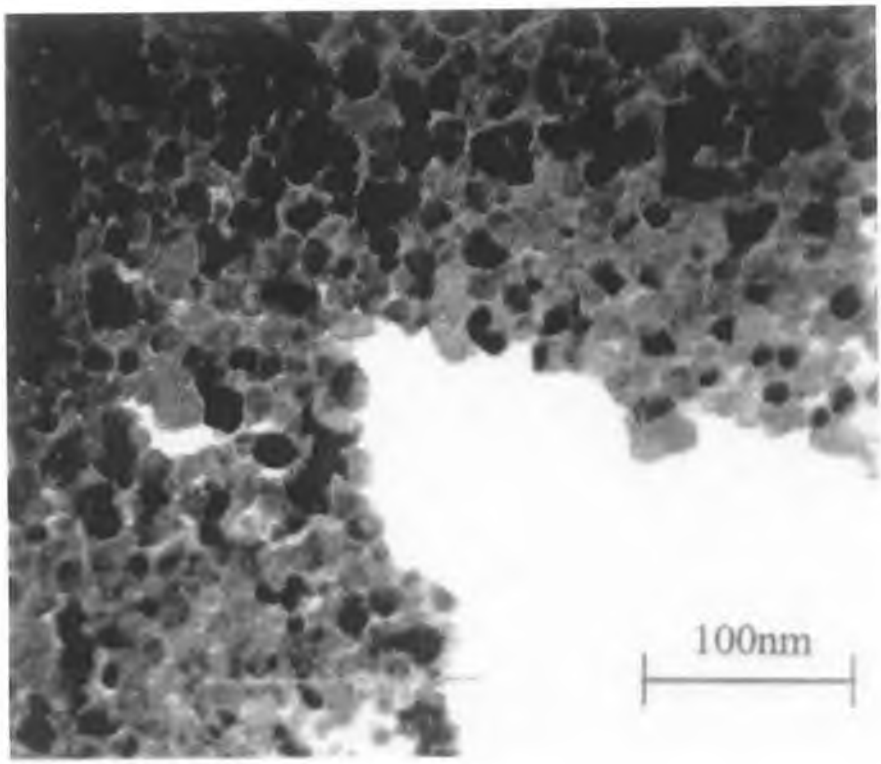

Figure 4.20: Bright Field TEM image of a crystalline region of the film.

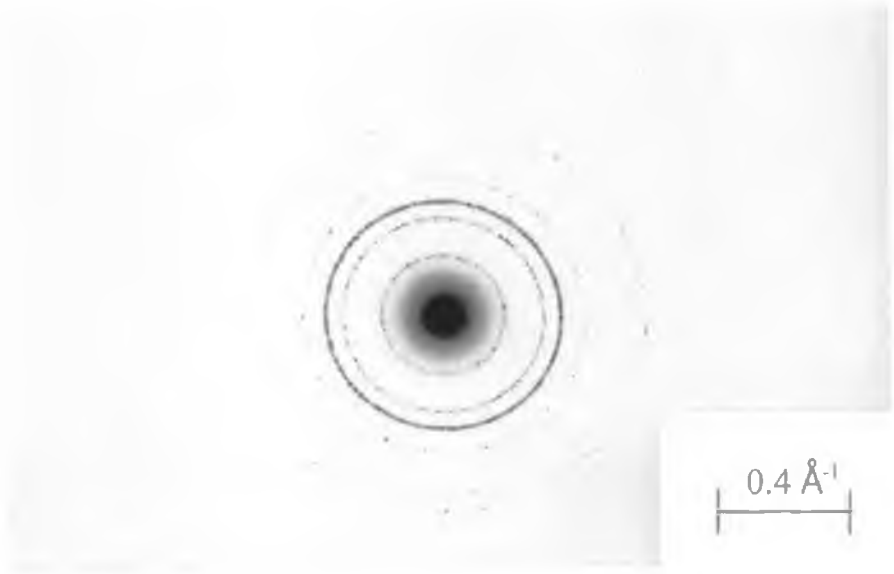

Figure 4.21: Selected area diffraction from a crystalline region.

Observed from TEM Diffraction			Calculated for β-C_3N_4			
d(Å)	Intensity	Ratio d/d_{max}	d(Å)	(hkl)	Intensity	Ratio d/d_{max}
5.2 ± 0.15	*m*	1.0	5.54	100	*m*	1.0
3.1 ± 0.15	*m*	0.60	3.20	110	*m*	0.58
2.6 ± 0.15	*s*	0.50	2.77	200	*s*	0.50
2.2 ± 0.1	*m*	0.42	2.24	101	*s*	0.40
			2.095	210	*m*	0.38
1.8 ± 0.1	*vw*	0.34	1.945	111	*m*	0.35
1.7 ± 0.1	*w*	0.32	1.85	300	*m*	0.33
1.5 ± 0.1	*m*	0.29	1.59	211	*w*	0.29
			1.54	310	*w*	0.28
1.4 ± 0.1	*vw*	0.27	1.48	301	*w*	0.27
1.3 ± 0.05	*w*	0.25	1.35	221	*w*	0.24
1.25 ± 0.05	*vw*	0.24	1.28	320	*w*	0.23
1.21 ± 0.05	*vw*	0.23	1.23	002	*m*	0.22
1.15 ± 0.05	*vw*	0.22	1.13	321	*w*	0.20
1.12 ± 0.05	*w*	0.22	1.125	202	*w*	0.20

Table 4.2: Comparison between the interplanar spacing information obtained experimentally and that obtained by calculation from β-C_3N_4.

Observed d_{hkl}	Diamond		Chaoite		Lonsdaleite		Graphite		Graphite		Graphite		α-C_3N_4 calculated		β-C_3N_4 calculated	
	d	(hkl)	*d*	(hkl)	*d*	(hkl)	*d*	(hkl)	*d*	(hkl)	*d*	(hkl)	*d*	(hkl)	*d*	(hkl)
5.2 ± 0.15													5.66	100	5.54	100
			4.47	110												
			4.26	111												
			4.12													
			3.71	201									3.64	101		
3.1 ± 0.15			3.22	104			3.35	003	3.35	002	3.36	002	3.27	110	3.20	110
			3.03	203												
			2.94	210									2.83	200	2.77	200
2.6 ± 0.15			2.55	301												
			2.46	213									2.43	201		
													2.37	002		
			2.28	205												
2.2 ± 0.1			2.24	220	2.19	100							2.19	102	2.24	101
	2.06	111	2.10	304	2.06	002	2.08	101	2.13	100	2.13	100	2.14	210	2.10	210
			1.98				1.96	012	2.03	101	2.03	101	1.95	211	1.95	111
			1.91	305	1.92	101							1.92	112		
													1.89	300	1.85	300
1.8 ± 0.1									1.80	102	1.80	102	1.75	301		
1.7 ± 0.1							1.68	006	1.68	004	1.68	004				
							1.62	104					1.59	212	1.59	211
													1.57	310		
1.5 ± 0.1			1.50	227	1.50	102	1.46	015	1.54	103	1.55	103	1.52	103	1.54	310
													1.49	311	1.48	301
1.4 ± 0.1			1.37	416									1.35	222	1.35	221
1.3 ± 0.05			1.29	600					1.32	104			1.31	312		
1.25 ± 0.05	1.26	220	1.26	336	1.26	110	1.23	110	1.23	110	1.23	110	1.27	213	1.28	320
													1.25	321	1.23	002
1.21 ± 0.05													1.21	303		
			1.20	516			1.19	107					1.20	411		
1.15 ± 0.05			1.18	427	1.17		1.15	113	1.15	112	1.16	112	1.18	004		
1.12 ± 0.05							1.12	009	1.13	105	1.14	105	1.14	322	1.13	321
									1.12	006	1.12	006			1.12	202
	1.07	311	1.08	339	1.08	112	1.08	018	1.05	201	1.05	201				

Table 4.3: Comparison between the interplanar spacings found experimentally and those expected for other likely crystalline phases.

4.9 Summary and discussion

The information obtained from structural analysis of the films by RBS, XPS, IR and Raman indicates clearly that the nature of the nitrogen incorporation in sputtered carbon nitride films changes with the amount of nitrogen incorporated. The strong IR activity observed in the 1100-1800 cm^{-1} is mainly due to N atoms substituting C atoms in an sp^2 carbon network. The IR and Raman absorption of the CN bond vibration indicates that N atoms substitute for the C atoms in the lattices of amorphous graphite rings and also chemically bond to C forming C≡N bond structures. Hu et al.[44] demonstrated, by using *ab initio* Hartree-Fock (HF) and semi-empirical calculations, that a nitrogen-driven sp^3 to sp^2 transformation occurs in carbon nitride materials when nitrogen concentration is larger than 12 at.%. They showed that above 12 at.% N, there are thermodynamics and kinetic preferences for sp^2 vs. sp^3-bonded clusters, as observed here. There exist a critical nitrogen partial pressure in the sputtering gas at ~25-50 % N_2 in the sputtering gas, corresponding to ~20 at.% N content in the films. Above this point, a structural rearrangement occurs within the film, in which an increasing amount of nitrogen in the films occurs in the form of N-N bonds. It is suggested that this N-N bonding form part of the overall carbon network.

The evolution of the C=N, C≡N and N=N bond intensities in amorphous carbon nitride films deposited by reactive magnetron sputtering process has been described. It has also been shown that between the Raman D and G peaks there is strong evidence for a third peak at 1455 cm^{-1}, designated the 'N' peak, which has been assigned to the N=N stretching vibration. As nitrogen incorporation in the film increases, the N=N bonding intensity increases. It is proposed a graphite-like structure dominated by C=N sp^2 phase, with some proportion of C-C, C=C, C≡N and N=N.

The effect of deposition parameters on the bonding structure within the film was also investigated. It was shown that the increase in substrate bias does not have a significant effect in the nitrogen content but causes a decrease in the C≡N bonding which means a more extended structure with less terminating sites. From the observed decrease of the Raman active regions with increasing deposition temperature, a

reduction of nitrogen content for films deposited at higher deposition temperatures was suggested. In addition, out-diffusion and a corresponding loss of nitrogen have been observed during post-deposition annealing of the investigated carbon nitride films.

The analysis of the XPS spectra reported before was made bearing in mind the IR and Raman spectra obtained previously. An important aspect that should be mentioned here is that XPS is a surface sensitive method whereas IR and Raman give information on the bulk structure. Wixom[45] estimated from a scaling of force constants that the C-N absorption in β-C_3N_4 should be in the range 1212-1265 cm^{-1}. It is clear then that the strong absorption band observed in the IR spectra from 1100 to 1800 cm^{-1}, which is basically a superposition of the analogue D and G Raman active modes due to N replacement of C in the sixfold carbon ring structure, covers the IR active absorption region where the β-C_3N_4 should be identified. From a spectroscopy point of view, the broad band shapes always indicates poorly defined structures. The IR active band indicates a degree of disorder level in the films, which is not characteristic of a diamond phase. The IR data do not reveal the existence of any β-C_3N_4 structure.

Several bonding configurations of nitrogen atoms in the graphite ring structure are possible. N atoms can bond as sp^2 configurations either twofold coordinated in the lattice seen in the pyridine like structure, or as in the threefold-coordinated lattice seen in the pyrrole structure.[46] The most likely candidate is the pyridine structure depicted in *figure 4.22a*, according to the interpretation of the IR, Raman and XPS spectra. The pyridine configuration has two σ bonds, one $p\pi$ bond, and two electrons in a filled valence band. The pyridine ring has C=C and C=N bonds and when it forms part of a structure, in-plane are out-of-plane vibrations causes characteristic bands in the IR and Raman spectra at ~1400-1600 cm^{-1} and 650-850 cm^{-1}, respectively.[16]

From the methods applied, no definite model of the structure of the films could be obtained; such a model has to take into account that the films contain graphitic structures and some proportion of C-N triple bonds and N-N bonds. In order to have an idea of how the different bonds considered can coexist in the same molecular structure, a proposed molecular structure of an amorphous region of the films is shown in *figure 4.22b* and *4.22c*. The actual structure in three dimensions is expected to be much more complicated that this simple picture. This particular molecular structure would have a composition of 66% C and 34% N. The main types of bonding encountered are:

- N bonded to two C, to one sp^3 and one sp^2-C forming one double and one single bond in a hexagonal ring structure. Each nitrogen atom substituting into an sp^2 ring removes one bond between that ring and the local environment, by the formation of lone pair electrons. Rings containing excess nitrogen are likely to be volatile and therefore readily lost from the network, hence sp^2 bonded carbon with greater than two nitrogen atoms per ring are rare.[47]

- N having only one neighbouring C atom, forming triple bonds bonded to aromatic rings, which act as network terminators.

- N sp^2 substitution in sp^2 carbon in aromatic structures, forming N=N. They probably exist as in aromatic azo compounds, linking hexagonal structures.

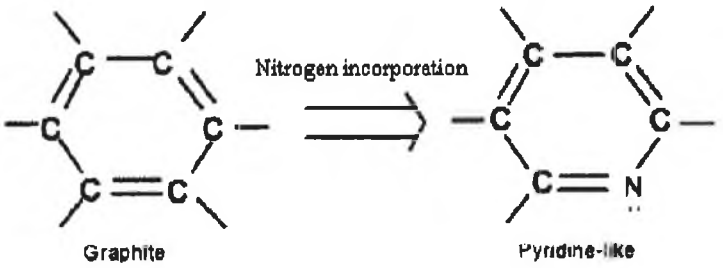

(a)

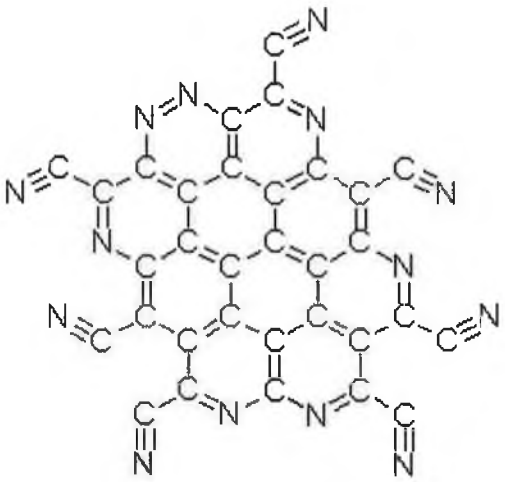

(b) (c)

Figure 4.22: (a): N atom in graphite ring structure (pyridine-like); (b) and (c): N incorporation in graphite-like aromatic carbon clusters. Blue spheres represent nitrogen atoms and grey spheres carbon atoms.

With the techniques considered so far, there is no evidence of N with three singly bonded C neighbours, as required for the β-C_3N_4 phase. However, crystalline regions were observed with TEM in carbon nitride samples grown at 100% Npp. Small crystalline regions could be co-existing with extended amorphous regions. The effect of nitrogen partial pressure and its implications for the formation of β-C_3N_4 are discussed in chapter 6.

References

1. M.Y. Chen, X. Lin, V.P. Dravid, W. Chung, M.S. Wong and W.D. Sproul, Surf. Coat. Technol. 54/55 (1992) 360.
2. N. Nakayama, Y. Tsuchiya, S. Tamada, K. Kosuge, S. Nagata, K. Takahiro and S. Yamaguchi, J. Appl. Phys. 32 (1993) L1465.
3. L.C. Feldman and J.W. Mayer, Fundamentals of surface and thin film analysis, North Holland, NY (1986).
4. W.T. Zheng, H. Sjöström, I. Ivanov, K.Z. Xing, E. Broitman, W.R.Salaneck, J.E. Greene and J.-E. Sundgren, J. Vac. Sci. Technol. A 14 (1996) 2696.
5. H. Sjöström, I Ivanov, M. Johansson, L. Hultman, J. E. Sundgren, S.V. Hainsworth, T. F. Page and L. R. Wallenberg, Thin Solid Films, 246, (1994) 103.
6. L. Maissel, Handbook of thin film technology, McGraw Hill, NY (1970).
7. V.P. Dymont, E.M. Nekrashevich and I.M. Starchenko, Solid State Comms. 111 (1999) 443.
8. Z. J. Zhang, S. Fan and C.M. Lieber, Appl. Phys. Lett. 66 (1996) 2639.
9. N. Mutsukura, K.Akita, Thin Solid Films, 349 (1999) 115.
10. S-C. Seo, D.C. Ingram, H.H. Richardson, J. Vac. Sci. Technol. A 13 (1995) 2856.
11. Y. Kusano, J.E. Evetts, R.E. Somekh and I,M, Hutchings, Thin Solid Films, 332 (1998) 56.
12. J. Wei, P. Hing and Z.Q. Mo, Wear, 225 (1999) 1141.
13. J.H. Kaufman, S. Metin and D.D. Sarpenstein, Phys. Rev. B 39 (1989) 13053.
14. J. Seth, R. Padiyath, S.V. Babu, Diam. Relat. Mater. 3 (1994) 210.
15. F. Weich, J. Widany, Th. Frauenheim, Phys. Rev. Lett. 78 (1997) 3326.
16. N.B. Colthup, L.H. Daly, S.E. Wiberly, Introduction to Infrared and Raman Spectroscopy, 3rd ed., Academic Press, NY (1990).
17. J. Shiao, R.H. Hoffman, Thin Solid Films, 283 (1996) 145.
18. B. C. Holloway, D.K. Shuh, M.A. Kelly, W. Tong, J.A. Carlisle, I. Jimenez, D.G.J. Sutherland, L.J. Terminello, P. Pianett and S. Hagstrom, Thin Solid Films, 290-291 (1996) 94.
19. W.T. Zheng, E. Broitman, N. Hellgren, K.Z. Xing, I. Ivanov, H. Sjostrom, L. Hultman and J.-E. Sundgren, Thin Solid Films, 308-309 (1997) 223.

20. C. Ronning, H. Feldermann, R. Merk, H.Hofsass, P. Reinke and J.-U. Thiele, Phys. Rev. B. 58 (1998) 2207.
21. D. Marton, K.J. Boyd and J.W. Rabalais, International Journal of Modern Physics B 9 (1995) 3527.
22. P. Hammer, N.M. Victoria and F. Alvarez, J. Vac. Sci. Technol. A 16 (1998) 2941.
23. P. Hammer, M.A. Baker, C. Lenardi and W. Gissler, J. Vac. Sci. Technol. A 15 (1997) 107.
24. I. Gouzman, R. Brener, A. Hoffman, Surf. Sci. 331-333 (1995) 283.
25. S. Kobayashi, S. Nozaki, H. Morisaki, S. Fukui and S. Masaki, Thin Solid Films, 281-282 (1996) 289.
26. J. Bulir, M. Jelinek, V. Vorlicek, J. Zemek and V. Perina, Thin Solid Films, 292 (1997) 318.
27. B.C. Holloway, O. Kraft, D.K. Shuh, M.A. Kelly, W.D. Nix, P. Pianetta and S. Hagstrom, Appl. Phys. Lett. 74 (1999) 3290.
28. J.F. Moulder, W.F. Stickle, P.E. Sobolad and K.D. Bomden, Handbook of X-ray photoelectron spectroscopy, Perkin-Elmer Corp. Minnesota (1992).
29. J.Sun, Y. Zhang, X. He, W. Liu, C.S. Lee and S.T. Lee, Materials Letters, 38 (1999) 98.
30. A. Mansour and D. Ugolini, Phys. Rev. B. 47 (1993) 10201.
31. S. Lopez, H.M. Dunlop, M. Benmalek, G. Tourillon, M.-S. Wong and D. Sproul, Surface and interface analysis, 25 (1997) 827.
32. T.R. Lu, C.T. Kuo, J.R. Yang, L.C. Chen, K.H. Chen and T.M. Chen, Surf. Coat. Technol. 115 (1999) 116.
33. Y-S. Jin, T. Shibata, Y. Matsuda and H. Fujiyama, Thin Solid Films 345 (1999) 18.
34. P. Petrov, D. Dimitrov, G. Beshkov, V. Krastev, S. Nemska and Ch. Georgiev, Vacuum 52 (1999) 501.
35. Y. Taki, T. Kitagawa, O. Takai, Thin Solid Films, 304 (1997) 183.
36. J.H. Kim, D.H. Ahn, Y.H. Kim and H.K. Baik, J. Appl. Phys. 82 (1997) 658.
37. C-Y. Hsu, F.C-N. Hong, Diam. Relat. Mater. 8 (1999) 1315.
38. W. Zheng and J.E. Sundgren, Chin. Phys. Lett. 15 (1998) 120.

39. J. Koskinen, J.-P. Hirvonen, J. Levoska and P. Torri, Diam. Relat. Mater. 5 (1996) 669.

40. C. W. Ong, X.-A. Zhao, Y.C. Tsang, C.L. Choy and P.W. Chan, Thin Solid Films, 280 (1996) 1.

41. A.K.M.S. Chowdhury, D.C. Cameron and M.J. Gregg, "Structural characterisation of sputtered deposited CN_x films by transmission electron microscopy", Supplement to Proceedings to the Royal Microscopical Society, 33 (1998).

42. K.M. Yu, L.M. Cohen, E.E. Haller, W.L. Hansen, A.Y. Liu and I.C. Wu, Phys. Rev. B 49 (1994) 5034.

43. J. Szmidt, A. Werbowy, K. Zdunek, A. Sokowaska, J. Konwerska, S. Mitura, Diam. Relat. Mater. 5 (1996) 564.

44. J. Hu, P. Yang, and C. M. Lieber, Phys. Rev. B. 57 (1997) R3185.

45. M.R. Wixom, J. Am. Ceram. Soc. 73 (1990) 1973.

46. Y. Liu, C. Jiaa and H. Do, Surf. Coat. Technol. 115 (1999) 95.

47. A.R. Merchant, D.G. McCulloch, D.R. McKeinze, Y. Yin, L. Hall and E.G. Gernster, J. Appl. Phys. 79 (1996) 6914.

CHAPTER 5

MECHANICAL PROPERTIES OF CARBON NITRIDE

Since nitrogenation induces modifications in the film structure, a change in mechanical and tribological properties is expected. These properties are investigated throughout this chapter. Part I describes the nanoindentation technique, which is now widely used to study the mechanical behaviour of thin films. The instrument employed for nanoindentation studies as well as the analysis method used to obtain hardness and elastic modulus values are described. In the last sections of part I, the friction and stress measurement systems employed are also described. Part II deals with the results and discussion of the mechanical analyses performed on the deposited carbon nitride films. Results from these studies are presented and discussed. The different mechanical properties of the films (hardness, coefficient of friction, stress...) are then related to the bonding structure.

PART I

5.1 MEASUREMENT TECHNIQUES

5.1.1 Nanoindentation testing

In the past years, there has been a considerable interest in characterizing and understanding the properties of coated systems for particular applications. Hardness measurements are particularly critical for thin coatings (≤10 μm). Furthermore, coating properties may vary from point to point across the substrate microstructure. Thus, hardness measurements need to be made at both low-test loads and high spatial resolutions.[1,2] Indentation hardness tests are the most widely used for measuring mechanical properties of thin films. The extension of this technique into the submicrometre regime provides a way to measure mechanical properties of extremely small volumes directly.

Indentation testing becomes nanoindentation when the size of the indenter is too small to be accurately resolved by optical microscopy, which is generally used in microindentation, where single-valued measurements of contact area are made. Nanoindentation normally implies the continuous recording of the distance moved by the indenter (penetration depth) and of the applied load. With this technique, each test gives a complete loading/unloading cycle, rather than just a single reading. Methods have been developed for interpreting the load-displacement data directly to obtain mechanical properties without the need to image indentations to determine their size.

The main advantages of using nanoindentation techniques to characterize the mechanical properties of thin films include:

- test depths can be less than typical coating thickness;
- thin film response can be measured with the coating in-situ on the substrate;
- variable penetration depths can be used to check substrate influence on the measurements;
- usually, the instruments used allow several experiments to be performed (e.g. creep, fatigue, bending etc.).

5.1.2 Nanoindentation data

Hardness (H) is usually defined as $H = L/A$, where L is the applied load, and A is the indent area projected onto the plane of the surface. Since the projected area is not explicitly measured in nanoindentation testing, it does not give values of absolute hardness directly. However, direct information can be obtained on work of indentation (elastic and plastic), elastic recovery and relative hardness as an index of plastic deformation. In order to derive indirect information on the material properties, some assumptions are needed, namely:

- Separation of plastic from elastic effects.
- Correction for geometric imperfection of indenter.
- Relation between hardness and flow properties.

The simplest way to measure deformation is by means of "slow-loading" tests, where the indentation depth is plotted as a function of slowly varying load. *Figure 5.1* shows a typical depth-load cycle of a material that deforms both elastically and plastically. A fresh location on the specimen is selected, and contact is made at a load of a few μN or less. Then, the load is raised at the required rate until the desired maximum is reached, and is then decreased, at the same rate. The "unloading curve" is not vertical since the specimen shows partial elastic recovery as the indenter is forced back, which allows to obtain information on the moduli of interest.

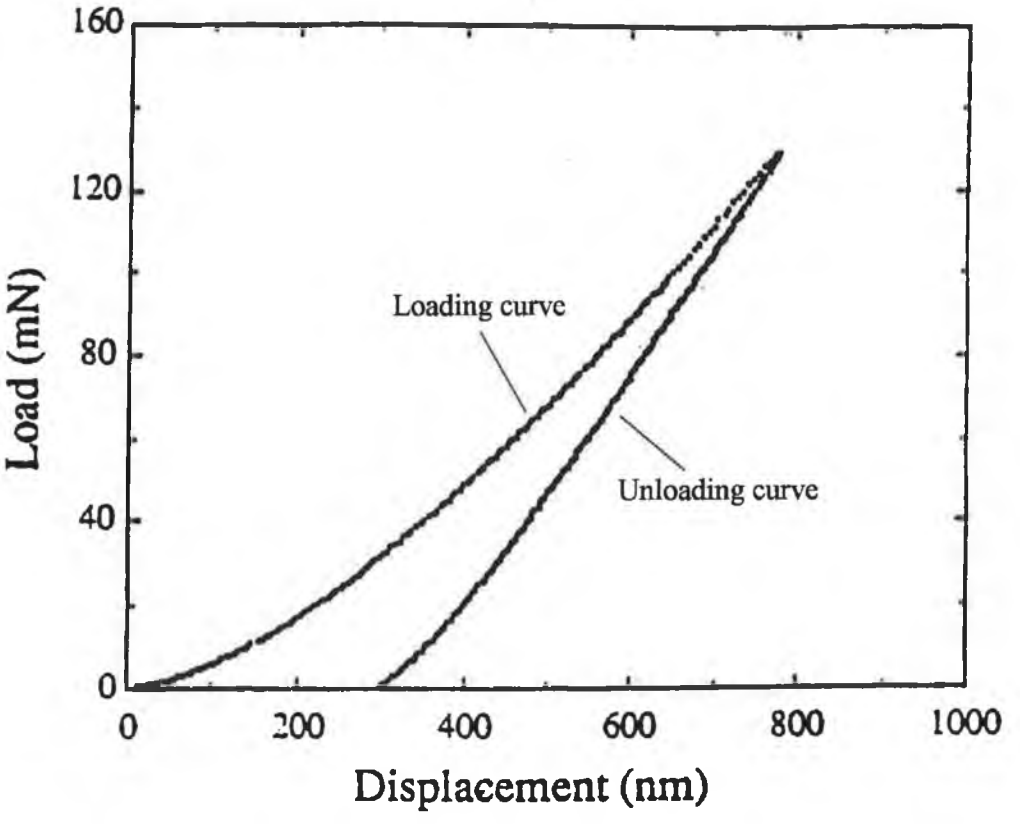

Figure 5.1: Typical load-displacement curve for a material deforming both elastically and plastically.

5.1.2.1 Oliver and Pharr method

A method for determining the elastic and plastic contributions to the displacement to obtain the hardness, as well as for relating the elastic displacement to Young's modulus of the sample, is required. Two well-known methods have been developed for this purpose: the Doerner and Nix method[3] and the Oliver and Pharr method,[4,5] which is an improved version of the former and is described in this section. Oliver and Pharr have provided a model based on analytical solutions for several indenter geometries. It also accounts for curvature in the unloading data and provides a physically justifiable procedure for determining the depth that should be used in conjunction with the indenter shape to establish the contact area at peak load. *Figure 5.2* is a schematic illustration of what occurs when a force is applied to an indenter in contact with a surface. In general

terms we can say that an impression is produce which consists of permanent (plastic) deformation and temporary (elastic) deformation and the surface outside the area of contact deflects elastically. Elastic deformation is recovered, as the indenter is withdrawn.

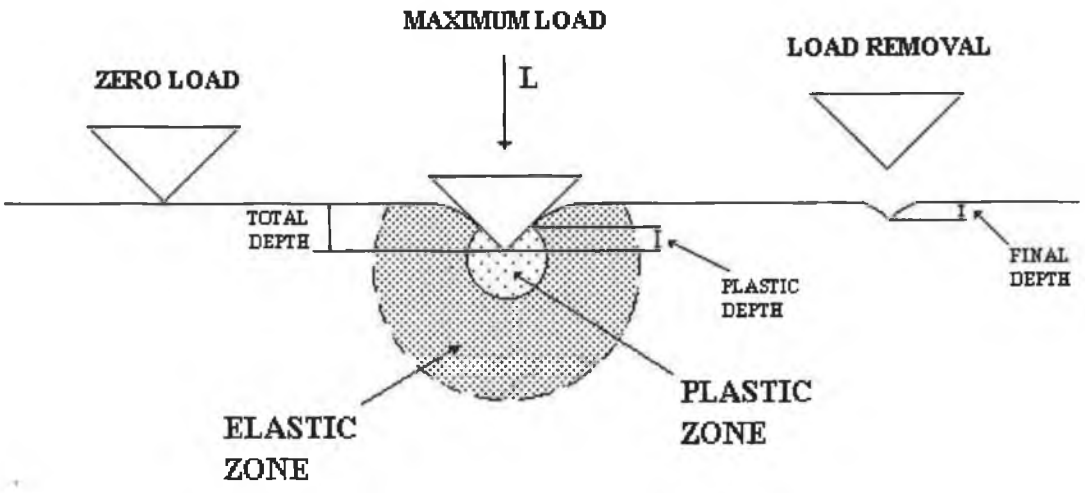

Figure 5.2: Schematic representation of the indenting process illustrating the decreasing indentation depth upon unload.

A schematic representation of this process is given in *figure 5.3a*, where the contact depth (h_c), which is an essential parameter in the Oliver and Pharr method, is depicted. As seen in *figure 5.3b*, the contact depth h_c is the distance along the indenter vertical axis, which is in contact with the specimen surface when the maximum load is applied.

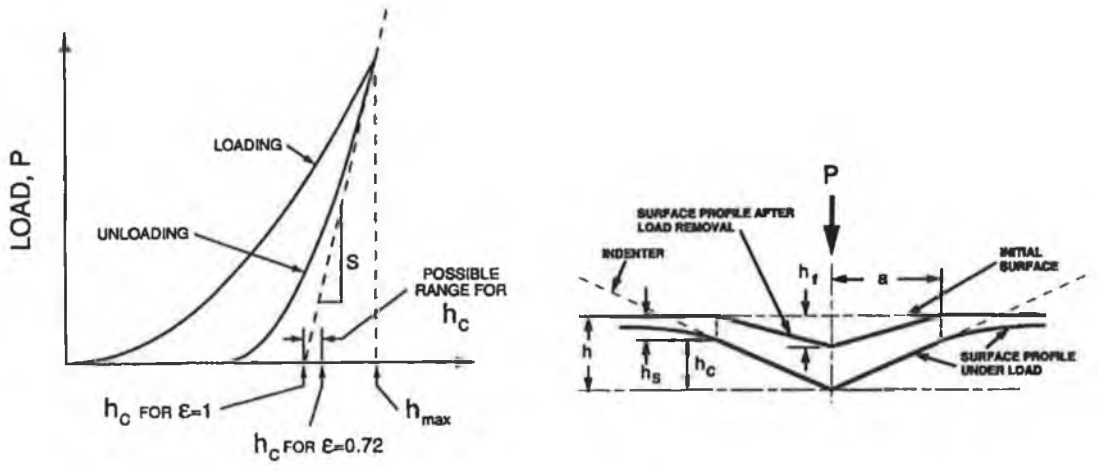

(a) (b)

Figure 5.3: (a) Schematic representation of the load versus indenter displacement, showing a graphical interpretation of the contact depth h_c. (b) Section through an indentation showing the parameters used in the analysis.

The load-displacement data shown in *figure 5.3* can be analyzed according to the "canonical indentation relation":[6]

$$S = \frac{\partial P}{\partial h} = \frac{2}{\sqrt{\pi}} Er\sqrt{A} \qquad (1)$$

where S is defined as the contact stiffness measured from the upper portion of the unloading data, P is load, h is displacement, Er is the elastic modulus and A is the projected area of the elastic contact. By measuring S and assuming all deformation on unloading is elastic, Er can be derived if the contact area is previously determined. The effects of non-rigid indenters on the load-displacement curve can be accounted for by defining a reduced modulus Er as:[7]

$$\frac{1}{Er} = \frac{(1-\nu_i^2)}{Ei} + \frac{(1-\nu_m^2)}{Em} \qquad (2)$$

where Ei and νi are the Young's modulus and Poisson's ratio for the indenter and Em and νm are the same parameters for the sample.

Elastic contact mechanics predicts, for a variety of tip shapes, a power law force-displacement curve on unloading:[8]

$$P = \alpha(h - h_f)^m \qquad (3)$$

where P is the indenter load, and α and m are constants that depend on the indenter shape. The stiffness S is calculated by fitting a power law to the unloading data and using the tangent at maximum load. To determine the contact depth from the experimental data of *figure 5.3*, it is noted that $h_c = h_{max} - h_s$, where h_s is the displacement of the surface at the contact perimeter. Since h_{max} can be determined experimentally, the key of the analysis is to determine h_s. Sneddon's expression for a conical indenter outside the area of contact gives:[6]

$$h_s = \frac{(\pi - 2)}{\pi}(h - h_f) \qquad (4)$$

and Sneddon's force-displacement relationship for the conical indenter yields

$$(h - h_f) = 2\frac{P}{S} \qquad (5)$$

where S is the stiffness. Combining equations (4) and (5) and since the contact area of interest is that at peak load, results the following expression:

$$h_s = \varepsilon \frac{P_{max}}{S} \qquad (6)$$

where $\varepsilon = \frac{2}{\pi}(\pi - 2) = 0.72$ for a conical indenter.

For a variety of tip shapes, analytical models[6] give different ε values. For a paraboloid of revolution ε=0.75 and for a flat punch ε=1. Doerner and Nix method[3] is based on the flat punch approximation, where the contact depth (h_c) is given by the intercept of the tangent at h_{max} to the unloading curve with the displacement axis. In *figure 5.3*, the range of values for h_c considered are indicated, depending on the value of ε (the indenter considered).

Now, the area of contact can be determined by the geometry of the indenter and the depth of contact, h_c; the model assumes that the indenter geometry can be described by an area function F(h) which relates the cross-sectional area of the indenter to the distance from its tip, h; its functional form can be established experimentally prior to analysis; then, the projected contact area at peak load can be calculated from the relation $A = F(h_c)$. Now, the elastic modulus can be determined from equations (1) and (2) and the hardness can be calculated from its definition as the mean pressure the material will support under load: $H = \frac{P_{max}}{A}$.

5.1.2.2 Substrate effects

Since indentation experiments are performed with the coating in-situ on the substrate, the substrate effect is a very important factor to bear in mind when doing measurements. A value of plastic depth (h_p)/film thickness (t_f) ratio has to be chosen in order to avoid the substrate affecting hardness and elastic modulus measurements; this is illustrated in *figure 5.4*. The suitable h_p/t_f ratio depends strongly on properties of film, surface and interface. There are some empirical rules that give ratios of 1/10, 1/3 and 1/4, depending on the difference between film and substrate, which are not always precise. Surface conditions like contamination, roughness, etc. also affect the results, therefore, to measure the mechanical properties of thin films, indentations must be large enough to avoid surface effects, yet small enough to avoid the influence of the substrate.

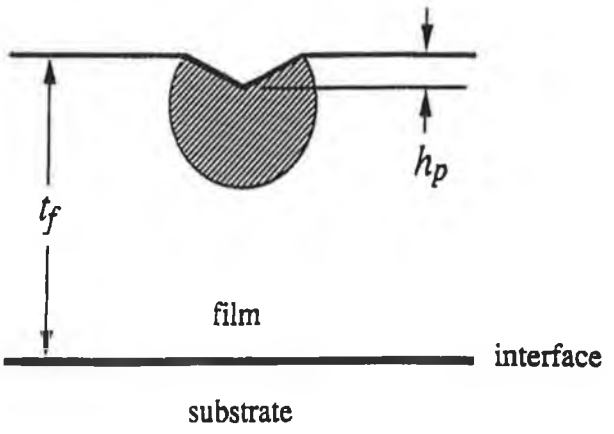

Figure 5.4: Substrate effects.

5.1.2.3 Nanoindentation conclusions

- Hardness values of thin films are quite difficult to determine since it is an ambiguous parameter for characterizing the deformation responses of materials showing mixed elastic and plastic behaviour.

- The nanoindentation technique is capable of producing more information than hardness values alone since the load-displacement curve can be considered as a "fingerprint" of the coated system which enables its characterization by determining the elastic modulus, work of indentation, elastic recovery, etc.

- Different analysis methods and experimental errors make it difficult to compare results from different groups due to:
  -Inelastic displacements during unloading due to thermal drift and plastic deformation.
  -Appropriate calibration of the tip shape and machine compliance.
  -Consistency of testing procedures.

- Nanoindentation is the only possibility for direct measurement of particular small volumes and is an excellent method for comparative purposes.

5.1.3 Nanoindentation instrument

The first commercial instruments for nanoindentation experiments appeared in the mid 1980's when the development of "depth-sensing" instruments with depth and load resolutions better than 10 nm and 1 mN respectively was possible and when analysis methods for interpreting load-displacement data directly to obtain mechanical properties were developed. The NanoTest 500 instrument (Micromaterials Limited, Wrexham, UK) is the instrument used in this project to study the mechanical properties of carbon nitride films. The instrument measures the movement of a stylus in contact with a surface. For hardness measurements, a programmed load is applied and the stylus is impressed into the surface. *Figure 5.5* shows an schematic of the instrument. A coil is mounted at the top of a pendulum with the diamond indenter attached to it. When a coil current is present, the coil is attracted towards a permanent magnet, which produces the movement of the diamond used as the indenter, towards the specimen. The diamond displacement is measured by means of a parallel plate capacitor, one plate being attached to the diamond holder. With this arrangement, when the diamond moves, the capacitance changes and this is measured by a capacitance bridge unit. The limit stop defines the maximum outward movement of the diamond as well as the orientation operation of the pendulum when a load is applied. The balance weights are used to adjust the equilibrium position of the pendulum with no current through the coil. Specimens are simply loaded into the NanoTest, mounted on a stub by means of a rapid setting adhesive. The depth resolution is better than 0.1 nm and the force resolution better than 100 nN.

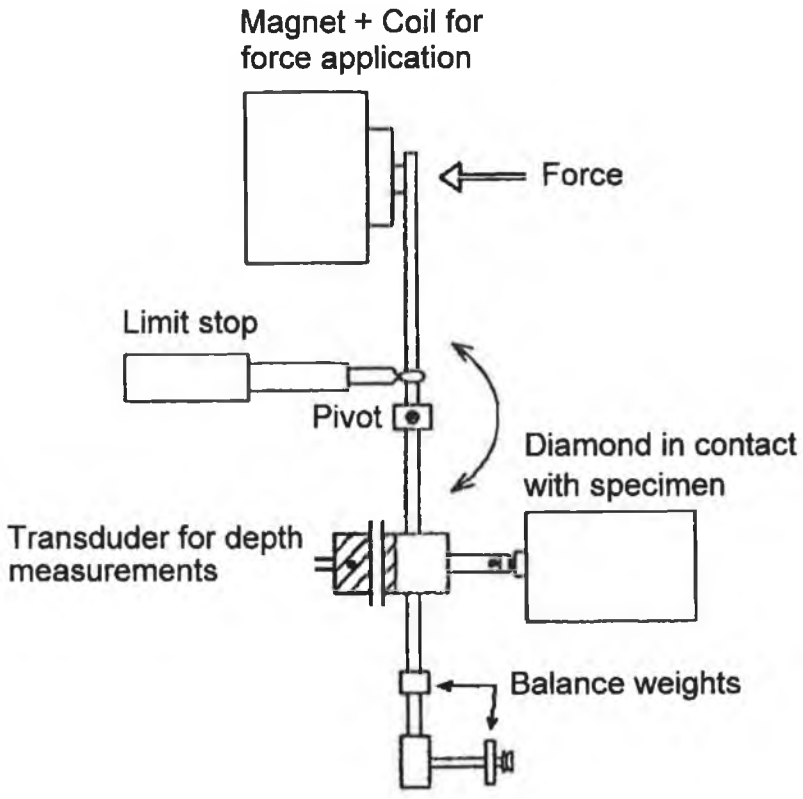

Figure 5.5: Nanotest concept.

5.1.3.1 Principle of operation

Since the operating environment is of crucial importance when doing nanohardness measurements, the system is mounted in a controlled environment enclosure. On commencement of testing, the specimen is very slowly brought into contact with the stylus. The load applied to the stylus at this stage is extremely small, and the stylus is essentially just "touching" the surface. For indentation measurements, the depth of penetration is then measured as a load ramp is applied. The data is then transferred to the system computer, decoded and automatically analyzed by a comprehensive software package. Typically, a test is performed a predetermined number of times when a large number of measurements may be necessary to produce reliable statistical information. Prior to each test, the specimen is moved to a new location. In a typical test, the computer

will record the load, depth, transverse displacement and time. Depth and load calibrations are performed when required. A fused quartz sample is normally employed to check the level of accuracy of the instrument.

5.1.3.2 Hardness and elastic modulus measurements

Hardness is defined as the average pressure under the indenter, calculated as the applied force divided by the projected area of contact between the indenter and the specimen. Indentation measurements of hardness require the application of a sufficiently high load to induce plastic deformation. Hardness values are calculated from the expression $H = P_m / kh_c^2$, where P_m is the applied force for maximum penetration and the denominator is the projected area of indentation for a particular diamond geometry. In a Berkovitch geometry, which is the trihedral diamond geometry employed, as in a conical geometry, the cross-sectional area varies as the square of the depth of contact.[5] It also has the same area to depth ratio as the Vickers diamond. The theoretical projected indentation area as a function of the plastic indentation depth is given by the expression $A = 24.5 \times h_c^2$ for ideal indenter geometry[9,10] where h_c is the contact depth.

However, the diamond tip is not perfect, hence, for true hardness measurements, the tip area must be measured as a function of depth, which requires electron microscopy techniques which were not available. The alternative approach taken was to produce a hardness vs. depth curve for a known homogeneous material of constant hardness (such as fused quartz) and assume that any curvature is due to diamond geometry effects.[5] A diamond area function was then derived from this curvature. In some cases, material from indented films can adhere to the diamond tip, changing the diamond geometry; frequent indentation of a known reference surface, under standard conditions, was performed, with the diamond being cleaned after any departure from normal behaviour. After some experiments, the area function for the diamond used was taken as:

$$A = k1 \times h_c^2 + k2 \times h_c \qquad (7)$$

where k1=19.99732 and k2=28848.75x10^{-9}; for practical materials, the total depth measured during loading is the sum of the plastic and elastic displacement. The elastic contribution must be subtracted from the data to obtain hardness and the contact depth (h_c) was calculated as previously discussed applying the Oliver and Pharr method.

By the same method, the reduced modulus is calculated by fitting a power law relation to the unloading curve and using the tangent at maximum load to calculate the stiffness as described previously. The elastic or Young's modulus can then be calculated from equations (1) and (2), if the Poisson's ratio of the material being analyzed is known, where the elastic modulus for the diamond indenter is 1000 GPa and Poisson's ratio is 0.25. Variations of film's Poisson's ratio (ν_m) does not have a major effect in elastic modulus calculation. If we take ν_i = 0.25, a reduced modulus of 100 GPa is equal to an elastic modulus of 103 GPa, so that the reduced modulus values can be approximately taken as good approximations of the actual elastic modulus values.

5.1.3.3 Elastic/plastic work measurements

The plastic work (W_P) is retained by the specimen after completion of an indentation and is determined by measuring the area under the load vs. depth hysteresis curve. The elastic work (W_E) performed during indentation is subsequently released as the indenter is withdrawn from the specimen; for an ideal plastic material, the elastic work is zero. W_E is calculated from the area shown in *figure 5.6* where the relationship between W_E and W_P is shown.

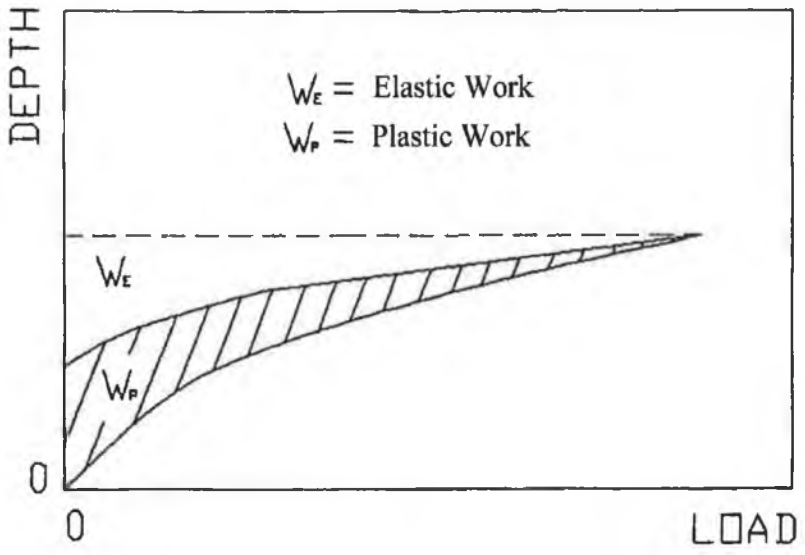

Figure 5.6: Work performed during indentation.

5.1.4 Friction Measurement System

The instrument used was an Implant Sciences Corporation ISC-200PC Tribometer, which basically is a pin-on-disk system consisting of a tribometer and a computer for data acquisition. *Figure 5.7* shows a schematic of the apparatus. A test disk (sample to be measured) is mounted in a cup that comes in contact with a pin attached to a precision balance lever arm, which is used to apply vertical loads to the pin and to read the friction force on the pin. A load of 50 gm is applied on the pin that revolves about the test disk center against a stationary disk. In any case, the wear track produced on the disk is a circle, involving multiple passes on the same track. A load cell on the top platform measures the reaction friction force when hooked to the lever arm. The analogue friction output is transmitted to the computer and a friction coefficient is displayed on the screen. Friction was measured in normal (uncontrolled) atmosphere with a tungsten carbide ball as the rubbing surface (pin) on a carbon nitride film deposited on a silicon substrate (disk).

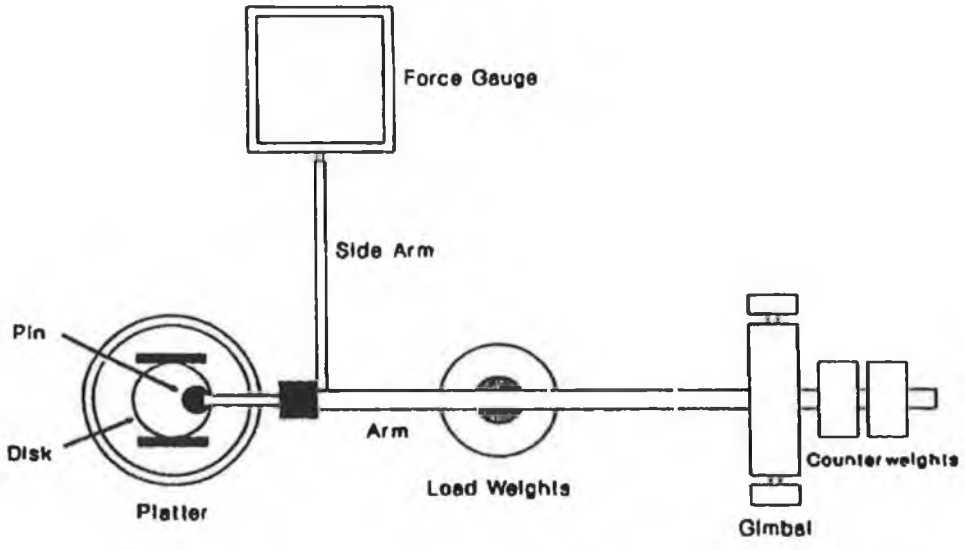

Figure 5.7: Schematic of the ISC-200 Tribometer pin-on-disk tester.

The tester consists of the following parts:

1. Motor drive: A variable speed motor, capable of maintaining constant speed (± 1% of rated full load motor speed) under load. The motor is mounted in such manner that its vibration does not affect the test. Rotating speeds are typically in the range of 0.3 to 3 rad/s (60 to 600 rev/min).
2. Revolution counter: The machine is equipped with a revolution counter that records the number of disk revolutions, and shuts off after a pre-selected number of revolutions.
3. Pin specimen holder and lever arm: The system has a stationary specimen holder that is attached to a lever arm consisting of a pivot. Adding weights, as option of loading, produces a test force proportional to the mass of weights applied. Ideally, the pivot of the arm should be located in the plane of the wearing contact to avoid extraneous loading forces due to the sliding friction. The pin holder and the arm are of substantial construction to reduce vibrational motion during the test.
4. Wear measurement system and data acquisition: The instrument has a sensitivity of higher than 2.0 μm. The analogue output data are transferred to a computer for analysis. Thus, the frictional coefficient is directly displayed on the screen.

5.1.5 Stress measurements

Intrinsic film stress was determined by the bending beam method where the curvature of the film-substrate combination was measured using the Tencor surface profilometer described in chapter 4. When a thin film is deposited on a substrate, it will be bent depending on the type of stress. Tensile stress will produce a concave coated surface. Similarly, compressive stress will result in a convex coated surface. The bent geometry of a film deposited on a substrate can be observed as shown in *figure 5.8*:

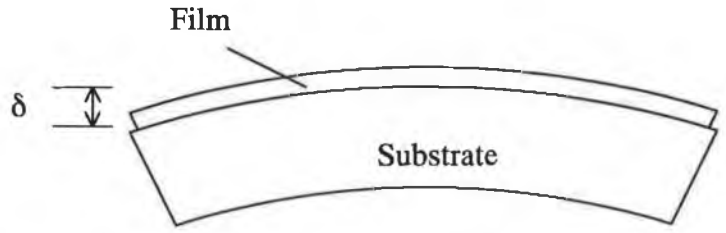

Figure 5.8: Intrinsic stress of a carbon nitride thin film.

The film stress is calculated by:[11]

$$\sigma = \frac{4E_s d_s^2 \delta}{3(1-\nu_s) l^2 d_f}$$

where,

E_s = Elastic modulus of the silicon substrate (1.6×10^{11} Pa)

d_s = Substrate thickness = $508 \pm 20 \times 10^{-6}$ m

ν_s = Poisson's ratio of silicon substrate (0.33)

l = Substrate length

d_f = Film thickness

δ = Maximum deflection

The curvatures of the bent films were measured by the surface profilometer. The film surface is scanned by the mechanical profilometer and the control unit receives the scanned signal and generates the surface profile as output. The instrument resolution is 0.02 μm and as all the measured deflections were at least 1 μm, the data seems to be sufficiently accurate. All scans are carried out from the printed profiles.

PART II

5.2 RESULTS

5.2.1 Nanoindentation measurements of carbon nitride films

Two series of carbon nitride thin films grown at different substrate bias voltage and nitrogen partial pressures were investigated with the nanoindentation technique previously described. Prior to nanoindentation measurements, the thickness of the films was measured using a Tencor surface profilometer. The thickness of the investigated films varied between 1 and 1.4 μm. The samples were firmly glued to an aluminium stub holder and then allowed to thermally equilibrate within the nanotester cabinet for 5 hours in order to minimize thermal drift. The machine had been previously calibrated using the Oliver and Pharr method for indentations in fused quartz. The data from the load coil and capacitor were processed using the provided software which converts the load and displacement in volts to load in mN and displacement in nm and corrects for load frame stiffness, thermal drift, spring constants, etc.

A typical indentation cycle was: (i) approach of the specimen to the indenter; (ii) load at a set rate to a set indentation depth limit; (iii) hold the maximum load constant for 10 seconds to eliminate time-dependent effects; (iv) unload at the same rate. The data was then plotted to produce the "load-displacement fingerprints" of the carbon nitride films being analyzed.

For consistency sake, a maximum (on-load) indentation depth of 100nm was chosen for all the measurements, giving a depth/thickness ratio of less than 1/10, which is considered small enough to preclude substrate influences on measurements.[12] The initial load chosen was 0.05 mN, and the loading rate 0.11 mN/sec. For each sample, at least four experiments were performed; each experiment consisted of 15 or more scans

(indentations), with 10 μm of separation between successive indentations. After recording the load versus depth curves, the suspicious curves were discarded. The data was then analyzed with the Oliver and Pharr method, and the values for hardness, reduced modulus, plastic work and elastic work were averaged for each sample.

5.2.1.1 Nanoindentation results

The first experiments were carried out on 3 carbon nitride films grown using a conventional planar reactive magnetron sputtering process,[13] grown at different nitrogen partial pressure (Npp), a total pressure of $5x10^{-3}$ mbar, 2 A magnetron current and a floating substrate bias (~17V). The results obtained (hardness (H), reduced modulus (Er), plastic work (Wp) and elastic work (We)), along with the nitrogen content in the films (as measured by RBS), are given in *table 5.1*.

SAMPLE	N at. %	Npp (%)	H (GPa)	Er (GPa)	Wp (pJ)	We (pJ)
H0	1.5	0	11	135	34	65
H1	11.2	25	8.6	115	37	53
H3	13.2	75	8.4	100	27	55

Table 5.1: Nanoindentation results for carbon nitride films deposited with a conventional magnetron sputtering system.

The second series of samples investigated was the series PCNX, which are carbon nitride films grown using the Penning magnetron source, varying the substrate bias (Vs). The rest of deposition parameters were: 100% nitrogen partial pressure, a total pressure of $1.5x10^{-4}$ mbar and 3 A magnetron current. Results for these samples are shown in *table 5.2*.

SAMPLE	Vb(V)	HARDNESS(GPa)	Er (GPa)	Wp(pJ)	We(pJ)	at%N
PCN2	0	7	102	32	51	26
PCN7	-25	8.6	110	29	54	36
PCN3	-50	9	114	38	57	39
PCN8	-75	8	105	33	53	37

Table 5.2: Nanoindentation results for carbon nitride films deposited with the Penning magnetron source at different substrate bias (0, -25, -50, and –75 V).

The last series of samples investigated was the PCN1X series. These carbon nitride films were grown with the Penning magnetron source, at different nitrogen partial pressures (N_2 %), at a total pressure of $1x10^{-3}$ mbar, 3 A magnetron current and -50 V substrate bias. The results obtained for this series are given in *table 5.3*.

SAMPLE	N_2(%)	HARDNESS(GPa)	Er (GPa)	Wp(pJ)	We(pJ)	at%N
PCN18	0	11.4	153	34	66	0
PCN25	15	10.4	132	34	66	23.8
PCN17	25	9	107	29	60	32.3
PCN16	50	8.6	93	27	57	36.3
PCN15	75	8.2	86	24	55	33.1
PCN19	100	7.2	82	25	45	32.5

Table 5.3: Nanoindentation results for carbon nitride films deposited at different nitrogen partial pressures (0, 15, 25, 50, 75 and 100% Npp).

Other typical indentation parameters are given in *table 5.4*, namely, maximum load (Pm), maximum depth (h_{max}) and contact depth (h_c); the contact depth (h_c) and the maximum load (Pmax) are the parameters used to calculate the hardness values from the formula $H = P_{max} / (k_1 \times h_c^2 + k_2 \times h_c)$, as discussed earlier.

SAMPLE	P_{max} (mN)	h_{max}(nm)	h_c(nm)
PCN18	3	84-87	62-64
PCN25	2.6-2.8	89-90	62-64
PCN17	2.2-2.3	90-91	61-63
PCN16	2.1-2.2	91-92	62-63
PCN15	2-2.1	90-93	61-63
PCN19	2	92-94	67-68

Table 5.4: Maximum load (P_{max}), maximum indentation depth (h_{max}) and contact depth (h_c) of nanoindentation experiments on carbon nitride films.

Figure 5.9a is a load-depth hysteresis curve for PCN18 sample where the previous parameters are indicated. *Figure 5.9b* is the corresponding curve for PCN15; it can be seen the higher maximum load, for similar penetration depths, for the harder film (PCN18).

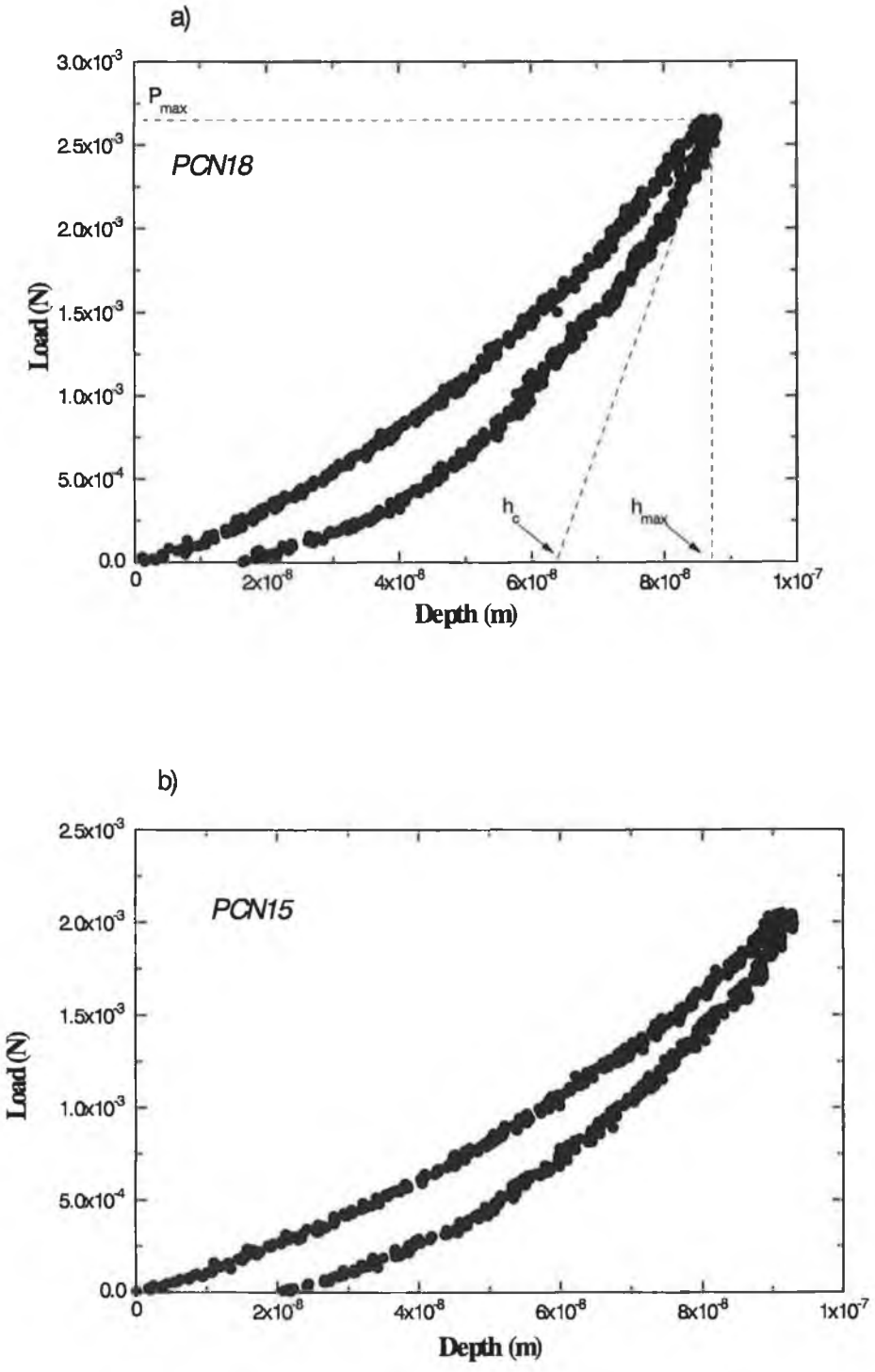

Figure 5.9: Load vs. Depth curve for PCN18 (a) and PCN15 (b).

Figure 5.10 compares the load-depth curves for silicon (100), which was used as the substrate material, and for the silicon substrate coated with a carbon nitride film (PCN16); both were tested to a maximum load of 5 mN.

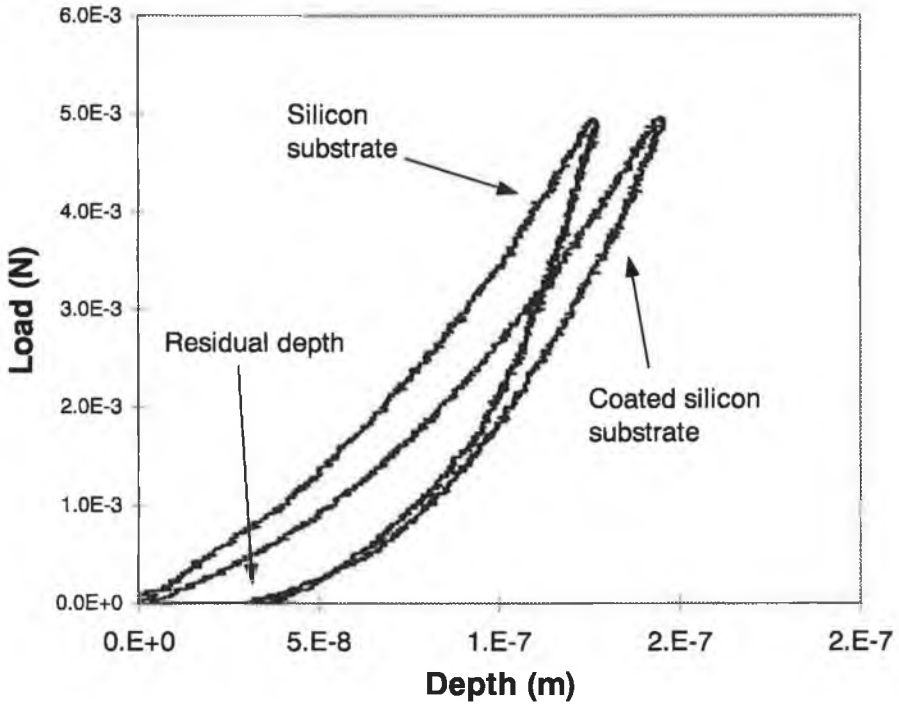

Figure 5.10: Load-Depth curves for silicon (100) substrate alone and silicon substrate coated with a 1.1μm carbon nitride film (PCN16).

It can be seen that the maximum indentation depth is higher for the coated silicon, which indicates that the carbon nitride film is softer than the silicon substrate. The lower slope on unloading indicates lower stiffness or elastic modulus for the coated silicon. The plastic work (Wp) is also reduced (note the smaller area inside the curve) for the coated silicon, as well as the residual depth. This means that a larger proportion of the deformation is elastic for the coated silicon; this can be measured by the percentage elastic recovery factor (%R), which reflects the difference between fully plastic (0%) and fully elastic (100%) behaviour and is calculated using the formula:

$$\%R = \left[\left(h_{\max} - h_{res}\right)/h_{\max}\right] \times 100 \qquad (8)$$

All calculated values are given in *table 5.5*. Normally, the higher the indenter penetration depth for the same maximum load (h_{max}) the lower the hardness. Also from equation (8) the lower the residual depth, the higher the elastically recovery (%R).

Material	H (GPa)	Er (GPa)	Wp(pJ)	We(pJ)	h_{max}(nm)	h_{res}(nm)	%R
Silicon	10.5	155	12	14	125	39	68.8
CNx	9.7	110	8	18	142	30	78.8

Table 5.5: Nanoindentation values of the silicon substrate and a carbon nitride film deposited at 50% Npp (PCN16).

The hardness for PCN16 is now 9.7 GPa as opposed to a value of 8.6 GPa given in *table 5.3*. This is due to the higher penetration depth, of about 142nm, used this time, which is about 13% of the film thickness (1.1μm). This is probably causing substrate influences in the hardness and modulus measurements.

The dependence of hardness on nitrogen partial pressure and nitrogen content is better seen in *figures 5.11* and *5.12* respectively. In *figure 5.13* all the series investigated are shown, including the films that were grown with conventional magnetron sputtering. There is a considerable amount of scatter in the data. For both types of films, there is an initial decrease in hardness as nitrogen is increased, but above a certain amount, the hardness increases again but still remains lower than the original value. It is clear that nitrogen content alone cannot predict hardness. It should be noted that the target power and pressure are not constant for all the films on this graph. These parameters on their own, however, did not have major effects in the hardness values.

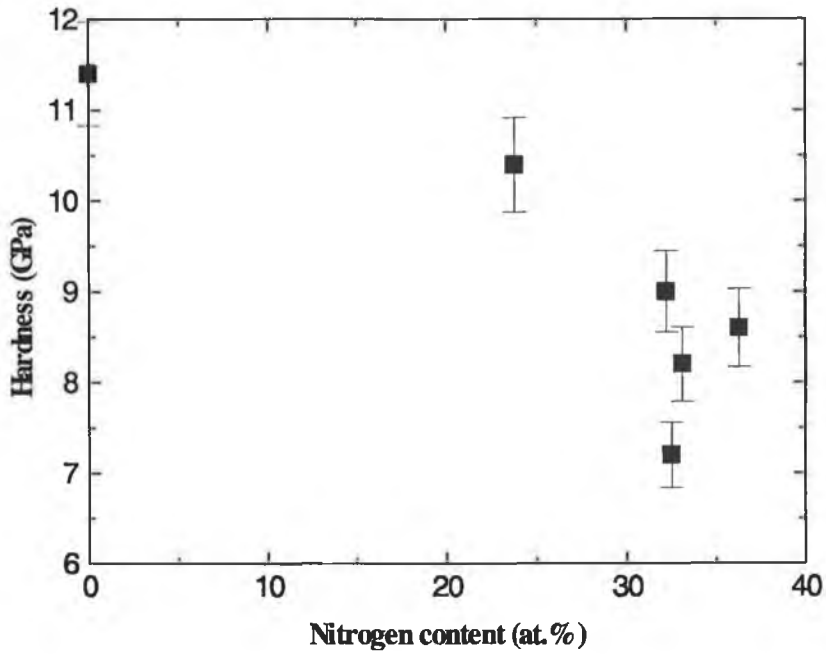

Figure 5.11: Hardness versus nitrogen content.

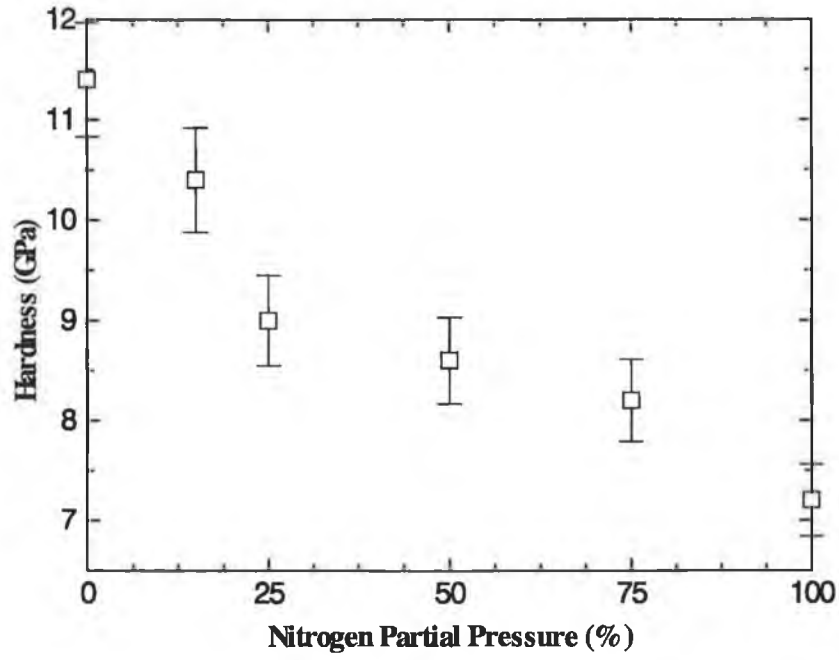

Figure 5.12: Hardness versus N_2 partial pressure.

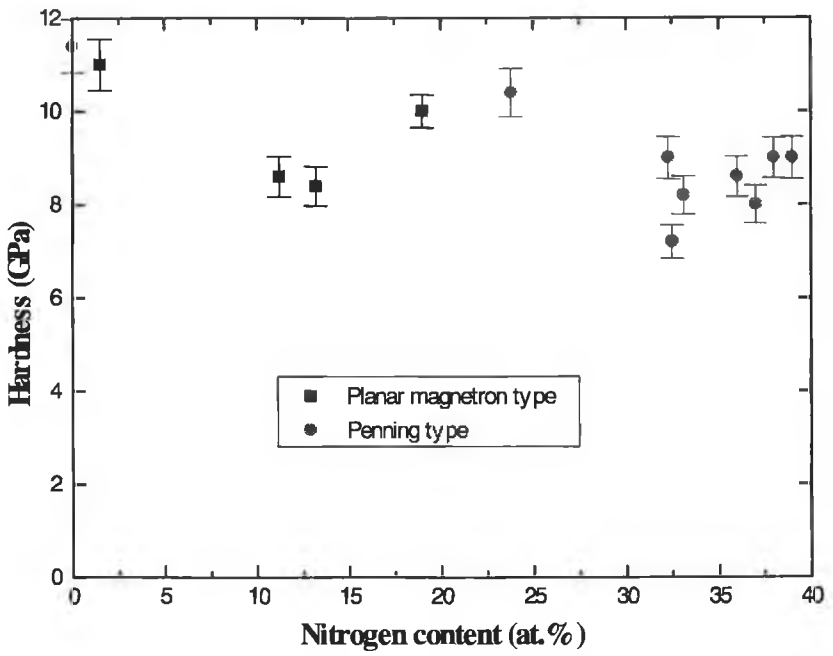

Figure 5.13: Hardness versus nitrogen content for films grown using Penning and planar magnetron sputtering configurations.

5.2.1.2 Relation between structure and film properties

Hardness for the PCNX series was plotted against the IR absorption coefficient corresponding to the carbon-nitrogen triple and double bond peaks; the plots are shown in *figures 5.14* and *5.15* respectively. Hardness values correlate reasonably well with the C≡N bond concentration. This C≡N phase, which is an impurity phase in the chemical structure of carbon nitride, called cyanogen, disrupts the structure of the film, which becomes weaker. The only documented amorphous solid compound of carbon and nitrogen is "paracyanogen",[14] which is an amorphous CN_x polymer consisting of -C=N-C= sixfold rings with carbon in the sp^2 hybridization. If the carbon-nitrogen single bond that links the adjacent rings breaks, due to the presence of sufficient energetic atoms, cyanogen is formed as -C=N-C≡N, and the chain of rings is stopped, resulting in a weakened and softer structure. Wei et al.[15] found a decrease in hardness due to excess of

C≡N bonding, which also decreased the wear resistance resulting in a reduction of film fracture toughness.

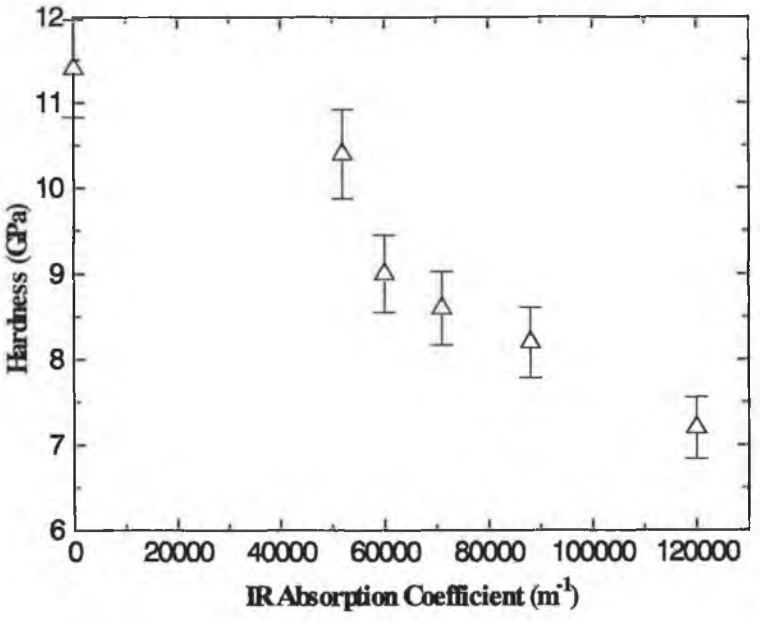

Figure 5.14: Hardness versus C≡N bond concentration.

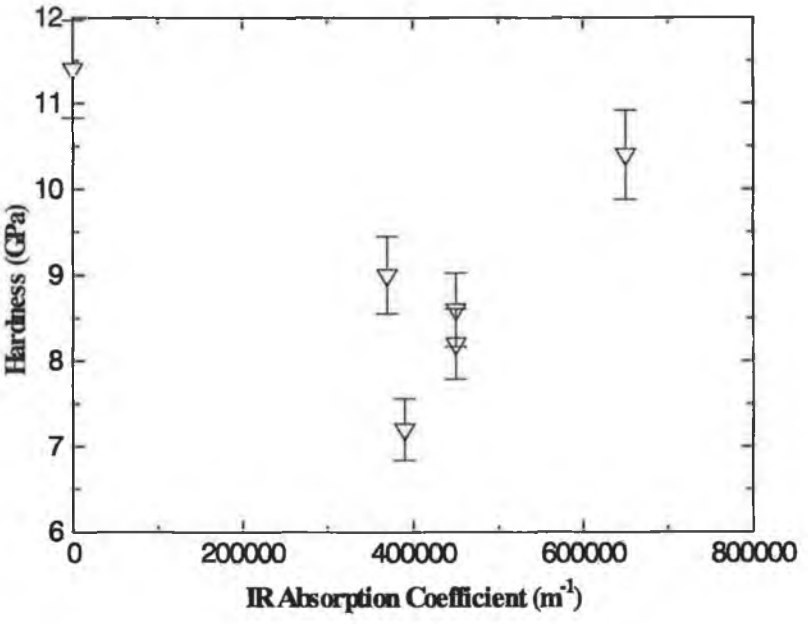

Figure 5.15: Hardness versus C=N bond concentration.

The presence of nitrogen in the carbon network causes the sp^2 bonds (C=C and C=N) to be favored.[16] *Figure 5.15* does not indicate a drop of hardness with C=N bond concentration, due to the fact that the C≡N bond controls the hardness, i.e. the C≡N bond appears to be significantly weaker than the others. Finally, *figure 5.16* shows a plot of hardness against refractive index as measured by ellipsometry where an increase in hardness with refractive index can be observed. A decrease in refractive index can be related to an increase of the void fraction of a-CN_x films.[17] This is caused by N atoms forming C≡N bonds, which induces loss of conectiveness in the amorphous network and hence lower hardness.

Sometimes, a decrease in hardness with nitrogen incorporation has been found in literature.[18] This is usually explained by a broken symmetry in sp^2 carbon domains caused by the formation of C=N with increasing nitrogen content, where no evidence of tetrahedral sp^3 carbon was found.[18] The incorporation of hydrogen into the film can stabilize sp^3 bonds at the expenses of sp^2 bonds,[19] and will result in a more diamond-like structure, and hence harder films. That is why hydrogenated amorphous carbon films are called diamond like carbon (DLC), i.e. they consist of a mixture of sp^2 and sp^3 bonding.

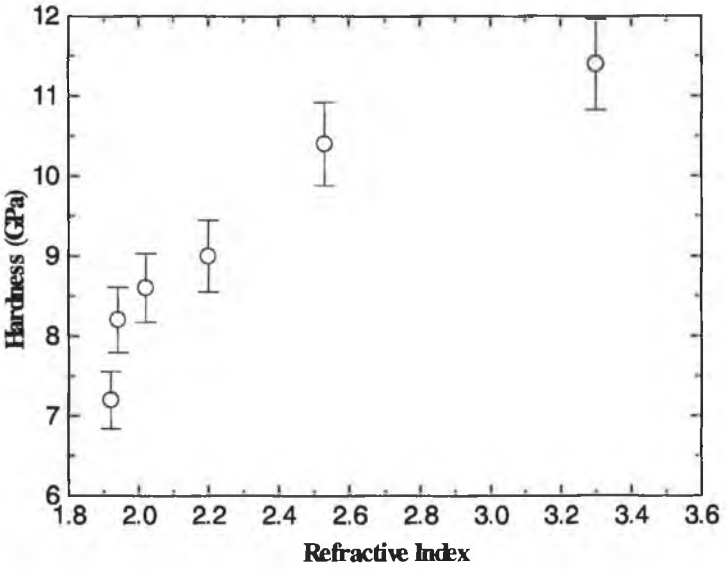

Figure 5.16: Hardness versus refractive index.

5.2.1.3 Effect of process parameters

Indentation analyses were also performed on carbon nitride films grown at different substrate bias and deposition temperatures. *Figure 5.17* shows a plot of hardness against substrate bias. It can be seen that hardness has a peak value in the range -100 to -150 V. Valence band XPS measurements show that the valence band spectra of films grown in the substrate bias interval between -75 and -150 V are more characteristic of a 'diamond-like' material. The fact that hardness also reaches a maximum in this range confirms the higher sp^3 or 'diamond-like' nature observed for carbon nitride films deposited at a certain substrate bias energy range. This is discussed in chapter 6.

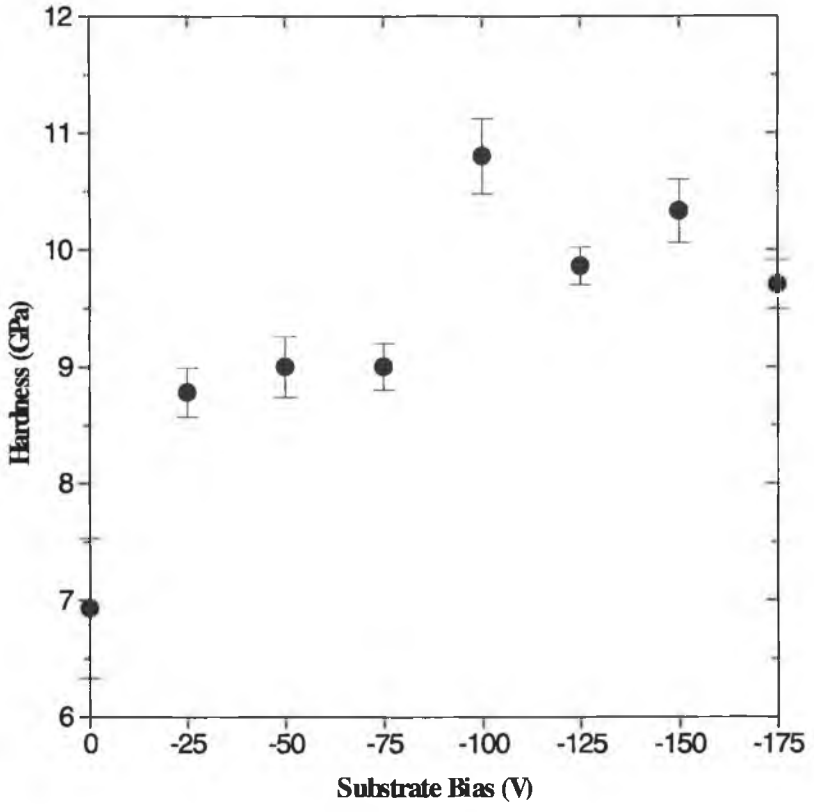

Figure 5.17: Hardness as a function of negative substrate bias.

Hardness measurements were performed on films annealed at 550 and 600°C for 15 minutes. The hardness decreased form ~9 GPa to 4 and 3 GPa at 550 and 600°C annealing temperature respectively as seen in *figure 5.18a*. Therefore, carbon nitride films became softer, even though the nitrogen content was reduced. This may be due to the breaking of carbon-nitrogen bonds, which leaves vacant lattice sites. The nitrogen atoms so produced are likely to combine as N_2 molecules in the film and may disrupt the structure as they desorb, which leaves behind voids in the film and as a consequence a weakened bonding structure. This interpretation is supported by the appearance of the films, which become less specular after annealing. Samples grown at deposition temperatures from 280 to 420° C exhibited similar values of hardness, as seen in *figure 5.18b*. Here, a decrease in nitrogen content is also expected with higher deposition temperature, as discussed earlier, and the structure becomes more like the films deposited at lower nitrogen partial pressures. Therefore, the nature of nitrogen loss with annealing and deposition temperature is quite different in the temperature range studied.

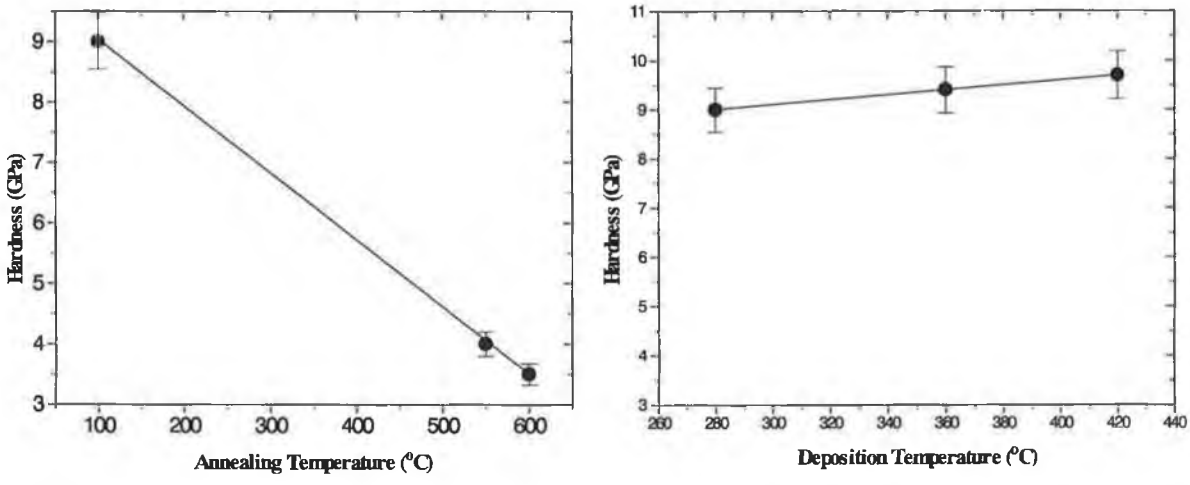

Figure 5.18: Hardness as a function of: (a) annealing temperature, (b) deposition temperature.

5.2.2 Analysis of nanoindentation load-displacement curves

The approach considered so far for determining modulus and hardness have been widely applied for coated systems, despite the fact that the unloading curves may not fit the model particularly well. The central problem with these approaches is the determination of the true contact area between the indenter and the material being tested. The problem is maximum for coatings with high elastic moduli and high hardness, i.e. the contact area is small (and thus the tip-end geometry needs to be known precisely). The unloading segment of the load-displacement curves obtained for carbon nitride films deposited on silicon do not fit well any existing model. In this case, the area of contact is continuously decreasing due to extreme elastic recovery. By contrast, the loading curve is well behaved. An alternative approach was developed by Hainsworth.[20] It predicts the loading curves of materials indented by a Berkovitch indenter. They established a relationship between elastic modulus (E), hardness (H), indenter geometry and the resultant displacement δ for a given load P and derived an expression of the form:

$$P = K_m \delta^2 \qquad (1)$$

where K_m is the equivalent of Loubet's elasto-plastic parameter, given by[21]

$$K_m = E\left(\phi\sqrt{\frac{E}{H}} + \psi\sqrt{\frac{H}{E}}\right)^{-2} \qquad (2)$$

The value of K_m can then be directly compared with the value K_{exp} derived from the experimentally determined P vs. δ^2 relationships, i.e.

$$K_{exp} = \frac{P}{\delta^2} \qquad (3)$$

By fitting plots of the P vs. δ^2 relationship from a wide range of materials, Hainsworth et al.[20] found that by making $\phi = 0.194$ and $\psi = 0.930$, the loading curve of a wide range of materials exhibiting elasto-plastic deformation can be well modeled, so that $K_m \approx K_{exp}$. The main conclusion is that if K_{exp} is found from best fitting the experimental data, then, if E is known, a corresponding value for H can be calculated (and viceversa).

Manipulating equation (1) and (2), the following quadratic equation is obtained, from which, once K_m is derived from the slope of the $P \propto \delta^2$ curve, E or H can be calculated if the other one is known.

$$H^2 + H\left(\frac{2\phi E}{\psi} - \frac{E^2}{\psi^2 k_m}\right) + \left(\frac{\phi E}{\psi}\right)^2 = 0 \qquad (4)$$

In order to correct the possible low hardness values obtained in the previous sections (H ~8-11 GPa), this analysis was employed for the load-displacement curves obtained before for one film containing no nitrogen and H ~11.4 GPa (named C), one film containing ~36 at.% N and H ~9 GPa (named CN_x) and the silicon substrate employed with H ~10.5 GPa. The loading curves from P vs. δ^2 relationships were fitted by a linear equation, and then the values of K_m were derived as shown in *figure 5.19*. Curve C was translated upwards for clarity. The highest value of K_m (highest slope) was found for the C film, followed by the Si substrate.

Now, to calculate the hardness (H) from equation (4) it is necessary to estimate a value for the elastic modulus (E). Taking the reduced modulus calculated before (90-150 GPa) did not give real numbers when equation (4) was applied. Since the films showed a good elastic recovery, an E value of ~330 GPa was assumed, similar to the one calculated by Hainsworth for their CN_x films applying this analysis. Taking E=330 GPa, hardness values were calculated as 17 GPa for C, 13 GPa for Si, and 11 GPa for CN_x. Because the E values for amorphous carbon nitride films investigated here are expected to be lower than 330 GPa, and E values increase for increasing K_m, E values of 200 and 300 GPa

where assumed for CN_x and C, obtaining H =14.4 and 19.4 GPa respectively. Assuming even a lower E value of 175 GPa for CN_x, gives an H ~ 17 GPa. Lower values of E produced complex numbers. From these results, hardness of 14.4-17 GPa and 17-19.4 GPa were estimated for CN_x and C films respectively. According to these results, the Oliver and Pharr method underestimate the hardness, but not by a significant amount.

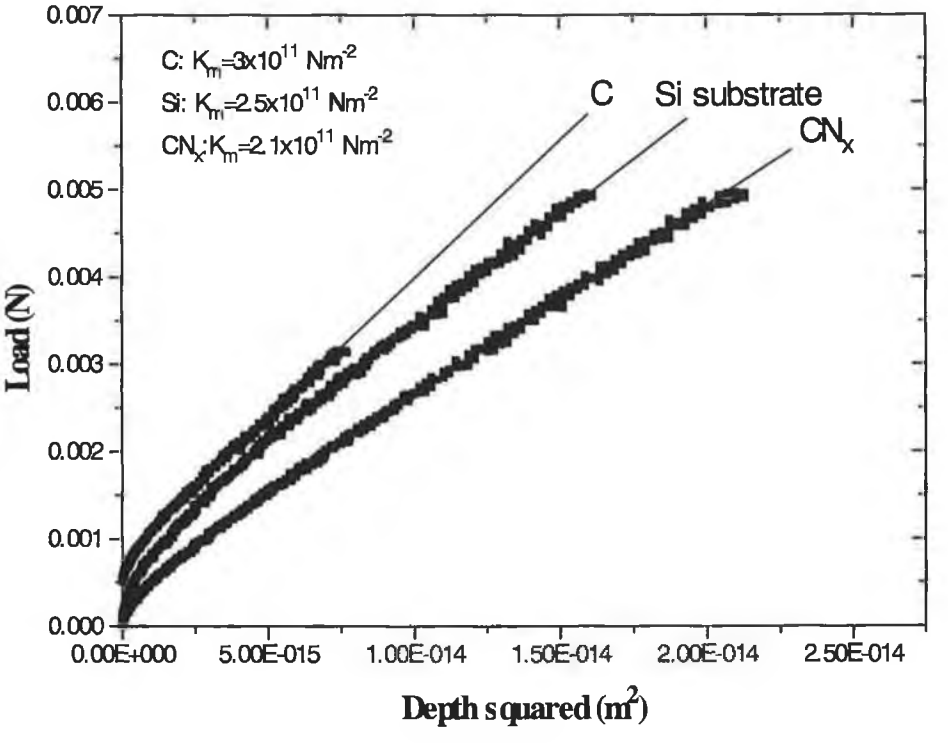

Figure 5.19: Nanoindentation data replotted as load vs. depth squared.

5.2.3 Friction measurements

The carbon nitride films investigated correspond to one of the first PCN series of films deposited varying the substrate bias from 0 to –75 V in steps of –25 V. All the films were grown in a pure nitrogen atmosphere at a total pressure of $1x10^{-3}$ mbar. The coefficients of friction obtained for each film, along with their hardness are given in *table 5.6*. In the evaluation of the frictional value (μ) of the four samples studied, PCN2 ranked the best, followed by PCN8, PCN7, and finally PCN3 with the highest value of μ, as can be seen

in *figure 5.20*. Photographs of the wear track produced in samples PCN2 and PCN3 taken at x50 magnification are shown in *figure 5.21*.

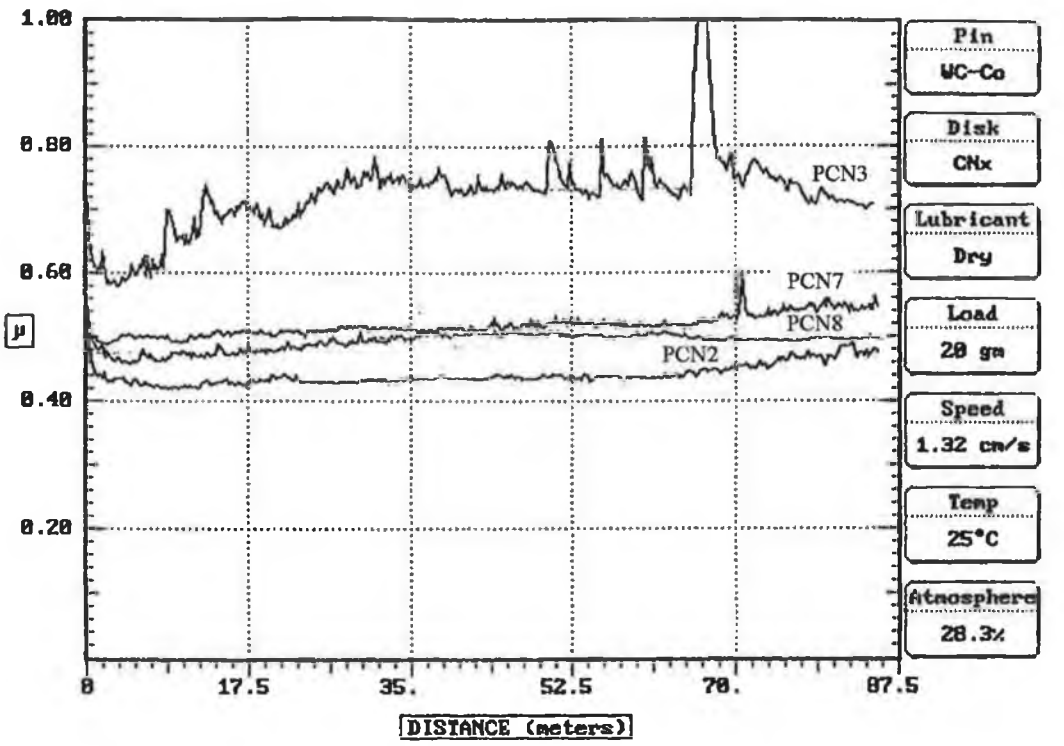

Figure 5.20: Frictional values.

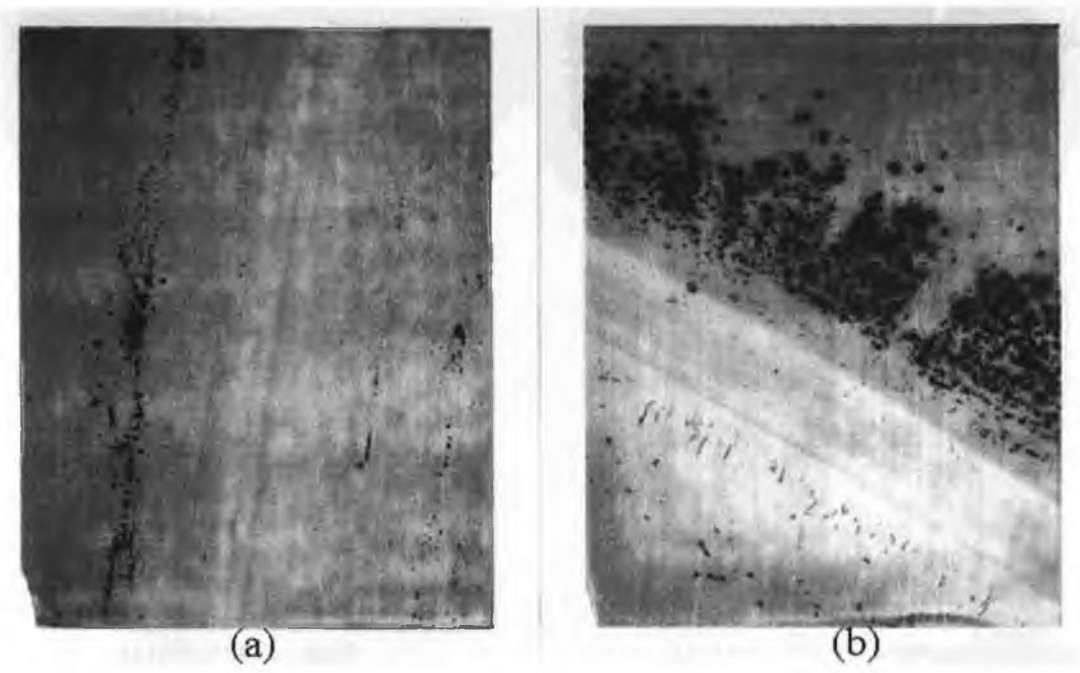

Figure 5.21: Wear track produced in (a) PCN2 film and (b) PCN3 film.

PCN2 produced very little wear debris as observed in *figure 5.21a*, resulting in a lower value of coefficient of friction. *Figure 5.21b* is a picture of the weartrack produced in PCN3. It can be seen that the wear is smooth but on one side cracks perpendicular to the wear track were formed. In addition, significant wear debris was produced on the opposite side of the weartrack. This behaviour can be explained by a hard brittle film delaminating under loading which causes abration wear during friction evaluation. In the other three samples, no cracks were observed near the weartrack.

SAMPLE	Vb(V)	HARDNESS(GPa)	Coefficient of friction, μ.
PCN2	0	7	0.42
PCN7	-25	8.6	0.5
PCN3	-50	9	0.74
PCN8	-75	8	0.48

Table 5.6: Coefficient of friction and hardness for films deposited at different substrate bias.

The initial 4-5 meters of frictional evaluation is associated with "bedding in", which is caused by a hard pin interacting with a softer meeting surface, therefore, it is the steady state response that is taken for coefficient of friction evaluation. These results showed that higher coefficient of friction films correspond with higher hardness as summarised in *table 5.6*. The coefficient of friction and the hardness vary with substrate bias in a similar fashion to the 2200 cm^{-1} IR absorption coefficient corresponding to the C≡N bond, peaking at a bias of approximately –50 V, as can be seen in *figure 5.22*. This confirms the presence of C≡N bonds in the carbon network as terminating sites, which weakens the structure. Hajek et al.[22] also found that harder films exhibited higher frictional values than softer films, in which the wear debris produced was proposed to act as a solid lubricant.

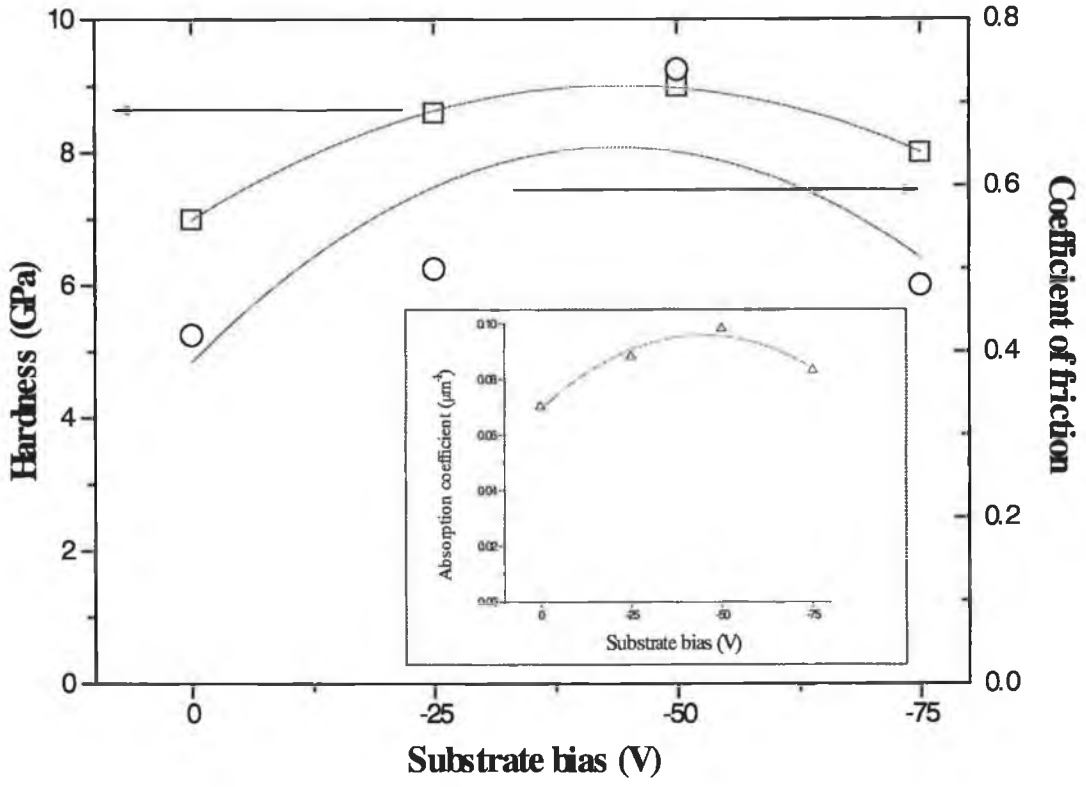

Figure 5.22: Hardness and coefficient of friction as a function of substrate bias. In the inset: absorption coefficient of the 2200 cm^{-1} peak as a function of substrate bias.

5.2.4 Stress measurements

Film stress usually develops in thin films during deposition. It was also found to be independent of film thickness indicating that the stress was introduced at the film-substrate interface during the initial growth process rather than in the bulk of the film. Indeed, if the stress of the films per unit thickness is plotted against the reciprocal of film thickness, as in *figure 5.23*, the graph extends to zero or even slightly tensile values of stress as thickness increases (i.e. as 1/thickness tends to zero). Thus, the addition of nitrogen bonding in the films significantly relieves the high levels of stress normally found in hard carbon films.

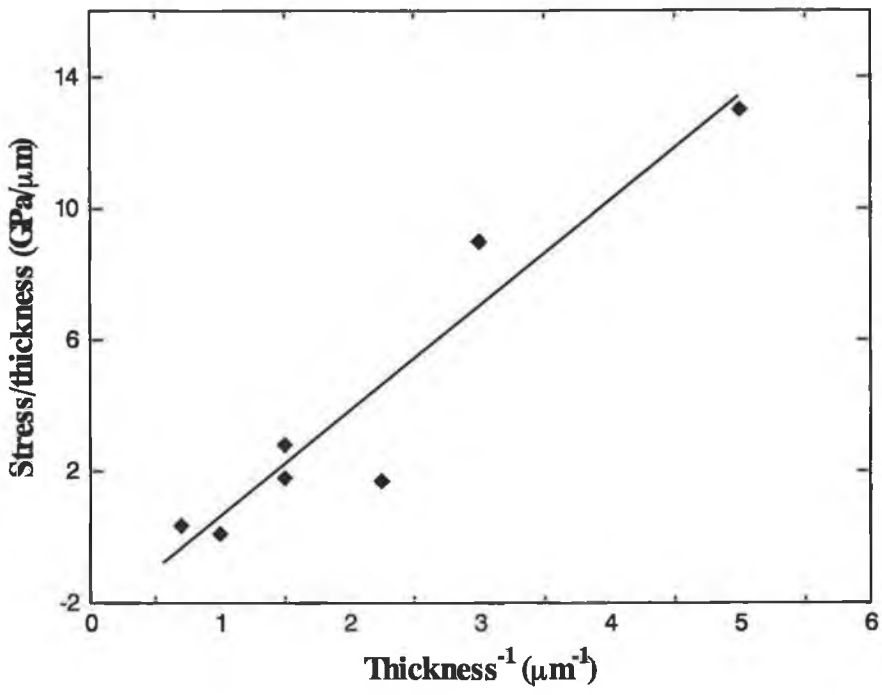

Figure 5.23: Stress as a function of thickness^{-1} of carbon nitride films.

Finally, investigations of the variation of the intrinsic stress as a function of substrate bias (from 0 to –75 V) for fixed deposition pressure, gas composition and magnetron power, revealed a monotonic increase, as shown in *figure 5.24*. The stress appears to be controlled by the deposited ion energy, due to the high bombarding ion flux at the substrate.

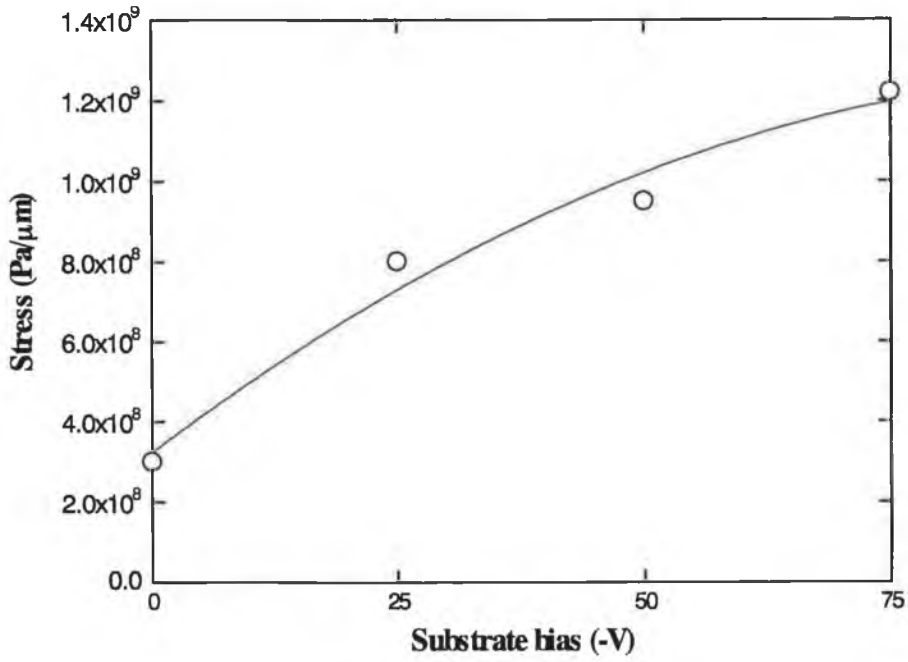

Figure 5.24: Intrinsic stress as a function of substrate bias.

5.2.5 Summary and discussion

Nanoindentation technique has proved to be a very useful technique to study the mechanical behaviour of carbon nitride films, allowing to obtain very interesting mechanical "fingerprints" of the behaviour of thin films under load. Another question is the degree of accuracy of the hardness and modulus values obtained. The hardness values were quite reproducible, but because of the uncertainty in calculating the projected area and the interaction between film and substrate, extracting intrinsic hardness values from indentation measurements presents a particularly complex problem.[23] The analysis method used, as other current models, rely on the assumption that the unloading curve can be fitted with a power law with a constant exponent, which does not work well for materials with extremely high elastic recovery. In these cases, determining the true contact area between the indenter and the material being tested is particularly difficult, since it is continuously decreasing due to the high elastic recovery, so that that analysis

methods tend to overestimate the contact area and then underestimate the hardness, especially for materials with very high elastic modulus. However, the method described here is useful for comparative purposes to study variations of hardness/modulus with deposition conditions.

The local structural property that distinguishes potentially superhard and dense C_3N_4 structures from low density, softer material is the carbon coordination: hard materials require tetrahedral or sp^3-bonded carbon in the C_3N_4 network, while sp^2-bonded carbon will lead to much softer materials. This requirement of having sp^3-bonded carbon in a hard carbon nitride is completely analogous to that in amorphous diamond-like carbon (DLC).[24]

Generally, nitrogen-containing carbon films, grown by dc magnetron sputtering, have been amorphous, with only small indications of crystalline phase and the hardness of the films has not yet been observed to increase as the nitrogen content increases,[25,26] as we obtained for our films. The hardness results obtained for our carbon nitride films (7-10 GPa), do not differ much from those obtained by other groups,[27,28] which used dc magnetron sputtering of a graphite target in a nitrogen atmosphere. In these works, the nanoindentation response of the carbon nitride films represents that of the amorphous network, and the maximum hardness values found (13-15 GPa) are comparable to that of amorphous hard carbon. There are also some studies[29] that reported values of up to 55 GPa for amorphous carbon nitride, which were explained by an structure where nitrogen atoms are bonded to carbon in an sp^3-like configuration, causing the weak Van der Waals type bonding between the sp^2-bonded graphitic basal planes to be replaced by strong covalent bonds, creating a three dimensional network of covalently bonded atoms.

In all cases, one has always to bear in mind the uncertainty when reporting hardness values for carbon nitride films, an all the errors incorporated through the approximations and curve fits needed for calculation of elastic modulus and hardness. The incorporation of nitrogen into the films might increase the proportion of sp^2 to sp^3 hybridization. This is probably due to the formation of C=N double bonds in a network of trigonally bonded

amorphous carbon, perhaps associated with the formation of a structure containing cyanogen rings, which are known to polymerize to form a group of materials called paracyanogen.[14]

From the studies done so far, it can be said that mainly sp and sp^2 bonding states are present in the films, with little sp^3 bonding present. The film hardness appears to be controlled by the C≡N bond concentration rather than nitrogen content, i.e. C≡N bonds appear to be significantly weaker than the others.

The higher values of hardness for nitrogen containing films were found when substrate bias in the range of –100 to –150 V were applied. As discussed later in chapter 6, this is related to an increase in the sp^3-bonding nature of the films. The maximum hardness is still low, since the films are inhomogeneous and the hardness values will be dominated by the properties of the amorphous regions. Deposition temperature in the range 280-420°C does not have a significant effect in hardness. Annealing of the films at 600°C, however, resulted in a sharp drop in hardness due to the structure disruption caused by nitrogen atoms as they desorb from the film surface.

The steady state mean coefficients of friction of ~0.4–0.7 obtained for carbon nitride films are very similar to values reported for films with similar hardness.[22,30] Higher coefficients of friction were found for harder films deposited at different substrate bias. Hard brittle films delaminate under load and cause abration wear during friction evaluation. Finally, the stress is shown to be concentrated at the film-substrate interface whereas the bulk of the film is stress-free. The stress is increased at higher substrate bias as ion bombardment increases.

References

1. T.F. Page & J.C. Knight, Surface and Coatings Technology, 39/40 (1989), 339.
2. A.J. Whitehead & T.F. Page, Thin Solid Films, 220 (1992), 277.
3. H.F. Doerner and W.D. Nix, J. Mater. Res. Soc. 1, 4 (1986), 601.
4. W.C. Oliver and G.M. Pharr, J. Mater. Res. Soc. 7 (1992) 1564.
5. W.C. Oliver, G.M. Pharr, and D.N. Lucas, Mechanical Properties And Deformation Behaviour of Materials having Ultra-Fine Microstructures, M. Nastasi (ed) (1993) 417.
6. I.N. Sneddon, Int. J. Engng. Sci. 3(1965) 47.
7. D. Tabor, Proc. R. Soc. A 192 (1948) 247.
8. J.W. Harding and I.N. Sneddon, Proc. Cambridge Philos. Soc. 41 (1945) 12.
9. Operation Manual (Part I and II), Nano Test 500, Micro Materials Ltd., Wrexham Technology Park, Wrexham, UK (1994).
10. N. Savvides and T.J Bell, J. Appl. Phys. 72 (1992) 2791.
11. G.G. Stoney, Proc. Roy. Soc., London (1909) 172.
12. C.N. Peggs, I.C. Leigh, "Recommended procedure for micro-indentation Vickers hardness test", Report MOM 62, U.K. National Physical Laboratory, England (1983).
13. P.V. Kola, D.C. Cameron, M.S.J. Hashmi, Surface and Coatings Technology, 68/69 (1994) 188.
14. N.N. Greenwood and A. Earnshaw, Chemistry of elements, Pergamon, NY (1984)
15. B. Wei, B. Zhang and K.E. Johnson, J. Appl. Phys. 83 (1998) 2491.
16. C.A. Davis, Y. Yin, D.R. Mckeinze, L.E. Hall, E. Kravtchinskaia and V.S. Veerasamy, J. Non-Crystalline Solids, in press.
17. S. Lee, S.J. Park, S. Oh, W.M. Kim, J.H. Bae, B. Cheong, S.G. Kim, Thin Solid Films, 308-309 (1997) 135.
18. N. Axen, G.A. Botton, H.Q. Lou, R.E. Somekh and I.M. Hutchings, Surf. and Coat. Technol. 81 (1996) 262.
19. B.V. Spitsyn, L.L. Bouilow, B.V. Berjaguin, J. Cryst. Growth. 52 (1981) 219.
20. S.V. Hainsworth, H.W. Chandler, and T.F. Page, J. Mater. Res. 122 (8) (1996) 1987.

21. J.L. Loubet, J.M. Georges and J. Meille, Microindentation techniques in material science and engineering, American society for testing materials, Philadelphia (1986) 72.
22. V. Hajek, K. Rusnak, J. Vlcek, L. martinu and H.M. Hawthorne, Wear 213 (1997) 80.
23. F.R. Brotzen, International Materials Reviews, 39, 1 (1994) 24.
24. J. Robertson, Adv. Phys. 35 (1986) 317.
25. Dong Li, S. Lopez, Y.W. Chung, M.S. Wong and W.D. Sproul, J. Vac. Sci. Technol. A. 13 (1995) 1063.
26. Dong Li, Yip-Wak Chung, Ming-Show Wong and Willian D. Sproul, Tribology Transactions, Vol. 37, 3 (1994) 479.
27. X. Wang, P.J. Martin, T.J. Kinder, Thin Solid Films, 256 (1995) 148.
28. K.G. Freider, M.J. Tarlov, G.J. Gillen, G.E. Poirier, L.H. Robins, L.K. Ives, W.D. Bowers, R.B. Marinenko and D.T. Smith, J. Mater. Res. 10 (1995) 3079.
29. H. Sjöström, L. Hultman, J-E Sundren, S.V. Hainsworth, T.F. Page and G. Theunissen, J. Vac. Sci. Technol. A 14 (1996) 56.
30. Y. Kusano, Z.H. Barber, J.E. Evetts and I.M. Hutchings, "Tribological and mechanical properties of carbon nitride films deposited by ionised magnetron sputtering", ICMCTF'99, Thin Solid Films, in press.

CHAPTER 6

ELECTRONIC STATES OF CARBON NITRIDE

In this chapter, the electronic structure of the deposited carbon nitride films is analysed using different techniques. XPS and UPS techniques were used to measure the binding energies of the valence electrons. Mapping the valence band (VB) of carbon nitride films is important for further improvement of their opto-electronic properties. Furthermore, it is shown that the valence band XPS spectra can be a good indicator of structural changes in carbon nitride films. The relationship between band structure, density of states, and the photoemission spectra is also discussed. Electron spin resonance (ESR) measurements are used to investigate the paramagnetic species that give rise to the spectra and the spin density concentration. The findings are related with structural changes within the film that occur due to the increase in nitrogen partial pressure (Npp). The electron energy loss (EELS) spectra of carbon nitride grown are also correlated with structural changes due to a change in Npp.

6.1 Introduction to photoemission valence band spectra

The valence band (VB) electrons are responsible for bonding and thus significant changes in the density of states (DOS) occur during structural modification, either induced by changing the substrate bias or the nitrogen partial pressure. The valence band region is often loosely defined as approximately the first 30 eV of binding energy. In this region, the principal contributors to the spectra arise from the energy levels that have suffered extensive molecular (orbital) or solid (band) involvement. The spectrum in this region consists of many closely spaced levels giving rise to a band structure. *Figure 6.1* illustrates the density of electron states for the cases of insulators and conductors. In the case of an insulator, the occupied valence band is separated from the empty conduction band, whilst in the case of a metal these bands overlap and the uppermost occupied state is termed the Fermi level (E_F). In the figure, it can be noted that E_F is not the true zero point of the electron energy scale, although

binding energies (BEs) are often referred to this point. The true zero is the vacuum level (E_{vc}) and, to a first approximation, $E_F - E_{vc} = \phi$, where ϕ is the work function of the material.

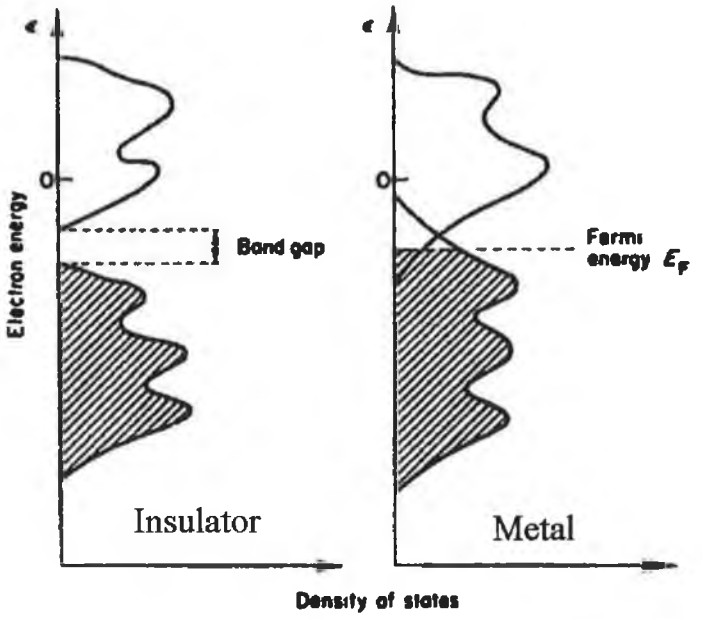

Figure 6.1: Density of electron states of an insulator and a metal. The shadow region indicates occupied energy levels.

The valence and conduction states of solids present special difficulties for the interpretation of absorption and reflection spectra because the quantum states form continuous bands of significant width rather than the discrete states, which characterise atoms. Due to these continuous bands, the valence and conduction states of solids are difficult to interpret from 'conventional' optical spectra data, such as the optical absorption and reflection spectra and the optical constants (α,n) obtained from such spectra. The difficulty arise from the fact that transitions from the valence to the conduction band usually involve a large range of possible initial and final state energies for a given photon energy. The photoemission method involves the photoinjection of carriers from valence or core states into the vacuum and the analysis of the energy distribution of the emitted electrons as a function of photon energy. *Figure 6.2* illustrates the photoemission process.

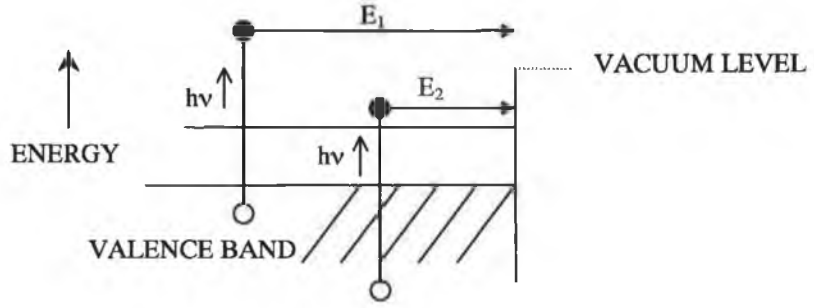

$\eta(h\nu,E)dE$ = Probability of hν exciting electrons to final state at energy $E+dE$

$\alpha \Leftrightarrow \int \eta(h\nu,E)dE$ and $N(E,h\nu)dE \Leftrightarrow \eta(h\nu,E)dE$

N(E,hν) = Energy distribution of photoemission.

Figure 6.2: Relation between optical constants and the energy distribution of photoemission.

The essence of the use of photoemission to study the electronic structure of solids is determining η(E,hν), the probability of a photon of energy hν exciting an electron to a final state at energy E. In contrast, it is the integral of η(E,hν) over all final states which is related to the optical parameters such as the absorption coefficient α. The optical constants are determined by the integral over all final states. For example,

$$\alpha \propto \int \eta(h\nu,E)dE$$

It is because of this integration over final states that it is so difficult to obtain unambiguous information on the quantum states from reflection or absorption measurements or from the optical constants themselves.

Photoemission is useful because it serves to remove the integration over final states. In photoemission, the excited electrons are allowed to escape into vacuum where their energy can be measured. From this measurement, the energy distribution of the emitted electrons $N(E,h\nu)$ can be obtained. It gives the number of electrons emitted per photon absorbed in a given interval of energy. The inelastic scattering of electrons

between the moment of excitation and escape into the vacuum must be taken into account. Most of the interpretation of valence band spectra obtained from photoemission data is based in the 'three-step model'.[1] It approximates the photoemission process as three consecutive events: optical excitation, transport of the electrons to the surface and escape of the electrons across the potential barrier at the surface into vacuum. *Figure 6.3* indicates what happens to an energy distribution curve (valence band spectrum) between the time it is excited and when it reaches the surface and escapes into vacuum. An initial optically excited distribution is shown on the left. Changes in this distribution as it approaches the surface are indicated. In this figure, E_g is the band gap separating the valence band from the conduction band, E_a is the potential barrier at the surface and E_i is the energy of the electron in the valence band before being excited by a photon of energy hν.

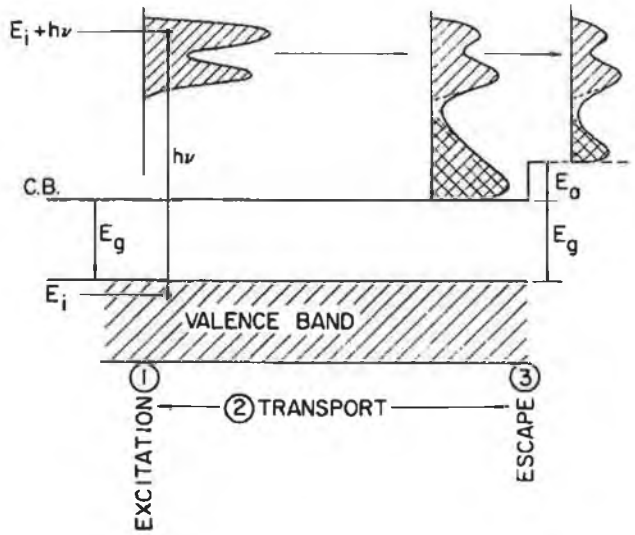

Figure 6.3: The three-step photoemission process.

A hypothetical density of states is sketched which will depend on the details of the electronic structure. As they move towards the surface, the excited electrons lose energy due to inelastic scattering, which is mainly caused by electron-electron scattering between the excited electron and the valence electrons, and electron-phonon scattering between the lattice and the electron.

In *figure 6.3*, the low energy peak appears as the excited electron move to the surface due principally to electron-electron scattering. Because of the large energy loss associated with this event, the scattered electrons are often effectively removed from the distribution or else simply provide a monotonic background. This is important because the electrons are normally removed from the energy distribution curve (EDC) without producing new structure, which would confuse the interpretation of the data. As shown in *figure 6.3*, the main structure of the density of states remains in the EDC's after scattering and a new peak of low energy electrons appears near the low energy cut-off of the EDC. To summarise, scattering will remove electrons from the original distribution. This can cause broadening in structure and changes in the relative intensities of peaks in that distribution. Except for these changes, there is a close one-to-one relationship between structure in the measured EDC's and that in the excited distribution, N(E,hv).

The last step in photoemission is the escape of the electrons across the potential barrier at the surface. The principal effect here is to cut off the low energy portion of the EDC's in such a way that the magnitude of the EDC's increases gradually from their threshold voltage, as indicated in *figure 6.3*. The three-step model is an approximation of the photoemission event, which allows for relatively easy treatment, but has its limitations, especially when the escape depth becomes shorter.

Figure 6.1 shows that at low energies, the unoccupied states have structure. Consequently, if photo-electrons ejected from filled levels have kinetic energies which fall within this structured region, the observed intensity will be a convolution of the filled and empty density of states. This is the case in ultra-violet photoelectron spectroscopy (UPS) and gives rise to the strong dependence of valence-band spectra on photon energy. In the case of XPS, the kinetic energies of the valence photoelectrons are such that the final states are quite devoid of structure; thus, the observed density of states closely reflects the initial filled density of states. The XPS spectra of single-crystal diamond, Silicon and Germanium show a strong similarity to the corresponding density of states.[2] The VB spectra obtained by XPS or UPS relates closely to the occupied density of states structure, and is useful in the study of the

electronic structure of materials, fundamental to many aspects of device applications. In the case of polymers, valence bands reveal structural information often unobtainable from core-level studies. The different structures that conform the VB arise from both density of states and photo-emission cross-section effects. Let's consider first the various factors that contribute to the photoemission intensity. The photoemission intensity at a given energy E may be written as[3]

$$I(E) \sim \rho'(E)\rho'(h\omega - E)\sigma(h\omega, E)$$

where $\rho'(E)$ is the density of initial states, $\rho'(h\omega-E)$ is the density of final states of the system including the final state of the photoelectron, and $\sigma(h\omega,E)$ is the cross-section of the process. If a one electron model is assumed,[3] at high excitation energies (~1254 eV if Mg Kα radiation is used) the conduction bands are expected to be very free-electron-like and thus featureless, reducing the intensity expression to

$$I(E) \sim \rho'(E)\sigma(h\omega, E)$$

Cross-sections for photoelectron emission from valence levels are much lower than for core levels, giving rise to low intensities in general. In carbon, the cross-section term is extremely important, as $\sigma(hw,E)$ is a very strong function of E in the valence band region.[3] The valence bands arise mostly from the 2s and 2p atomic states, and the cross-section ratio for photoemission by Mg $K\alpha_{12}$ X-rays is $\sigma(2s)/\sigma(2p) \sim 13$.[4] Hence, even a small change of the sp^3 characteristic to the more s-like sp^2 hybridisation will change the shape of the carbon valence band significantly. In summary, the intensity of the valence band spectra depends on density of states as well as on photoemission cross section where the second one is strongly dependent on the excitation energy.

6.2 XPS valence band spectra

The XPS VB spectra were obtained from XPS analyses, which were carried out with a monochromated Mg Kα (1253.6 eV) X-ray source with an energy resolution of ~0.5 eV. The binding energy values of the photoelectron peaks were measured with an accuracy of ± 0.05 eV. The spectrometer was calibrated to position the $4f_{5/2,7/2}$

photoelectron lines of clean pure Au foil at binding energies of 87.74 and 84.07 eV. The films were conductive enough such that substrate charging could be ignored.

XPS can be used to study the emission from weakly bound valence orbitals involved in chemical bonding. It is difficult to make a quantitative interpretation of the valence band (VB) spectra obtained, as discussed before, but they can be used as a 'fingerprint' of elements in different bonding environments which show only a weak chemical shift in core levels. Therefore, if we have the high-resolution X-ray photoemission spectra (XPS) of the total VB of carbon nitride, then it can be compared to other known XPS VB spectra, such as diamond, graphite, glassy carbons and polyethylene. From this comparison, it is possible to distinguish between graphite like, inter-linked carbon backbone and diamond like features and information can be obtained about the nature of the states in the valence band (s, p or sp character). Information is also obtained about the contribution of s or p electrons shared in σ and π bonds since they give rise to different features in the VB spectra.

Figure 6.4 shows the XPS VB band spectra of carbon nitride thin films deposited at different nitrogen partial pressures (Npp). The most striking feature in the spectra obtained with XPS is a peak located in the region 17-20 eV (peak II). This intense peak is related to s-p hybridised states, by comparing it to the VB spectra of graphite and diamond studied by McFeely et al.[3] shown in *figure 6.5*. Their observations indicate mainly s character at the bottom of the valence band (peak I) and mainly p character at the top (peak III), with considerable s-p mixing throughout (peak II). However, the s-p region in the films investigated here resembles more closely the intense peak II at region ~10-20 eV found when carbon forms a polymer with hydrogen (i.e. polyethylene, polypropylene, etc)[5] as shown in *figure 6.5*.

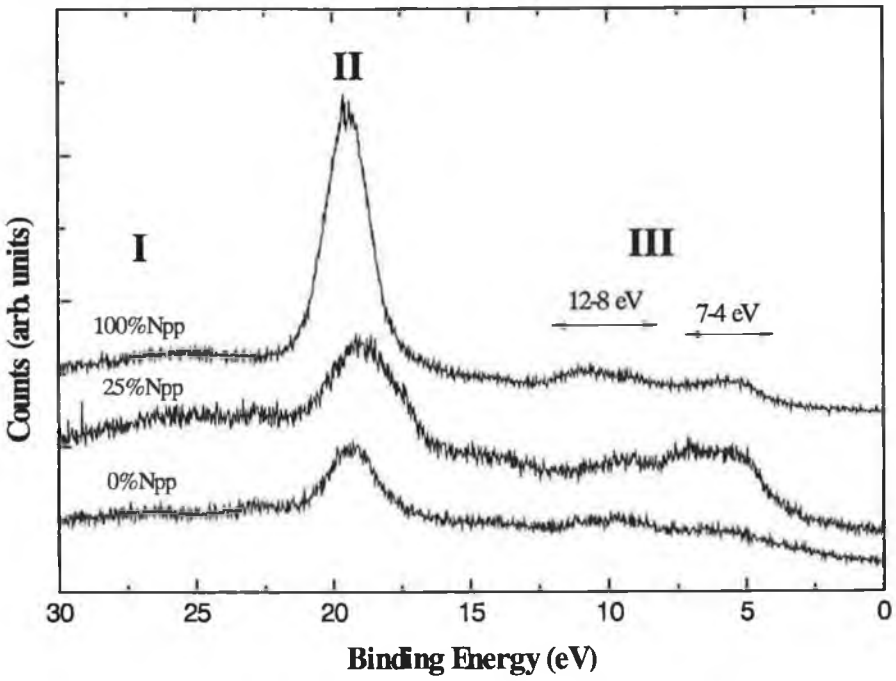

Figure 6.4: XPS valence band spectra of carbon nitride films deposited at different nitrogen partial pressures.

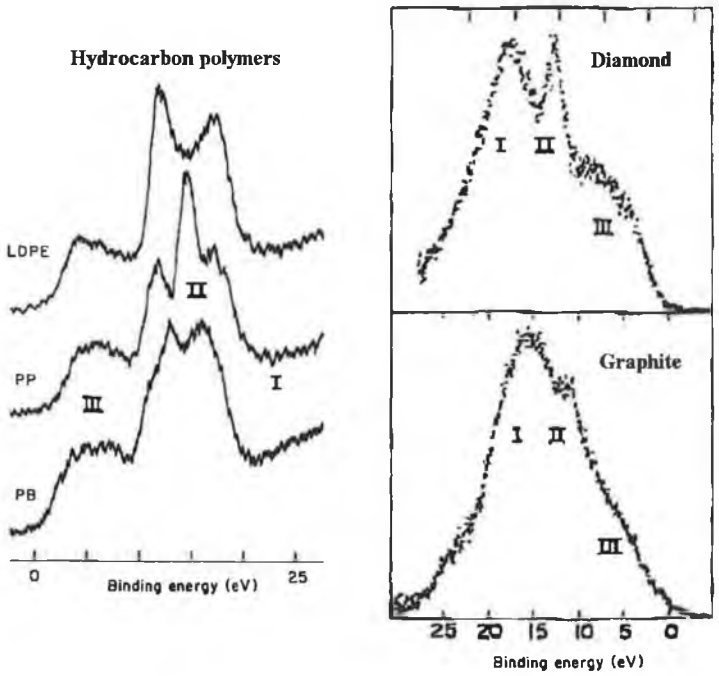

Figure 6.5: XPS valence band spectra of diamond, graphite and hydrocarbon polymers – polyethylene (LPDE), polypropylene (PP) and poly(but-1-ene) (PB).

The valence band spectra show the interlinked carbon backbone nature of the carbon nitride solid and thus identify the structural nature of this solid, which is significantly different from diamond-like and graphitic features. For the film grown at 100% Npp, the s-p hybridised peak dominates the VB spectra due to the fact that the nature of nitrogen incorporation changes when Npp >25%, as discussed in chapter 4. Above this value, an increasing amount of nitrogen occurs in the form of N=N bonds, which forms part of the structural network. The low binding energy side of the dominant peak (<15 eV) in the XPS VB spectra is attributed to p electrons. Two main features can be identified in this region at ~4-7 eV and ~8-12 eV. As N is included in the films, the feature located at ~ 4-7 eV intensifies, due to C 2p and N 2p electrons associated to π bonds in aromatic rings[6] and probably N lone-pair electrons, which are present when a N atom bonds to a C atom in a pyridine-like domain and when C-N triple bonds are formed. A band is also present at 8-12 eV, which is due to p electrons shared in C-N and C-C σ bonds.[7] The lack of intensity in all these features is due to the low cross-section for X-ray photoemission for 2p electrons.[8] Little structure can be distinguished in the interval 0-4 eV. When Npp=100%, it can be seen that the bottom region of the VB spectra (<15 eV) resembles more closely the film grown in a pure argon atmosphere (Npp=0%). At 100% Npp, the carbon nitride film gave a valence band that resembles more closely that of a polymeric compound with the more intense s-p peak.

In order to study in more detail the XPS valence band spectra, especially the low binding energy region, the energy range of the spectra between 0.1 and 30 eV was deconvoluted. The individual XPS spectra were resolved into Gaussian components with the background eliminated using a Shirley-type integral for correction for inelastic scattering. Deconvolution of the valence band spectra is not an exact process since the peaks are not well defined and there is plenty of opportunity for data manipulation but an attempt was made to realistically insert Gaussian components where peaks are visible in the spectra. The deconvoluted XPS VB spectra are shown in *figure 6.6*.

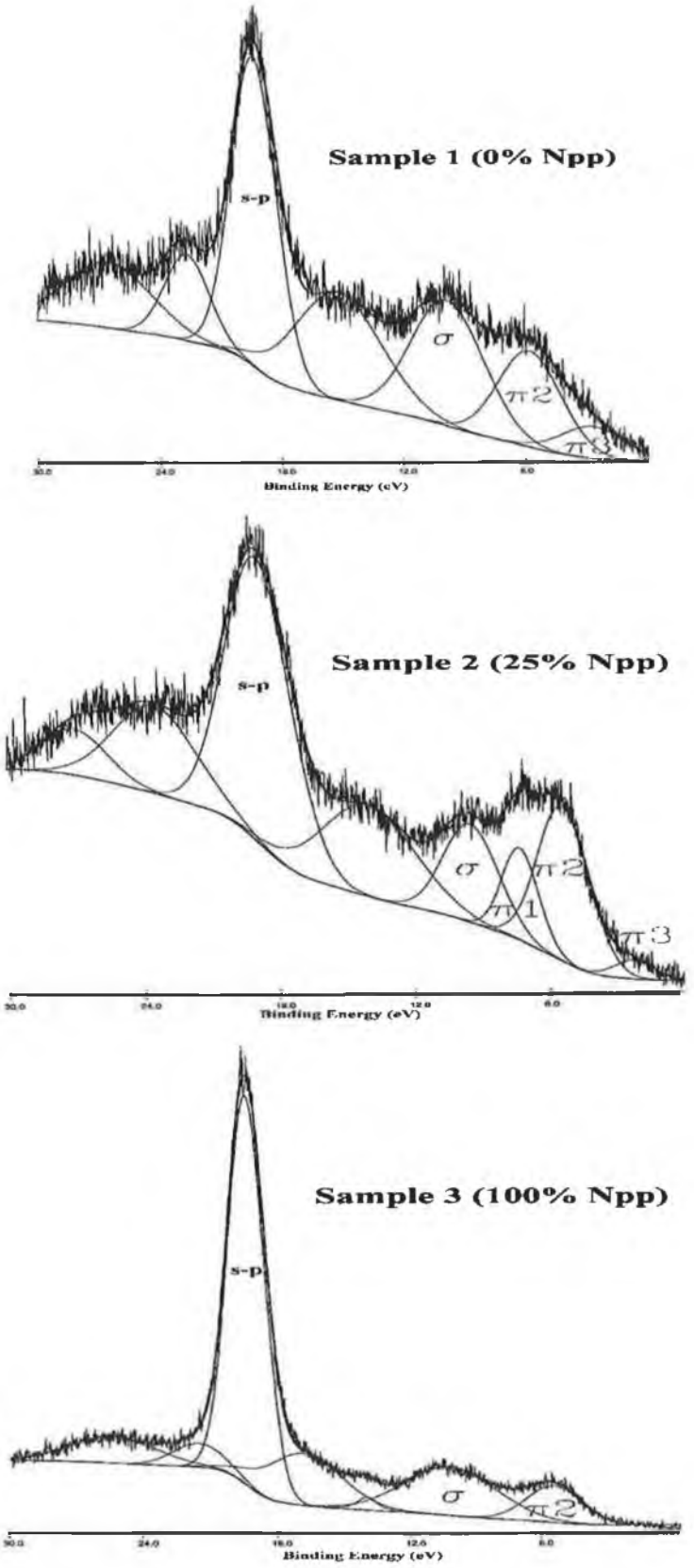

Figure 6.6: Deconvoluted XPS VB spectra showing the variation of the p-π, p-σ and the s-p mixed band in carbon nitride films

In the figure above, it can be seen that the s-p peak dominates the spectra in sample 3. On the other hand, the area of the π region (π2 peak) is small compared to the other samples bands (π1,π2 and π3 peaks). Theoretical DOS calculations for nitrogen substitutions of carbon in graphite assigned σ bonds at ~10 eV and π bonds at ~7 eV.[8] For sample 1, π2 peak arises from C 2p electrons, since no nitrogen incorporation is expected. For sample 2, the low energy region (π region) was best fitted with three peaks (π1,π2 and π3 peaks). The π1 peak occurring in sample 2 is possibly due to N 2p electrons that are shared in C=N and C≡N π bonds. In sample 3 the π region gets lower; for Npp=100%, the formation of C-N sp^3 σ bonds may be the reason for the change in the area ratio between π and σ regions. This will be further discussed with the UPS VB spectra in the next section

Valence band XPS spectra of carbon nitride films were used to study the change in bonding structure induced by substrate bias, since from Raman studies it appeared that it has no effect. XPS VB spectra of carbon films give a 'fingerprint' of the structural changes in the material and significant differences can be seen between the VB XPS spectra of diamond, graphite and polymeric carbon compounds.[9] Carbon nitride films have also been shown to exhibit similar features as mentioned before. *Figure 6.7* shows the evolution of the VB spectra as the bias is changed.

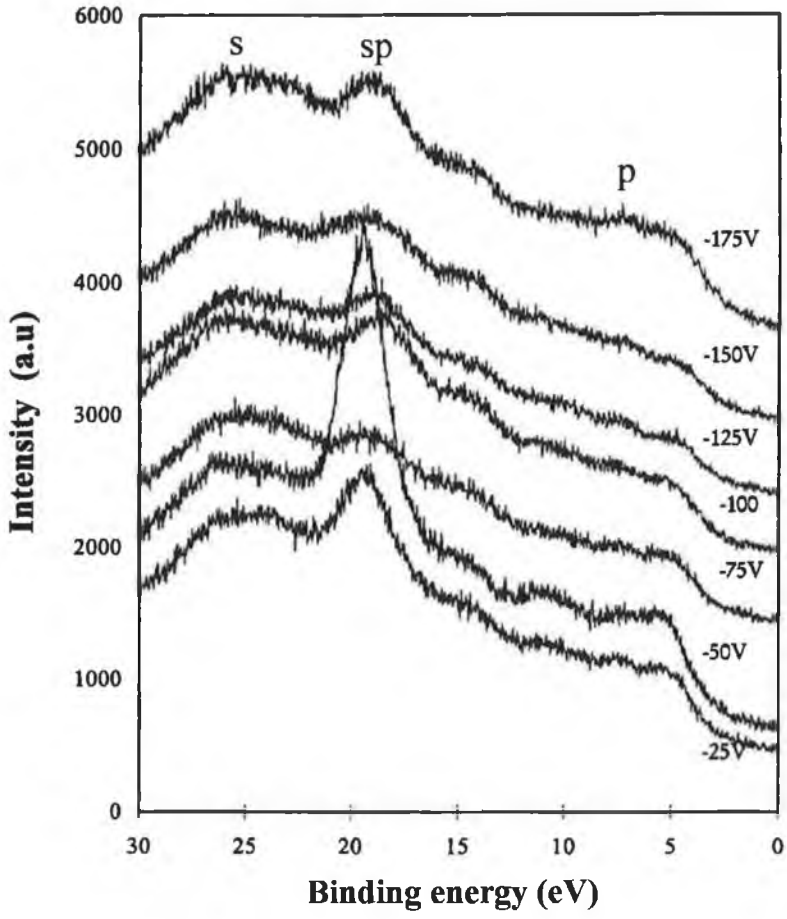

Figure 6.7: XPS VB spectra of carbon nitride films deposited at different substrate bias.

The spectra show three main features; a peak at ~25 eV due to s electrons, a peak at 15-20 eV due to sp hybridised electrons and a series of peaks from 5-15 eV attributed to p electrons. With bias ≤ -50 V, the spectra are dominated by the sp peak. By analogy with carbon films, this is indicative of a polymeric-type structure. When the film is deposited with -75 V ≤ bias ≤ -150 V the spectra show that the s and sp peaks are equal in height, a feature characteristic of the spectrum from diamond and with bias of -175 V the sp peak is beginning to increase again and also the 5 eV peak is becoming more prominent, similar to the samples with bias ≤ -75V i.e. it has a more polymeric structure. A similar mechanism to that which occurs in amorphous carbon where the sp^3 or 'diamond-like' nature increases in a certain ion energy range[10,11] is also occurring in carbon nitride films. These previous works on carbon films have shown that the proportion of sp^3 bonding can be influenced by controlling the energy

of the ions which bombard the substrate. The precise mechanism by which this is achieved is still the subject of argument, however, the models formulated, such as the "induced stress" models of Davis[10] and McKenzie[11] exhibit the same macroscopic behaviour whereby the sp^3 fraction is maximised within a restricted range of ion energy from approximately 50 to 250 eV. Outside this range the sp^3 fraction is reduced due to either the ion energy being too low to cause significant change to the structure or too high such that the desired bond type is disrupted. The control of the incoming ion energy on carbon nitride films grown by magnetron sputtering is achieved by controlling the substrate bias during deposition.

6.3 UPS valence band spectra

Ultraviolet photoemission spectroscopy (UPS) can be used to study a material when there is no previous knowledge of the electronic structure. UPS has been used to study amorphous materials such as amorphous Germanium.[1] The data obtained showed very little structure; just a single broad peak which moves monotonically to higher energy with increasing photon energy. This behaviour suggests that the structure originates from the valence band. The behaviour of the amorphous EDC's suggest optical transitions which depend primarily on the density of states and conservation of energy. The UPS spectra of the carbon nitride films are usually dominated by 2p electron states and are interpreted mainly in terms of the partial p-density of states (DOS), weighted with the corresponding photoionisation cross sections. Atomic photoionisation cross sections for C 2s and 2p electron states are 1.2 and 1.9 Mb, and for N 2s an 2p are 1.9 and 4.4 Mb at 40.8 eV (He II radiation) photon energy. He II was used, which is usually better than He I (21.2 eV), to avoid surface contamination of samples.[12]

The valence band (VB) spectra were obtained using the He II line ($h\nu$ = 40.8 eV) from a He resonant lamp. VB spectra of three carbon nitride films deposited at nitrogen partial pressures of 0%(sample1), 25%(sample 2) and 100%(sample 3) are shown in *figure 6.8*:

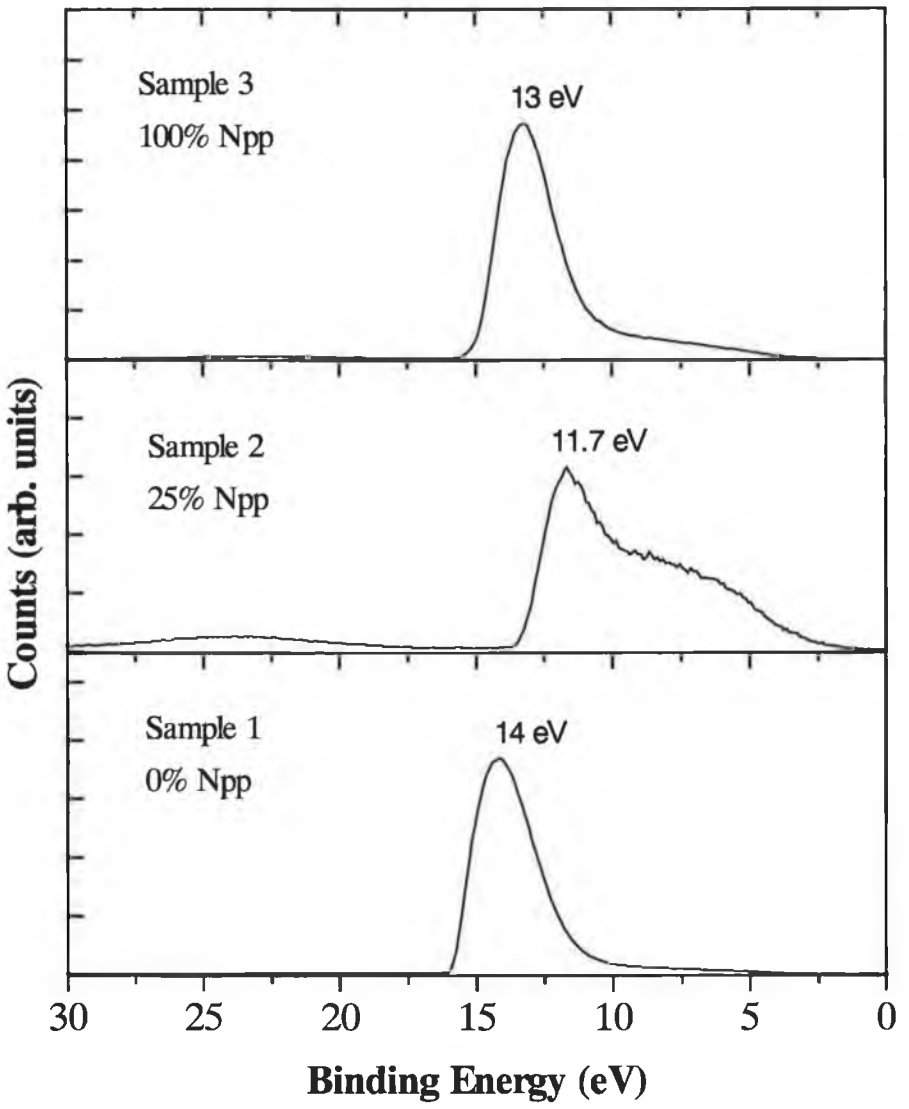

Figure 6.8: UPS valence band of carbon nitride films deposited at different nitrogen partial pressures.

The measured UPS VB spectra display basically a very prominent peak in the 13-15 eV region for samples 1 and 3, and a leading shoulder starting at about 10-12 eV. These two features are typically observed in amorphous materials but at much lower binding energies (7.5 and 4 eV) and are related to the p-σ and p-π contributions to the DOS respectively.[12] In sample 2, the prominent peak visible in the other two samples

is absent, but the low energy region structure becomes more significant. The intensity of the spectra for sample 2 was much lower than for the other two samples. The hint of a kink at 23 eV is reminiscent of the mixed s and p character present in graphite and diamond.

Mansour et al.[12] decomposed the UPS VB spectra of nitrogen-containing diamond-like films obtained from a He II source into p-π and p-σ bands, suggesting that carbon structure becomes more graphitic as the nitrogen content in the films increases. They observed no obvious nitrogen-related features in the VB spectra. The UPS VB of hydrogenated a-CN_x films obtained using a He II source was also investigated by Bhattacharyya et al.[13] They decomposed the VB into p-π, p-σ, a mixture of s-p and 2s bands. The intensity of the p-π band was observed to increase as the films become more sp^2 bonded with the addition of nitrogen, and hence more graphite-like and more conductive. Souto et al.[6] assigned a band located at 4.5 eV to lone-pair electrons belonging to N atoms and N and C were assumed to form a structure similar to crystalline carbon nitride, where C is sp^3 hybridised.

The UPS VB spectra of the three films investigated were deconvoluted using a Gaussian fit as shown in *figure 6.9*. The same considerations apply to deconvolution of the UPS peaks as to XPS. The measured UPS spectrum has been adjusted for the work function of the films by setting the valence band edge to 0 eV energy since the bandgap in carbon films similar to these is effectively zero.[14] *Table 6.1* shows the evolution of the peak positions and heights for the XPS and UPS VB spectra. The heights of the peaks obtained using the two techniques cannot be directly compared because of the different ionisation cross-section of the states to x-rays and ultraviolet radiation. However, it is expected to find similar features although the spectra look different and the trends in behaviour in both cases can be identified.

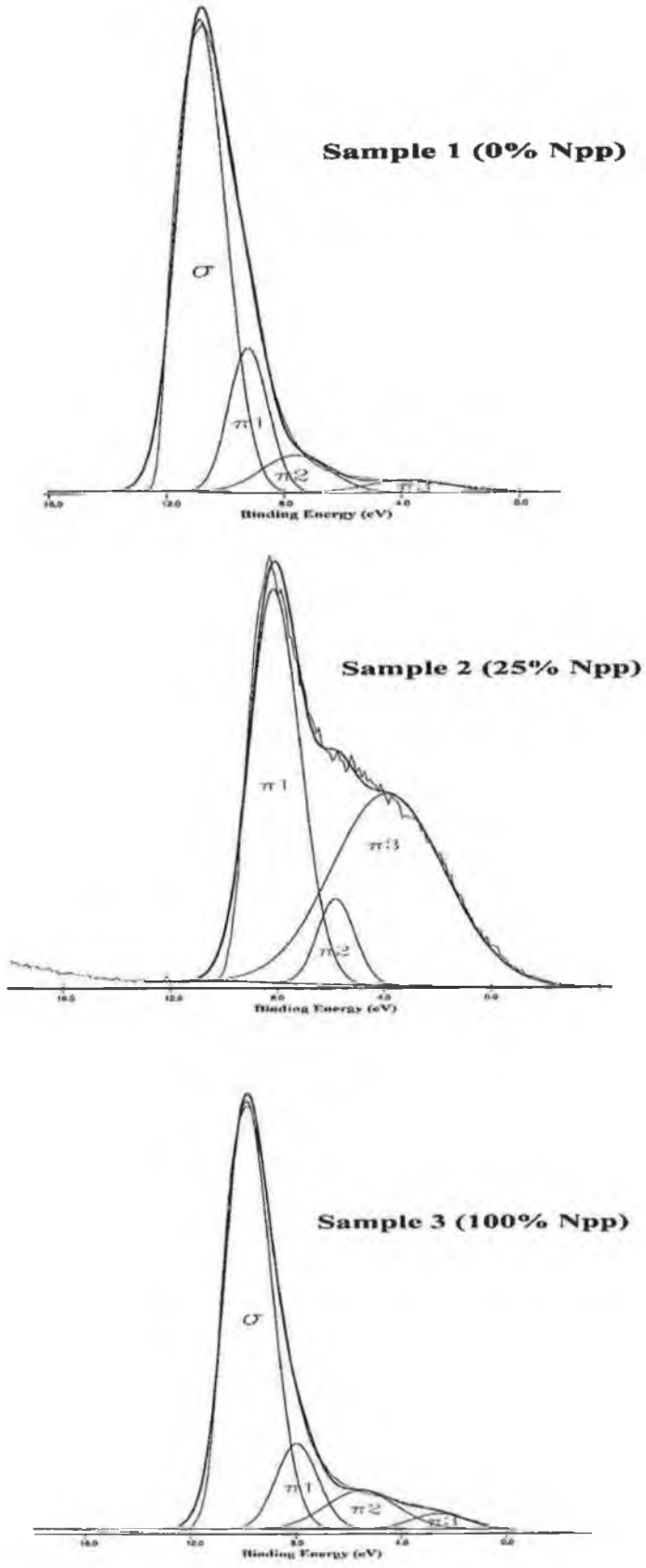

Figure 6.9: Deconvoluted UPS VB spectra of carbon nitride films grown at 0, 25 and 100% Npp.

N_2 partial pressure		σ peak	π_1	π_2	π_3	area(σ) + Σarea(π)
0% (Sample 1)	XPS	9.8	-	5.1	2.7	1.1
	UPS	9.7	7.8	5.5	2.6	2.8
25% (Sample 2)	XPS	9.5	7.3	5.4	2.3	0.5
	UPS	-	8.0	5.8	3.8	0
100% (Sample 3)	XPS	10.3	-	5.7	-	2.2
	UPS	10.7	9.2	7.6	3.7	2.4

Table 6.1: Position of Gaussian peaks deconvoluted from XPS and UPS spectra and relative area of σ to π peaks.

The π bands are associated with p electrons shared in π graphite-like bonds at sp^2 sites. It can be seen that the intensity of the π region is much higher for sample 2. According to the investigations mentioned, this region is due to C 2p and N 2p electrons associated to π bonds in aromatic rings containing at least one substitutional N atom. The larger π peak, called π1, at ~8 eV is probably due to C=C π bond in aromatic rings, although it is occurring at a higher binding energy than that calculated by Souto et al.[6] in un-nitrogenated films. The smaller π peak, called π2, at ~5.5 eV is due to other π bond configurations, perhaps those which occur in sp bonded C atoms involving N 2p electrons. There is also evidence of a small peak, π3, at ~2.6 eV whose origin is not clear but may be due to lone-pair electrons from some residual nitrogen in the films. The presence of the later peaks in sample 1 is due to residual nitrogen incorporation (~4 at.% N).

Both the XPS and UPS show a similar trend as the N_2 partial pressure is increased from 0 to 100%. In the XPS spectrum of sample 1, aside from the peaks due to s-p electrons, there is a peak at 9.8 eV (σ) and a π peak, probably π2, at 5.1 eV. There is also a suggestion of a π3 peak at 2.7 eV as is found in UPS. In both XPS and UPS spectra of sample 1, the area of the σ peak is larger than the sum of the areas of the π peaks. Uncertainties in determining the exact position of the Fermi level may account for small shifts between the spectra.

The spectra of sample 2 (25% Npp) show significant differences. In both UPS and XPS the π peaks are much larger than the σ peak, indeed in the UPS the σ peak disappears. The π peaks in the UPS are resolvable into three components. By comparison with theoretical calculations,[8] the π3 peak may be due to lone pair electrons on N atoms which are bonded to C atoms in a non-doping configuration such as C≡N or a pyridine-like arrangement.[15] Similar behaviour is seen in the XPS peaks where the π peaks increase greatly and there is a split in the low energy part showing greater evidence of a π2 and π3 component.

With a 100% N_2 atmosphere (sample 3), although there is very little change in the N concentration in the films, there is a major change in the bonding. The σ peak again becomes large, the σ to π ratio becomes comparable or larger than in the case where there is no nitrogen, and in UPS the π2 and π3 peaks due to lone pair electrons and sp bonding electrons decrease indicating a relative reduction in the sp and sp^2 bonding and therefore an increase in the sp^3 fraction. This is also echoed in the XPS data. The peak positions also show a shift to higher binding energy as the nitrogen content increases, behaviour which was predicted from theoretical calculations.[6]

The results indicate that at 100% Npp, the film becomes again less graphitic, with less electrons shared in π bonds. Above 25% Npp, nitrogen is not substituting C in aromatic graphite-like rings, but is mainly incorporated as N-N planar aromatic rings (nitrogen saturation) and probably C-N sp^3 bonds. The formation of these bonds explains the higher σ band intensity with respect to the π bands.

The σ peak in the UPS spectra is associated with C-N and C-C σ states, but is normally found in literature at lower binding energies (~11-7 eV).[6,13] The increase of the π bands from sample 1 to sample 2 could be explained as follows: up to 25% Npp, N atoms form hybridised bonds with C (mainly C=N and C≡N) and substitute for C atoms in a planar position within a graphitic-like structure. This is causing an increase in the π bonding seen in XPS and UPS. The position of both π and σ bands are found to vary indicating a strong change in the structure of the samples. Up to 25% Npp, the role of nitrogen is to substitute carbon in aromatic rings forming mainly double bonds

in a non-doping configuration such as in pyridine. Above 25% Npp, the creation of C=N bonds gets saturated. There is an increase of N-N bonds and at increased levels of Npp, the formation of tetrahedral configuration of C-C and C-N (σ bonding) increases. That is why the σ band increases with respect to the π band in the XPS and UPS VB spectra. To summarise, at low Npp levels, nitrogen breaks the symmetry of the carbon aromatic ring structure, forming mainly C=N and C≡N hence increasing the π bonding. At Npp=100%, nitrogen disrupts the aromatic ring structure and facilitates a more three dimensional network which helps the formation of sp^3 bonds.

6.4 Electron spin resonance spectroscopy (ESR)

When an atom or molecule with an unpaired electron is placed in a magnetic field, the spin of the unpaired electrons can align either in the same direction or in opposite direction as the field. ESR measures the absorption of microwave radiation by an unpaired electron when it is placed in a strong magnetic field. Thus, the sample of interest is placed in a static magnetic field, and is irradiated with microwave radiation. The magnetic component of the microwave radiation will interact with the molecules containing magnetic dipoles, and magnetic dipole transitions will occur at one or more characteristic frequencies. Magnetic dipoles attributable to electrons arise from net spin angular momenta. Resonant absorption of radiation in a static magnetic field is called "paramagnetic resonance" or "electron spin resonance". Examples of systems with net electron spin momentum are free radicals, point defects in solids and transition-metal complexes.

The magnetic dipole moment μ is defined by the expression

$$W = -\underline{\mu} \,.\, \underline{H} = -\mu H \cos(\mu,H)$$

Here, W is the energy of the magnetic dipole of moment μ in a field H, and (μ,H) represents the angle between μ and H. Proper interpretation of ESR spectra requires quantum mechanic topics.[16] Transitions between two energy levels induced by an electromagnetic field of the appropriate frequency ν occurs if the photon energy hν matches the energy level separation ΔW. Then

$$\Delta W = h\nu = g\beta H_r,$$

H_r is the magnetic field at which the resonance condition is met; g is the gyromagnetic tensor and β is called the Bohr magneton. For a free electron g = 2.0032; different systems show deviation of this value, and could be sufficiently distinctive so as to provide a reasonable identification of the paramagnetic species involved. The g value, also called the resonance factor, is a function of the field orientation relative to crystal or molecular axes.

For comparison, ESR has been studied in amorphous silicon (a-Si) for many years, long before the introduction of hydrogen to reduce the spin signal. Typically, a-Si exhibits ESR spin densities of $\geq 10^{18}$ cm^{-3}, which have usually been attributed to Si dangling bonds. When hydrogen is added to the films, the spin densities go down dramatically to produce a-Si:H containing spin densities of $\leq 10^{15}$ cm^{-3}. The derivative of the ESR absorption has an almost symmetrical Lorentzian-Gaussian shape, with an asymmetric tail at lower fields and a g-value of 2.0055.[17] The high defect density in a-Si prevents the films from being doped substitutionally. The conductivity of a-Si:H has been shown to decrease rapidly with increasing spin density, where the electron life times are controlled by a fast recombination center that has an ESR signal at g = 2.0055. In a-C:H, a similar situation occurs where carbon dangling bonds are satisfied by hydrogen incorporation.[18] In a-C:N:H, the defect density was found to decrease upon nitrogenation, and the resistivity also increased.[19] This was explained by an increase in structural order, which will decrease the density of defects that generate free carriers, dangling bonds and unpaired electrons. However, N has also been found to decrease the resistivity of a-C:N:H with high defect densities ($\sim 10^{20}$ cm^{-3}) by increasing aromatic clusters rather than by a doping effect.[20]

ESR measurements were made at room temperature using 100kHz field modulation, a microwave frequency of about 9.9GHz and a TM_{110} mode cavity. The modulation amplitude and microwave power were kept low enough to avoid distortion of the signal. The magnetic field was calibrated using a proton NMR probe and a g-marker was also used. Spin populations were determined by comparing the integrated area of

the signal with that of a standard Varian sample of pitch in KCl; the spin populations (and average spin concentrations) are estimated to be correct within a factor of 2 but their relative values are correct to within about ± 20%.

Figure 6.10 shows how changing the nitrogen partial pressure affects the ESR spectrum (the derivative of the ESR absorption). The spectrum of the nitrogen free sample is asymmetric; it has a zero-crossing g value of 2.0055 ± 0.0002 and peak-to-peak linewidth of 0.55 ± 0.05mT. Increasing the Npp to 50% leaves the spectrum shape, width and g value unchanged within error but as *figure 6.11a* shows, the spin concentration drops from $2.6\times10^{18}cm^{-3}$ for the nitrogen free film to $2.1\times10^{17}cm^{-3}$. However, as *figures 6.10* and *6.11b* show, the spectrum shape, width and zero crossing g value all change as the Npp is increased from 50 to 75 and to 100%. The line shape becomes more nearly symmetrical and the g value steadily decreases to 2.0027 ± 0.0002 at the 100% value. The peak-to-peak linewidth has values of 1.09 ± 0.08mT and 0.60 ± 0.04mT at Npp values of 75% and 100% respectively. *Figure 6.11a* shows that the spin concentration rises as Npp is increased above 50% and reaches $2.0\times10^{18}cm^{-3}$ at Npp = 100%.

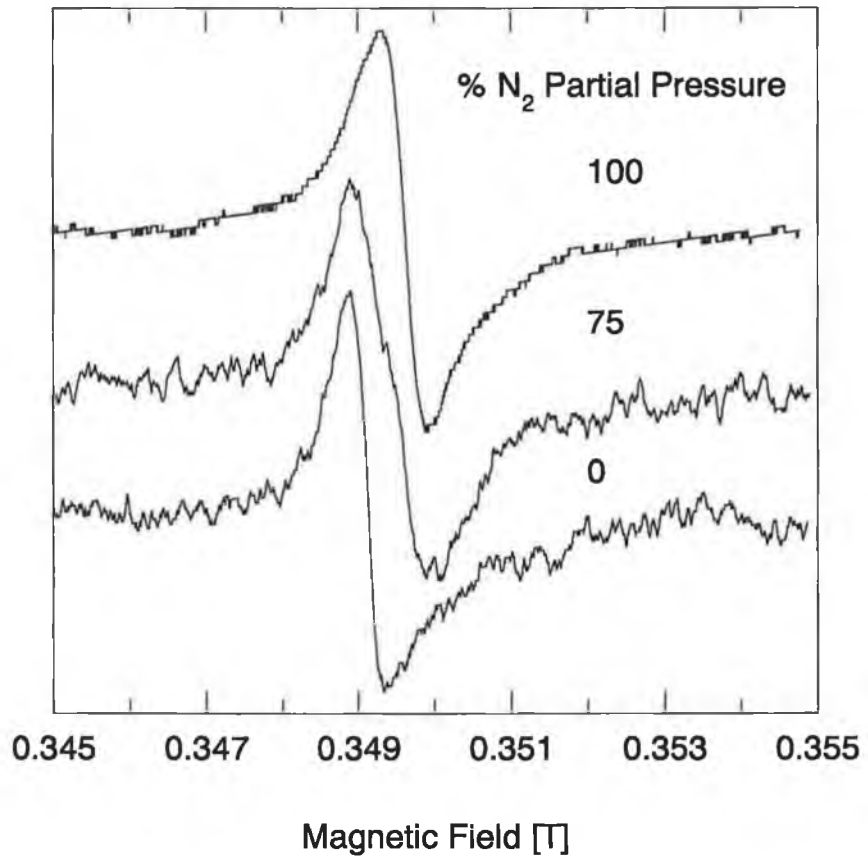

Figure 6.10: ESR spectra of carbon nitride films grown at different Npp.

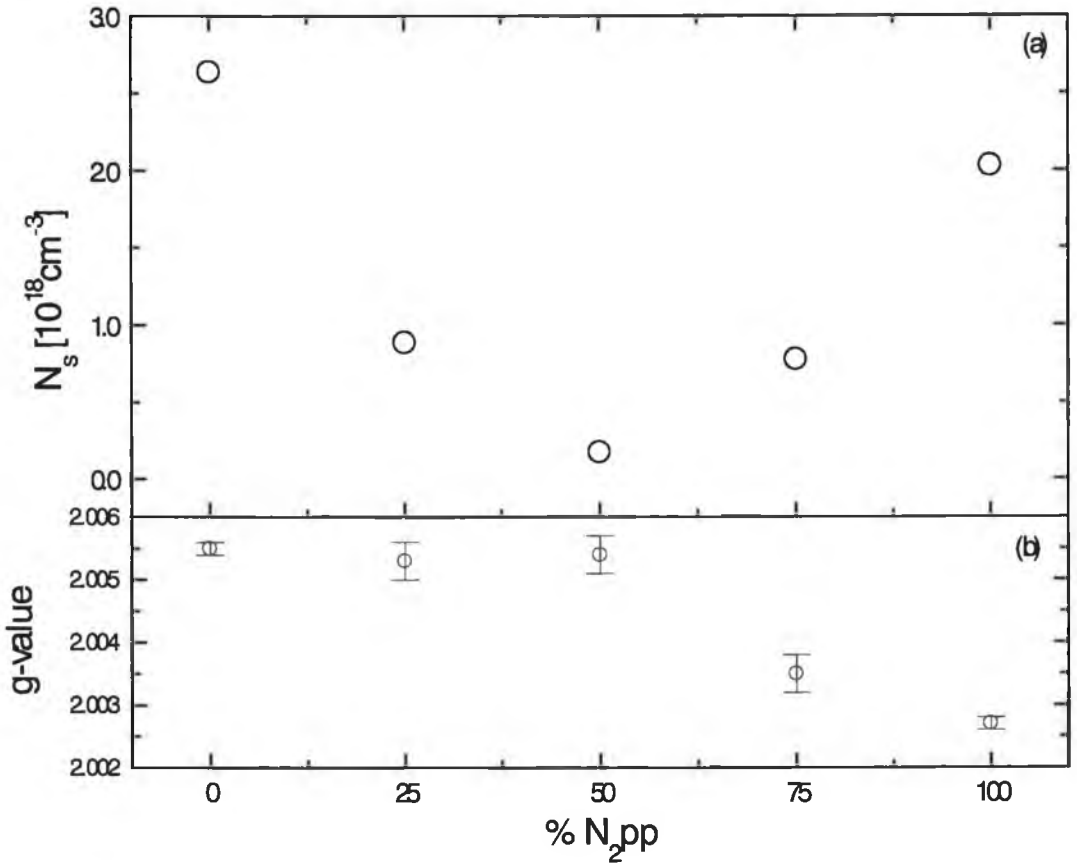

Figure 6.11: Spin concentration and g values as a function of N_2 partial pressure.

These results give rise to several questions - What paramagnetic species give rise to the spectra and why do both the spectra and spin concentration vary with Npp as shown?. The g value of 2.0027 ± 0.0002 and symmetric shape of the spectrum for the Npp = 100% sample are characteristic of the signal frequently reported for a-C:H, ta-C and other forms of carbon[15,21,22] and attributed to an unpaired electron from carbon which is to a greater or lesser extent delocalized. On the other hand, the spectrum of the Npp = 0% sample is very unusual for a-C. Since this sample is graphite-like it is relevant to consider the ESR signal for graphite which is attributed to the conduction electrons and is characterised by a g tensor of axial symmetry with $g_\perp = 2.0026$ and $g_{||} > g_\perp$ with axis parallel to the c-axis.[23] This, however, does not explain the spectrum obtained here, which, if it were to be a powder pattern of centres with an axial g tensor, would correspond to $g_{||} < g_\perp$. Another possibility is that the asymmetry is associated with the high conductivity of the sample. Graphite crystals 0.1 mm thick were observed to give a Dysonian shaped signal.[22] However, the skin depth of the Npp

= 0% sample with resistivity 0.3 Ωcm is 0.28 mm at 9.9 GHz - much greater than the thickness of the film (8×10^{-5} mm), so this explanation is not plausible either. A third possibility is that the spectrum is the superposition of 2 lines - one arising from paramagnetic centres in the film and another from those in the silicon substrate or at its surface. The latter may be Si dangling bonds produced during the initial stages of film deposition; these usually give a symmetric line with g = 2.0055. As regards the variation with Npp of the spin concentration, the initial drop may arise by replacement of a C atom in a dangling bond site by a N atom in a pyridine-like; this situation is similar to the pasivation of silicon dangling bonds in a-Si by the introduction of hydrogen. The dangling bonds associated with C atoms are also being bonded to N as C≡N; these two N bonding configurations leave the N atom with a lone pair of electrons with antiparallel spins and so do not give an ESR signal. The spins in the film come from sp^2 defects with a g value of about 2.003. Upon nitrogenation, these defects are healed and consequently, their density decreases. The subsequent rise in spin concentration, when Npp exceeds 50%, is related to the structural rearrangement referred to before, where it was seen that the nature of nitrogen incorporation changes. This is caused either by the nitrogen entering the structure in a doping configuration which must therefore be part of an extended structure[15] or in a non-doping configuration other than C≡N which does not terminate the carbon bonds. With Npp > 50%, sp^3 bonding within the film is favoured and N-N and C-N bonds are created, as discussed before.

It is a difficult task to find an interrelationship between structure and spin density in amorphous carbon nitride films. Variation of spin density can be used to identify defect centres, whereas a change in the optical gap confirms the structural variation. Nitrogenated carbon films studied by Bhattacharyya et al.[24] exhibit a decrease of the optical gap with nitrogen content which is accompanied by a decrease in spin density, except at high nitrogen concentrations. This modifies the structure of the material. The decrease in spin density observed here is also accompanied by a decrease in the optical gap. For high nitrogen partial pressures (> 50%), this similarity still holds and the spin density increases while the optical gap starts increasing slightly as will be seen in chapter 7.

Is not trivial to estimate where in the middle of the gap the defects are located. A decrease in the optical gap was observed for the carbon nitride films. In an energy band diagram suggested in chapter 7, the defects are distributed between tail states appended to extended states as well as at the middle of the band gap. Silva et al.[15] found a rapid decrease in spin density from $4x10^{20}$ cm^{-3} to values below 10^{18} cm^{-3} with increasing nitrogen content in their a-C:H:N films. They mentioned two possible reasons: either the total defect density has decreased, or the defects have been converted from their paramagnetic to diamagnetic configuration by the transfer of electrons from N sites. The diamagnetic defects are expected in the presence of dopants, because the donor electrons will fall down from the donor level into the singly occupied defect level and make it fully occupied and diamagnetic. Care has to be taken when comparing the carbon nitride films investigated here with Silva's work and some others mentioned where in most cases the presence of hydrogen has a dramatic effect on the behaviour of carbon nitride films when doped and also on the density of the dangling bonds. Here, no doping effect was found when increasing N content. On the other hand, the total defect density has also been correlated with the network disorder and Urbach slope, as occurs in a-Si:H.[17] The slight decrease in slope seen in chapter 7 suggest that at least part of the decrease in spin density is due to a decrease in the total defect density.

Demichelis et al.[25] deposited amorphous carbon nitride films, in which the spin density decreased with nitrogen partial pressure. They proposed that the ESR active centres sit near the border of the sp^2 clusters, and that N is expected to stabilise the sp^3 phase and to reduce the size and number of sp^2 clusters. N reduces the amount of the disordered part of the sp^2 phase (probably increasing sp^3) with respect to the ordered sp^2 phase. Therefore, the ESR signal arises from the disordered sp^2 phase. They also found an increase in the band gap. In the films deposited here, the picture is different and more complicated. Initially (up to 50% Npp), N substitutes C in aromatic rings, and is causing a decrease of the spin density as explained before. Then, for Npp > 50%, N is found bonded to itself and probably to sp^3-C and dangling bonds are created (the band gap increases slightly). At Npp=100%, a complex overall structure results

which gives rise to an increased number of dangling bonds at the edges of the aromatic rings which causes an increase in the spin density.

An increase in negative bias reduces the spin density of the films, as shown in *figure 6.12*. On the other hand, *figure 6.13* shows the peak-to-peak linewidth, which increases substrate bias. Results given in previous chapters showed that increasing negative bias produces films with a more extended carbon network with less terminating sites. A plausible explanation is that due to the increased bias, the carriers (associated with spin) become more mobile. Therefore, the relaxation time τ is reduced. The relaxation time is inversely proportional to the ESR linewidth ΔB_{pp} ($\tau=C/\Delta B_{pp}$).[24] As seen in *figure 6.13*, ΔB_{pp}, which is the peak-to-peak linewidth, increases with bias which is compatible with the decrease in relaxation time and the decrease in the resistivity of the films with substrate bias as will be seen in chapter 7.

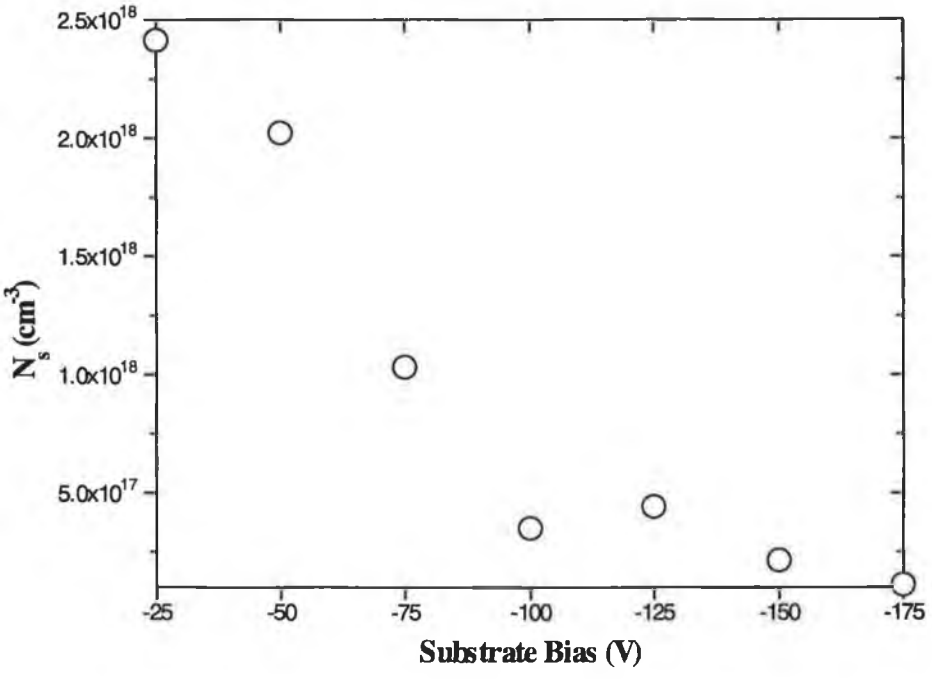

Figure 6.12: Spin density as a function of substrate bias.

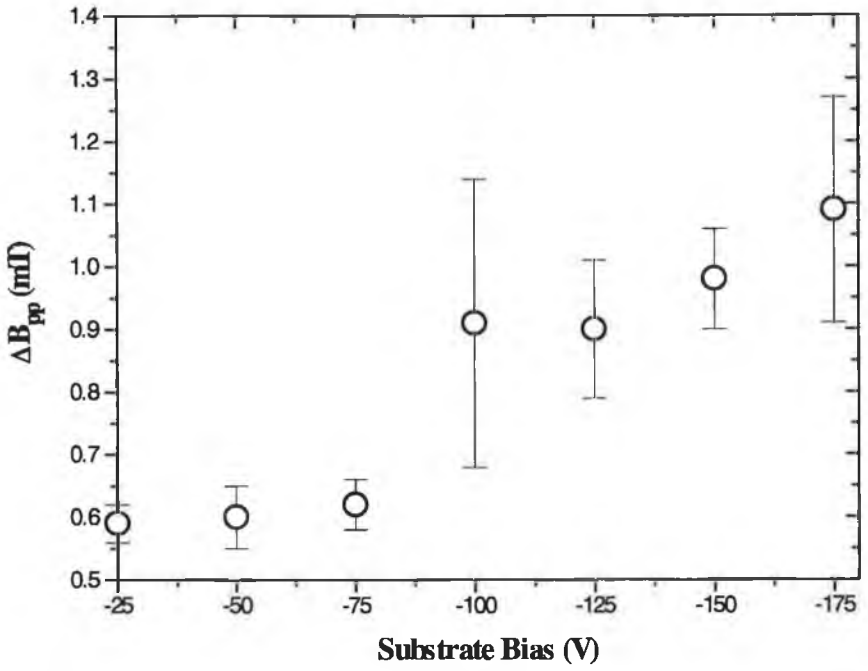

Figure 6.13: ESR linewidth as a function of substrate bias.

6.5 Electron energy loss spectroscopy (EELS)

Electron energy loss spectroscopy (EELS) is the study of the energy distribution of electrons, which have interacted with a specimen. The basic two components in an EELS experiment are a source of electrons and a device (the spectrometer) for analysing the scattered electrons.[26] The portion of the spectrum extending from the edge of the zero-loss peak out to about 50 eV is usually called the "low-loss" region. The energy losses in this region are due to interactions in which valence or conduction electrons are excited. The best known of these events is the "plasmon" excitation. Plasmon excitations occur in metal and alloys, which have a large number of free electrons. A fast electron incident on the sample disturbs the equilibrium of the "gas" of electrons, which is set into oscillation. Because many valence electrons are involved this is known as a "collective excitation". The frequency of the oscillation w_p is proportional to $(n_E)^{1/2}$ where n_E is the density of free electrons involved in the oscillation.[25] To generate an oscillation requires an energy $E_p = hw_p$ where h is the

Planck's constant, so the incident electron suffers an energy loss of E_p (plasmon energy) if it excites a plasmon.

The plasmon peaks of carbon appear in the low-energy region of the EELS spectra at different energies for different forms of carbon, as shown in *figure 6.14*.[27] Two prominent peaks have been found in the EELS spectrum of graphite at 6-7 eV (P1) and 29 eV (P2/P3). The lower energy peak corresponds to plasma oscillations in which one π electron having the sp^2 hybrid orbital is involved. The higher energy $\pi+\sigma$ peak arises from all valence electrons per atom, which include the three σ electrons of the strong coplanar bonds joining a carbon atom to its three neighbours within the layer. Owing to the high electron density in diamond, the four valence electrons plasmon energy becomes larger (34.4 eV). The plasmon peak of diamond-like carbon (DLC) is observed at 28 eV. Therefore, the positions of these plasmon peaks of valence electrons have been found to be a characteristic parameter of carbon structure. The spectra for CN films obtained by Lopez et al.[27] are also shown. It can be seen that the plasmon structure is similar to DLC but shifted to lower energies (~24 eV). The EELS spectra of dc sputtered carbon is quite similar to that of graphite, except for the 6-7 eV peak, which is less pronounced in the carbon film. EELS studies of carbon films have been involved only with the valence excitation, i.e., the low-energy loss spectra with a major plasmon peak at an energy lower than the $\pi+\sigma$ loss of graphite, and with a π loss peak much weaker or absent.[28]

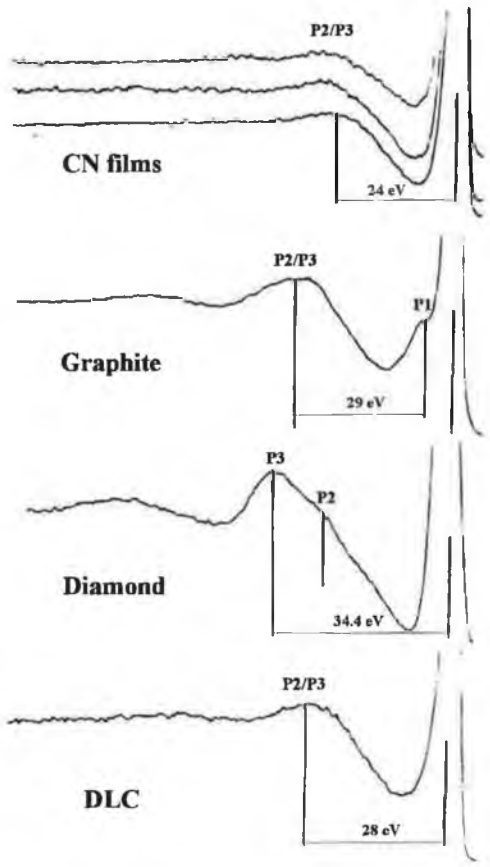

Figure 6.14: Plasmon loss structure of carbon nitride, diamond, graphite and amorphous carbon.

The EELS spectra of carbon nitride films studied in this work might provide some clues to the structural characterization. EELS spectra for three carbon nitride films grown at 0, 25 and 100% Npp were investigated. Samples were run at excitation/e-beam energies of ~3000 V, ~1000 V and 120 V. Data was recorded on Kratos XSAM-600 using VSW EG5 0-5kV e-gun. The elastic line is clearly identifiable in each plot and the position of the bands of interest can be interpolated from the energy scales of the resulting plots. The structure seen does not really depend on the excitation energy. The spectra with the best signal to noise ratio were selected and the "zero" position was taken as the apparent centre of the elastic peak.

The EELS spectra of carbon nitride films are shown in *figure 6.15*. The spectra exhibits two main features: a small peak at about 6.5 eV, corresponding to the $\pi \rightarrow \pi^*$ transition and an intense and very broad peak in the region of the $\pi+\sigma$ plasmon energy

E_p with a maximum between 23 and 25 eV. The presence of the former peak manifests sp^2 sites in the amorphous carbon network.[29] The later peak is much better defined and sharper for the 25% Npp sample, while the observed loss signals for the other two samples are rather poorly defined. The results indicate a change of the structure of the films, as also seen with the previous techniques, when the Npp is increased from 25 to 100%. There is no significance difference in the plasmon energies for the samples analysed. The position of the peak at ~24 eV and the loss features are very similar to those found by other workers[30,31] consistent with a high proportion of sp^2 bonding. The shape of the spectrum for the sample grown at 25% Npp is somewhat different, more similar to graphite than for the other two samples, probably indicating a higher sp^2 content. Carbon nitride films are known to be amorphous and the EELS spectra presented here testify to this.

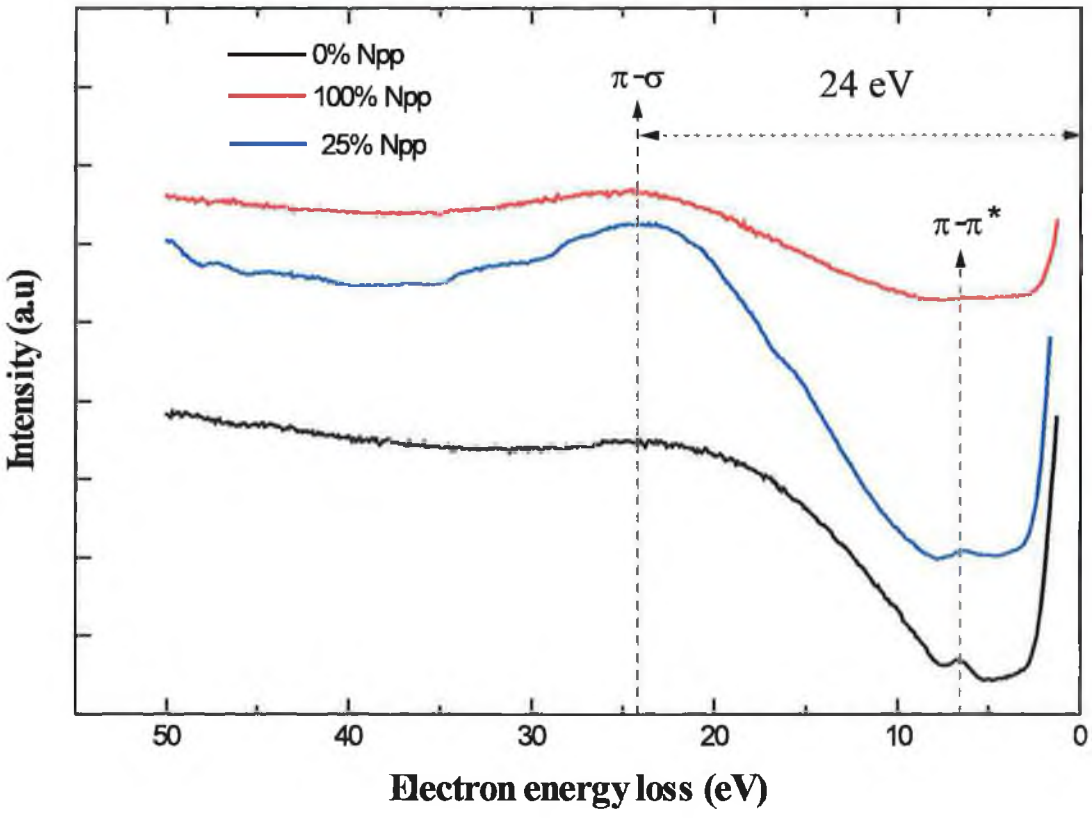

Figure 6.15: Plasmon loss features in the EELS spectra of carbon nitride films deposited at 0, 50 and 100% Npp.

The plasmon oscillation w_p is expected to correlate with the effective concentration of electrons participating in the plasma resonance using the Drude model, where the plasmon pulsation (w_p) is described by the following equation (in Gaussian units):[24]

$$w_p^2 = \frac{4\pi e^2}{m} n_e \qquad (1)$$

where e and m are the charge and mass of an electron and n_e is the density of electrons. The plasmon pulsation (w_p) is related to the plasmon energy (E_p) by $E_p = (h/2\pi)w_p$ (2), where h is the Planck's constant. The density of valence electrons can be calculated from the $\pi+\sigma$ peak position since the energy loss (> 20 eV) is much greater than an electron interband transition energy.[32] For the samples investigated here, locating the $\pi+\sigma$ loss peak position accurately is difficult since the signal/noise ratio is poor. However, the maximum of the peak for the samples analysed could be located at 24 eV, as seen in *figure 6.15*. Assuming E_p=24 eV and using equations (1) and (2), a valence-band density of ~4.2×10^{23} cm^{-3} was calculated. Furthermore, the valence electron density (n_E) is related to the mass density (ρ) and the nitrogen content (x) according to:[12]

$$n_E = \rho(n_C + xn_N/A_C + xA_N)L_A \qquad (3)$$

where L_A is Avogadro's number, A_C (=12) and A_N (=14) are the atomic weights of C and N, respectively, and n_C (=4) and n_N (=5) are the number of valence electrons of C and N, respectively. The density of the films was estimated to be 2.07 g/cm^3 for the nitrogen-free sample, and 2.03-2.04 g/cm^3 for the nitrogen-containing samples. This value is typical of DLC films and coincides with the lower limit of the accepted range of values of hard a-C:H, as opposed to soft polymeric films with density values ranging from 0.9 to 1.6 g/cm^3.[12]

The mass density (ρ) was determined from the density of valence electrons and the concentration of carbon and nitrogen. However, since nitrogen has more valence electrons than carbon and the plasmon energy is proportional to the square root of

electron density, the nitrogen containing samples for the same atom density should have higher plasmon energies.[33] Therefore, the similar plasmon energy assumed here for samples with and without nitrogen indicates that the nitrogen rich films consists of a lower density network than a-C, as it was found, even though the difference was very small.

The π-π^* plasmon peak intensity was found to vary with excitation energy in an irregular manner, therefore it is dificult to say whether the intensity or the position of the π-π^* plasmon peak changes significantly to signature any change in sp^2 bonds. The peak at about 6.5 eV has been found to arise from π electrons of either aromatic carbon rings or graphitic constituents.[34] In carbon nitride films, an increase of this peak signals the enhancement of π-bonded electrons.[35] The slight broadening of the π-π^* loss peak observed in the 25% Npp sample film indicates a larger spread of π states, and maybe the presence of several cluster sizes.[29] The shape of the spectrum resembles more that of graphite, so that an increase in the graphitic phase would be consistent with the changes observed in the π-related features of the valence band. At 100% Npp, the spectrum resembles more the one observed for the film grown at 0% Npp. EELS data confirms the similarity between the 0 and 100% Npp films and the difference of the 25% Npp films which show both a broader π-π^* peak and a much larger π-σ peak which would also indicate a higher density of π states.

6.6 Summary

A general overview of the photoemission process in solids has been given. This has served to introduce techniques such as XPS and UPS which are used to investigate the valence band (VB) spectra of solids. Changes in the valence band structure were reported for carbon nitride films deposited by Penning type DC magnetron sputtering as the N_2 partial pressure (Npp) is increased from 0 to 100% while keeping other parameters unchanged. The VB spectra suggest an interlinked carbon backbone nature, which is significantly different from diamond-like and graphitic features.

It has been shown that the bonding structure varies greatly with changes in the Npp, even though this results in very little difference in the nitrogen content of the films. Carbon nitride films shows reduced sp^3 type bonding with increasing in nitrogen content which then increases as the Npp is further increased. As Npp is increased from 0 to 25% the ratio of π to σ bonding becomes very large and there is evidence from XPS and UPS that the nitrogen bonds in an sp configuration with lone pair electrons on the N atom. At high Npp the N bonding changes and the σ to π ratio increases markedly indicating that there is much more of an sp^3 bonding nature in the films.

The effects of substrate bias during deposition on the VB have also been investigated. It was shown that the VB spectrum is more characteristic of a 'diamond-like' material at substrate bias between -75 and -150 V. It is therefore concluded that ion bombardment in this range causes a process of 'densification' or 'stress induction' which maximises the carbon sp^3 bonding, similar to that which occurs in carbon films.

Variations in the electron spin density are also seen to vary in conjunction with changes in Npp. ESR data indicates that when the Npp is increased to 50%, the spin density shows a consistent decrease which again concurs with the idea of the N bonding to C in C=N and C≡N non-doping configurations. This has the effect of reducing the number of unpaired electrons because of the termination of the carbon dangling bonds with nitrogen atoms; this situation is similar to the pasivation of silicon dangling bonds in a-Si by the introduction of hydrogen. Above 50% Npp, sp^3 bonding is favoured and the spin density starts to increase. The spin density reduces with negative bias which produces films with a more extended carbon network with less terminating sites.

EELS studies of carbon nitride films deposited at different Npp confirm the increase in sp^3 bonding for the films grown at 100% Npp with respect to the ones grown at 25% Npp. From the EELS spectra, the mass density values of the films were estimated to be between 2 and 2.1 g/cm^3.

The data obtained for the electronic states of carbon nitride films as investigated by XPS, UPS, ESR and EELS shows that with high nitrogen partial pressures the growth process is significantly changed; the absence of Ar^+ ions or energetic neutrals which are considerably heavier than N_2^+ ions may be less disruptive of the growth process whereby the nitrogen and carbon bond together.

These results show that under the deposition conditions described in chapter 4 the production of β-C_3N_4 crystalline phase is more likely to occur i.e. when a sputtering gas containing 100% N_2 is used rather than an Ar/N_2 mixture.

References

1. B.O. Seraphin, Optical properties of solids: new developments, North-Holland publishing Co. NY (1976).
2. M. Cardona and L. Ley, Photoemission in solids, (Topics in applied physics; v. 26-27) Springer-Verlag Berlin, NY (1943).
3. F.R. McFeely, S.P. Kowalczyk, L.Ley, R.G. Cavell, R.A. Pollak and D.A. Shirley, Phys. Rev. B, 9, 12 (1974) 5268.
4. W.M. Lau, L.J. Huang, I. Bello, and Y.M. Yiu, J. Appl. Phys. 75 (1994) 3385.
5. D. Briggs, M.P. Seah, Practical Surface Analysis by Auger and X-ray Photoelectron Spectroscopy, Wiley, NY (1983) 365.
6. S. Souto, M. Pickholz, M.C. dos Santos and F. Alvarez, Phys. Rev. B 57 (1998) 2536.
7. P. Hammer, N.M. Victoria and F. Alvarez, J. Vac. Sci. Technol. A 16 (1998) 2941.
8. M.C. dos Santos and F. Alvarez, Phys. Rev. B 58 (1998) 13918.
9. S. C. Sharma, M. Green, R. C. Hyer, C. A. Dark, T. D. Black, A. R. Chourasia, D. R. Chopra and K. K. Mishra, J. Mater. Res. 5 (1990) 2424.
10. C.A. Davis, Thin Solid Films, 226 (1993) 30.
11. D. R. McKenzie, D. Muller and B. A. Pailthorpe, Phys. Rev. Lett. 67 (1991) 773.
12. A. Mansour and D. Ugolini, Phys. Rev. B 47 (1993) 10201.
13. S. Bhattacharyya, C. Cardinaud and G. Turban, J. Appl. Phys. 83 (1998) 4491.

14. J. Robertson and E. P. O'Reilly, Phys. Rev. B, 35 (1987) 2946.
15. S. R. P. Silva, J. Robertson, G. A. J. Amaratunga, R. Rafferty, M. L. Brown, J. Schwan, D. Franceschini and G. Mariotto. J. Appl. Phys. 81 (1997) 2626.
16. J.E. Wertz, J.R. Bolton, Electron spin resonance: elemental theory and practical applications, McGraw Hill, NY (1972).
17. J.I. Pankove, Semiconductors and semimetals 21 C, Academic Press, SD (1984)
18. R.J. Gambino and J.A. Thompson, Solid State Comms. 34 (1980) 15.
19. S. Lin, K. Noonan, B. J. Feldman, D. Min and M. T. Jones. Solid State Comms. 80 (1991) 101.
20. J. Schwan, V. Batori, S. Ulrich, H. Ehrhardt and S.R.P. Silva, J. Appl. Phys. 84 (1998) 2071.
21. M. Chowalla, J. Robertson, C. W. Chen, S. R. P. Silva, C. A. Davis, G. A. J. Amaratunga and W. I. Milne. J. Appl. Phys. 81 (1997) 139.
22. D.J. Miller and D.R. McKeinze, Thin Solid Films, 108 (1983) 257.
23. G. Wagoner, Phys. Rev. 118, (1960) 647.
24. S. Bhattacharyya, C. Vallee, C. Cardinaud, O. Chauvet and G. Turban, J. Appl. Phys. 85 (1999) 2162.
25. F. Demichelis, X.F. Rong, S. Schreiter, A. Tagliaferro, C. De Martino, Diam. Relat. Mater. 4 (1995) 361.
26. J.J. Hren, J.I. Goldstein and D.C. Joy, Introduction to analytical electron microscopy, Plenum Press, NY (1979).
27. S. Lopez, H.M. Dunlop, M. Benmalek, G. Tourillon, M.-S. Wong and W.D. Sproul, Surface and Interface Analysis, 25 (1997) 827.
28. H-C. Tsai and D.B. Bogy, J. Vac. Sci. Technol. A 5 (1987) 3287.
29. R. Kleber, K. Jung, H. Ehrhardt, I. Muhling, K. Breuer, H. Metz and F. Engelke, Thin Solid Films, 205 (1991) 274.
30. M.A. Baker and P. Hammer, Surface and Interface Analysis, 25 (1997) 629.
31. W. Kulisch, M.P. Delplancke-Ogletree, J. Bulir, M. Jelinek, K. Jurek, J. Zemek and J. Klimovic, Diam. Relat. Mater. 8 (1999) 1039.
32. Y. Wang, H. Chen, R.W. Hoffman and J. C. Angus, J. Mater. Res. 5 (1990) 2378.
33. A.R. Merchant, D.G. McCulloch, D.R. McKeinze, Y. Yin, L. Hall and E. G. Gernster, J. Appl. Phys. 79 (1996) 6914.

34. P. Oelhafen, J.L. Freeouf, J.M. E. Harper and J.J. Cuomo, Thin Solid Films, 120 (1984) 231.

35. F. Fendrich, L. Jastrabik, L. Pajasova, D. Chvostova, L. Soukup and K. Rusnak, Diam. Relat. Mater. 7 (1998) 417.

CHAPTER 7

ELECTRICAL/OPTICAL PROPERTIES OF CARBON NITRIDE

In this chapter, electrical and optical measurements on reactively sputtered carbon nitride films are described in order to investigate film properties such as resistivity, mobility, activation energy, optical gap, absorption coefficient and refractive index. In Part I of this chapter, all the different aspects of the measurement techniques used are described. Regarding resistivity measurements, two different methods are described: four-point probe and van der Pauw structures, as well as a sandwich configuration for tranverse resistivity measurements. In the final section, an account is given of the arrangement employed for temperature-dependent resistivity measurements.

Light can be used to study the nature of solid surfaces because it yields information about the change in optical constants, which arise from a change in atomic bonding in the material. Two light-source tools where used here: ultraviolet/visible spectroscopy and ellipsometry.

Part II deals with the results, as well as a discussion of their significance in relation to the electrical and optical behaviour of the films; electrical and optical properties are then related to the film microstructure. The conclusions that can be drawn from such results are presented. Finally, in part III, an account is given of electron emission experiments of nitrogen containing films performed in a diffusion-pumped system. Electron emission measurements are reported and then compared with materials with good emission characteristics, which have great potential for applications in flat panel displays.

PART I

7.1 MEASUREMENT TECHNIQUES

7.1.1 General considerations

The study of the electrical properties of thin films has been essential since the solid-state revolution, which established new roles for thin film electrical conductors, insulators and devices. Microscopic thin-film based integrated circuit chips are more efficient and reliable than large discrete electrical components. In order to investigate the electrical conduction properties of thin films, one has to start by seeking the nature, magnitude and attributes of the material transport properties such as electrical d.c. resistivity (ρ) and mobility (μ) in the basic equations of current flow through a material. The magnitude of the current density J is given by

$$\underline{J} = nq\underline{\upsilon} \ ,$$

where n is the concentration of carriers, q is the electron charge and ν is the velocity of the charges which for most materials is proportional to the applied electric field E so that

$$\underline{\upsilon} = \mu \underline{E} \ ,$$

where the proportionally constant μ is known as the mobility, and by Ohm's law ($\underline{J} = \sigma \underline{E}$), the conductivity σ is expressed by:

$$\sigma = 1\backslash\rho = nq\mu$$

In order to understand the thin-film behaviour, there are some considerations (enumerated below) to bear in mind, which give thin films unique characteristics:

1. *Size effects*- They are due to the physically small dimensions involved, giving for example surface scattering effects.
2. *Method of film preparation*- Electrical properties of thin films are a strong function of the deposition conditions employed, which give varying structural and electronic defect concentrations, dislocation densities, void content, density, grain morphology, chemical composition and stoichiometry, electron trap densities, etc.
3. *Degree of film continuity*- Conduction mechanisms in discontinuous, island structure films differ from those in continuous films.
4. *Electrode effects*- The metal electrode material employed for electrical measurements influence the electrical response of thin films. Factors such as interfacial adhesion, stress, interdifussion and absorbed impurities alter the charge transport at the interface region.
5. *Conduction at high electric fields*- Moderate voltages applied across very small dimensions make high field effects readily accessible in thin films.

It is also important to consider the various scattering processes that contribute to the total metal film's resistivity (ρ_T) which can be expressed as (Matthiessen's rule):

$$\rho_T = \rho_{th} + \rho_i + \rho_d \qquad (1)$$

where ρ_{th}, ρ_i, ρ_d are the individual thermal, impurity and defect resistivities. Electron collisions with vibrating atoms (phonons) displaced from their equilibrium lattice positions are the source of the thermal (ρ_{th}) contribution, which increases linearly with temperature. Impurity atoms, defects such as vacancies, and grain boundaries locally disrupt the periodic electric potential of the lattice and therefore electrons are effectively scattered. An alternative formulation of (1) in terms of the respective mean free-electron lengths (λ) between collisions has the form:

$$1/\lambda_T = 1/\lambda_{th} + 1/\lambda_i + 1/\lambda_d \qquad (2)$$

which results from the inverse proportionality between ρ and λ, so that $\rho \propto 1/\lambda$. In films of thickness d that are sufficiently thin so that $d<\lambda_T$, the possibility arises that a new source of scattering due to the film surface will increase the measured film

resistivity. Grain boundaries, across which crystal orientations change, also act as effective electron scatterers and therefore, as the crystallite size becomes smaller than the electron mean-free path, the film resistivity increases.

In general, thin metal films are more resistive, while insulating films are more conductive than their respective bulk counterparts. The differences between film and bulk electrical properties are relatively small for the case of metals. In insulators, the difference can be huge.[1] Carbon nitride films produced in this work posses a mainly amorphous structure and their conduction behaviour can be quite different to that occurring in metals and other crystalline materials. The transport properties of the deposited films are related to the bonding structure, the extent of structural disorder and the density of states. The transport properties of the films will be discussed in part II in the light of existing models for electron states in amorphous materials. Extensive reviews of transport properties in amorphous materials may be found in Elliot[2] and Kazmerski.[3]

7.1.2 Thin film resistivity

Several techniques are employed to measure electrical properties of thin films. Electrodes are normally placed on opposite film surfaces for insulating films, where current flows through the film thickness. Small circular electrodes are normally evaporated onto the film, serving as a set of contacts, while the substrate serves as the other contact.

For more conductive films, all electrodes are preferably placed on the same film surface. In these cases, four terminal configurations are used; two of these terminals are used to pass a current through the film and the other two are used to measure the voltage developed. The next two sections give a description of the techniques used for resistivity measurements of the films investigated in this work.

7.1.2.1 Four-point probe technique

Four-point probe methods are the most commonly used for measuring resistivity. The in-line type four-point probe is illustrated in *figure 7.1*. It can be used to measure the resistivity of specimens having a wide variety of shapes, including those with irregular boundaries as well as the resistivity of smaller regions included in a matrix with different electrical properties.

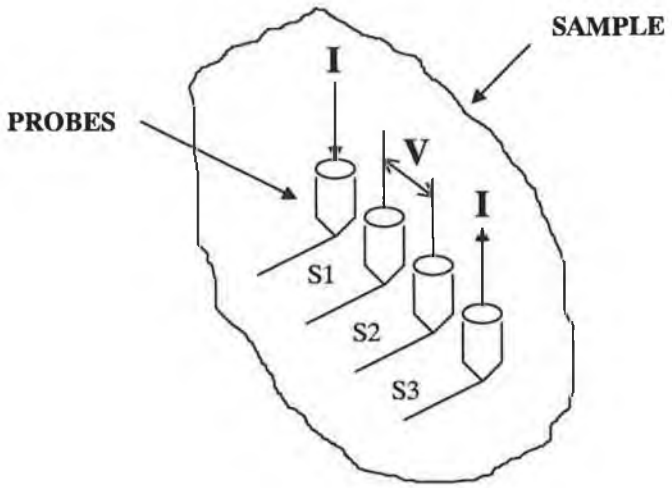

Figure 7.1: In-line four-point probe.

The probe arrangement used for resistivity measurements consists of four pointed equispaced probes in contact with a plane surface of the material to be measured. A current I is passed through the outer probes while the potential difference V is measured between the inner probes, as depicted in *figure 7.1*. For measurements, the probes are considered to be far from any of the other boundaries of the specimen so that the latter may represent an essentially semi-infinite volume of uniform resistivity, which is given by the following relation,[4,5]

$$\rho = \frac{V}{I} \times \frac{2 \times \pi}{\frac{1}{S1} + \frac{1}{S3} - \frac{1}{S1+S2} - \frac{1}{S2+S3}} \quad (1)$$

where S1, S2, and S3 are the separation between the probes, which are normally equally spaced, so that S1=S2=S3=S, and equation (1) becomes:

$$\rho = \frac{V}{I} \times 2 \times \pi \times S \quad (2)$$

The deviation of this formula for the case being discussed is given in Appendix B. If the sample to be measured has a thickness d << S, and is resting on an insulating support, it may be considered as essentially two-dimensional like an infinite sheet having an infinitesimal thickness. In such a case, and if the film is large in extent compared with the probe assembly, equation (2) becomes,[4]

$$\rho = \frac{V}{I} \times \frac{\pi}{\ln 2} \times d = 4.5324 \times d \times \frac{V}{I} \quad (3)$$

For the measurements carried out in this project, a multi-position four-point probe with S=1mm was used. The measurements can be made using either d.c or a.c current. Two different setups were employed. For insulating samples, where the voltage to be measured is going to be very small, a.c current should be used, since the noise accompanying the measured voltage can be almost eliminated by using a lock-in amplifier.

For d.c current, the electrical circuitry used for a four-point probe measurement is very simple and consists only of an ammeter (electrometer), voltmeter and power supply, with a 1KΩ resistance to limit the current, connected as shown in *figure 7.2*.

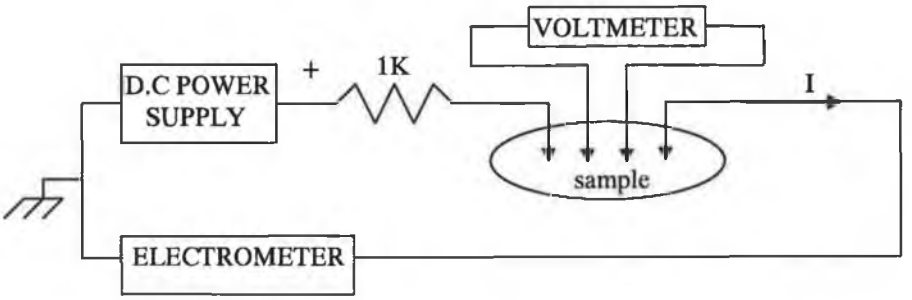

Figure 7.2: Experimental setup for measurements with d.c current.

This arrangement works well for medium and high conductive films. However, for insulating films, the voltage developed between the inner probes can be unmeasurable with a standard voltmeter; for such cases, a simple circuit to buffer the voltage was designed, consisting of four operational amplifiers. Two amplifiers were used to buffer the voltage across a 10 MΩ resistance to calculate the current from the measured voltage and the other two amplifiers were used to buffer the voltage across the inner points of the four-point probe. The circuit schematic for this configuration is given in *figure 7.3a*. The required components for this circuit were mounted in a printed board and enclosed in a box. Some additional components had to be included such as variable resistances (to eliminate the offset of the operational amplifier) and two-way connectors (to connect the circuit to the four-point probe). The resultant printed board is shown in *figure 7.3b*.

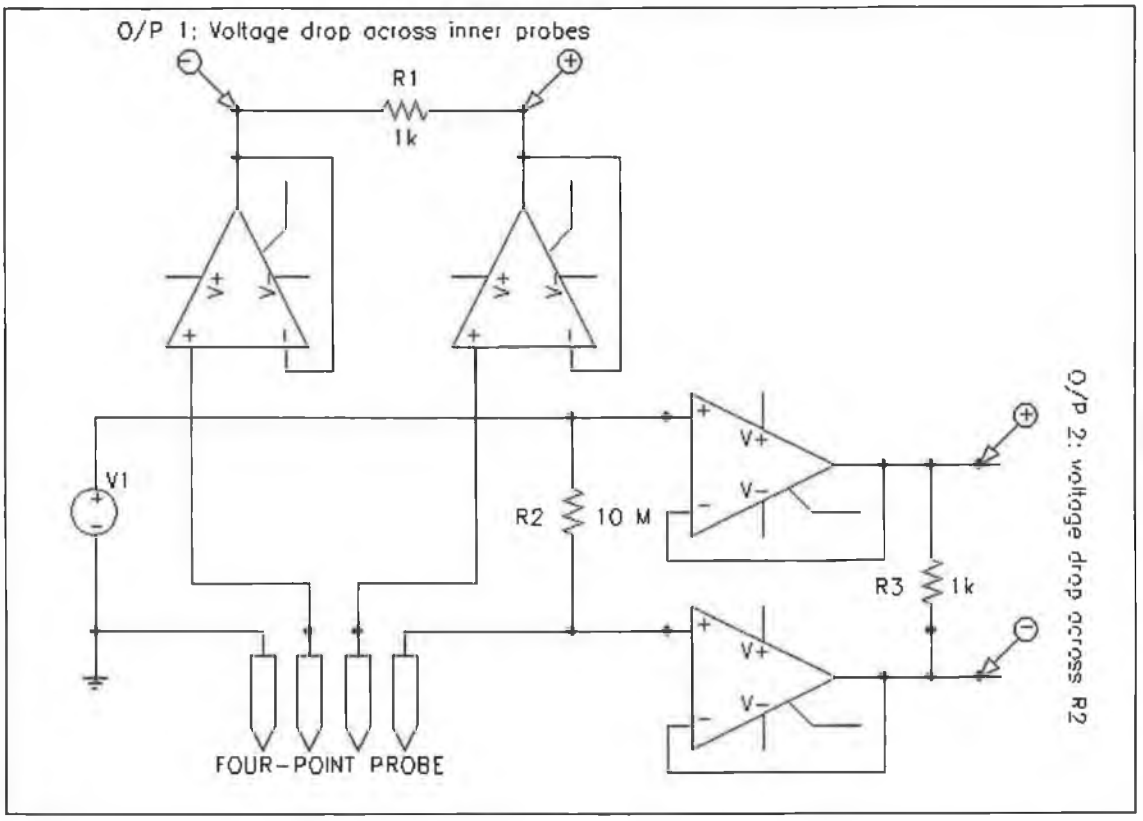

Figure 7.3a: Circuit diagram to buffer the measured voltages.

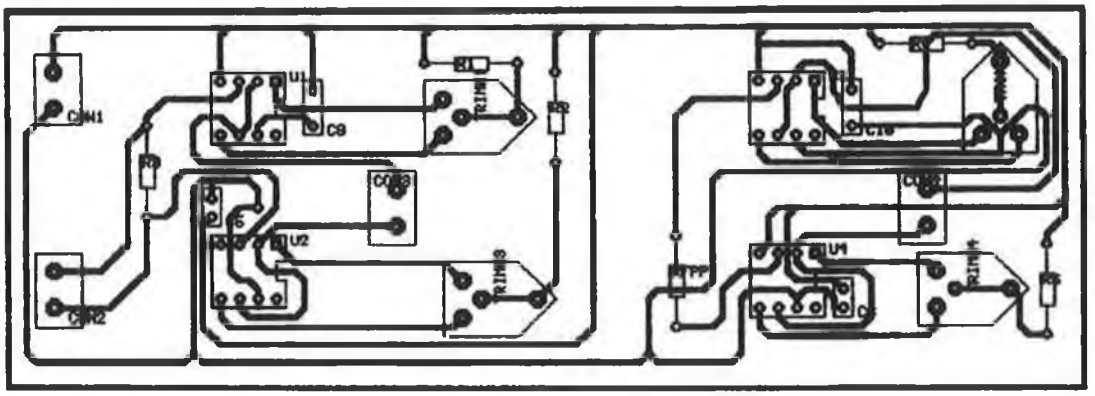

Figure 7.3b: Printed circuit board of the buffer circuit.

The second arrangement for resistivity measurements using a.c current employed an oscillator as the signal generator, an ammeter, and a lock-in amplifier to measure the voltage between the inner probes, connected as shown in *figure 7.4*. The lock-in amplifier is a precision a.c voltmeter; in order to minimise the signal to noise ratio, it modulates the signal to be measured with a reference signal.

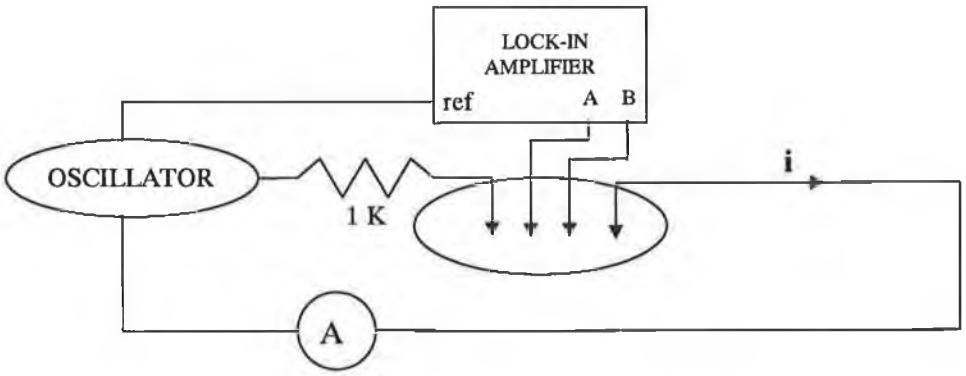

Figure 7.4: Experimental setup for measurements with a.c current.

The supply voltage when using d.c current was normally set to 20 volts and when using a.c current, the oscillator was normally set to 1 V rms at a frequency of 1kHz; this signal was also the reference signal for the lock-in amplifier, as shown in *figure 7.4*.

7.1.2.2 Van der Pauw structures

Van der Pauw[6] developed a perfectly general method to determine the resistivity of a film using four probes located arbitrarily on the film surface. The van der Pauw arrangement for resistivity measurements is shown in *figure 7.5a*. Two sets of current-voltage measurements are required using alternate contacts. The validity of this method requires the sample to be flat, homogeneous and isotropic, with true point contacts on the surface, which is normally the most difficult requirement to satisfy.

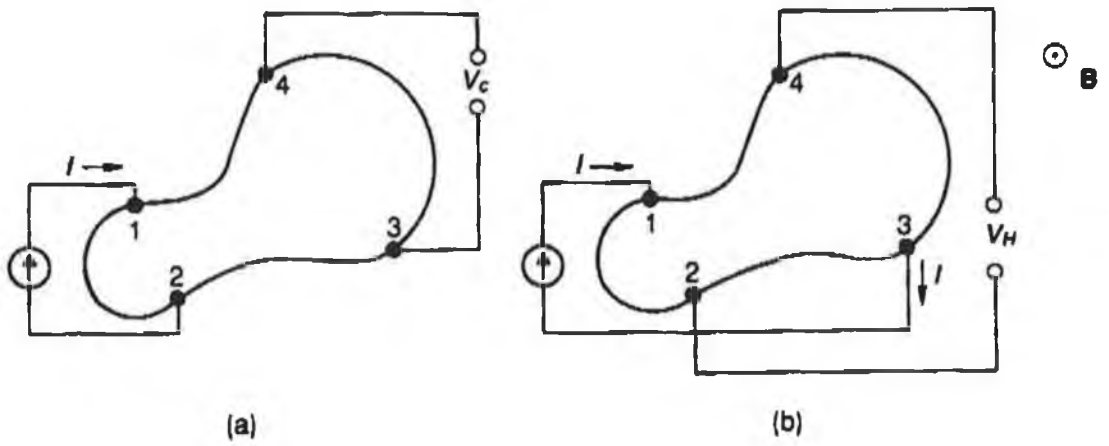

Figure 7.5: Arrangements for van der Pauw measurements: (a) Resistivity; (b) Hall effect.

From the results of van der Pauw's calculations, the resistivity can be calculated from equation (4), where $R_{ij,kl} = V_{kl} / I_{ij}$, if current enters contact i and leaves contact j, and $V_{kl} = V_k - V_l$, d is the film thickness and f is a correction factor used to correct the results for asymmetric sample shape.[7]

$$\rho = \frac{\pi \times d}{\ln 2}\left[\frac{R_{21,34} + R_{32,41}}{2}\right] \times f \qquad (4)$$

Hall effect measurements on these structures can also be performed if the configuration of *figure 7.5b* is used, in which the current and voltage contacts are crossed, and a magnetic field B is applied perpendicular to the sample surface. The Hall effect is briefly described below. The Hall coefficient is obtained from

$$R_H = \frac{d}{B} \times \left[\frac{R_{31,24} + R_{42,13}}{2}\right] \qquad (5)$$

where $R_{ij,kl} = V_{kl} / I_{ij}$ as in equation (4)

Although this technique is applicable to specimens of arbitrary shape, a symmetrical shape is nearly always used. There are several sample geometries, which are used for

van der Pauw measurements, depending on the accuracy required and the feasibility of fabrication. For carbon nitride films investigated here, a symmetrical Greek cross shape was chosen, since it is one of the most accurate van der Pauw structures for avoiding finite-contact size corrections.[5] Furthermore, this shape can be easily obtained by using a mask during film growth. Thin films with a Greek cross shape were deposited onto silicon oxide substrates with an arm width of 3mm and equal arm lengths greater than the arm width to minimise contact-size errors. The Greek cross pattern was generated by using a shadow mask during deposition. The samples were then pasted onto a supporting board, with contacts soldered at the back of the board for connecting the measurement instruments.

For putting on the contact onto the cross arm terminals, very thin flexible wire was used; crude contacts were made using a mixture of silver paint and epoxy hardener which was cured at 60°C for 6 hours. The instruments required are the same as for four-point probe measurements, namely an ammeter (electrometer), a voltmeter and a power supply, connected as shown in *figure 7.6*.

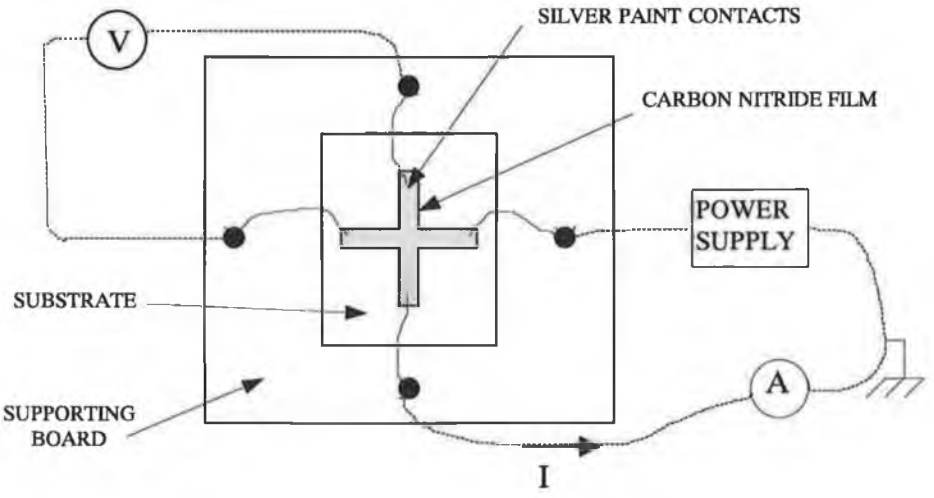

Figure 7.6: Van der Pauw resistivity measurements arrangement.

The Hall effect was discovered by E.H. Hall[8] (1879) and is widely used in the semiconductor industry because of its simplicity and the importance of the parameters

it measures, namely carrier concentration and mobility. The prototype structure for Hall-effect measurements is shown in *figure 7.7*.

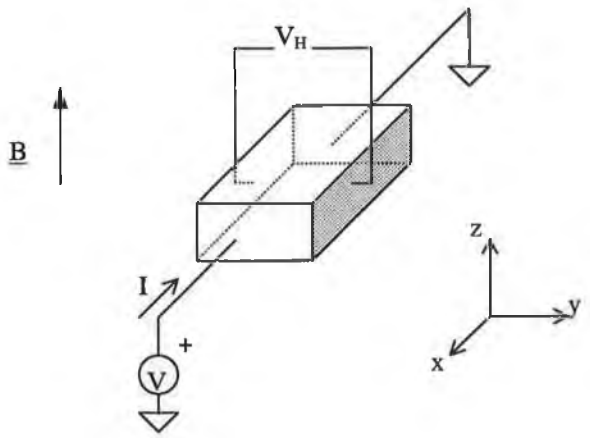

Figure 7.7: Hall-bar configuration for Hall-effect measurements.

In the simplest model of the Hall effect, the charge carriers are assumed to be electrons which are travelling with a velocity v in the x direction upon the application of an electric field. Upon application of a magnetic field $\underline{B}$ in the z direction, the electrons experience a force $-e\underline{v}\times\underline{B}$, which will have a y component $-e(\underline{v}\times\underline{B})_y=-e(v_zB_x-v_xB_z)=ev_xB_z$. The electronic charge will build up on the +y face of the sample until an opposing force $-eE_y$ just balances the ev_xB_z force. With this balance, the electrons again have no y component of velocity, just as was the case when $B=0$. The total current density is $j_x=-nev_x$, so that $eE_y=ev_xB_z=-eBj_x/ne$. The Hall coefficient R_H is defined as

$$R_H = \frac{E_y}{j_x B} = -\frac{1}{ne}$$

The general working equations to carry out a simple Hall effect experiment are:

$$\mu_H = |R_H \times \sigma|$$

$$n_H = \frac{1}{|e \times R_H|}$$

where μ_H is the Hall mobility, σ is the conductivity, R_H is the Hall coefficient, n_H is the Hall carrier concentration and e is the electron charge. When the electrons all have the same magnitude of x-axis velocity, then $\mu_H = \mu$ (conductivity mobility) and $n_H=n$ defined by the equation $\sigma=ne\mu$. The Hall-bar configuration[7] of *figure 7.7* is the most simple geometry to analyse, but is not a feasible configuration to use for thin films, therefore, the van der Pauw method described earlier was employed using the configuration shown in *figure 7.6*. The current and voltage contacts were crossed, and a permanent magnet capable of providing a magnetic field of 0.2 Tesla was used. Equation (5) was used to evaluate the Hall coefficient.

7.1.2.3 Transverse resistivity measurements

The transverse resistivity of the films was also examined by making a sandwich configuration such as the one showed in *figure 7.8*. An Edwards 306A vacuum coating system with a Tungsten wire source was used to evaporate a layer of aluminium on top of the silicon substrates prior to deposition. Then, the deposition of the carbon nitride film was performed for less than 5 minutes to ensure film adhesion to the aluminium layer. After deposition, aluminium dots were evaporated on top of the films by using a mask to serve as a set of contacts. A description of the evaporator used is given in Appendix C. The aluminium dots were approximately of diameter D = 2mm and the film thickness d ~ 0.2 μm. From these values, the resistivity through the film thickness was calculated using the equation:

$$\rho = R \times \frac{(\pi \times D^2)/4}{d};$$

the resistance value R was calculated using a curve tracer by placing the two measurement pointers on the aluminium electrodes on top and bottom of the film. If the pointers were placed on two aluminium dots on the sample surface, longitudinal resistivity measurements can be obtained by using the equation:

$$\rho = R \times \frac{d \times D}{L},$$

where L is the distance between the aluminium dots.

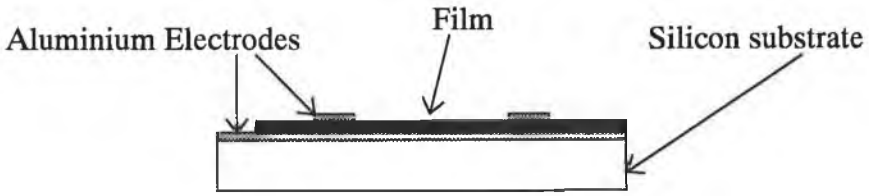

Figure 7.8: Sandwich configuration for transversal resistivity measurements.

7.1.3 Temperature-dependent resistivity measurements

Insight into the conduction mechanism of the films can be obtained from the variation of the electrical resistivity with film temperature. For temperature-dependent resistivity measurements, cross-shaped films were mounted in a cryostat capable of operation in the temperature range 90 K < T < 330 K. An schematic of the system used is illustrated in *figure 7.9*. Wire connections for van der Pauw resistivity measurements were made on the arm terminals of the crossed shaped films with silver paint. These wires go all the way up to the other end of the inner vacuum tube, and out the cryostat where the electrical instruments (power supply, voltmeter and ammeter) required for resistivity measurements were connected. Once the connections were ready, the two valves were opened and the double-skinned walls of the cryostat and the inner tube where the sample is located were pumped down to a pressure of approximately 70 mTorr. This is done in order to achieve the highest possible temperature range for the experiments. Finally, the two valves were closed and liquid nitrogen was poured into the cryostat. The temperature was controlled by means of a digital PID controller.

Starting from the lowest temperature (~90 K), the samples were heated in steps of 10 K. The PID controller adjusts the temperature in each step, at a rate that depends on the parameters set in the controller. When the temperature stabilised in each step, readings of voltage and current were taken. The sample was placed in contact with a resistance heater and a thermocouple was placed on the film surface as shown in next page.

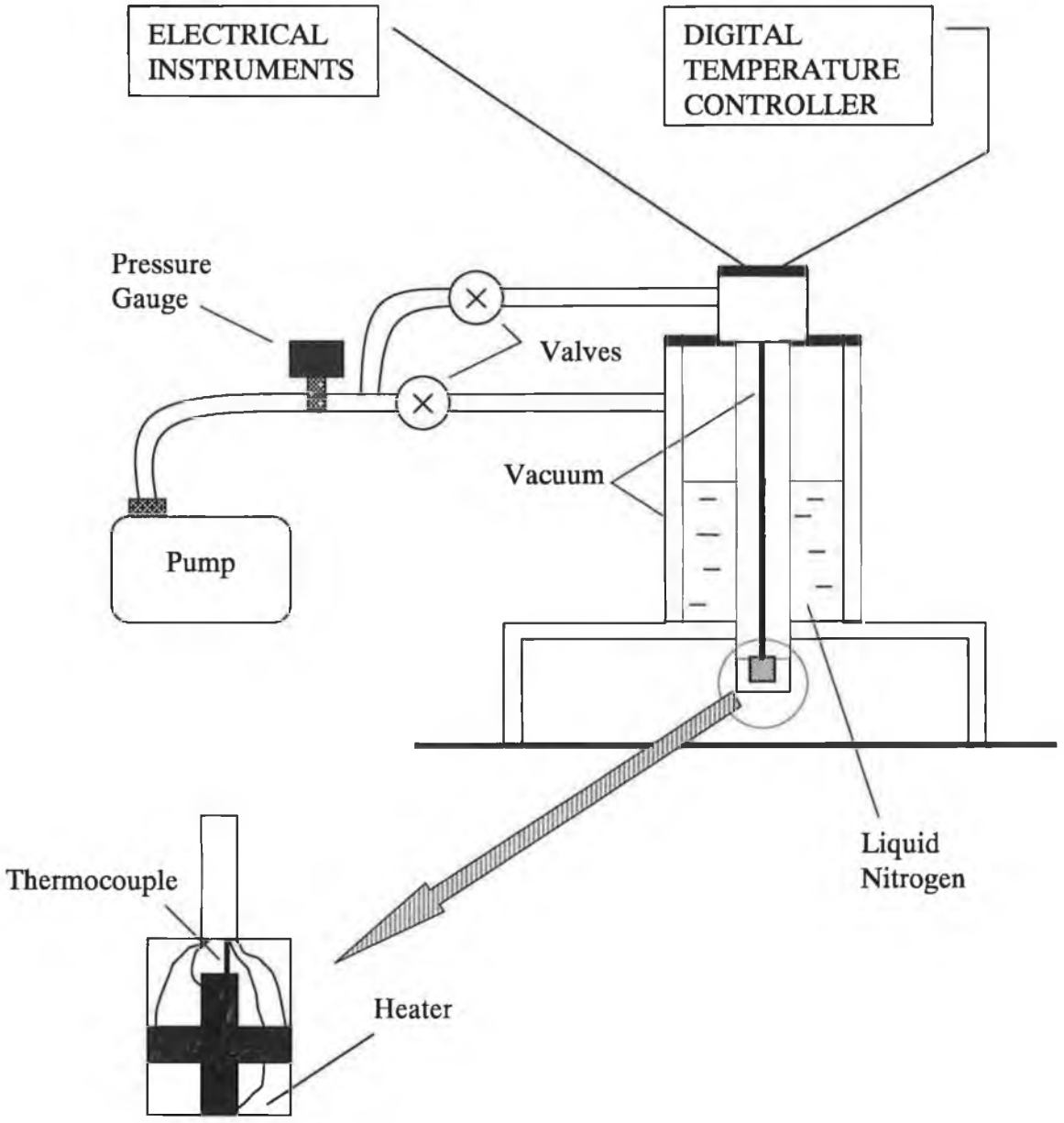

Figure 7.9: Schematic for measurements of resistivity as a function of temperature.

7.1.4 Optical absorption

The absorption coefficient (α) can provide important information about the optical interband transitions in semiconductors. The optical absorption coefficient of films deposited on borosilicate glass substrates was calculated by using a Varian Model 118 spectrophotometer. For many amorphous semiconductors, the typical variation of optical absorption in the visible and near infrared regions are as shown in *figure 7.10*. At low photon energies, the absorption is low, that is, the material is highly transmitting until a critical wavelength is reached. At this point, there is a rise in absorption called the *fundamental absorption edge*. The optical transition associated with this edge involves the interaction of an electromagnetic wave with an electron in the valence band, which is raised across the fundamental gap into the conduction band.

The absorption curve may be divided into three regions:[9] a weak absorption tail *C*, an exponential region *B* which may cover four to five orders of magnitude and for which the slope is largely independent of temperature (except at high temperatures), and a region *A* of high absorption which obeys a power law $\alpha = (E - E_g)/E$, from which an optical energy gap E_g can be defined. The forms of the absorption coefficient α as a function of photon energy $h\omega$ depend on the dependence on energy of the density of states for the bands containing the initial and final states. Under the assumption of parabolic bands, the absorption in many amorphous materials is observed to obey the relation $\alpha = (E - E_g)^2/E$.[10] However, there are exceptions to this quadratic relation.

The optical band gap (Eg) of the carbon nitride films was deduced from measurements of the optical absorption coefficient (α) as a function of the photon energy (E). According to the previous equation, a plot of $\sqrt{\alpha E}$ versus E, which is called a Tauc plot,[10] should yield a straight line. The optical band gap (Eg) is deduced from the intercept of this line with the photon energy axis. The validity of the calculated gap and its relation with the density of states is discussed in part II.

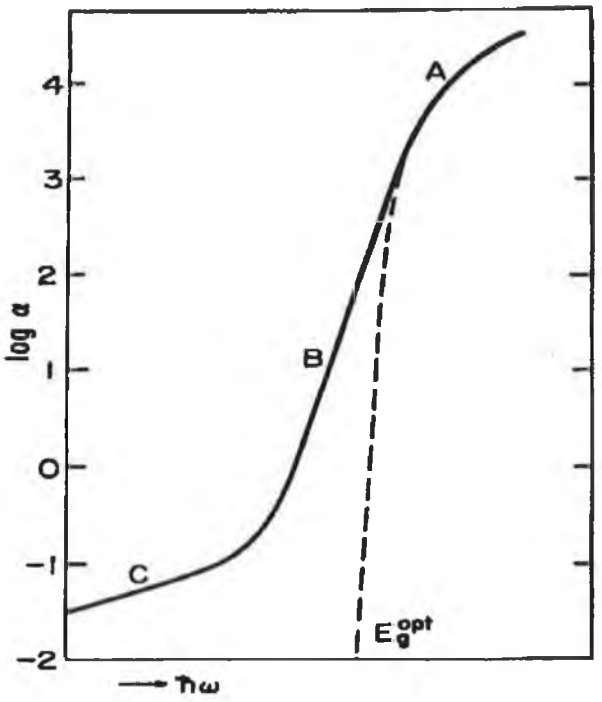

Figure 7.10: Parts A, B and C of the absorption edge.

7.1.5 Ellipsometry

When electromagnetic radiation propagates in materials, because of the presence of charge, there is a change in the wave velocity and intensity of the radiation described by the complex index of refraction: $N = n - ik$, where n is the real index of refraction and k is the extinction coefficient. In highly absorbing metals, n is usually small compared with k. Dielectric films used for optical purposes are highly non-absorbing and k is vanishingly small compared with n.

Ellipsometry is a non-destructive technique in which the refractive index of a surface can be measured. Measurements on thin films are made under the assumption that there is an abrupt interface between the substrate and the film. When two linearly polarised light waves with the same wavelength are combined in phase, the resultant wave is also linearly polarised. However, when they are combined out of phase, they are elliptically polarised.

Ellipsometry is based on the fact that a monochromatic and linearly polarised electromagnetic wave changes its state of polarisation if it strikes an interface between two media in a non-perpendicular fashion. When light passes from one medium to another, some of the incident light is reflected, while some enters the second medium. The phase difference between the parallel component (E_s) and the perpendicular component (E_p) of the incident wave is denoted δ_1 and for the outgoing wave δ_2 (see *figure 7.11*).

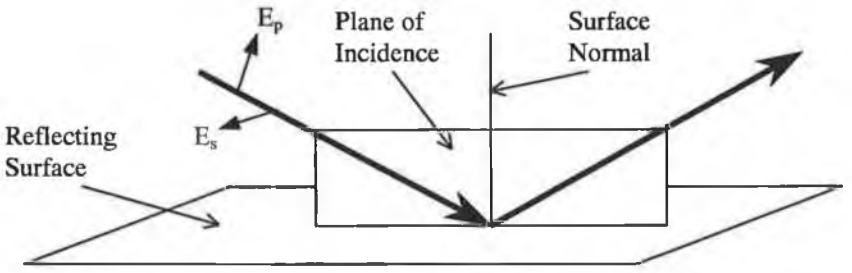

Figure 7.11: Reflection of a light beam from a surface.

Then, the change in phase difference that occurs upon reflection is given as delta $\Delta = \delta_1 - \delta_2$.[11] Ellipsometry, based on the reflection of light from the surface of a sample, measures the change in phase difference Δ between the incident and reflected waves, and the ratio of the magnitudes of the total reflection coefficients (ψ) such that[11]

$$\tan\psi e^{j\Delta} = \frac{R^p}{R^s}$$

where R^p = reflectance in plane of incidence

R^s = reflectance normal to plane of incidence

$e^{j\Delta}$ = exponential complex notation of Δ

Calculations based on Δ and ψ and the index of refraction (n) for the substrate and the angle of incidence of the light beam (ϕ) will yield values for the index of refraction (n) and the extinction coefficient (k) for a film on a substrate. Based on plots of Δ vs. ψ, with different beam wavelengths (λ) and incident angle (ϕ), different values of n can

be plotted. The curve on which the measured point, given by co-ordinates (ψ,Δ), falls, indicates the refractive index of the film.[11]

The refractive index was measured on films deposited onto Silicon substrates. Ellipsometric measurements were made on an Auto EL-3 Rudolph Research null ellipsometer, using λ = 632.8 nm.

Spectroscopic ellipsometry was also used to measure the change of polarisation of light as it is reflected from the film surface in the ultraviolet (UV), visible (VIS) and near infrared (NIR) region. With this technique, the refractive index and the extinction coefficient were derived as a function of light photon energy.

PART II

7.2 RESULTS AND DISCUSSION

7.2.1 Resistivity of carbon nitride films

As previously discussed, there are some practical differences between bulk measurements and measurements in thin films. One of the most important is substrate conduction. Carbon nitride films were first grown onto polished n-type silicon substrates with a resistivity in the range 5 to 9 Ωcm. This implies that if the layer deposited has a similar or higher resistivity, the substrate is likely to conduct a significant amount of current during resistivity measurements, depending on the relative thickness of film and substrate. Firstly, to check the four-point probe performance, the resistivity of the silicon substrate was measured with the four-point probe. Since the silicon is in the form of a wafer, equation (2) was used. Furthermore, since its thickness is less than 5S, where S is the probe spacing, a correction factor F_1 is needed; this factor is determined from the following graph:[12]

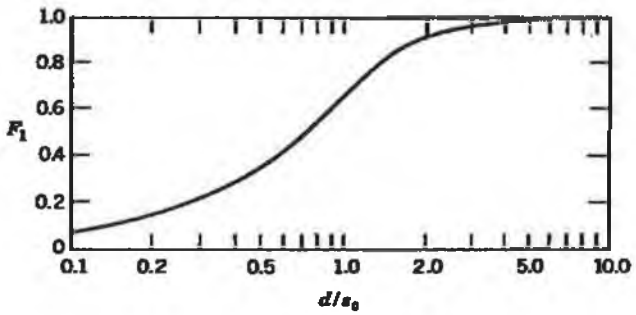

Figure 7.12: Correction factor.

The thickness of the silicon wafer is d=0.5mm and S=1mm; these values give a correction factor F_1 of approximately 0.33, so that the resistivity was calculated from the following equation:

$$\rho = 2 \times \pi \times 0.1 \times \frac{V}{I} \times 0.33 \ (\Omega\text{cm})$$

The experiments were performed at room temperature with both experimental setups described earlier (with d.c and a.c current). Resistivity values from 7 to 8 Ωcm were calculated for the silicon substrates using both setups. The first measurements of carbon nitride films gave rather low values of resistivity (< 10^{-2} Ωcm), which might have been affected by substrate conduction. In order to minimise substrate effects, the silicon wafers were oxidised at 1200° C for 5 hours, to create an insulating support for the films. Soda-lime glasses were also tried as substrates, but adhesion of the film was found to be very poor and most of the films started peeling off after a few hours of being deposited.

The first resistivity measurements of carbon nitride films were done in two series of films grown at different deposition pressures ($1x10^{-3}$ and $1x10^{-2}$ mbar), varying the percentage of nitrogen in the argon/nitrogen gas mixture used during deposition. The other deposition parameters were 3 A magnetron current, -50 V substrate bias, with a deposition time of 30 minutes, giving a thickness ranging from 1.1 to 1.9 μm, thicker films resulting for higher nitrogen partial pressures. *Figure 7.13* represents a plot of the measured resistivity of carbon nitride films grown on the silicon oxide substrates prepared. It can be clearly seen that nitrogen containing films exhibited higher resistivity (2-4 orders of magnitude) than nitrogen-free films in both cases. Films deposited at a higher pressure showed a higher resistivity.

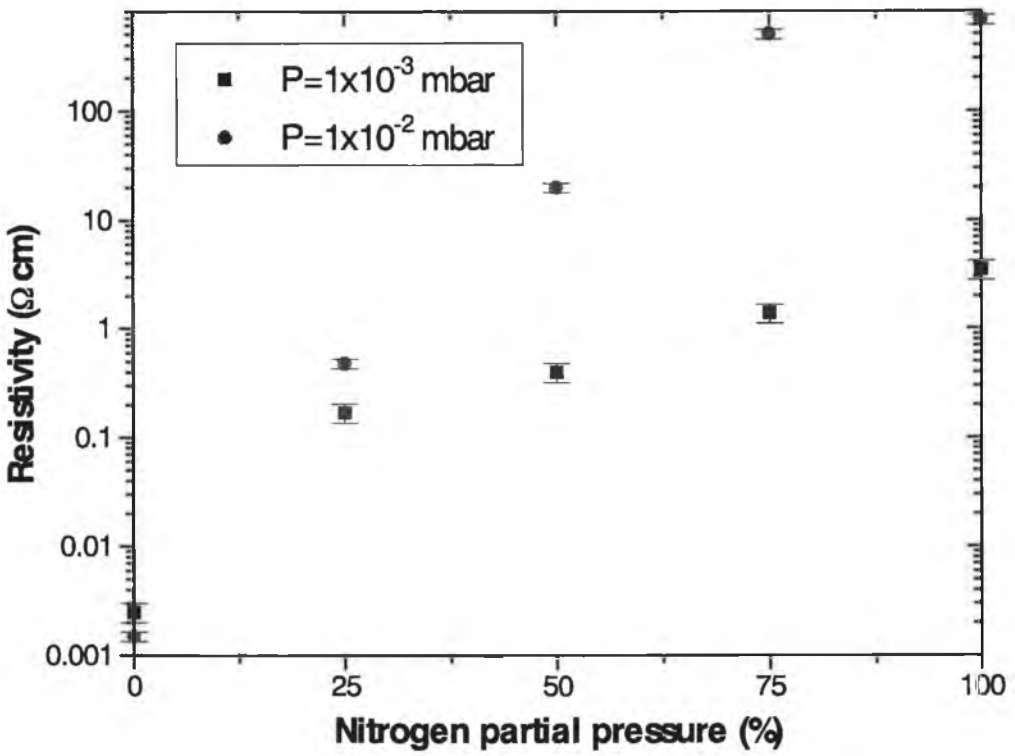

Figure 7.13: Resistivity vs. Nitrogen partial pressure (Npp) for films grown at $P=1x10^{-3}$ mbar and $1x10^{-2}$ mbar.

As already mentioned in chapter 4, hydrogen was detected from IR studies in films deposited at higher pressures ($1x10^{-2}$ mbar) where an absorption peak corresponding to N-H stretching mode (wavelength of 3100 cm^{-1}) was found. This presence of hydrogen in the films is probably due to residual water vapour contamination during deposition. These films peeled off after a few minutes of being deposited due to hydrogen incorporation, which causes poisoning of the film growth.[13] The hydrogen content critically determines film structure and is key in obtaining a wide optical gap and high electrical resistivity as it passivates the dangling bonds in the amorphous structure.[14,15] Incorporation of hydrogen in a-C magnetron sputtered layers results in terminating sp^2-bonded clusters and sp^3 bonded networks. Such terminations will result in a decrease in the mobility of the electrons and an increase in the number and

extent of atomic voids in the film.[16] Therefore, hydrogen incorporation is the reason for the observed increase in resistivity for the films grown at higher pressures.

From this stage onwards, the electrical measurements were focused on films grown at a pressure of $1x10^{-3}$ mbar, with resistivity values from less than $1x10^{-2}$ Ωcm for pure carbon films (0% Npp) to 3-4 Ωcm for films with the highest nitrogen contents (100% Npp).

Another series of samples (named PCNG series) was grown using the same deposition parameters and for Npp = 0, 15, 25, 50, 75 and 100%. However, this time using soda-lime glass substrates and using a shadow mask to grow a Greek cross shape on the substrates for van der Pauw measurements. The deposition time was now reduced to 7 minutes in order to improve the adhesion of the coatings to the glass substrates, which gave thickness ranging from 0.2 to 0.4 μm.

Figure 7.14 show resistivity values obtained using the four-point probe technique on films deposited on oxidise silicon (series 1) and the van der Pauw approach on Greek cross shaped films deposited on glass (series 2). As can be seen from the graph, there is a relatively good agreement between both sets of measurements, with the van der Pauw method giving the higher values of resistivity, probably due to the different substrates used. The range of resistivity values ($2x10^{-3}$ Ωcm to 4 Ωcm) obtained with both techniques for films deposited on different substrates agrees well with the previously measured values (showed in *figure 7.13*).

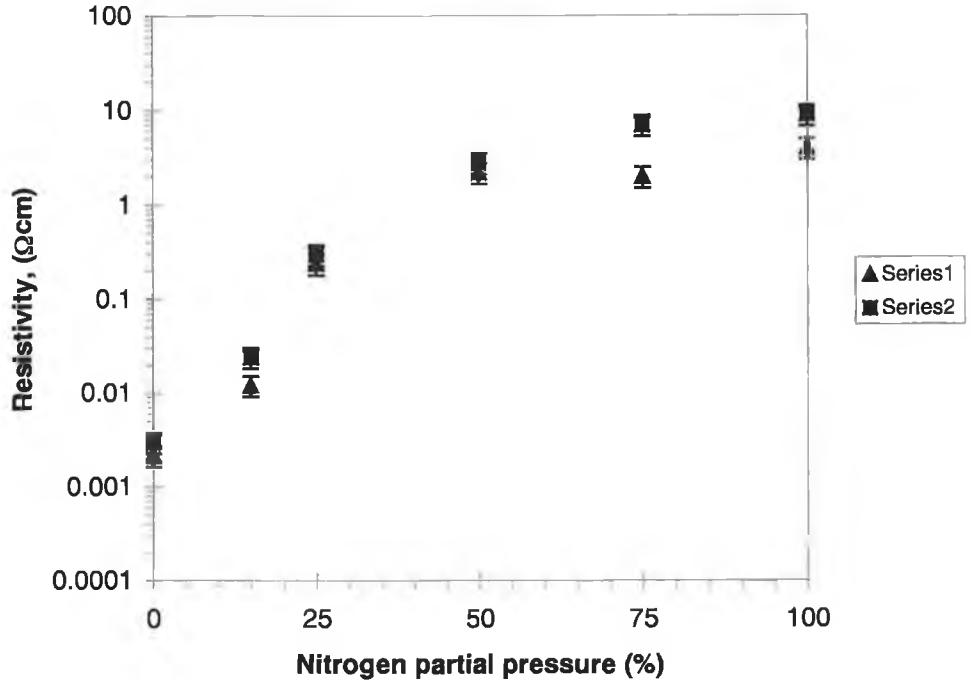

Figure 7.14: Resistivity vs. Nitrogen partial pressure; series 1: Four-point probe technique on films deposited onto oxidise silicon substrates and series 2: Van der Pauw technique on cross-shaped films deposited onto glass substrates.

From RBS results, iron contamination in the range 1 to 6 at.% was detected. This iron content was thought to be affecting the measured resistivity values, since it is known that iron atoms can act as acceptors in amorphous hydrogenated carbon films producing a p-type degenerated semiconductor.[17] The problem with contamination in the films was due to sputtering of the screws clamping the target and the backing copper plate. A new series of films were grown without iron contamination (named M series), using silicon oxide and borosilicate glasses as substrates with nitrogen partial pressure of 0, 25, 50, 75, 90 and 100%. Since it was problematic to maintain an stable plasma for more than ten minutes, the deposition times varied from 5-6 minutes for films deposited at 25% or less N_2 partial pressure, to 8-9 minutes for films deposited at 50% N_2 partial pressure or more. The film thickness ranged from 0.1 to 0.4 μm. Next graph (*figure 7.15*) indicates the resistivity values measured for films deposited on glass (series 1), which were approximately twice as high as those for films deposited on silicon oxide, due to substrate effects, which become more significant now that the film thickness decreases with respect to the first two series of samples.

The new resistivity values for films deposited on glass range from $1.2x10^{-2}$ Ωcm to 4 Ωcm, and are very close to those obtained previously. From these results, it was now clear that the iron content in the films is not acting as a dopant, and essentially is not affecting the resistivity values of the carbon nitride films.

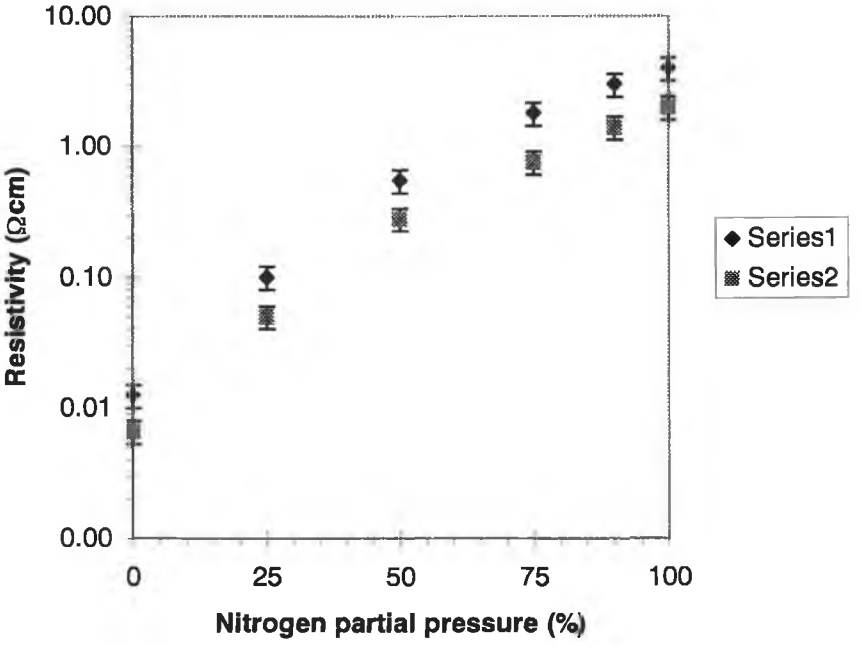

Figure 7.15: Resistivity as a function of nitrogen partial pressure; series 1: films deposited on glass substrates; series 2: films deposited on silicon oxide substrates.

A plot of resistivity (as measured for series 1) as a function of nitrogen content (or N/(N+C) ratio) as measured by RBS is shown in *figure 7.16*. The maximum nitrogen incorporation was 39 at.% N or N/(N+C) = 0.39. It can be seen that nitrogen containing films show higher resistivity (from 1 to 3 orders of magnitude) than nitrogen free films. This indicates that nitrogen is not present in the film as a donor impurity but as an element of a chemical compound in a non-doping configuration. It also illustrates that the resistivity does not show a very clear dependence with the total nitrogen content present in the film, since films with the highest nitrogen content does not necessarily have the highest resistivity values.

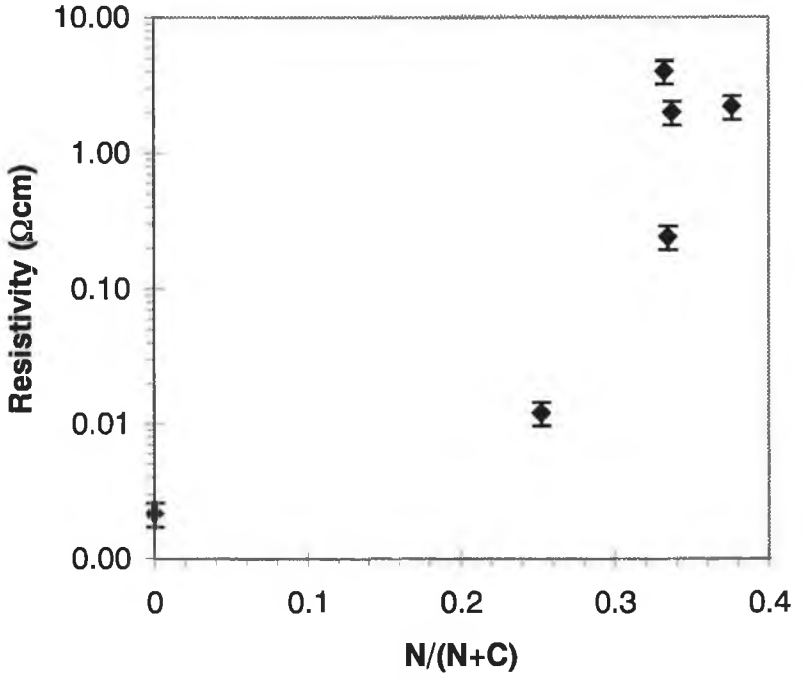

Figure 7.16: Resistivity versus N/(N+C) ratio for PCNG series.

From infrared studies, as mentioned in chapter 4, the bonding structure of the films was determined by measuring the IR absorption due to C=N and C≡N bonds. The resistivity was plotted against the calculated C=N and C≡N bonds absorption coefficient, as shown in *figures 7.17* and *7.18*. As already seen in chapter 4, the IR absorption due to C=N and C≡N bonds was found not to correlate directly with the nitrogen content of the films. Above 20 at.% N, the IR absorption due to C=N and C≡N bonds did not change significantly, suggesting that the excess nitrogen may be incorporated in an invisible bonding structure, such as a N-N bond. This excess nitrogen does not have an effect in the resistivity of the films, which seems to be controlled by the C≡N bond concentration. It can be seen that the resistivity of the films depends more clearly on C≡N bond concentrations rather than on C=N bond concentration or total nitrogen content.

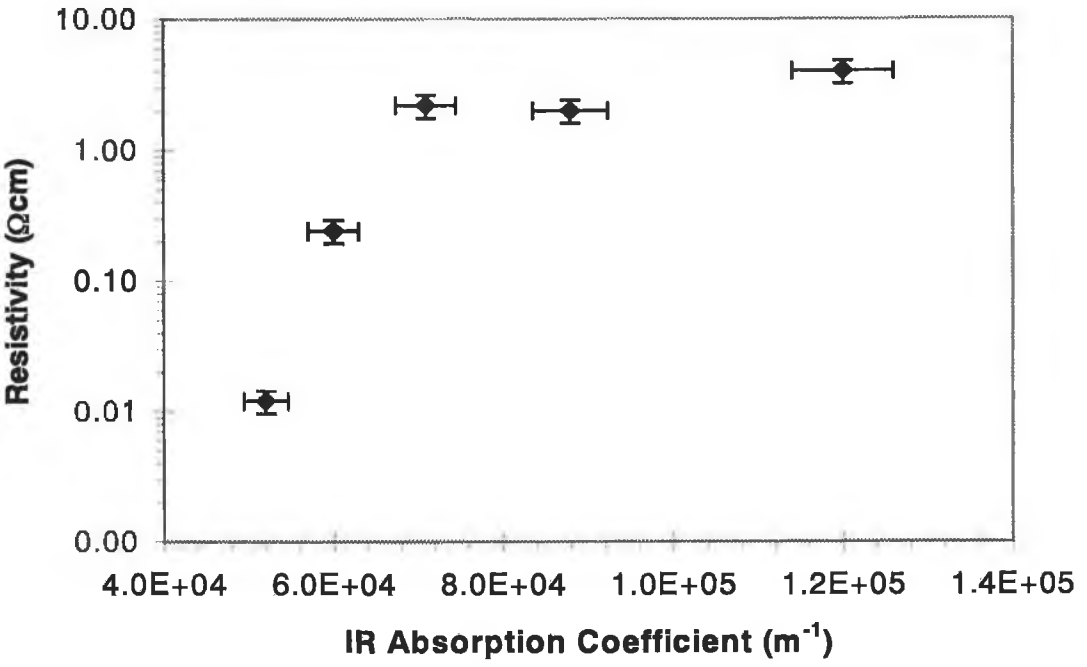

Figure 7.17: Resistivity versus C≡N bond concentration.

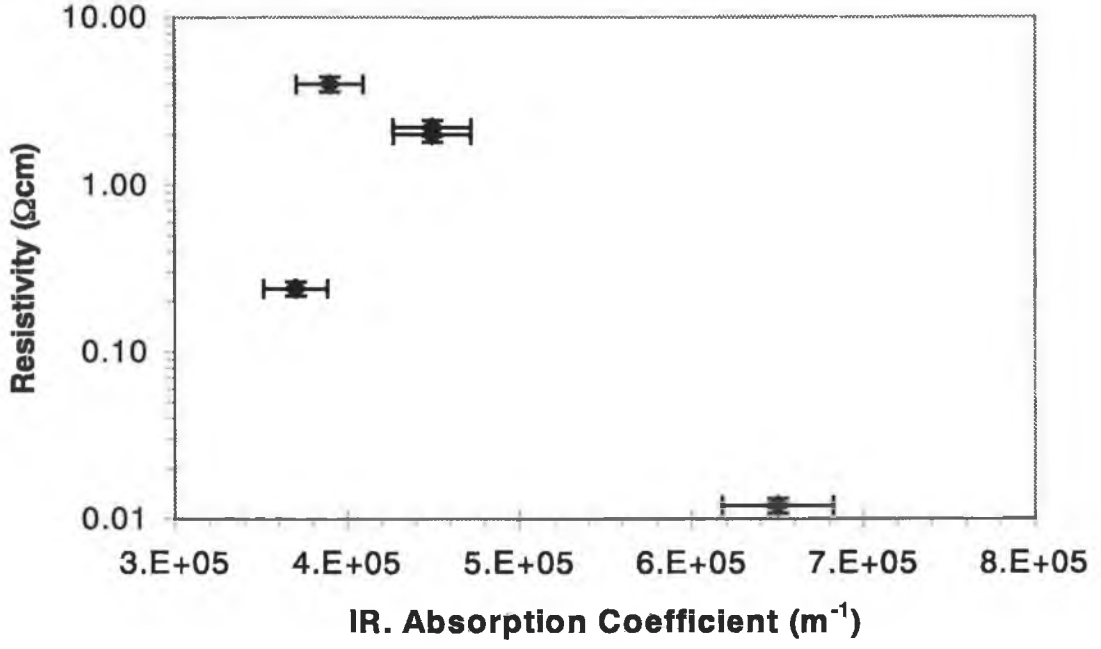

Figure 7.18: Resistivity versus C=N bond concentration.

7.2.1.1 Transverse resistivity

The transverse (through film) resistivity was investigated, as previously indicated, in a sandwich configuration. For these measurements, samples were grown with 100% nitrogen atmosphere. A Resistance in the range 5-10 Ω was measured and the calculated resistivity values ranged from $7.8x10^3$ Ωcm to $1.5x10^4$ Ωcm. These resistivity values were up to 3 orders of magnitude higher than the lateral resistivity measured previously, which may be an indication of a pronounced anisotropical electrical behaviour typical of graphite-like layers.[18] This anisotropic behaviour is either due to a material structure consisting of graphitic layers aligned parallel to the substrate, or to a gradient in film properties caused by floating deposition conditions. Vogel et al.[19] mentioned that this effect is caused by the occurrence of non-localized π electron states in the network. They considered their hydrogenated amorphous carbon r.f. sputtered layers to be composed only of polymeric hydrocarbon areas and sp^2-hybridised (aromatic) carbon areas. Stenzel et al.[20] ascribed the anisotropical electrical properties of their nitrogenated a-C:H films to the anisotropy of the sp^2 orbitals. Effects of the resistance of the contacts on the film's resistivity measurements cannot be excluded.

7.2.1.2 Electron mobility

In amorphous films, mobility measurements are difficult to perform and interpret because of the disordered structure of the material. The value of the Hall mobility (μ_H) expected is small, and typical measured values ranged from $5x10^{-3}$ to 0.5 cm^2/Vs. For a typical value, $\mu_H \sim 10^{-2}$ cm^2/Vs, one must measure a Hall voltage (V_H) of the order of 10 μV. Another difficulty is the often high noise level of V_H, particularly if the current contacts to the sample are not ohmic. Unfortunately, no measurable Hall voltage was seen in the field and temperature range studied; from the maximum resolution of the voltmeter used, the mobility of the charge carriers (assumed to be electrons) must be lower than 0.3 cm^2/Vs and the carrier concentration higher than $7x10^{18}$ cm^{-3}.

Maximum values of 10 cm^2/Vs have been found for nitrogenated a-C:H and a-Si:H.[21] This may indicate that carbon nitride films have a higher defect density in the gap, which results in lower electron mobility. Another possibility to explain the lower mobility would be conduction dominated by hopping rather than extended carriers. The proposed conduction mechanism of the deposited films is discussed in section 7.2.5. A crude hot-tip technique was used to observe that the thermopower of the films was indicative of n-type conduction.

7.2.1.3 Effect of substrate bias

The effect of negative substrate bias on the resistivity of the carbon nitride films (grown in a pure N_2 atmosphere) was investigated and related to a change in film structure. There is a decrease in the resistivity with an increase in substrate bias as illustrated in *figure 7.19*.

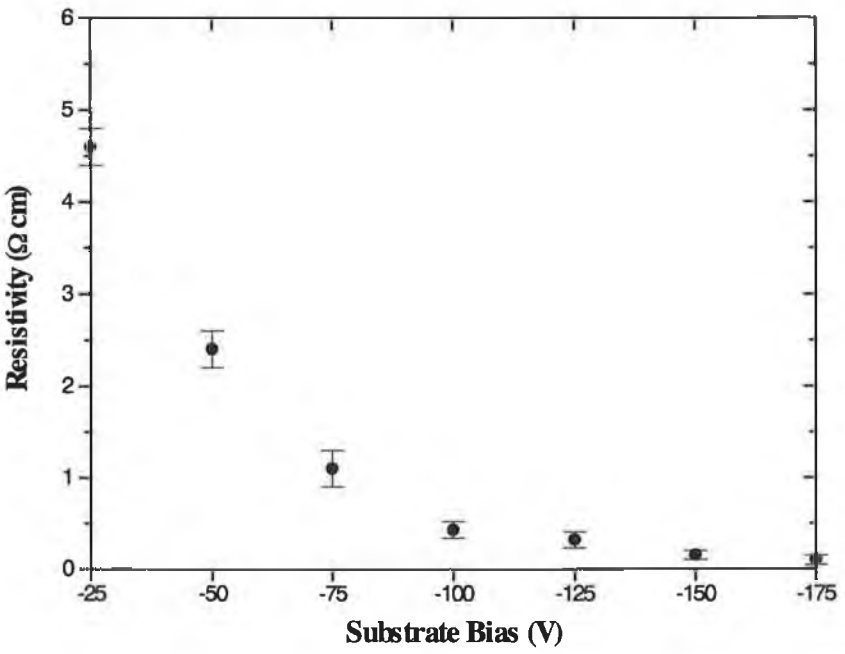

Figure 7.19: Resistivity as a function of substrate bias.

The observed drop in film resistivity cannot be related with nitrogen content, since the amount of nitrogen incorporated does not depend on the substrate bias, as mentioned

in chapter 4. J. Seth et al.[22] also found a decrease in resistivity with an increase in the substrate bias voltage in their nitrogenated carbon films deposited by excimer laser ablation of graphite. Electrical properties of a-C have been proposed to be dominated by the π states of the sp^2 sites because they form the valence and conduction band edges.[23] At sp^2 sites, π bonding favours clustering of aromatic rings into graphitic sheets. Axen et al.[24] found that the sp^2 hybridisation increased with substrate bias voltage in their magnetron sputtered carbon nitride films, originating from C=N double bonds.

The measured drop in electrical resistivity cannot be attributed to an increase in sp^2 bonding, as this is not expected in the carbon nitride films investigated in this work. In chapter 4, it was shown that the IR absorption due to the C≡N bonds decreases with bias voltage. From the previous investigations in films deposited at different nitrogen partial pressures, it is known that as the amount of C≡N bonds relative to C=N increases, there is a rise of the film resistivity as more bond-terminating sites are created. Therefore, as substrate bias is increased, the accompanying decrease in the number of C≡N bonds linked to carbon nitride aromatic rings facilitates electrical transport within the film by increasing of conduction paths by cross-linking.

7.2.1.4 Effect of deposition temperature

The resistivity of carbon nitride films deposited onto oxidise silicon substrates at different deposition temperatures (T_d) was also investigated. In *figure 7.20* the resistivity of films deposited with no additional heat (max. T_d ~ 290°C) is compared with the resistivity for films deposited at max. T_d ~ 360°C and max. T_d ~ 420°C. In the graph, it can be seen the gradual drop in resistivity with deposition temperature. This drop in resistivity is similar as the one observed with substrate bias. In chapter 4, it was mentioned that the increase in deposition temperature causes desorption of C≡N species from the growth surface which forms volatile cyanogen molecules (C_2N_2) resulting in a deficiency of nitrogen in the films. The properties of the films grown at higher deposition temperatures are closer to those of graphite and the observed drop in resistivity testifies to this.

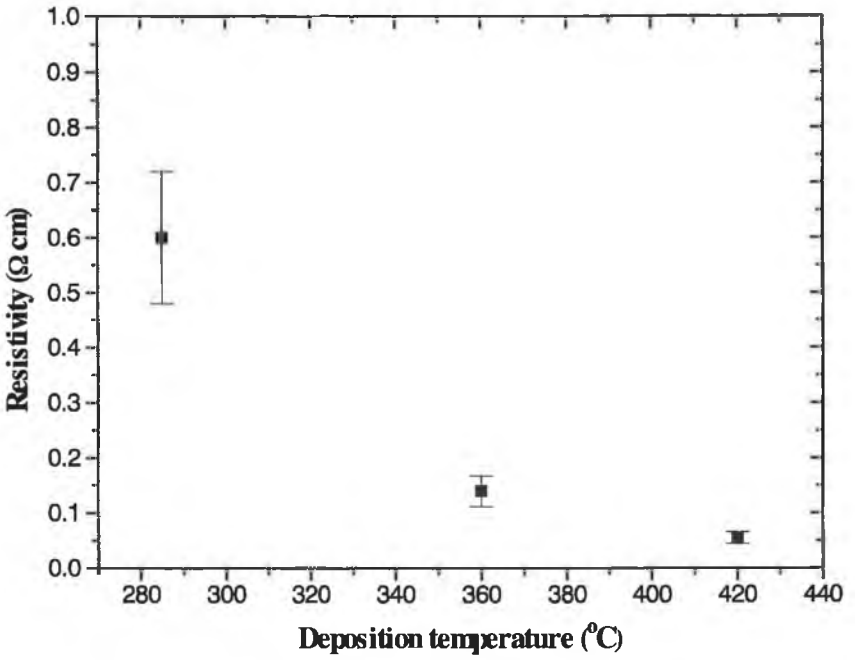

Figure 7.20: Resistivity as a function of deposition temperature

7.2.1.5 Nitrogen doping in amorphous carbon: discussion

In order to get a deeper insight into the effects of nitrogen incorporation into any type of carbon network, it may be helpful to have an idea of how nitrogen has been found to affect the carbon structure. It is well known that semiconducting forms of a-C and hydrogenated a-C (a-C:H) can be doped electronically using nitrogen.[25,26,27] Electrical doping of diamond-like carbon (DLC) was reported by Silva et al.[28] where the forward current was increased by eight orders of magnitude. P. Stumm et al.[29] reported nitrogen doping of tetrahedral amorphous carbon (ta-C), where N is incorporated into the network at diamond-like sites, allowing the Fermi level to move towards the conduction band. Schwan et al.[30] demonstrated the inefficiency of N doping of a-C:H due to the high density of states in the gap. Lee et al.[31] observed an increase in conductivity with nitrogen incorporation in r.f. sputtered carbon films, and they ascribed this to the increase of sp^2 content. It is still not clear whether the N itself acts as a true dopant by adding charge carriers or whether its presence during film growth induces structural and/or compositional changes to the amorphous carbon network

which then explain the electrical properties. The analysis of the effect of nitrogen in different forms of carbon is quite complicated due to the ability of nitrogen to adopt a variety of different bonding configurations,[32] such as those shown in *figure 7.21*.

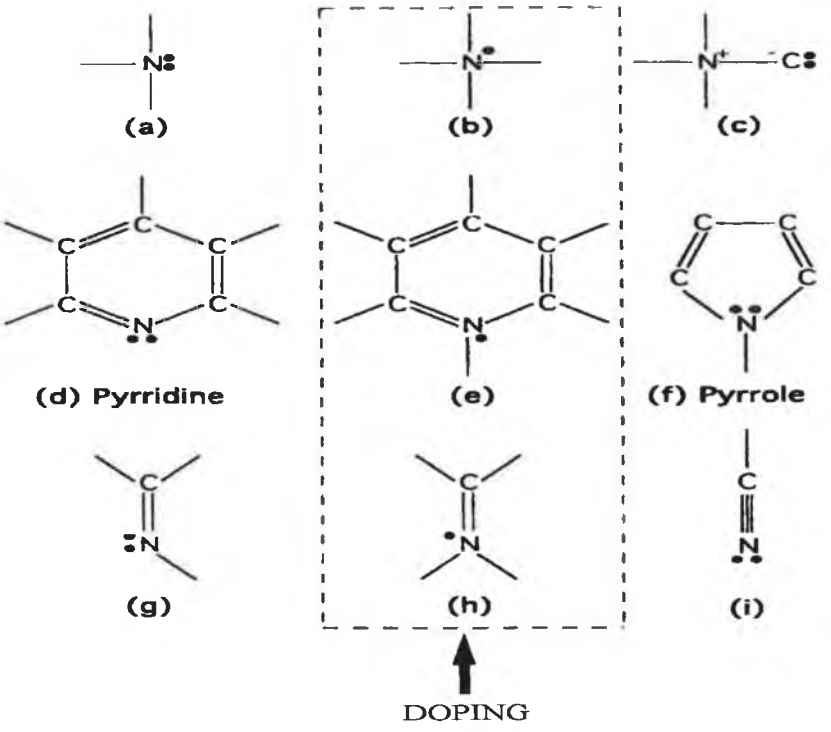

Figure 7.21: Some of the possible configurations of nitrogen in a-C.

Valence electrons are either paired in bonds (shown as a line), unpaired (a dot), or paired in a nonbonding "lone pair" state (shown as two dots). Nitrogen has five valence electrons. In configurations (a), (b) and (c), the N atom only forms σ bonds. (a) represents the stable configuration of N to be found in Si_3N_4. N forms three σ bonds with the remaining two electrons in a lone pair. In (b), it uses four electrons in σ bonds and the fifth is unpaired and available for doping. There are other configurations, because N can also form π bonds. N can substitute for C in a benzene ring [(d)/(e)]. Nitrogen can have just two neighbours within the ring, using three bonding electrons (two σ and one π), leaving two electrons as a lone pair (d). This pyridine configuration is nondoping. Alternatively (e), three electrons can form σ bonds, a fourth forms a π bond (as in benzene), and the fifth is unpaired and enters an antibonding π* state. This electron is available for "π" doping. Another alternative (f) is for the N to have to bond to three neighbours, as in (e), but in a five-fold ring, so it

uses three electrons in bonds and two as a lone pair. This "pyrrole" configuration is also nondoping. There are also other variants of π bonding. A double bonded unit (g) uses two electrons in σ bonds, one in a π bond, leaving a lone pair. This is nondoping. A double bonded unit (h) uses three electrons in σ bonds, one in a π bond, and the fifth in a nonbonding π* state, available for doping. The last configuration is a "chain terminating" cyano (or nitrile) grouping (i), in which N forms a triple bond and a lone pair. This in nondoping. It is relatively stable, being related to that found in the N_2 molecule itself. This variety of configurations available for N, most of which are nondoping, indicates why N is likely to be a weak dopant. The configurations are nondoping because the fifth N electron enters a π state, rather than a π^* state.

In order to understand the role of nitrogen in the electrical conduction of the films investigated here, it is important to understand the nature of the nitrogen-free films, i.e. pure sputtered carbon material. Graphite consists of hexagonal layers of sp^2 sites weakly bonded together by van der Waals forces into ABAB stacking sequence along the c axis. Resistivity is high along the basal plane but low along the c axis. As graphite is the stable allotrope of carbon, many disordered forms of carbon have structures based on this lattice.[33] In *table 7.1*, typical values of resistivity (along the c axis, parallel to substrate) and optical gap of carbon films (a-C Penning) and nitrogenated carbon films (a-C:N Penning) investigated here are compared with different forms of carbon. Glassy carbon contains approximately 100% sp^2, evaporated/sputtered a-C 90-99% sp^2, ta-C 10-20% sp^2, while a-C:H (DLC) may comprise 10-40% sp^2 depending on deposition method/treatment, and diamond is 100% sp^3. As the percentage of sp^2 increases, the resistivity decreases. The sputtered films obtained in this work are expected to have a structure dominated by extended graphite-like regions, with a high sp^2 content, hence the resistivity values are between those of a-C:H and graphite. In sputtered a-C films, the conduction mechanism is normally graphite-like. Electrons that are not used for the σ bonds develop standing waves across the whole molecule. These π electrons respond to an electrical field by moving toward the side of the molecule nearer the positive electrode. These electrons are said to be delocalized and have wave characteristics as they move throughout the material. The structural modification which results from an increased incorporation of

dopant nitrogen atoms leads to decreased graphite-like regions within the a-C structure, which also leads to an increase in film resistivity.

	Resistivity (Ωcm)	Optical gap (eV)
Diamond	10^{18}	5.5
ta-C	10^{8} - 10^{10}	2 - 3
a-C:H	10^{7} - 10^{16}	1.5 - 4
a-C	10^{-1} - 10^{-3}	0.4 - 0.7
a-C (Penning)	10^{-2} - 10^{-3}	0.4 - 0.5
a-C:N (Penning)	10^{-1} - 10	0.1 - 0.2
Graphite	10^{-4}	~ 0

Table 7.1: Resistivity and optical gap of carbon nitride and different forms of carbon.

When nitrogen is incorporated in sputtered a-C films, it is not going to add extra conduction electrons; on the other hand, N starts to adopt an sp^2 bonded, substitutional configuration in the sp^2 bonded C network, as in a pyridine site. At the same time, N also bonds to C forming triple bonds. This -C≡N bonding arrangement precludes an extended inorganic carbon nitride solid and represents a cyanogen-like impurity phase. It was indicated before that the resistivity of the films correlate well with the amount of C≡N triple bonds. As the amount of C≡N bonds relative to C=N, and maybe C-N bonds increases, there is a rise of the film resistivity and the mechanical properties are degraded since nitrogen serves as network terminator in C≡N bonds. This bonding configuration difficult electron movement within the film, causing an increase in resistivity. Similar correlation was found by Zhang et al.[34] in their magnetron sputtered a-CN_x films.

7.2.2 Activation energy

Figure 7.21 shows a plot of the natural logarithm of resistivity as a function of the inverse of temperature for films deposited with 100, 50, 25, and 0% nitrogen partial pressure, with modified targets to avoid iron contamination (series M). In the high

temperature region (1/T<8E-3) it can be seen that the plot follows a straight line of nature $\rho=\rho_o exp(Ea/kT)$, where Ea is the activation energy. For films grown at 25 and 50% Npp, the plot only goes to 1/T= 8E-3(T=125 K), because of jumps that occurred during measurements, believed to be caused by the contacts on the film being affected by low temperatures. The activation energy (Ea) of the films was calculated from the slopes above 166 K (1/T<6E-3) and values are given in *table 7.2*, along with the resistivity, nitrogen content in atomic % (as measured by RBS) and nitrogen gas percentage during sputtering. The activation energy results are discussed in section 7.2.4.

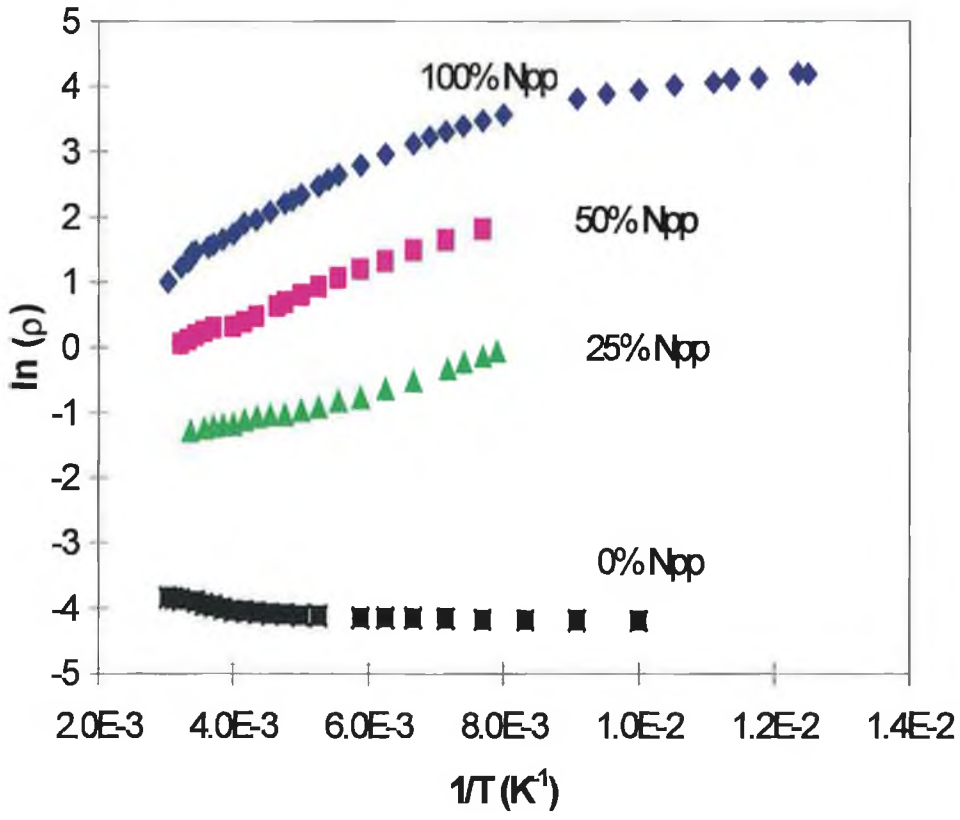

Figure 7.21: Dependence of ln(ρ) on 1/T for films deposited with 100, 50, 25 and 0% nitrogen partial pressure (Npp).

Samples (Series M)	Npp (%)	at% N	ρ(Ωxcm)	Ea (eV)
1	100	36.6	3-4	0.0485
2	50	34.9	$4.5x10^{-1}$	0.0350
3	25	29.9	$1x10^{-1}$	0.0188
4	0	0.035	$1\text{-}2x10^{-2}$	≤0

Table 7.2: Nitrogen content, resistivity and activation energy of carbon nitride films deposited at different nitrogen partial pressures (Npp).

7.2.3 Absorption coefficient/Tauc gap

The absorption coefficient of carbon nitride films deposited at different nitrogen partial pressures is shown in the next figure:

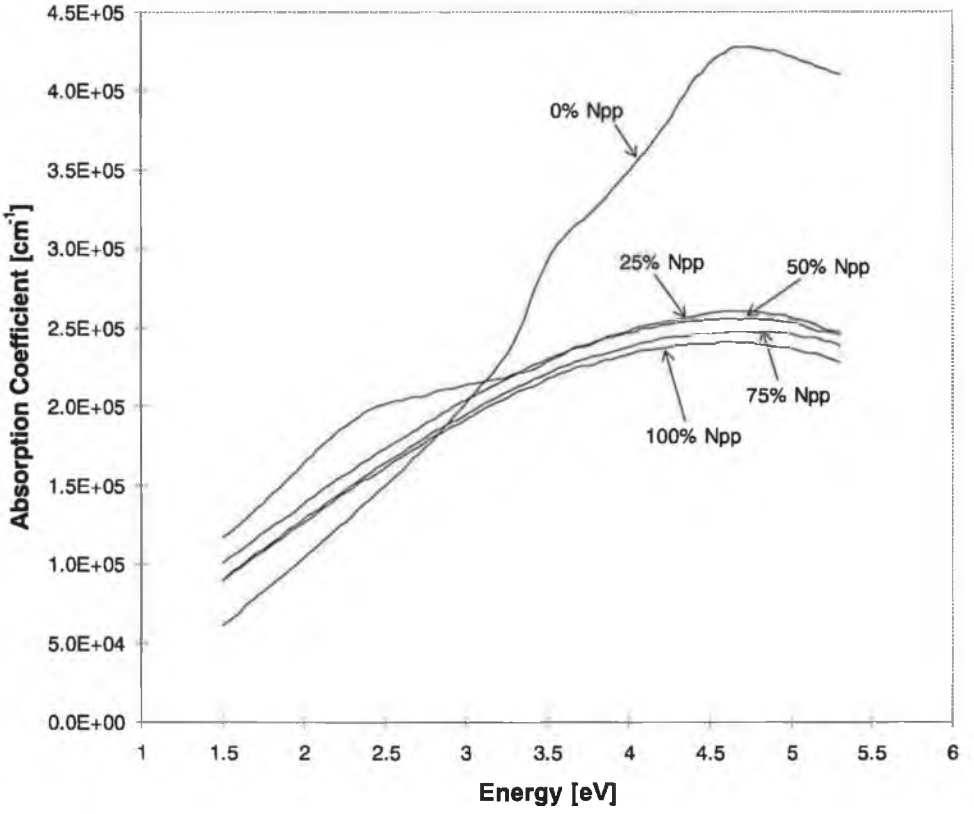

Figure 7.22: Absorption Coefficient vs. Photon Energy.

The absorption of the films shows a decrease with decreasing photon energy in the visible (VIS) and ultraviolet (UV) region, which is a typical behaviour of semiconductors. In contrast to crystalline semiconductors, the optical absorption edge of amorphous semiconductors is dificult to define experimentally. The features observed in the UV-VIS spectra are indicative of an absorption edge.[35]

The absorption edge is observed to be much broader than in other semiconductors, especially crystalline semiconductors, which exhibit a sharp threshold absorption edge, indicating a high degree of disorder in the films. There is no pronounced feature in the absorption edge which can be directly related to an optical gap. This is related to a non-direct optical transition in which electron momentum is not conserved (total disorder).[9] The theory of interband absorption shows that in the high absorption region the absorption coefficient α varies with energy E according to the relation

$$\alpha E = B(E - E_g)^m$$

where B is a parameter that depends on the transition probability and m is a number which characterises the transition process.[10] An analysis of the absorption spectrum obtained for the deposited carbon nitride films shows that the spectral variations in α, inside the fundamental absorption region, can be described by the above equation with m=2, up to a photon energy of 2.5-3 eV. This dependence is typical of indirect allowed transition, with an energy gap E_g depending on the deposition conditions. To estimate the optical band gap E_g, a Tauc plot was constructed as described in section 7.1.4. The absorption coefficient α is plotted against the photon energy E as follows:

$$(\alpha E)^{1/2} = B(E - E_g)$$

The optical band gap E_g can be deduced from the intercept of the extrapolated straight lines with the E axis as shown in *figure 7.23*. The variation of the deduced optical band gap as a function of Npp for carbon nitride films (PCNG films deposited on glass) is presented in *figure 7.24*.

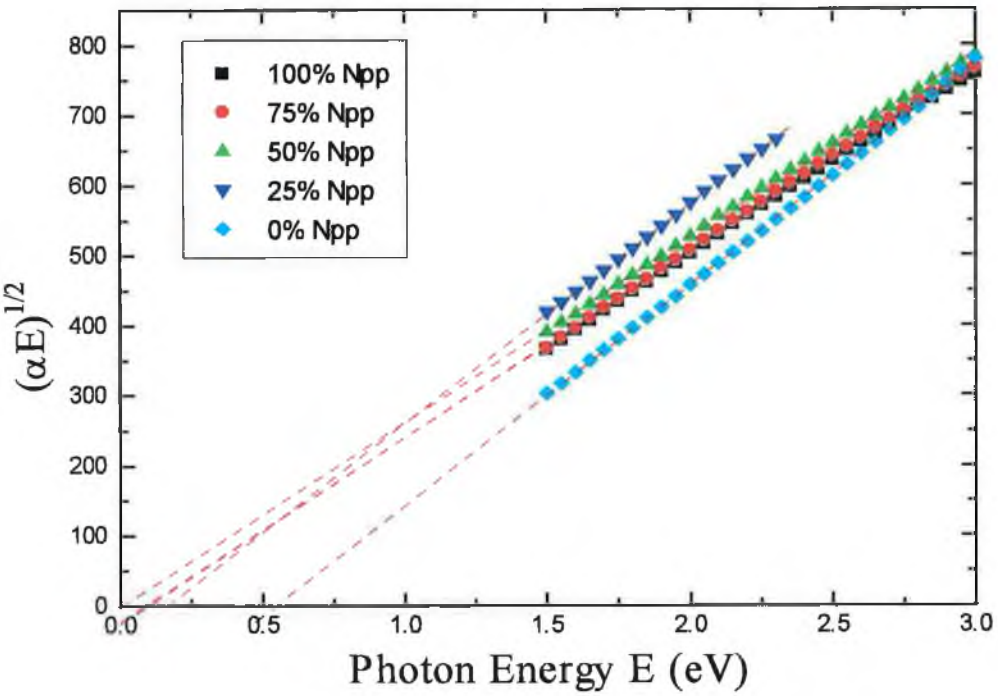

Figure 7.23: Tauc plots for films deposited with 100, 75, 50, 25 and 0% nitrogen partial pressure.

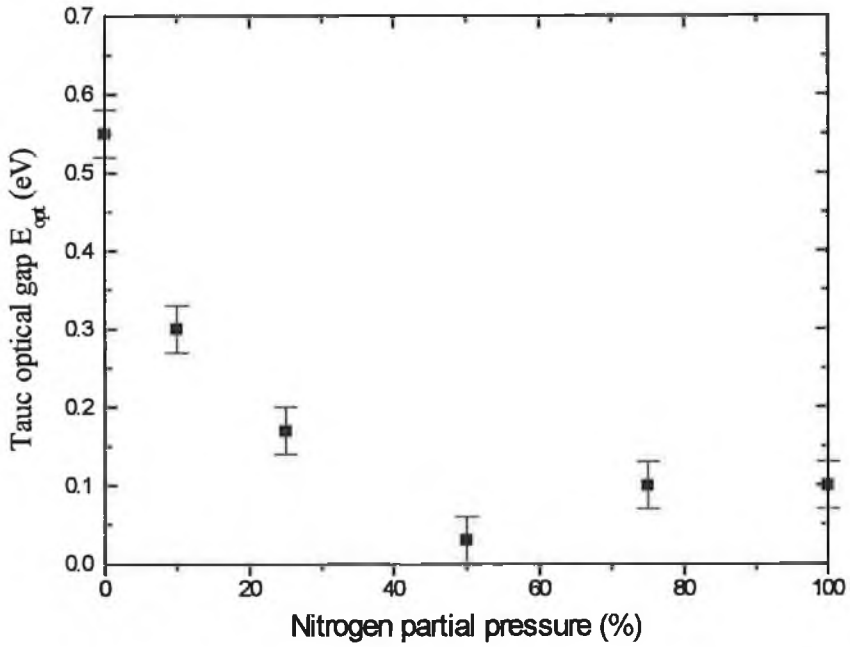

Figure 7.24: Tauc optical gap as a function of nitrogen partial pressure.

For 0% Npp (a-C film), the gap is approximately 0.55eV. This value agrees with the suggestion made by others[36,37] that a-C films prepared by evaporation or sputtering are predominantly sp^2 bonded with an optical gap of 0.4-0.7 eV. Such films are hard although the number of interconnecting sp^3 sites is small. Electrical and optical properties are determined by aromatic or graphite-like ring clusters, which grow in extent on increasing the deposition or substrate temperature.[36] The effect of disorder in the band gap of a-C and a-C:H was widely studied by Robertson et al.[38] They studied structures containing different configurations of sp^2 and sp^3 sites, and established a dependence of the band gap with the sp^2 fraction (size of aromatic clusters in the carbon network). A decrease in the optical gap is thus accompanied by an increase in size of the sp^2 hybridised clusters. Graphite-like layers with large clusters tend to exhibit anisotropical electrical properties caused by the anisotropy (polarity) of the sp^2 orbitals. At an sp^2 site, only three of the four valence electrons are used in σ bonds; the fourth enters a π orbital which lies normal to the σ bonding plane. The importance of the π states is that they are only weakly bonding so that they usually lie closest to the Fermi level (E_F). The π and π^* states from the sp^2sites will therefore form both the valence and conduction band states in a-C.

In chapter 6 it was seen that carbon nitride films show reduced sp^3 type bonding when Npp is increased form 0 to 25%. At higher Npp (>50%), a change in bonding configuration occurs which results in an increase of the sp^3 bonding nature of the films. In *figure 7.24*, it can be seen that as Npp increases to 50% the band gap shrinks to less than 0.1 eV. Above 50% Npp, the band gap starts increasing. This behaviour correlates with to the ESR spectra and the VB spectra of films deposited at different Npp investigated in chapter 6 and confirms that above 50% Npp the sp^3 bonding structure is favoured.

Today, it seems generally recognised that the dc electrical conductivity and the optical band gap of amorphous carbon are determined by the size of aromatic clusters in the carbon network. The decrease in the band gap has been attributed either to increased structural order or to the growing sp^2 cluster size which results in π and π^* band broadening.[22] Demichelis et al.[39] mentioned that nitrogen is expected to stabilise the

sp^3 phase in a-CN_x films and to reduce the number of sp^2 clusters, resulting in an increase in the optical gap. A decrease in optical gap was found for a-CN films deposited by ion beam/laser ablation method,[28] which was attributed to an increase of the structural order in sp^2 bonded clusters. The optical gap values found are within the range of those found by Hammer et al.[40] for ion beam deposited carbon nitride films, consisting predominantly of sp^2 hybridised aromatic rings. For the deposited CN_x films, the relative high surface conductivity and the low band gap suggest an electronic structure having a large number of π-type band tail states indicating a structure which consists mostly of sp^2 hybridised aromatic rings. Typical amorphous hydrogenated materials, such as a-Si:H, a-Ge:H and a-C:H exhibit band gaps of ~1.5 ~ 2 eV, which consist of a mainly tetrahedrally sp^3 bonded network, with very low residual dangling bonds.

7.2.4 Conduction mechanism in disordered materials - Proposed energy band diagram for amorphous carbon nitride

In this section, the electrical behaviour of deposited carbon nitride films is discussed in the light of existing models for the transport properties of disordered materials. First, a brief description of a general accepted conduction model for disordered amorphous semiconductors is given which is followed by a proposed energy band diagram of carbon nitride films based on the presented model along with a discussion of the transport properties of the films.

7.4.2.1 Conduction in disordered materials

When considering the electronic properties of amorphous materials, the question of localization is central to consideration. To ascertain whether particular electronic states are localized or extended, transport measurements are usually employed, in which the carrier's intrinsic drift mobility (its response to an electric field) is determined. If the mobility is high (>>1 cm^2/Vs) and decreases with increasing temperature, the measurements are typically viewed in terms of a scattering picture (metal conduction) and the conduction occurs via extended states in the conduction

band. Alternatively, if the mobility is low (<<1 cm^2/Vs) and increases with increasing temperature, the transport is usually interpreted within a hopping picture where the participating electronic states are localized.[3]

One of the effects of disorder and doping of the electronic structure of amorphous semiconductors is the introduction of states in the pseudo-gap. These states (defects) affect properties of the material such as conductivity and electron spin resonance. The band diagram of the deposited carbon nitride films that is presented in the next section follows the Mott-CFO model[10] for the density of states in amorphous semiconductors which is shown in *figure 7.25*. The model shows conduction and valence bands with tails of localized states and sharp energies of transition to extended states which are mobility edges (E_c^m and E_v^m). Within this model, the separation between the upper valence-band mobility edge and the lower conduction-band mobility edge is designated the mobility gap. Amorphous semiconductors contain a number of localized trap-like states within the mobility gap.

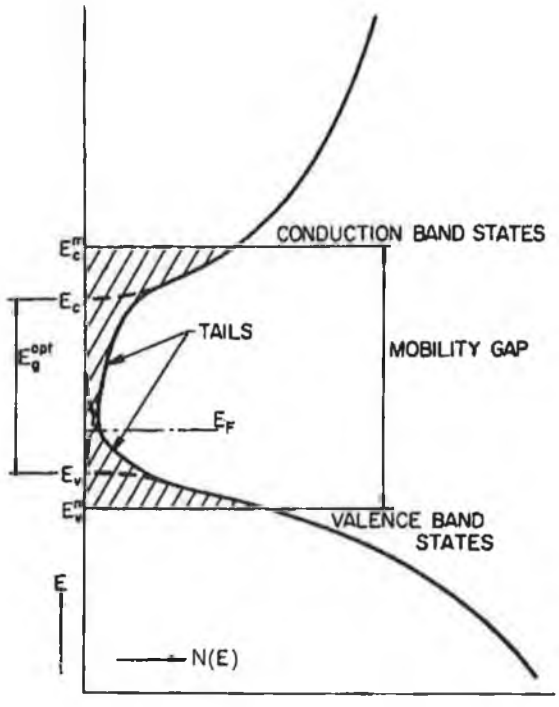

Figure 7.25: Density of states N(E) as a function of energy E in amorphous semiconductors according to the Mott-CFO model.

The details of the density of states (DOS) will determine which conduction mechanism dominates over a given temperature range. The charge carriers which exist above the mobility edge are presumed to behave much like carriers in crystalline silicon, manifesting high intrinsic mobilities, and interacting only weakly with the atomic vibrations. In amorphous semiconductors on the other hand, the carriers posses very low mobilities and interact strongly with the atomic vibrations, probably forming small polarons. The question of polaron formation has been addressed by Kazmerski et al.[3] A polaron is basically a self-trapped carrier and the associated atomic displacement pattern. The polaron model of conduction views charge carriers as relaxing into self-trapped states which lie within the absorption gap. Charge transport is then characterised in terms of hopping motion with rather low mobilities which increase with increasing temperature. The mobility of polarons is generally rather low because self-trapped carriers can only move in response to an alteration in the positions of the atoms of the solid.

In general, disorder tends to impede and restrict motion, thereby facilitating self-trapping and localization. Various amorphous semiconductors appear to posses sufficiently large density of defects so that conduction associated with direct motion between defect states dominates the transport over significant temperature ranges. With the model described in *figure 7.25* for the density of states in an amorphous semiconductor, there are three possible mechanisms of conduction:[9]

1) Transport by carriers excited beyond the mobility edges into non-localized (extended) states at E_c^m or E_v^m. The conductivity for electrons has the form

$$\sigma = \sigma_0 \exp\left(-\frac{E_c^m - E_F}{kT}\right)$$

A plot of $\ln\sigma$ versus 1/T will yield a straight line if E_c^m-E_F is a linear function of T over the temperature range measured.

2) Transport by carriers excited into localized states at the band edges and hopping at energies close to E_c or E_v (fixed range hopping). For this process, the conduction for electrons is given by:

$$\sigma = \sigma_1 \exp\left(-\frac{E_c - E_F + w_1}{kT}\right)$$

where w_1 is the activation energy for hopping. A linear dependence of $\ln\sigma$ versus 1/T is also expected here.

3) Transport by carriers near the Fermi level (E_F) which can hop between localized states (variable range hopping). The conductivity is given by

$$\sigma = \sigma_2 \exp(-w_2/kT)$$

where w_2 is the hopping energy.

Conduction mechanism (1) dominates at high temperatures, while mechanisms (2) and (3) dominate at low temperatures. For low mobilities (< $1cm^2/Vs$), the conduction can be dominated by hopping even at room temperature if the density of defect states is high enough.[41]

7.4.2.2 Conduction in carbon nitride films – proposed energy band diagram-

Because of the disordered structure of the deposited carbon nitride films, carriers will find their motion impeded and they are then expected to self-trap and form small polarons and thereby suffer a more extreme localization. Deposited films appear to have rather low Hall mobilities (< 0.3 cm^2/Vs) which suggests that the localized view discussed above is appropriate for carbon nitride films. In addition, from the lack of long-range order expected in amorphous carbon nitride films, conduction and valence band tails are expected in the density of states (DOS). The extent of these tails depends on the amount of inherent disorder.

The electrical conduction mechanism for the carbon nitride films is controlled by the position of the Fermi level (E_F) and the amount of localized electronic states. The activation energy measurements described earlier suggest that the variation in the conductivity of nitrogenated films arises due to movement of the Fermi level. For nitrogen containing films and T > 166 K, a plot of resistivity vs. the inverese of temperature follows a straight line, $\rho=\rho_o\exp(Ea/kT)$; such a temperature dependence may describe three different conduction mechanisms: fixed range hopping, extended

state conduction and thermally activated hoping in band tails.[9] The activated conduction mechanism occurring via carriers excited beyond the mobility edge is typical of insulating a-C:H layers with activation energies of 0.11-0.12 eV.[18] The low activation energy and Hall mobility found for deposited CN_x films suggest a mixed conduction mechanism by thermally activated hoping and fixed range hoping at the Fermi level for temperatures below room temperature. At higher temperatures, activated conduction mechanism occurring via carriers excited beyond the mobility edge is more likely to occur becoming then the dominant conduction mechanism.

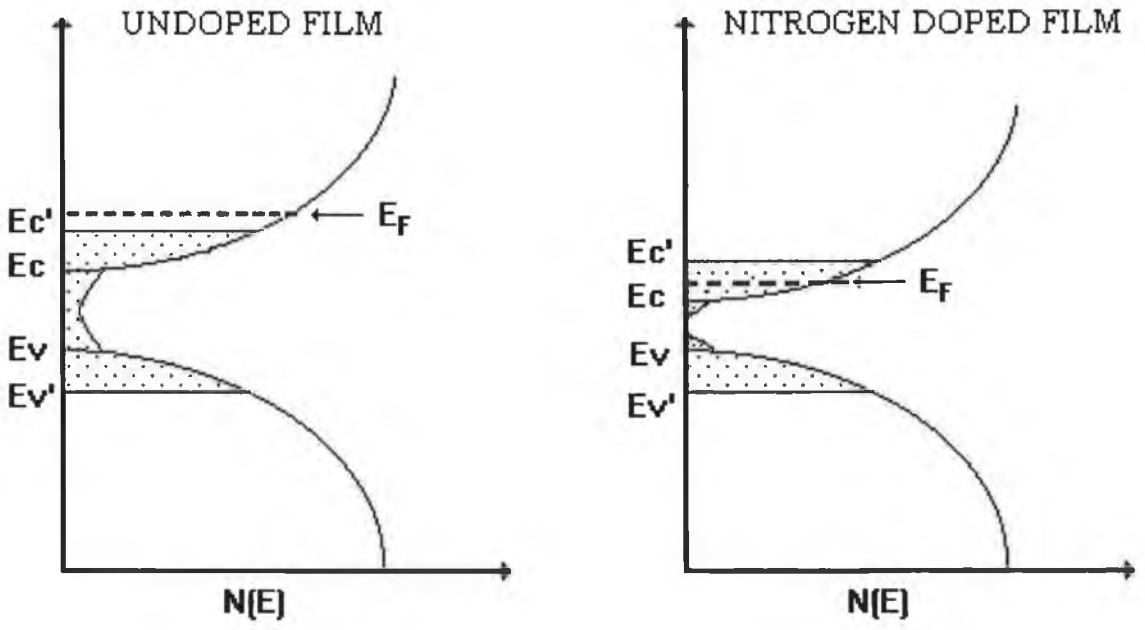

Figure 7.26: Proposed energy band diagram for the density of states (DOS) in nitrogen-free films and nitrogen-containing films.

The proposed electronic band structure for the nitrogen free film and nitrogen containing films is shown in *figure 7.26*. E_c' and E_v' are mobility edges that separate extended states from localized states (dotted region in *figure 7.26*) in the conduction and valence bands respectively and E_F represents the Fermi level. These mobility edges are normally present in non-crystalline systems. The ranges E_c'-E_c and E_v-E_v' contain localized states originating from the lack of long-range order.[9] The states inside the optical gap are strictly localized in deep levels.[42] According to the model

considered here, the absorption curve of *figure 7.22* is very probably associated with transitions from the localized valence band states below E_v into the extended conduction band states above E_c' and the calculated Tauc optical gap is related to the extrapolation of the density of the states deeper in the bands (E_c-E_v).[43] Some absorption can also occur within the mobility gap which is associated with the excitation of carriers out of traps[3] and therefore, as mentioned before, without independent knowledge of the density of states, it is not possible to know whether this is a real gap or some other characteristic energy associated with the mobility gap.

The activation energy (E_a) of the nitrogen-containing films calculated previously represents E_c'-E_F for high temperatures or E_c'-E_F+w_1 (w_1 is the activation energy for hopping) for low temperatures. The activation energy (E_a) increases with nitrogen content. The temperature-dependent resistivity relation of the pure carbon films cannot be fitted by any formula describing a conduction mechanism of amorphous semiconductors. These films exhibit only a small variation of $\rho(T)$ over the measured temperature range, which might indicate a different conduction mechanism. Experimentally, the defect states of a-C (σ and π states predominantly) can form a continuous distribution across its pseudogap and these allow conduction by variable range hoping.[44,45] The behaviour of these films can be understood in terms of a large concentration of graphite bonds.[18,41] The activation energy (E_a) indicates that E_c'-E_F is negative for pure carbon films. This behaviour is typical of that due to an Anderson transition with a change from metallic to semiconducting behaviour as nitrogen is incorporated in the films.[9]

As the nitrogen content in the films decreases, more and more localized states are created and when all states in the band are localized, the Anderson transition occurs. A donor state band is probably present in the conduction band of the nitrogen free film. This donor state would arise from the π delocalized electrons responsible for the graphite-like conduction observed in nitrogen free films. The change in bond structure caused by the addition of nitrogen narrows the measured Tauc gap, leaving fewer donor states present and causing the Fermi level to move below the conduction band, as observed in *figure 7.26*.

7.2.5 Refractive index/extinction coefficient

The refractive index of the films grown on silicon substrate was measured by ellipsometry using λ=632.8nm. *Figure 7.27* shows a plot of refractive index versus nitrogen content, where it can be seen that the nitrogen-free film have the highest value of refractive index. The refractive index decreases with nitrogen content, even though there is not a clear correlation. On the other hand, there is a better dependence of refractive index with C≡N bond concentrations as shown in *figure 7.28*. *Figure 7.29* shows the poor relation between refractive index and C=N bond concentration. The observed decrease in refractive index can be attributed to the increase of sp^3 fraction. But it can more clearly be attributed to the increase of the void fraction in the a-CN films.[46] The void-fraction increase can be caused by the nitrogen atoms forming a triple bond with a carbon atom. Since C≡N bonding saturates all valence electrons of nitrogen, it produces bond-terminating sites and induces the loss of connectiveness of the amorphous carbon network, which results in a less densely packed structure. This would explain the monotonic decrease of the refractive index as the number of network terminating C≡N bonding increases. This argument is also consistent with the observed dependence of hardness with C≡N bond density investigated in chapter 5.

Films with the highest conductivity (with (N/N+C) <0.3) have the highest refractive indices. The n values for the nitrogen containing films (n = 2.5 - 1.9) are comparable to those obtained by Wang et al.[47] for magnetron sputtered a-C:N films. The decrease in index of refraction can be also correlated to the decrease in the density of the films. Stenzel et al.[48] observed a decrease in refractive index (2.9 → 1.6) with decreasing mass density in differently deposited amorphous carbon layers. Sreenivas et al.[49] also attributed the reduction in refractive index from 1.9 to 1.6 in their N doped DLC films to a decrease in the mass density of the films with nitrogen content.

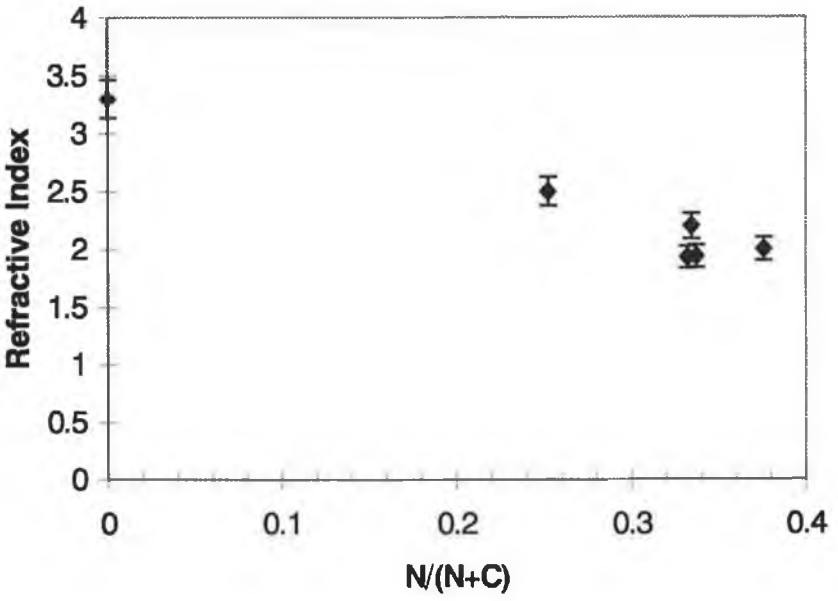

Figure 7.27: Refractive index versus nitrogen content.

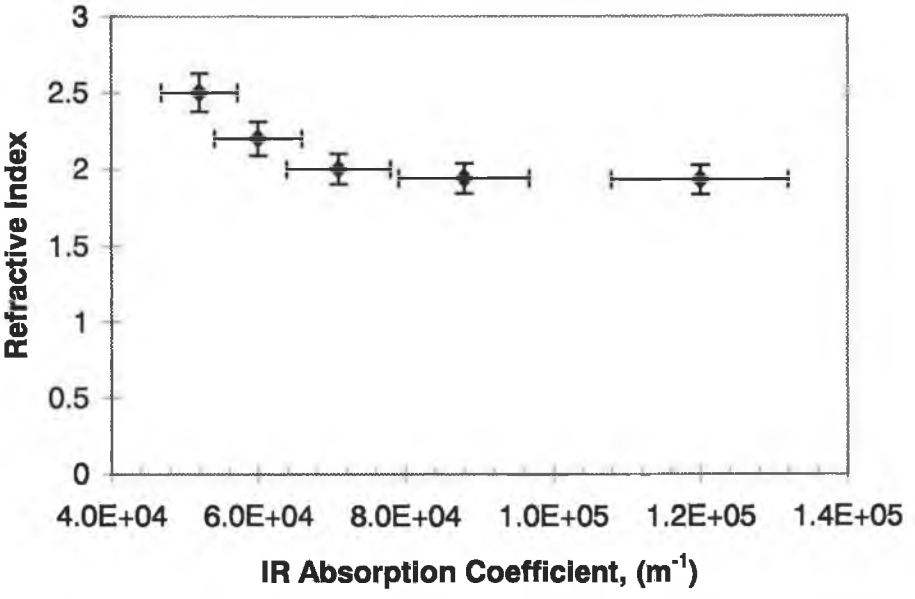

Figure 7.28: Refractive index versus C≡N absorption coefficient.

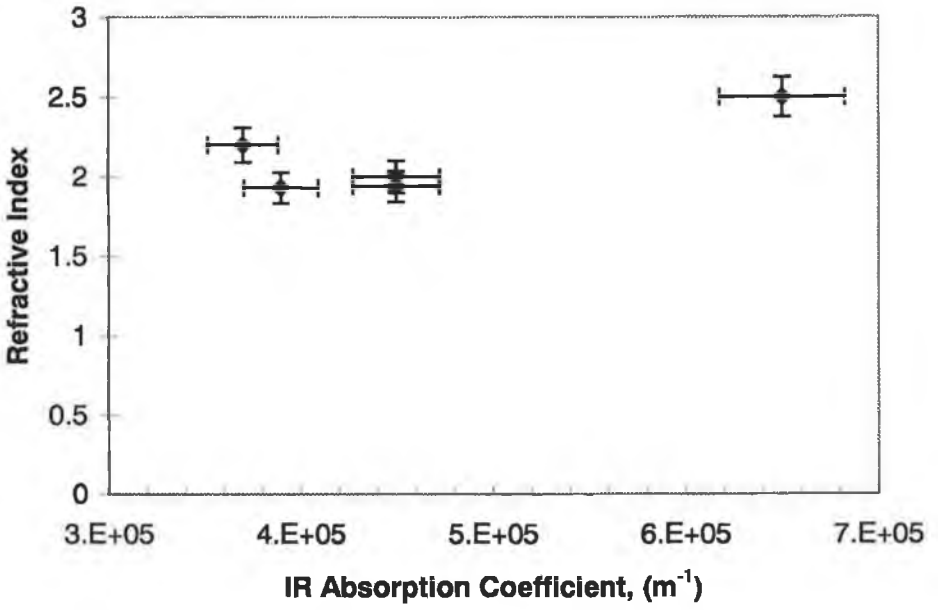

Figure 5.29: Refractive index versus C=N absorption coefficient.

The following figures show the refractive index and extinction coefficient of carbon nitride films deposited at different nitrogen partial pressures as a function of photon energy.

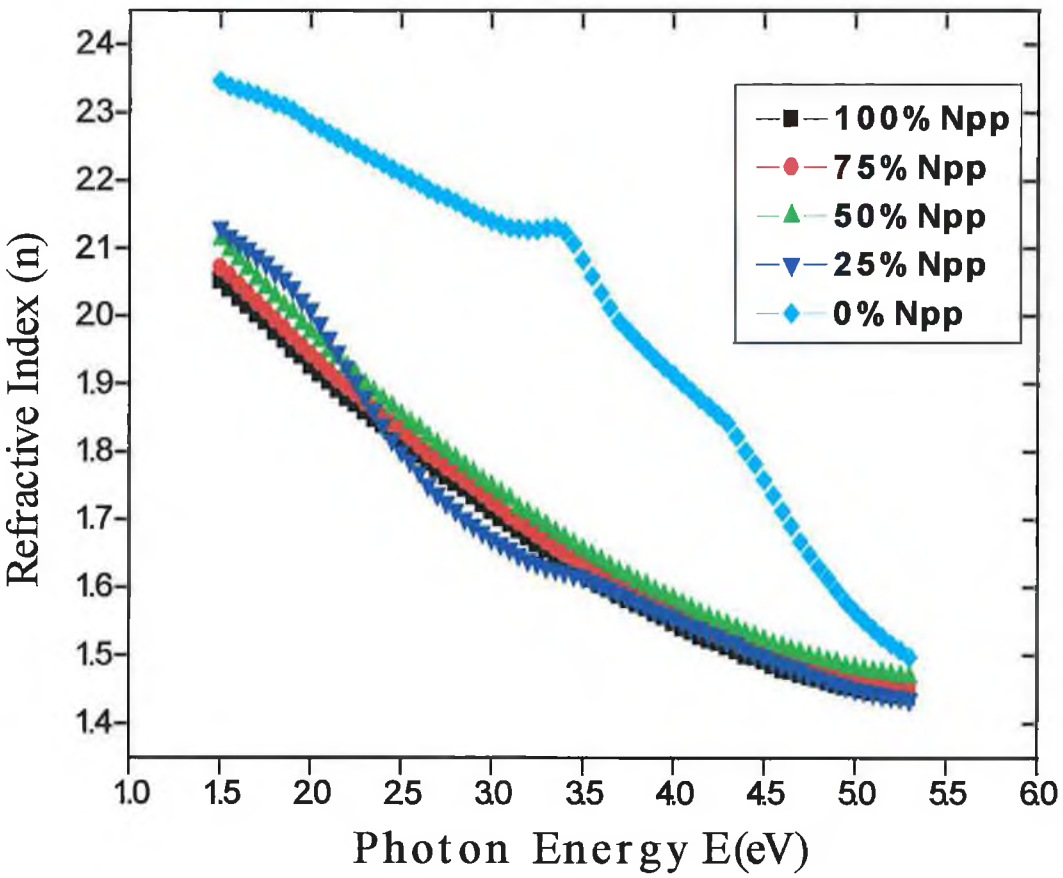

Figure 7.30: Refractive Index vs. Photon Energy.

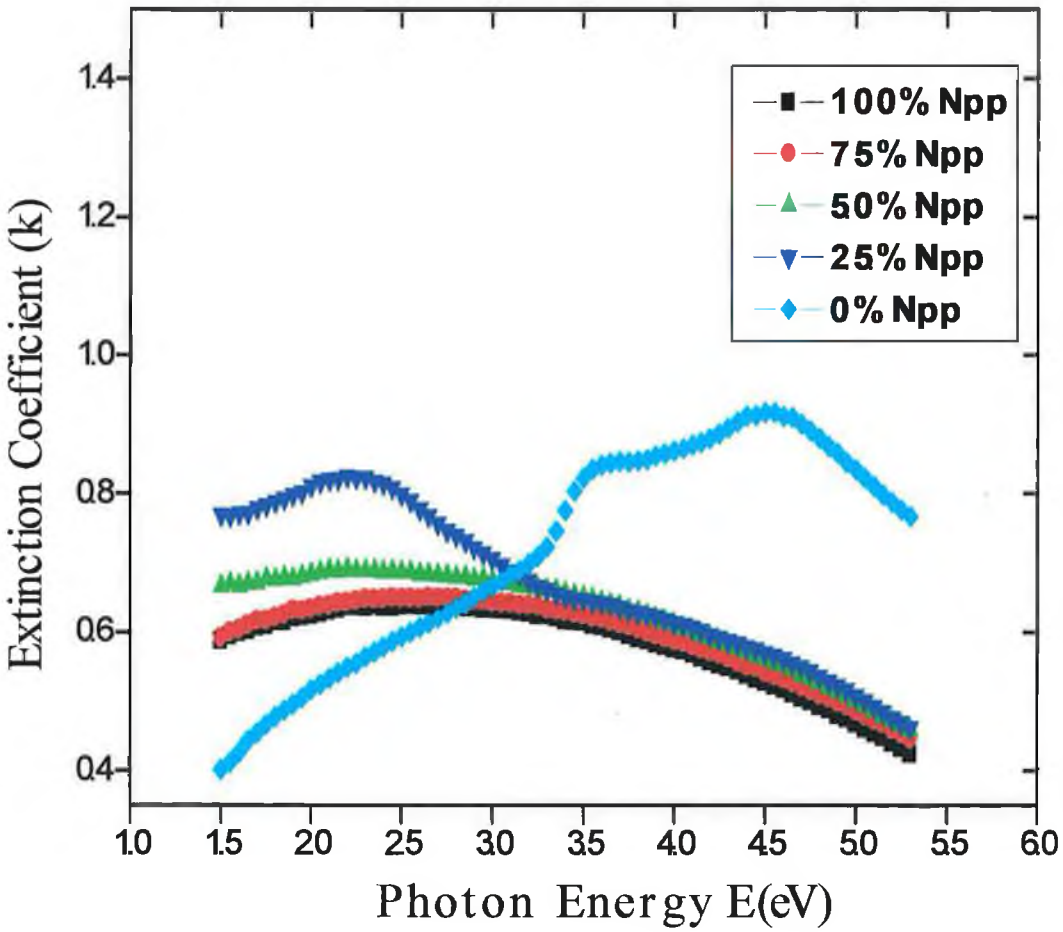

Figure 7.31: Extinction coefficient vs. Photon Energy.

Since all the synthesized CN_x thin films were dominantly amorphous, their optical properties such as refractive index n and extinction coefficient k are expected to have the characteristics of an amorphous semiconductor. The refractive index (n) is a decreasing function of photon energy (*figure 7.30*) while the extinction coefficient (k) exhibits a different behaviour (*figure 7.31*). In other reports of CN_x amorphous films[45,50] the refractive index (n) is generally found to decrease with photon energy whereas the extinction coefficient (k) is found to increase with photon energy in the range 1.5 to 3.5 eV.

Here, it can be seen that the n values of the deposited CN_x films grown at 50, 75 and 100% Npp depend linearly on the photon energy in the range 1.5-3.5 eV with an equivalent wavelength of 826-354 nm. The samples grown at 0 and 25% Npp have different features but follow the general trend.

Generally, the k value (like the absorption of the films) shows a rapid decrease with decreasing photon energy in the visible region, which is a typical behaviour of semiconductors.[35] In *figure 7.31*, it can be seen that the extinction coefficient k of the sample grown with Npp=0 is lower than the other CN_x films in the low photon energy region (E<3 eV), which is probably due to the high level of disorder and defects of the CN_x films which act as optical absorption and scattering centers in the film.[51] A similar trend in the extinction coefficient values was reported by Wang et al.[52] for a-CN_x films grown by ion-assisted arc deposition. If the k value at 632.8 nm is taken (which correspond to E ~1.96 eV), it can be seen that k increases from 0.5 (Npp=0%) to 0.8 (almost dispersionless) (Npp=25%) and then decreases to 0.65 (Npp=50%) and finally to 0.6 (Npp=75, 100%). The increase in the extinction coefficient signals the loss of transparency. The observed variation in the extinction coefficient might be attributed to the increase of size and/or number of sp^2 clusters.[53] It was reported by Savvides[54] that n and k of a-C films both decrease in the visible region with an increase in the sp^3/sp^2 ratio. In terms of the relationship between n, k, and carbon nitride bonding characteristics found here, both decreasing n and k (for Npp>25%) suggest that higher nitrogen partial pressures stabilise the sp^3-type bonding, as discussed in chapter 6.

7.2.6 Summary

Electrical properties of amorphous carbon nitride films were investigated. The electrical conductivity, as expected, is very dependent on the nature of the atomic bonds. The resistivity increase appears to be due to the amount of C≡N bonding rather than the total nitrogen concentration or other bond type. The main effects of including nitrogen appear to be due to structural changes in the film leading to different band-gap structures rather than a conventional doping effect. This is not surprising due to

the high concentration of nitrogen in the films, which is no longer a dilute dopant but has a major effect in the atomic rearrangements. The effect of nitrogen incorporation in the electrical properties of the films has proved to be very different to the effect it has when incorporated to semiconducting forms of a-C such as a-C:H and ta-C. The bonding structure of these forms of carbon is manly sp^3, which gives larger optical gaps and allow, in some cases, nitrogen doping to be efficient. The amorphous carbon produced in this work is highly conducting, consisting mainly of sp^2 sites, in which nitrogen can only take non-doping configurations. The absorption edge is observed to be very broad, indicating a high degree of disorder in the films. The measured optical band gap is low and decreases with nitrogen partial pressure. Above 50% Npp, the calculated gap increases slightly which signals an increase in the sp^3 nature of the bonding structure. No relation was found between the increase in resistivity and the measured Tauc optical gap.

The disordered structure and the low mobilities (<0.3 cm^2/Vs) derived from absorption and transport measurements of deposited carbon nitride films imply that the transport properties are similar to those found in the majority of amorphous semiconductors. In many cases amorphous semiconductors have sufficiently large density of defects so that conduction associated with direct motion between defect states dominates the transport over significant temperature ranges.

From thermal activation studies of the resistivity, the activation energy increases with the nitrogen content, suggesting a reduction in the density of defect states near the conduction band edge. The higher resistivity for nitrogen-doped films was also explained with the help of an energy band diagram, by the movement of the Fermi level below the conduction band. For temperatures above 166 K, the activation energy is a linear function of temperature and increases with nitrogen partial pressure. For temperatures below room temperature, the conduction mechanism is suggested to be dominated by a mixture of transport by carriers excited into localized states at the band edges (thermally activated hoping) and hopping at localized states close to the mobility edges (fixed range hopping). At higher temperatures, transport by carriers excited beyond the mobility edges into non-localized (extended) states is likely to be

the dominant conduction mechanism. Pure carbon films showed a small variation of resistivity as a function of temperature which indicates that the conduction mechanism is different to nitrogen-containing films and is related to a conduction typical of graphite with defects.

The resistivity of the films was found to decrease with substrate bias. As substrate bias is increased, the accompanying decrease in the amount of C≡N bonds linked to carbon nitride aromatic rings facilitates electrical transport within the film by increasing of conduction paths by cross-linking. The observed decrease in resistivity with deposition temperature was related to an increased graphitization of the films, giving properties closer to those of graphite, such as narrowing of the band gap and increased conductivity.

The refractive index also reduces with nitrogen content. In this case also, the C≡N bond density is the best predictor of the refractive index. The decrease in refractive index might also be accompanied by a decrease in film mass density. The behaviour of the refractive index and extinction coefficient for films deposited at different Npp confirms the increase in the sp^3/sp^2 ratio for Npp>25%.

PART III

7.3 FIELD EMISSION

7.3.1 Introduction to field emission devices and materials

The field emission display is a flat panel display in which electrons are emitted from an array of field emission cathodes, accelerated across a vacuum gap, and then they form and image as they hit a flat phosphor screen. DLC is a strong candidate for field emission cathodes in such displays because of its low electron affinity and chemical inertness. The potentially most important display application of field emitters is in flat-panel, matrix-addressed displays to replace conventional relatively bulky cathodic ray tubes (CRT).

The field emission of electrons from solids obeys the Fowler-Nordheim (F-N) equation for quantum mechanical tunnelling over a barrier,[55]

$$J = aE^2 \exp(-b\phi^{3/2} / \beta E)$$

where J is the current density in Am^{-2}, ϕ is the barrier height in eV, E is the electric field in Vm^{-1}, β is the field enhancement factor at sharp geometries, and a and b are constants (for practical purposes). The F-N theory describes the field emission of electrons from metals into vacuum due to an applied electric field.[56] Electrons from the cathode escape into vacuum through the barrier as opposed to jumping over it. The work function governs the electron emission from the cathode. This emission mechanism applied to a nominally flat cathode requires surface features, or protrusions, to produce a large enough field enhancement to allow the local electric field to be great enough to produce tunnelling.[57] Existing field emission displays (FED) use 'Spindt' tips of Mo or Si as cathodes, as shown in *figure 7.32a*. Amorphous carbon nitride coatings have been used on Silicon tips, which lowered the turn on voltage and increased the emission current.[58,59]

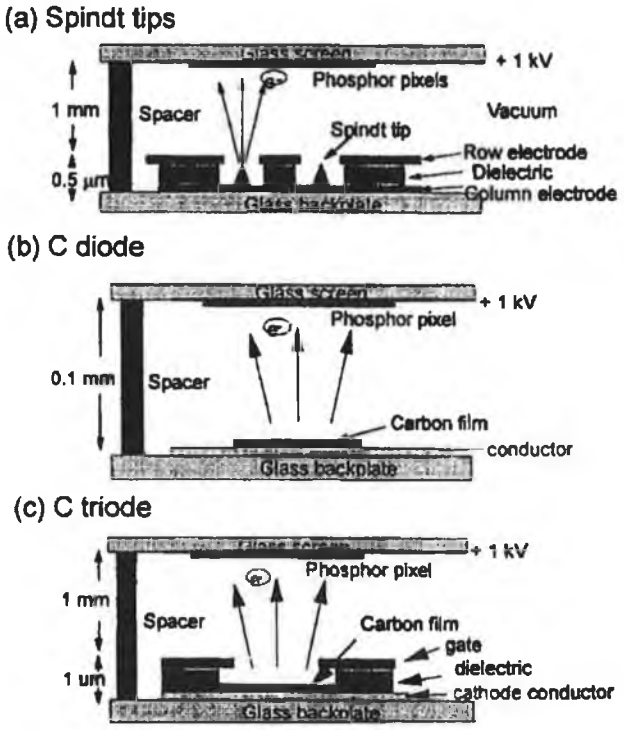

Figure 7.32: (a) Field emission displays using Spindt tips, (b) Carbon films in diode design and (c) Carbon films in triode design.

An alternative to this is the use of thin films of materials which naturally emit electrons at low electric fields (low electron affinity (EA) materials). EA is defined as the difference between the vacuum level and the conduction band of a material. Hydrogenated diamond surfaces have a negative electron affinity (NEA), and in principle can emit electrons with a minimal barrier. The electron emission from diamond films has been widely studied. The drawback is that diamond deposited by CVD requires growth temperatures above 600° C, which is incompatible with the insulating glass substrates needed to isolate each pixel. DLC can be deposited cheaply at room temperature and the absence of tips and the chemical inertness and low sputter yield of DLC minimises the poisoning and erosion of the cathodes. *Figure 7.32b* shows a schematic representation of the simplest FED using DLC. The DLC film is deposited as a series of thin film microcathodes connected as the rows of the matrix. The phosphor pixels are anodes and are connected as columns. It is a simple and relatively economic design.

In the triode configuration (*figure 7.32c*), the emission field is generated by gate electrodes placed close to the cathodes.

All materials must have a positive work function (E_{vac}-E_F) with the Fermi level E_F lying below the vacuum level E_{vac}. In most materials, the electron affinity is also positive with the conduction band minimum lying below E_{vac} as in *figure 7.33a*. In a NEA material, such as hydrogen terminated diamond, the conduction band minimum lies above E_{vac} (*figure 7.33b*). Electron emission properties of diamond are reviewed by Yater et al.[60] A number of wide gap semiconductors such as c-BN and AlN also have NEA. The low electron affinity in diamond derives fundamentally from its electronic bonding. In diamond, bonds are formed by the interaction of sp^3 hybrids, giving rise to the filled bonding (σ) and the empty anti-bonding (σ^*) states. These states develop into the valence and conduction bands respectively and the conduction band lies above the vacuum level as in *figure 7.33c*. Thus, the origin of the NEA in diamond and similar materials is primarily their wide band gap. However, despite the ability to emit electrons very easily, the emission current is not very high. This is due to the very low free carrier concentration in a perfect diamond resulting from its high band gap. That is why it is necessary to modify the band gap and the free carrier concentration by using n- or p-type doping.

Electron affinity (EA) depends fundamentally on the type of bonding, not the crystallinity, so that amorphous diamond-like carbon also has a low electron affinity. The amount of sp^3 bonding in any DLC depends on the deposition process used. The electronic structure of a-C depends on its sp^3 content; sp^3 sites form only σ bonds, while sp^2 sites form both σ and the weaker π bonds. The optical gap in a-C depends on the sp^2 content. The overall data for a-C:H suggests that the EA decreases with increasing sp^3 content.

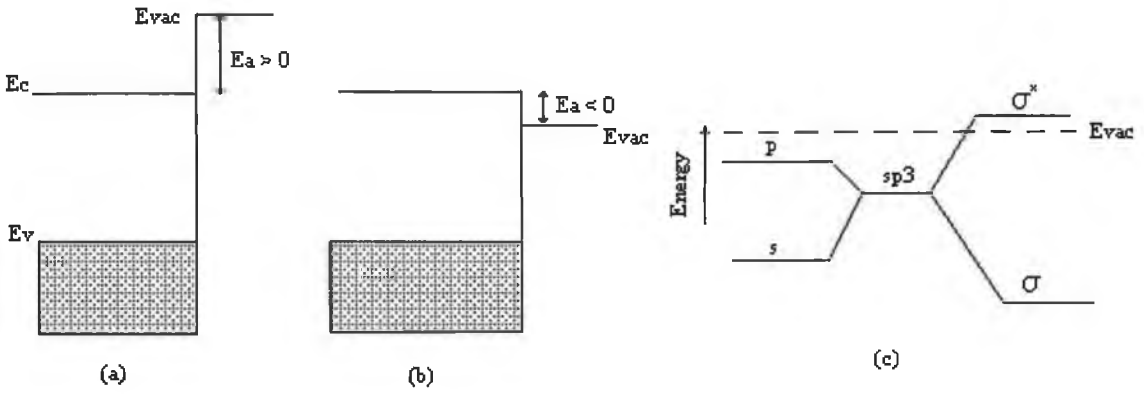

Figure 7.33: (a) Positive electron affinity, (b) Negative electron affinity (NEA), (c) Bands in diamond with the conduction band maximum lying above the vacuum level giving NEA.

Turn-on fields for diamond have been found to range from 0.5 to 20 V μm^{-1}. The first direct study of field emission from a-C:H was performed by Amaratunga and Silva.[61] With a band gap of 2.1 eV and 55% sp^2 content, the emission experiments were carried out on a-C:H samples deposited on n^{++}-Si using a parallel plate configuration with an anode of ITO coated glass and glass fibres used as spacers at pressures of $5x10^{-7}$ Torr. The turn on field found was 26 V μm^{-1}. The emission was greatly increased for a-C:H modified by nitrogen. For N doped samples emission is seen at fields in the order of 4-6 V μm^{-1}. The emission current is found to obey the Fowler-Nordheim equation, with an effective barrier height of $\phi \approx 0.05$ eV. Results reported by Munindrasa et al.[62] of field emission data when electrons a emitted to vacuum from a-C:H:N in a Si/a-C:H:N heterojunction structure indicate that the barrier to electron emission from a-C:H:N surface into vacuum is at the Si/a-C:H:N interface and can be almost completely overcome through electron heating in the conduction band due to the high electric field within it (high field transport). The best field emission properties were found for a-C films with high sp^3 content, with currents as high as 20-40 μA for electric field intensities < 20 V μm^{-1}.[63] The electron emission process that occurs in amorphous hydrogenated carbon nitride films has been suggested to be different from emission from diamond surfaces.[64,65] It is assumed that emission occurs from randomly occurring isolated protrusions at the film surface, which form a narrow

region of energy about E_F, rather like emission from a metal. Most of the emitted electrons come from the gap states not the conduction band.

7.3.2 Emission experiments on carbon nitride

The emission configuration arrangement is shown in *figure 7.34*. Highly doped (100) n^+-Si (0.001-0.0055 Ωcm) was used as the substrate material and the back contact to the films. Indium tin oxide (ITO) coated glass slides and Al evaporated onto glass slides were used as anodes. The contact to the anode was made using highly conducting silver paint. Phosphor powder was used on the ITO coated glass to try to detect the distribution of emission sites. Unfortunately, emission current was only detected when Al coated glass was used as anode possibly due to lower contact resistance. The spacing between the plate anode and the cathode was set at 50 μm using a Polyamide-Nylon insulating film as a spacer. A square hole was cut in the film spacer so that the overlap between cathode and anode was $1cm^2$. The experimental set up was mounted in a diffusion pumped chamber. A spring arrangement was used to press firmly the anode onto the spacer. Thin flexible wires were used for connections at the top and bottom contacts to minimise vibrations from the pumps. A scheme of the measurement equipment used is shown in *figure 7.35*. The electric field is obtained by taking the entire applied voltage to be dropped across the vacuum gap. The maximum electric field attainable was 20 V μm^{-1} due to the voltage supply limitation of 1000 V.

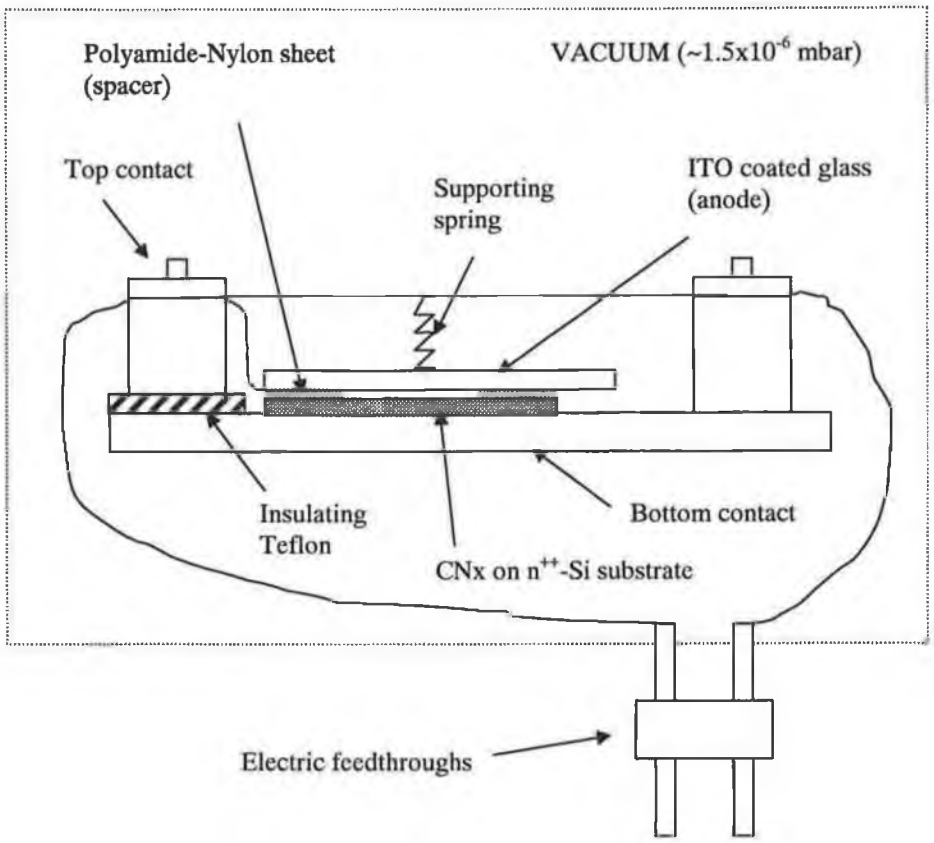

Top view:

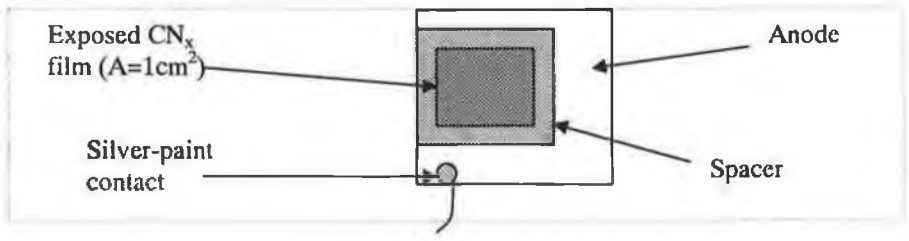

Figure 7.34: Electron emission configuration.

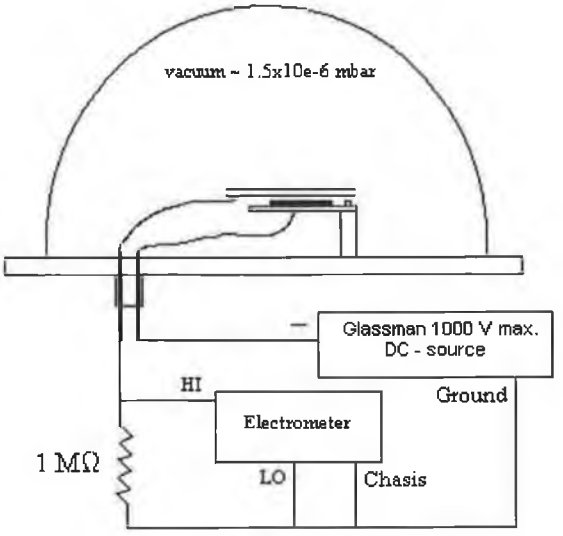

Figure 7.35: Experimental set up for electron emission measurements.

The measurements were carried out at a pressure of approximately $1.5x10^{-6}$ mbar. Films grown at different nitrogen partial pressures and different deposition temperature were analysed. Emission current was only present in films grown at 100% Npp; films were ~1 μm thick. In *figure 7.36*, current density (J) versus electric field (E) plots of two films grown with no additional heat (deposition temperature Td=280°C) and at Td=420°C are shown. The data in *figure 7.37* is plotted according to the Fowler-Nordheim (F-N) relationship for field emission. If the F-N relationship is put in the form:

$$\ln(J/E^2) = -b\phi^{3/2}/E + \ln(a)$$

then, a plot of $\ln(J/E^2)$ against 1/E should give a straight line if a F-N field emission behaviour is taking place in the films.

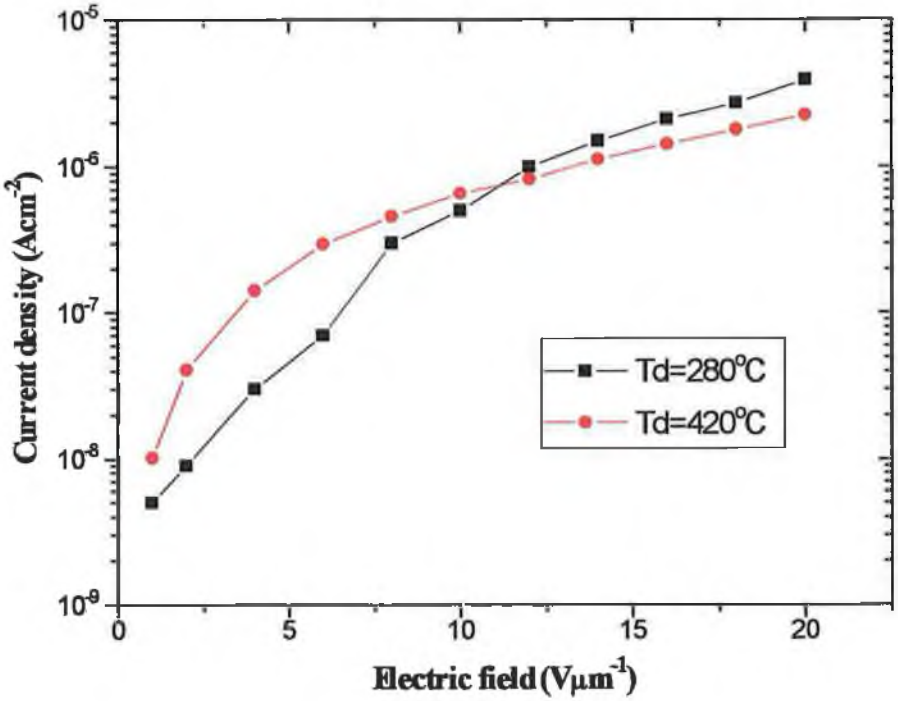

Figure 7.36: Electron emission characteristics of carbon nitride films deposited at different deposition temperatures and 100% Npp.

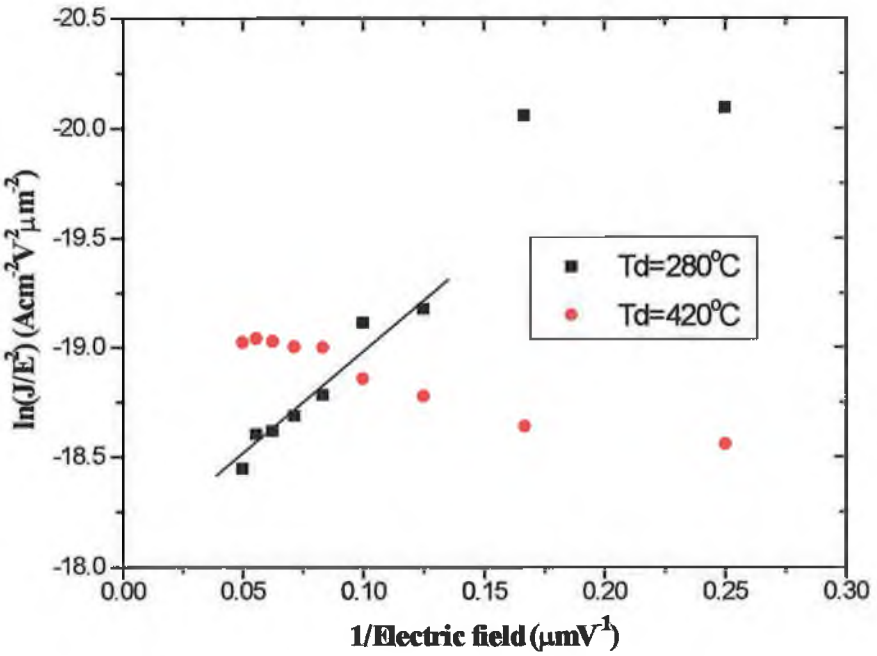

Figure 7.37: Fowler-Nordheim plots of carbon nitride films.

Figure 7.36 shows that both films exhibit similar emission behaviour. The turn on electric field for an emission current density of 1 μAcm^{-2} from the emission data are 14 V μm^{-1} for the low Td sample and 12 V μm^{-1} for the high Td sample. In the F-N relationship plotted in *figure 7.37*, it can be seen the low Td sample has a better fit than the high Td sample in the high field region. However, the $J \propto E^2$ relationship emanating from the F-N equation, which is applicable when electron emission from the surface is readily achieved,[66] cannot explain for itself the emission observed. According to the model proposed by Amaratunga[61] for emission in a-C:H:N, the electron emission observed here could be due to ionised donor centers due to the presence of the n^{++}-Si/a-CN heterojunction. As was also proposed by Munindrasa,[62] the barrier for field emission of electrons into vacuum comes from the Si/a-CN interface and the emission barrier into vacuum is overcome by electron heating in the conduction band due to high field transport. The high conductivity of the films can sustain the electron transport to the surface and makes electron emission possible. Electron emission might be due to a mixture of this mechanism and emission occurring from protrusions of the surface, as proposed by Modinos[64] for amorphous carbon nitride films.

Not enough studies have been performed to get more insight in the dependence of the vacuum electronic properties on nitrogen content in carbon nitride films. The emission mechanism of the films investigated here is different from that in diamond and materials with NEA. A high positive electron affinity is expected for carbon nitride films due to the small band gap. Carbon nitride films investigated here have low resistivity (~1 Ωcm) and low optical gap (~0.1 eV) indicating a low fraction of sp^3 sites in the amorphous sp^2 matrix. Despite these characteristics, some electron emission was measured. The high fraction of conducting amorphous sp^2 sites is presumably the reason for the measured current densities of up to 4 μAcm^{-2} at an electric field of 20 V μm^{-1}. It is clear that the field emission of $1mAcm^{-2}$ required for diode-type field emission displays cannot be obtained with the carbon nitride films investigated. An optimised microstructure consisting of graphitic sp^2 sites as conductor and n-type doped wide band gap sp^3 sites as field emitter is probably the ideal material for cold cathode emitters.

References

1. Milton Ohring, The material science of thin films, Academic Press, Boston (1992).
2. S.R. Elliott, Physics of amorphous materials, Longman, London, NY (1983).
3. L. Kazmerski, Polycrystalline and amorphous thin films and devices (Materials science and technology series), Academic Press, NY (1980).
4. Valdes, L.B., Proc, IRE, 42 (1954) 420.
5. H. Weider, Laboratory notes on electrical and galvanomagnetic measurements, Elsevier, Amsterdam (1979) 7-9.
6. L.J. van der Pauw, Philips Research Reports. 13, 1 (1958) 1-9.
7. David C. Look, Electrical characterisation of GaAs materials and devices, Wiley, NY (1989) 12-20.
8. E.H. Hall, "On a new action of the magnet on electric currents", Amer. J. Math, 2, (1879) 287-292.
9. N.F. Mott and E.A.David, Electronic Processes in non-crystalline materials, 2nd. ed., Clarendon, Oxford, (1979).
10. J.Tauc, Amorphous and Liquid Semiconductors, Plenum Press, (1974).
11. H.G. Tompkins, A Users Guide to Ellipsometry, Academic Press Inc., San Diego, (1993).
12. M.S. Tyagi, Introduction to semiconductor materials and devices, Wiley, NY (1991).
13. B.C. Holloway, D.K. Shuh, M.A. Kelly, W. Tong, J.A. Carlisle, I. Jimenez, D.G.J. Sutherland, L.J. Terminello, P. Pianetta, S. Hagstrom, Thin Solid Films, 290-291 (1996) 94.
14. Soon-Cheon Seo, David C. Ingram and Hugh H. Richardson, J. Vac. Sci. Technol. A 13, 6 (1995) 2856.
15. A. Grill and V. patel, Appl. Phys. Lett. 60, (1992) 2089.
16. N-H. Cho, K.M. Krishnan, D.K. Veirs, M.D. Rubin, C.B. Hopper, and B. Bhushan, J. Mater. Res.,5, 11, (1990) 2543.
17. He-Xiang Han and Bernard J. Feldman, Solid State Comms. 71, 10, (1989) 801.
18. M. Vogel, O. Stenzel, R. Petrich, G. Schaarschmidt, and W. Scharff, Thin Solid Films, 227 (1993) 74.

19. M. Vogel, O. Stenzel and W. Grünewald, Thin Solid Films, 209 (1992) 195.
20. O. Stenzel, M. Vogel, S. Ponitz, T. Wallendorf, C. Borczyskowski, F. Rozploch, Z. Krasilnik and N. Kalugin, Phys. Stat. Sol. (a) 140, (1993) 179.
21. J. Schwan, V. Batori, S. Ulrich H. Ehrhardt and S.R.P. Silva, J. Appl. Phys. 84, 4 (1998) 2071.
22. Jayshree Seth, R. Padiyath and S.V. Babu, Diam. Relat. Mater. 3 (1994) 210.
23. J. Robertson and E.P. O'Reilly, Phys. Rev. B 35 (1987) 2946.
24. N. Axen, G.A. Botton, H.Q. Lou, R.E. Somekh and I.M. Hutchings, Surface and Coatings Technology 81 (1996) 262.
25. O. Amir and R. Kalish, J. Appl. Phys. 70, 9 (1991) 4958.
26. P. Wood, T. Wydeven, O. Tsuji, Thin Solid Films, 28 (1995) 151.
27. S.R.P. Silva, J. Robertson, G.A.J. Amaratunga, B. Rafferty, L.M. Brown, J. Schwan, D.F. Franceschini, G. Mariotto, J. Appl. Phys. 81, 6 (1997) 2626.
28. S.R.P. Silva, K.J. Clay, S.P. Speakman, G.A.J. Amaratunga, Diam. Relat. Mater. 4 (1995) 977.
29. P. Stumm, D.A. Drabold and P.A. Fedders, J. Appl. Phys. 81, 3 (1997) 1289.
30. J. Schwan, W. Dworschak, K.Jung and H. Ehrhardt, Diam. Relat. Mater. 3 (1994) 1034.
31. Kwang Bae Lee, Duck Jung Lee and Yong Woo Shin, Mat. Res. Soc. Symp. Proc. 446 (1997) 401.
32. J. Robertson, C.A. Davis, Diam. Relat. Mater. 4 (1995) 441.
33. J. Robertson, Advance in Physics, 35 (1986) 317.
34. Bing Zhang and Bo Wei, IEEE transactions on magnetics, 33, 5 (1997) 3109.
35. Hsiao-chu Tsai and D.B. Bogy, J. Vac. Sci. Technol. A 5, 6 (1987) 3287.
36. T. Frauenheim, U. Stephan, K. Bewilogua, F. Jungnickel, P. Blaudeck and E. Fromm, Thin Solid Films, 182 (1989) 63.
37. K. Shimakawa and K. Miyake, Phys. Rev. B, 39, 11 (1989) 7578.
38. J. Robertson, E.P. O'Reilly, Phys. Rev. B, 35, 6 (1987) 2946.
39. F. Demichelis, X.F. Rong, S.Schreiter, A. tagliaferro, C. De Martino, Diam. Relat. Mater. 4 (1995) 361.

40. P. Hammer, M.A. Baker, C. Lenardi and W. Gissler, "Ion Beam Deposited Carbon Nitride Films: Characterization and Identification of Chemical Sputtering" IMCTF 96 Proceedings.
41. J.C. Dawson and C.J. Adkins, J. Phys.: Condensed Matter 7 (1995) 6297.
42. T. Iwasaki, M. Aono, S. Nitta, H. Habuchi, T. Itoh ans S. Nonomura, Diam. Relat. Mater. 8 (1999) 440.
43. J. Tauc, in Optical Properties Of Solids, ed. F. Abeles, North Holland, Amsterdam (1972) 277.
44. J.J. Hauser, Solid State Comms. 17 (1975) 1577.
45. J.J. Hauser and J.R. Patel, Solid State Comms. 18 (1976) 789.
46. S. Lee, S.J. Park, S. Oh, W.M. Kim, J.H. Bae, B. Cheong, S.G. Kim, Thin Solid Films, 308-309 (1997) 135.
47. X. Wang, P.J. Martin, Appl. Phys. Lett. 68, 9 (1996) 1177.
48. O. Stenzel, R. Petrich, Optical Engineering, 32 (1993) 2951.
49. G. Sreenivas, S.S. Ang and W.D. Brown, J. Electronic Materials, 23 (1994) 569.
50. M. Jelinek and W. Kulisch, Diam. Relat. Mater. 8 (1999) 1857.
51. Y.F. Ju, Z.M. Ren, W.D. Song and D.S.H. Chan, J. Appl. Phys. 84, 4 (1998) 2133.
52. X. Wang, P.J. Martin, T.J. Kinder, Thin Solid Films, 256 (1995) 148.
53. Ray Wen-Jui Chia, Eric Li, Seiki Sugi, G.G. Li, Helen Zhu, A.R. Forouhi, Iris Bloomer, Thin Solid Films, 308-309 (1997) 284.
54. N. Savvides, J. Appl. Phys. 59, 12 (1986) 4133.
55. I. Brodie and P.R. Schwoebel, Proceedings of the IEEE, 82 (1994) 106.
56. X. Wang, J.P. Zhao, Z.Y. Chen, S.Q. Yang, T.S. Shi and X.H. Liu, Thin Solid Films, 317 (1998) 356.
57. R.D. Forrest, A.P. Burden, S.R.P. Silva, L.K. Cheah and X. Shi, Appl. Phys. Lett. 73 (1998) 3784.
58. E.J. Chi, J.Y. Shim, H.K. Baik, S.M. Lee, Appl. Phys. Lett. 71 (1997) 324.
59. E.J. Chi, J.Y. Shim, D.J. Choi and H.K. Baik, J. Vac. Sci. Technol. B (1998) 1219.
60. J.E. Yater, A. Shih and R. Abrams, J. Vac. Sci. Technol. A 16 (1998) 913.
61. G.A.J. Amaratunga and S.R.P. Silva, Appl. Phys. Lett. 68 (1996) 2529.

62. D.A.I. Munindrasa, M. Chhowalla, G.A.J. Amaratunga, and S.R.P.Silva, Journal of non-crystalline solids, 227-230 (1998) 1106.
63. J.P. Zhao, X. Wang, Z.Y. Chen, S.Q. Yang, T.S. Shi, X.H. Liu and S.C. Zou, Nucl. Instr. and Meth. in Phys. Res. B 127/128 (1997) 817.
64. A. Modinos and J.P. Xanthakis, Appl. Phys. Lett. 73 (1998) 1875.
65. J.P. Xanthakis and A. Modinos, Diam. Relat. Mater. 8 (1999) 798.
66. S.R.P. Silva, G.A.J. Amaratunga, J.R. Barnes, Appl. Phys. Lett. 71 (1997) 1477.

CHAPTER 8

CONCLUSIONS AND RECOMMENDATIONS

This last chapter deals with the main conclusions that can be drawn from all the different investigations carried out for the completion of this thesis. Recommendations for future work that can be considered are given in some of the sections in terms of further exploiting the deposition of novel carbon nitride films using the Penning-type magnetron sputtering technique. Regarding electrical measurements, experimental set ups are also recommended from which more information may be obtained about the electronic states and electrical properties of the carbon nitride films, and are in principle suitable for studying films with an amorphous structure and lack of long range order.

8.1 Deposition technique

A novel dc magnetron sputtering technique based on the Penning-type geometry was used to deposit carbon nitride films. The deposition technique consists of two opposed targets, with very strong magnets placed behind them such that the magnetic flux lines are oriented along the axis between the targets. With this configuration, electrons experience strong magnetic confinement between the two targets, increasing the ionisation near the substrate which results in higher deposition rates (2-3μ/h) and higher nitrogen incorporation in the films (35-40 at.% N).

Optical mass spectroscopy showed high levels of nitrogen ions relative to neutrals and the presence of CN radicals which is due to nitrogen incorporation in the graphite targets. The incorporation mechanism of nitrogen into the carbon network is mainly determined by the arriving fluxes of nitrogen and carbon atoms on the growing surface.

8.2 Structure and composition of carbon nitride films

A brief introduction to spectroscopy techniques was given to understand how they can be useful in investigating the bonding structure of thin films. The carbon nitride films grown by magnetron sputtering technique were found to be mainly amorphous. However, from TEM analysis, there is also some evidence of crystalline regions co-existing with the mainly amorphous network. The lack of sensitivity in the techniques employed, the low intensity of the signal emanating from the crystalline regions and the possible overlapping of crystalline signals with the stronger amorphous signals made the detection of crystalline regions with the techniques considered here an impossible task.

8.2.1 Amorphous carbon nitride

Most of the investigated films were deposited in an Ar/N_2 gas mixture at $1x10^{-3}$ mbar total pressure with –50 V bias voltage and the maximum deposition temperature was recorded as 280°C. Graphite targets were used which were driven in constant current mode (3A). Films grown at higher pressures (~$1x10^{-2}$ mbar) showed high levels of stress due to hydrogen incorporation from residual moister inside the chamber.

RBS studies indicated that the nitrogen content in the films increases rapidly with nitrogen partial pressure (Npp) up to ~25 at.% N. Above 50% Npp, there is not a good correlation between nitrogen content and Npp. The deposition rate increases with nitrogen partial pressure due to enhanced momentum transfer to the sputtering targets. The effect of substrate bias on film composition was investigated. It has been shown that the composition of the films remains unchanged while the growth rate declines significantly probably due to chemical sputtering from the substrate.

An increase in deposition temperature was observed to cause a decrease of the nitrogen activated bands in the Raman spectra suggesting a decrease in nitrogen content. Post-deposition annealing treatment caused a decrease in nitrogen content. The mechanism of nitrogen loss is different in both cases.

IR spectra showed that nitrogen is bonded to carbon as C=N and C≡N, and forms part of the overall backbone structure. The IR spectra is dominated by a strong absorption peak at~1100-1800 cm^{-1} which becomes dipole-transition active under infrared energy excitation due to the symmetry breaking caused by N incorporation into the carbon network. This band can be identify with the Raman active G and D bands observed at 1550 cm^{-1} and 1360 cm^{-1} and attributed to graphitic and disordered sp^2 microdomains. However, when nitrogen content in the films exceeds ~25 at.%, the IR absorption due to nitrogen bonded to carbon remains unchanged. It was suggested that a significant amount of nitrogen is bonded in IR-invisible structures such as N-N bonds. Raman spectroscopy was used to proof this point. By deconvoluting the Raman D and G region, the existence of a third peak in between the D and G peaks was observed. This peak was assigned to the N=N stretching vibration. It was concluded that above 25 at.% N, an increasing amount of the nitrogen forms N=N bonds which causes an structural rearrangement within the film. The features observed in the IR and Raman spectra are quite similar with a broad active band in the range 1100-1800 cm^{-1} and the C≡N stretching peak at ~2200 cm^{-1}.

XPS peaks of the C1s and N1s core level electrons were assigned to different types of bonds by comparison with typical values found in literature and bearing in mind the structural information that was obtained previously by IR and Raman. The N1s peak positions were assigned to different type of bonds as follows: C≡N at ~398.8 eV, C=N at ~400 eV and N-N at ~401.2 eV. On the other hand, the C1s peaks were assigned as: C≡N at ~288.5 eV, C=N at ~286 eV and C-C/C-N at ~287.5 eV. A molecular structure of the amorphous regions was proposed in which N atoms adopt an sp^2 configuration in the graphite ring structure as the one seen in pyridine which has C=N and C=C bonds in the aromatic ring. The structure is completed by N=N bonds and C≡N bonds which act as network terminators.

The effect of substrate bias on the structure of deposited carbon nitride films has been investigated. Substrate bias did not seem to have a major effect in the films microstructure when analysing the variation of the Raman and IR spectra of the films deposited at different bias. Only the C≡N bond density appears to decrease with bias.

Valence band (VB) XPS measurements are shown to be more sensitive than Raman spectroscopy to changes in bonding structure. The effects of substrate bias during deposition on the VB have also been investigated. It was shown that the VB spectrum is more characteristic of a 'diamond-like' material at substrate bias between -75 and -150 V. The hardness also reaches a maximum in this range. It is therefore concluded that ion bombardment (controlled by the applied negative substrate bias) in this range causes a process of 'densification' or 'stress induction' which maximizes the carbon sp^3 bonding, similar to that which occurs in carbon films.

A heating plate was incorporated in the system to study the effect of increasing deposition temperature in the film microstructure. Maximum temperatures of 420°C were achieved with the new heating configuration. Increased deposition temperature was seen to promote graphitization of the films. The effect of lower deposition temperatures in the films remains a mystery, but is something that could be considered in the future. It should not be very difficult to incorporate water cooling or even liquid nitrogen cooling into the substrate platform, although if the substrate platform is biased, one has to ensure that the liquid flow and its associated pipework do not cause a partial electrical short by excessive resistive or capacitive coupling to ground.

8.2.2 Crystalline carbon nitride

To check for nanocrystalline areas which could co-exist with the mainly amorphous material, films deposited with 100% Npp atmosphere at $1x10^{-3}$ mbar and –50 V bias voltage, containing approximately 33 at.% N as measured by RBS were investigated by plan view transmission electron microscopy (TEM).[1] Some regions exhibit electron diffraction patterns showing sharp rings associated with diffraction from a crystalline medium. The calculated interplanar spacing values obtained from the nanocrystalline regions have a close correspondence with the theoretical values for β-C_3N_4.[2]

Some parameters of the plasma created with the Penning source were measured by a Langmuir probe. The measurements showed that the ion flux/neutral flux ratio (mainly N_2^+/N_2) is ~0.25 and the carbon atom flux/ion flux ratio (mainly C/N_2^+) is ~0.02. These parameters are very important for the formation of crystalline areas in

the films. The large overabundance of ionised nitrogen compared with carbon may be significant in the formation of the crystalline material. Also, the degree of ionisation in the inter-target region is >4% giving a very high concentration of excited and reactive species. So, the increased nitrogen ionisation possibilities the formation of areas of crystalline material, at relatively low temperatures (~280°C). However, the formation of paracyanogen still needs to be addressed in order to obtained carbon nitride films with larger crystalline regions. If the gaseous -C≡N is bonded to the surface, the triple bond is too strong to be broken, impeding the formation of a perfect sp^3 configuration. The use of high substrate temperatures in sputtering was seen to promote film graphitization. The main problem at high temperatures is dealing with the desorption of C≡N species from the growth surface which forms volatile cyanogen molecules resulting in a deficiency of nitrogen in the film. The use of low deposition temperatures (<200°C) may be an interesting way to proceed in order to improve the quality of the films.

The intense ionisation in the plasma and the high ion flux at the substrate provides a high concentration of atomic nitrogen, which helps to promote the β-C_3N_4 phase. In addition, biasing the substrate provides ion bombardment, which stimulates the formation of sp^3 hybrids. It is hoped that the volume fraction of the crystalline regions may be increased by depositing on substrates that have a better lattice match with β-C_3N_4 than silicon (100) such as silicon (111) or Si_3N_4 coated substrates. Use of ultrahigh pre-deposition vacuum is recommendable to minimise the residual concentration of water vapour in the reaction chamber. Avoiding the formation of C=N and C≡N bonds is the most important obstacle to overcome in the search for the pure β-C_3N_4 phase.

8.3 Mechanical properties

Nanoindentation technique was used to study the mechanical properties of the films. It proved to be a very useful technique with which to obtain relevant "mechanical fingerprints" of the behaviour of films under load. Hardness values of ~7-10 GPa and elastic modulus of 90-120 GPa were obtained. The mechanical properties of the films give an indication of the high sp^2 bonding concentration in the films, and are

dominated by the amorphous network, even though in films deposited at 100% Npp crystalline regions may be embedded in the overall network. The film hardness appears to be controlled by the amount of C≡N bonding, rather than the total nitrogen content. The C≡N bond terminates the carbon backbone leading to less tightly bound C atoms, and hence, a weaker structure. Carbon nitride films exhibited also a high elastic recovery as measured from load-displacement curves. The Oliver and Pharr method used for hardness and elastic modulus calculations tend to underestimate the hardness of films showing a high elastic recovery behaviour. Further analysis of nanoindentation curves (looking at the behaviour of the loading portion of the curve) produced hardness values of 14-17 GPa.

Increasing deposition temperature to 420°C did not have a major effect in the mechanical properties. Annealing above 550°C lead to a loss of nitrogen, which weakens the structure due to the disruption caused by N_2 molecules as they desorb from the surface. Hardness was found to drop dramatically from 9 to 3-4 GPa. The effect of negative substrate bias (Vs) on film hardness was also investigated. Hardness values peak at a substrate bias $-100\ V > Vs < -150\ V$. This is related to the higher concentration of sp^3 bonding occurring in this region of substrate bias.

Steady state mean coefficients of friction in the range 0.4-0.7 were obtained for carbon nitride films. Higher coefficients of friction were found for harder films deposited at different substrate bias. Hard brittle films delaminate under load and cause abration wear during friction evaluation. Finally, the stress is shown to be concentrated at the film-substrate interface whereas the bulk of the film is stress-free. The stress is increased at higher substrate bias as ion bombardment increases. The addition of nitrogen bonding in the films significantly relieves the high levels of stress normally found in hard carbon films.

8.4 Electronic states

The electronic structure of carbon nitride is rather complicated due to the formation of different bonds between carbon and nitrogen. The valence band (VB) spectra of a series of films deposited by reactive magnetron sputtering technique at different Npp was investigated by XPS and UPS. The VB spectra obtained were different in both cases, but they show similar features. The structures observed at low binding energies, corresponding to p electrons, are poorly defined and appear at different energies due to differences in photoionisation cross sections and the different excitation energies involved. By fitting the obtained spectra in the low binding energy region, the evolution of π and σ bands was described. UPS was found to be more sensitive to p electron states than XPS. The bands seen closest to the 'zero' of binding energy were attributed to p electrons shared in π bonds, while the band observed at higher energies were assigned to p electrons shared in σ bonds.

The observed trends indicated an increase in the π bonding when Npp is increased from 0 to 25%. At 100% Npp, the π bonding was found to decrease. This behaviour is explained as follows: up to 25% Npp, N atoms form hybridised bonds with C (mainly C=N and C≡N bonds) and substitute C atoms in a planar position within a graphitic-like structure. This is causing an increase in the π bonding seen in the XPS and UPS VB spectra. Up to 25% Npp, the role of nitrogen is to produce more sp^2 clusters and to substitute carbon in aromatic rings forming mainly triple and double bonds in a non-doping configuration such as the one seen in pyridine. Above 25% Npp, the creation of C=N bonds gets saturated. There is an increase of N=N bonds and at increased levels of Npp, the formation of tetrahedral configuration of C-C and C-N bonds is favored. With 100% Npp the C=N π signal gets relatively smaller and there is an increase in the σ bonding signal which presumably comes from the C-N sp^3 bonds. At high nitrogen partial pressures, N disrupts the aromatic ring structure and facilitates a more three dimensional network which helps the formation of sp^3 bonds.

The XPS generated VB spectra also gave an idea of the interlinked carbon backbone nature of the carbon nitride films. A peak corresponding to a mixture of s and p electron states was seen to dominate the spectra identifying the structural nature of this solid, which is significantly different from diamond-like and graphitic features. The UPS generated VB spectra confirms the structural rearrangement occurring when Npp>25%.

The ESR and EELS spectra of the films were also investigated. Increasing the Npp from 0 to 50% leaves the ESR spectra unchanged, but the spin concentration drops from $2.6x10^{18}$ cm^{-3} to $2.1x10^{17}$ cm^{-3}. This drop is related to the replacement of a C atom in a dangling bond site by a N atom in a pyridine-like domain, a situation which is similar to the pasivation of Si dangling bonds in a-Si by the introduction of H. An unusual g value of 2.005 was found for these samples which was due to the superposition of a signal coming from the Si substrate. The spin density increases for Npp>50%, which agrees with the observed structural rearrangement that occurs at high Npp. The increase in negative bias reduces the spin density of the films and increases the peak-to-peak line width observed in the ESR spectra. This was related to carriers (associated with spin) becoming more mobile, so that the relaxation time is reduced with negative bias, which agrees with the observed decrease in resistivity.

The EELS spectra of carbon nitride films exhibit two main features: a small peak at about 6.5 eV which was attributed to plasma oscillations in which π electrons are involved having the sp^2 configuration, and a broad peak attributed to oscillations from all valence electrons ($\pi+\sigma$ peak) at ~24 eV. The presence of the former peak is an unambiguous signature of the presence of sp^2 sites in the amorphous network. The observed overall change in the shape of the EELS spectra also signatures the structural change that occurs with increasing Npp during deposition. From the position of the $\pi+\sigma$ plasmon peak, the valence electron density was estimated as ~$4.2x10^{18}$ cm^{-3} and the mass density of the films as ~2-2.1 gcm^{-3}.

The bonding structure varies greatly with changes in the Npp, even though this results in very little difference in the nitrogen content of the films. The results show that when a sputtering gas containing 100% N_2 is used rather than an Ar/N_2 mixture, the

production of sp^3 bonded β-C_3N_4 is more likely to occur; the absence of Ar^+ ions or energetic neutrals which are heavier than N_2^+ ions may be less disruptive of the process whereby the nitrogen and carbon bond together.

8.5 Electrical/optical properties

Amorphous carbon nitride films deposited by an opposed target Penning-type magnetron sputtering source have been found to have low resistivity, which is indicative of a high graphitic content. Nitrogen free films have resistivities of ~10^{-2} Ωcm, which increased to 3-4 Ωcm for films with the highest nitrogen contents (36 at.% N). The resistivity was found to increase with nitrogen partial pressure during deposition, but appears to be controlled by the amount of C≡N bonding rather than the total nitrogen concentration or other bond type. The refractive index also reduces with nitrogen content. In this case also, the C≡N bond density is the best predictor of the refractive index. A broad absorption edge was observed in the VIS/UV spectral region indicating a high degree of disorder in the film with a behaviour typical of amorphous semiconductors. Small optical gaps of 0.4-0.1 eV were estimated by constructing Tauc plots from measurements of the optical absorption coefficient. The measured optical band gap is low and decreases with nitrogen partial pressure. Above 50% Npp, the calculated gap increases slightly which signals an increase in the sp^3 nature of the bonding structure. No relation was found between the increase in resistivity and the measured Tauc optical gap.

Hall effect measurements revealed that the films have low carrier mobilities (<0.3 cm^2/Vs) and carrier concentrations > $7x10^{18}$ cm^{-3}. Thermopower measurements indicated that the films are n-type. From thermal activation studies of the resistivity, the activation energy was found to increase with nitrogen content, suggesting a reduction in the density of defect states near the conduction band edge. The activation energy for nitrogen-free films is ~0 eV, while for nitrogen-containing films is ~0.05 eV. This behaviour is typical of a transition from metallic to semiconducting behaviour as nitrogen is incorporated in the films.

An energy diagram of the density of states (DOS) was suggested for the deposited carbon nitride films which was based on typical models proposed for disordered amorphous semiconductors. The disordered structure and the low mobilities derived from absorption and transport measurements of deposited carbon nitride films imply that the transport properties are dominated by the large density of defects so that conduction associated with direct motion between defect states dominates the transport over significant temperature ranges. For temperatures > 166 K, the activation energy is a linear function of temperature and increases with nitrogen partial pressure. For temperatures below room temperature, the conduction mechanism is suggested to be dominated by a mixture of transport by carriers excited into localized states at the band edges (thermally activated hoping) and hopping at localized states close to the mobility edges (fixed range hopping). At higher temperatures, transport by carriers excited beyond the mobility edges into non-localized (extended) states is likely to be the dominant conduction mechanism. Pure carbon films showed a small variation of resistivity as a function of temperature which indicates that the conduction mechanism is different to nitrogen-containing films and is related to a conduction typical of graphite with defects.

The main effects of including N appear to be due to structural changes in the film leading to different band gap structures rather than a conventional doping effect. This is not surprising due to the high concentration of nitrogen in the films, which is no longer a dilute dopant but has a major effect in the atomic rearrangements. The effect of nitrogen incorporation in the electrical properties of the films has proved to be very different to the effect it has when incorporated to semiconducting forms of a-C such as a-C:H and ta-C. This is due to the highly conducting a-C normally produced by sputtering, in which nitrogen takes mainly non-doping configurations.

The resistivity of the films was found to decrease with substrate bias. This was related to the decrease of the amount of C≡N bonds linked to aromatic rings, which facilitates electrical transport by cross-linking. The resistivity was also found to decrease with deposition temperature, which might be explained by a process of graphitization taking place as the deposition temperature increases.

The refractive index also reduces with nitrogen content. In this case also, the C≡N bond density is the best predictor of the refractive index. The decrease in refractive index might also be accompanied by a decrease in film mass density. The behaviour of the refractive index and extinction coefficient for films deposited at different Npp confirms the increase in the sp^3/sp^2 ratio for Npp>25%.

Carbon nitride films deposited by reactive magnetron sputtering were found to be mainly amorphous and all the analysis techniques employed (spectroscopy, electrical and optical measurements, nanoindentation studies, etc) gave evidence of a film structure and properties which are characteristic of an amorphous carbon nitride solid with a high sp^2 content. However, there is also some evidence of crystalline β-C_3N_4 areas coexisting with the mainly amorphous structure for films deposited at 100% Npp and there is room for further optimisation of the quality of carbon nitride films deposited by reactive Penning-type magnetron sputtering with respect to composition, structure and application-relevant properties.

8.5.1 Field emission

The electron emission properties of the films were investigated with an experimental set up suitable for emission experiments under vacuum. Emission current was only detected in films deposited at 100% Npp at deposition temperatures (Td) of 280°C and 420°C; the maximum emission current densities obtained were 3.9 and 2.2 $\mu A/cm^2$, respectively, for a maximum electric field of 20 V/μm. The turn on field voltages were in the range 12-14 V/μm. These results are well below those found for DLC films and other nitrogenated carbon films, due to the high sp^2 content of the films considered here, which causes a very small gap and therefore a high electron affinity. The emission current measured is suggested to be caused by emission occurring from protrusions of the surface and donor centers which exist due to the presence of the n^{++}-Si/a-CN interface. The conducting sp^2 sites present in the film can sustain the electron transport to the surface and make electron emission possible.

8.5.2 Recommendations for investigating states in the gap

Hall effect measurements on carbon nitride films were not very useful due to the low mobility of the films. Meaningful interpretation of Hall data is difficult on materials with carrier mobilities below about $1cm^2/Vs$. The mechanism of charge transport in such materials is basically different from the normal type of band conduction found in high mobility semiconductors. Due to the low mobility of the carbon nitride films investigated here, it is worth considering techniques which have been employed for analysing the states in the gap of a-Si. In glow discharge-deposited amorphous Si and Ge, the states in the gap are due to dangling bonds at vacancies, voids, or to impurities. States in the gap of a-Si and their effect on photoconductivity, and drift mobility has been extensively examined by Mott et al.[3]

8.5.2.1 Field effect measurements

Field effect measurements can be used to investigate the distribution of localized states in the gap and the field effect mobility, provided the total state density is not too high. With the field effect technique one measures changes in conductivity brought about by changing the carrier density in the films. The results can yield information about the number and distribution of states in the gap. A field effect experimental set up was used here for carbon nitride films. The technique has been applied successfully in a-Si[4] and in a-C[5] films. The experimental problem consists of applying a large external electric field normal to the specimen surface with minimum leakage current into the specimen. *Figure 8.1* shows the arrangement that was tried here. The film was deposited onto an oxidised Si substrate. The back of the substrate was coated with an Al layer which formed the field electrode F. The Al current electrodes A_1 and A_2 in the shape of dots were evaporated onto the carbon nitride films. A voltage V_F was applied to the field electrode inducing charge into the specimen. A constant potential difference V_A has to be applied across the current electrodes. Then, the specimen current I is recorded as the field voltage V_F is changed incrementally in equal steps.

Inconsistent results were obtained with this experimental set-up, which are believed to be caused by leakage currents originating from the oxidised Si substrate. The use of

quartz as the substrate may improve results since much higher fields can be applied with minimum leakage current and is possible to extend measurements to state densities > 10^{20} cm^{-3} eV^{-1}. High fields across a thinner good insulator between field electrode and specimen are desirable. [4]

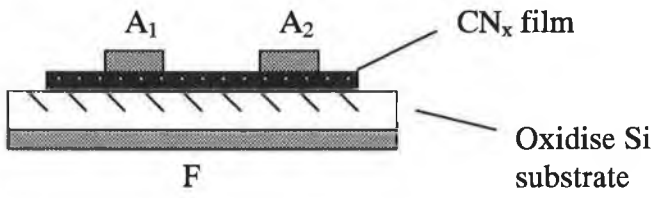

Figure 8.1: Specimen geometry used in field effect experiment.

If a positive potential is applied to F with respect to A_1 and A_2, the number of electronic charges induced in the specimen can be calculated from the known capacity of the arrangement. Almost all the induced charge will condense into localized states at the Fermi level and once the new steady state has been attained, the electronic states in the system will have been lowered with respect to the Fermi level. The observed change in conductivity allows the calculation of the change in electron energy at the specimen surface. Using a step-by-step increase in the potential applied to F, it becomes possible to move quite an appreciable part of the localized state distribution past the Fermi level. From the analysis of the results, the density of localized states N(E) per unit energy can be calculated as a function of energy.[5] Drift mobility and conductivity measurements need to be carried out for the detailed analysis of field effect data.[6]

8.5.2.2 Drift mobility measurements

Drift mobility measurements can also be considered in the future. The experimental set up would involve the design of some measurement device suitable for the special characteristics of the carbon nitride films. Drift mobility techniques however are particularly suited for specimens with low carrier mobility. The experiment involves the transient excitation of excess carriers within the specimen, and the timing of the

transit of these carriers in the applied field E_A. A suitable experimental set up is illustrated in *figure 8.2*.[7]

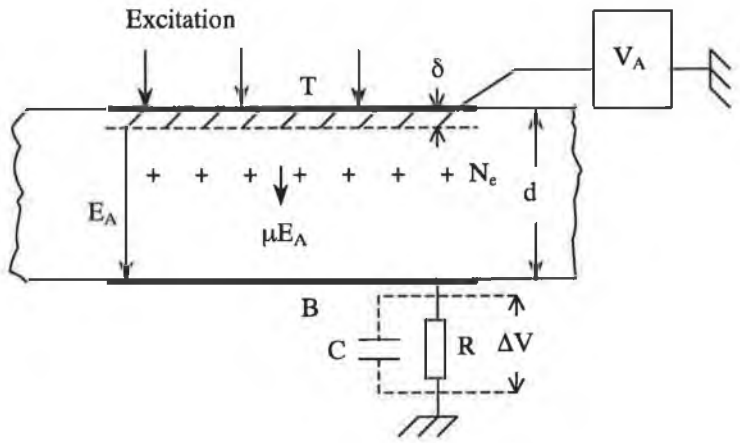

Figure 8.2: Drift mobility measurements set up.

The film of thickness d is fitted with evaporated metal electrodes T and B. The top electrode is connected to a steady or pulsed source of potential; the bottom electrode is returned to ground through a resistor R, normally much smaller than the specimen resistance. Excess carriers are generated by a short pulse (often in the nanosecond range) of electrons or photons. If, as is usually the case, the absorption depth δ of the excitation is a small fraction of the specimen thickness, a narrow sheet of carriers of one sign will be drawn across the specimen in the applied field (E_A) with a drift velocity μE_A. The transit time t_t is determined by measuring the potential ΔV as a function of time with sensitive, wide-band electronic equipment. C denotes the total input capacity of the detecting system. Once the transit time has been determined, the drift mobility is given by

$$\mu = \frac{d}{E_A t_t}$$

Both types of carriers can be investigated in the same specimen by reversing E_A.

These measurements are often complicated by trapping effects. Pulsed applied fields and the use of short transit times can solve some of the trapping problems. The

problems introduced by trapping and space charge effects and different methods of carrier excitation have been studied in detail by Spear et al.[8] The most common method employed for the transient generation of excess carriers is to illuminate the top electrode with a light flash of suitably short duration. The efficiency of electron-hole generation rises rapidly as the photon energy approaches that of the fundamental absorption edge, so that the majority of carriers are generated too close to the region of the illuminated surface. This can be a serious disadvantage. The density of imperfection centres is generally higher near a surface, and these, together with any surface states that might be present, will considerably shorten the carrier lifetimes in the generation region. Experimentally, the problem consists of finding a light source which produces an intense flash of sufficiently short duration ($t_e << t_t$) in a suitable spectral range. High-energy fast particles, such as electrons, can be used as a method of excitation and have normally many advantages over optical excitation[8], such as the possibility of controlling the penetration depth δ over a wide range.

References

1. A.K.M.S. Chowdhury, D.C. Cameron and M.J. Gregg, "Structural characterisation of sputtered deposited CN_x films by transmission electron microscopy", Suplement to Proceedings to the Royal Microscopical Society, 33 (1998).
2. K.M. Yu, M.L. Cohen, E.E. Haller, W.L. Hansen, A.Y. Liu and I.C. Wu, Phys. Rev. B 49 (1994) 5034.
3. N.F. Mott, E.A. Davis and R.A. Street, Phil. Mag. 32 (1975) 961.
4. A. Madam, P.G. Le Comber and W.E. Spear, J. Non-Cryst. Solids 20 (1976) 239.
5. J.C. Dawson and C.J. Adkins, J. Phys.: Condens. Matter 7 (1995) 6297.
6. W.E. Spear and P.G. Le Comber, J. Non-Cryst. Solids 8-10 (1972) 727.
7. W.E. Spear, Electronic transport properties of solids and liquids, Advance Physics 23 (1974) 523.
8. W.E. Spear, J. Non-Cryst. Solids 1 (1969) 197.

Appendix A

Heating plate assembly

The assembly drawing of the heating plate with a description of the different parts is attached in the next page. The four lamps used are Philips IRZ 500 Linear Heat Lamps. The end pieces of the lamps are 'metal caps'. The maximum permissible temperature measured on the heat lamp metal caps is 240°C. The pieces that needed cooling which were attached to the ends (No. 8 on drawing) are made from copper and are called heatsinks. These pieces were necessary to try and dissipate the heat away from the lamp ends. The Ceramic Insulators (No. 9 on drawing) were machined in the workshop from Macor Machinable Glass Ceramic RS No. 158-3095.

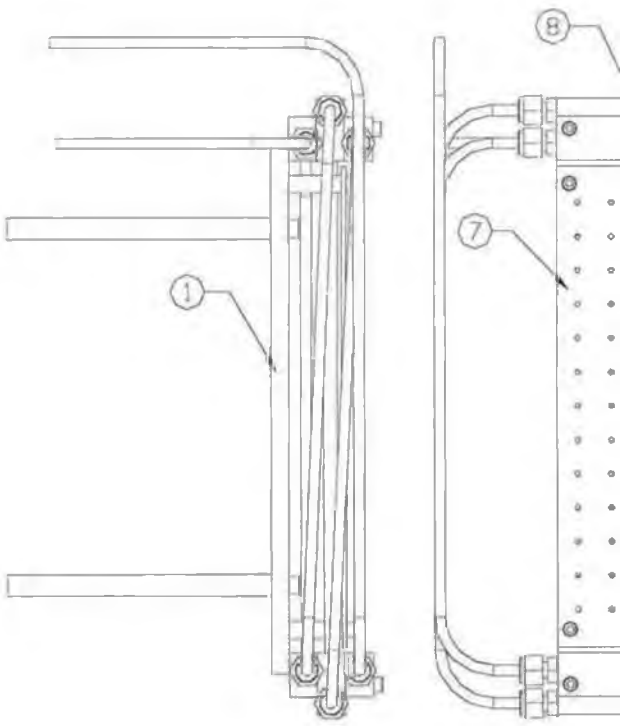
8
7
1

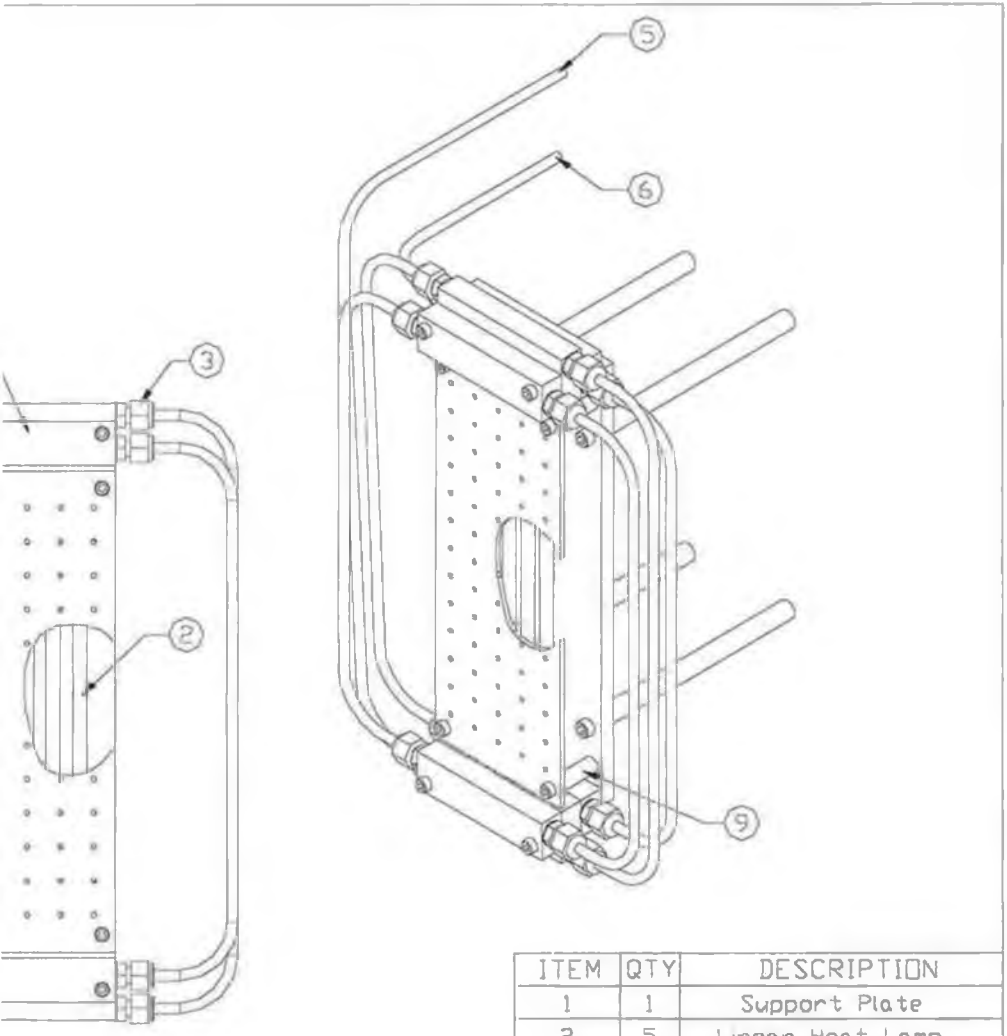

ITEM	QTY	DESCRIPTION
1	1	Support Plate
2	5	Linear Heat Lamp
3	12	Swageloc Tube Fitting
5	1	Water Outlet
6	1	Water Inlet
7	1	Molybdenum Plate
8	2	Lamp Heatsink
9	3	Ceramic Insulator

Appendix B

Deviation of formula for four-point probe measurements

The formula used in this research for the computation of thin film resistivity is derived below. This calculation is limited to the four-point probe method. The general assumptions are:

I. The resistivity of the material is uniform in the area of measurement.

II. The measurements should be made on surfaces which have a high recombination rate, such as mechanically lapped surfaces.

III. The surface on which the probes rest is flat with no surface leakage.

IV. The four probes used for resistivity measurements contact the surface at points that lie in a straight line.

V. The diameter of the contact between the metallic probes and the semiconductor should be small compared to the distance between probes.

VI. The probes are far from any of the other surfaces of the sample and the sample can thus be considered a semi-infinite volume of uniform resistivity material.

Figure B.1 shows the geometry being considered. Four probes are spaced s_1, s_2, and s_3, apart. Current I is passed through the outer probes (1 and 4) and the floating potential V is measured across the inner pair of probes 2 and 3.

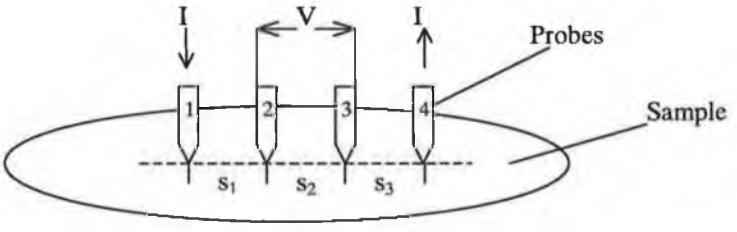

Figure B.1: Model for the four probe resistivity measurements.

The floating potential V_f at a distance r from an electrode carrying a current I in a material of resistivity ρ is given by[1]

$$V_f = \frac{\rho I}{2\pi r} \qquad (1)$$

In *figure B.1* there are two current-carrying electrodes (1 and 4), therefore the floating potential V_f, at any point in the film is the difference between the potential induced by each of the electrodes, since they carry currents of equal magnitude but in opposite directions. Thus:

$$V_f = \frac{\rho I}{2\pi}\left(\frac{1}{r_1} - \frac{1}{r_4}\right) \qquad (2)$$

where r_1 is the distance from probe 1 and r_4 is the distance from probe 4.

The floating potential at probe 2 (V_{f2}) and 3 (V_{f3}) can be calculated from (2) by substituting the proper distances as follows:

$$V_{f2} = \frac{\rho I}{2\pi}\left(\frac{1}{s_1} - \frac{1}{s_2 + s_3}\right)$$

$$V_{f3} = \frac{\rho I}{2\pi}\left(\frac{1}{s_1 + s_2} - \frac{1}{s_3}\right)$$

The potential difference V between the probes is then

$$V = V_{f2} - V_{f3} = \frac{\rho I}{2\pi}\left(\frac{1}{s_1} + \frac{1}{s_3} - \frac{1}{s_2 + s_3} - \frac{1}{s_1 + s_2}\right)$$

and now, the resistivity can be calculated from

$$\rho = \frac{V}{I}\frac{2\pi}{\left(\frac{1}{s_1} + \frac{1}{s_3} - \frac{1}{s_1 + s_2} - \frac{1}{s_2 + s_3}\right)}$$

When the point probe spacing is equal ($s_1 = s_2 = s_s = s$), the above simplifies to

$$\rho = \frac{V}{I} 2\pi s$$

In the particular case of resistivity measurements on a thin film resting on a non-conducting bottom surface, and for very small values of *w/s*, (where *w* is the film thickness and s is the probe spacing) such that the film can be considered as an infinitely thin slice, a solution by the method of images, gives:[2]

$$\rho = \frac{\pi w}{\ln 2} \frac{V}{I}$$

References

1. L.B. Valdes, "Effect of electrode spacing on the equivalent base resistance of point-contact transistors" Proc. I.R.E., vol. 40, Nov (1952) 1429.

2. L.B. Valdes, Proc. I.R.E., vol 42 Feb (1954) 424.

Appendix C

Resistance heating evaporator

An Edwards Coating system E306A, depicted in *figure C.1*, was used as a resistance heating (thermal) evaporator for the deposition of Aluminium electrodes on the substrates and carbon nitride films. Initially, the whole system was chemically cleaned using trichloroethylene, acetone, methanol and de-ionised water. For Al evaporation, a Tungsten coil was used. The system has two shutters. One was used to isolate the substrates from the source when outgassing of the system occurs. The second shutter, known as the crystal shutter, was used with the crystal thickness monitor. The system was also used for field emission experiments.

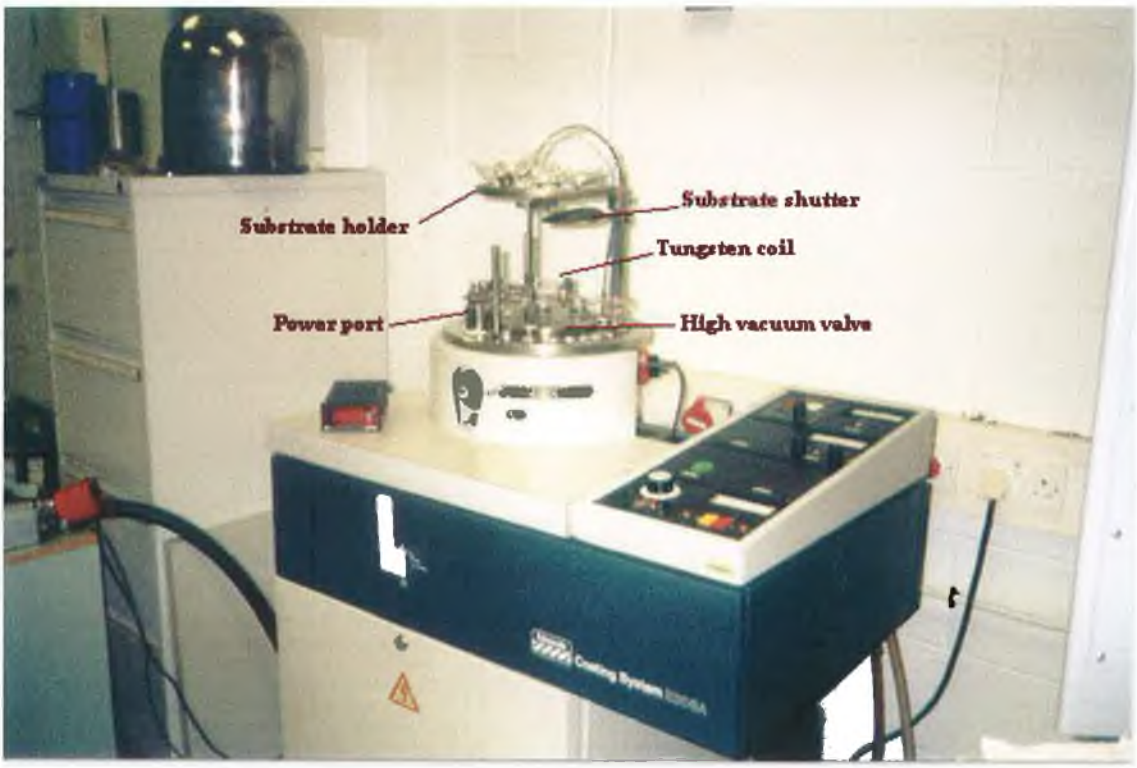

Figure C.1: Photograph of the resistance heating evaporator.

Appendix D

List of publications

1) M.A. Monclus, D.C. Cameron and A K M S Chowdhury, *"Electrical properties of reactively sputtered CN_x films"*, Thin Solid Films, 341, 1-2, (1999) 94.

2) M.A. Monclus, D.C. Cameron, R. Barklie, M. Collins, *"Electrical properties of reactively sputtered carbon nitride films"*, Surface and Coatings Technology, 116-119, (1999) 54.

3) M.A. Monclus, D.C. Cameron, A.K.M.S. Chowdhury, R. Barklie, M. Collins, *"Investigation of the valence band states of reactively sputtered carbon nitride films"*, Thin Solid Films, 355-356 (1999) 79.

4) M. A. Monclus, A. K. M. S. Chowdhury, D. C. Cameron, R. Barklie and M. Collins, *"The effect of nitrogen partial pressure on the bonding in sputtered CNx films: implications for formation of β-C_3N_4"*, presented at the 27th international conference on plasma surface engineering (PSE'99), Beijing, China.

5) M.J. Murphy, J. Monaghan, D.C. Cameron, A.K.M.S. Chowdury, M.Tyrrell, R. Walsh, M.A Monclus and M.S.J. Hashmi, *"A Penning type magnetron sputtering source and is use in the production of carbon nitride coatings"*, Journal of Vacuum Science and Technology A 17 (1999) 62.

6) J. Gilvarry, A.K.M.S. Chowdhury, M. Monclus, D.C Cameron, P.J McNally, and T. Tuomi, *"Stress behaviour of reactively sputtered nitrogenated carbon films"*, Surface and Coatings Technology 98, (1998) 979.

7) A.K.M.S. Chowdhury, M. Monclus, D.C Cameron, J. Gilvarry, M.J. Murphy, N.P Barradas, M.S.J. Hashmi, *"The composition and bonding structure of CN_x films and their influence on the mechanical properties"*, Thin Solid Films, 308-309, (1997) 130.

8) A.K.M.S. Chowdhury, D.C Cameron, M. Monclus, *"Effect of substrate negative bias on sp^2 to sp^3 phase transformation in carbon nitride thin films"*, presented at the 26th international conference on metallurgical coatings and thin films (ICMCTF'99) April 12-16, 1999, San Diego, California, USA.

9) D.P Dowling, K. Donelly, M. Monclus, M. McGuinness, *"The use of refractive index as a measure of diamond-like carbon film quality"*, Diamond and Related Materials, 7 (1998) 432.